ABSTRACT

Title of Dissertation:	ATOMISTIC AND THEORETICAL DESCRIPTION OF LIQUID FLOWS IN POLYELECTROLYTE-BRUSH-GRAFTED NANOCHANNELS
	Harnoor Singh Sachar, Doctor of Philosophy, 2021
Dissertation directed by:	Professor Siddhartha Das, Department of Mechanical Engineering

Polyelectrolyte (PE) chains grafted in close proximity stretch out to form a "brush"-like configuration. Such PE brushes can represent a special class of nanomaterials that are capable of exhibiting stimuli-responsive behavior. They can be manipulated as needed by changing the environmental conditions like pH, solvent quality, salt concentration, temperature, etc. This responsiveness renders them very useful for a plethora of applications such as lubrication, emulsion stabilization, current rectification, nanofluidic energy conversion, drug delivery, oil recovery, etc. Therefore, gaining fundamental insights into PE brush systems is of utmost importance for both industrial as well as academic research. In this dissertation, we make use of theoretical and computational tools to improve our understanding of planar PE brushes and then use this understanding to probe flows in PE brush-grafted nanochannels.

We begin our quest by conducting all-atom Molecular Dynamics (MD) simulations to probe the microstructure of planar PE brushes with an unprecedented atomistic resolution. This allows us to not only investigate the properties of the PE chains but also the local structure and arrangement of the counterions and water molecules trapped within the brushes. Next, we use our atomistic model to probe the effects of variation in charge density on the microstructure of weak polyionic brushes. Such a variation in the charge density is typically enforced by a change in the surrounding pH and is a characteristic behavior of pH-responsive (annealed) PE brushes.

Furthermore, we go on to develop the most exhaustive theoretical model for pH-responsive PE brushes known as the augmented Strong Stretching Theory (SST). Our model is an improvement over the existing state-of-the-art as it considers the effects of the excluded volume interactions and an expanded form of the mass action law. We further improve this model by including several non-Poisson Boltzmann effects, especially relevant at high salt concentrations. This improved model is in excellent agreement with the results of our all-atom MD simulations.

Next, we use our augmented SST to model pressure-driven transport in backbone-charged PE brush-grafted nanochannels. Our results are an improvement over previous electrokinetic studies that did not consider a thermodynamically self-consistent description of the brushes. Finally, we conduct all-atom MD simulations to probe the pressure-driven transport of water in PE brush-grafted nanochannels using an all-atom framework. The nanoscale energy conversion characteristics obtained from our simulations are in reasonable agreement with the predictions of our continuum framework and lie within the range of values reported by a prior experimental study.

ATOMISTIC AND THEORETICAL DESCRIPTION OF LIQUID FLOWS IN POLYELECTROLYTE-BRUSH-GRAFTED NANOCHANNELS

by

Harnoor Singh Sachar

Dissertation submitted to the Faculty of the Graduate School of the
University of Maryland, College Park, in partial fulfillment
of the requirements for the degree of
Doctor of Philosophy
2021

Advisory Committee:
Professor Siddhartha Das, Chair
Professor Amir Riaz
Professor Peter W. Chung
Professor Don DeVoe
Professor Silvina Matysiak, Dean's Representative

Acknowledgements

This work has been supported by the Department of Energy Office of Science grant DE-SC0017741. I would like to thank my advisor Dr. Siddhartha Das, the entire dissertation committee, and my colleagues for their valuable inputs and feedback. I acknowledge the computational support obtained from the Deepthought2 High-Performance Computing cluster at the University of Maryland. I would also like to express my gratitude to Dr. Peter W. Chung at the University of Maryland for providing his personal computational resources to carry out some of the simulations.

Table of Contents

Acknowledgements ii

Table of Contents iii

List of Tables vi

List of Figures viii

List of Abbreviations xvi

Chapter 1: Background and Motivation 1

1.1. Structure and Configuration of Polyelectrolyte Brushes 1
1.2. Flows in Polyelectrolyte Brush-grafted Nanochannels 3

Chapter 2: Densely Grafted Polyelectrolyte Brushes Trigger "Water-in-Salt" like Scenarios and Ultraconfinement Effect 6

2.1. Introduction 6
2.2. Results 9
2.2.1 All-atom MD Simulation Results for the PE Brush Configuration 9
2.2.2 Counterion Distribution, Structure, and Properties: Brush-induced "Water-in-Salt" Like Scenario and Counterion Confinement 15
2.2.3 Water Structure, and Properties: Brush-induced Confinement 22
2.3. Implications for Continuum Models 29
2.4. Effect of Multivalent Counterions 30
2.5. Simulation Details 35
2.6. Force Field Parameters 39
2.7. Conclusions 46

Chapter 3: All-atom Molecular Dynamics Simulations of Weak Polyionic Brushes: Influence of Charge Density on the Properties of Polyelectrolyte Chains, Brush-Supported Counterions, and Water Molecules 47

3.1. Introduction 48
3.2. Simulation Details 50
3.3. Results 55
3.3.1 PE Molecules: Brush Height and Chain Mobility 55
3.3.2 Counterions: Local Arrangement and Distribution 64
3.3.3 Water: Local Arrangement and Distribution 79
3.4. Force Field Parameters 95
3.5. Conclusions 104

Chapter 4: Revisiting the Strong Stretching Theory for pH-responsive Polyelectrolyte Brushes: Effects of Consideration of Excluded Volume Interactions and an Expanded Form of the Mass Action Law 105

4.1. Introduction 107

4.2. Self-Consistent Field Approach 111
4.2.1. Free Energy Equations 111
4.2.2. Variational Formalism 115
4.3. Results 122
4.3.1. Effects of Consideration of Excluded Volume Interactions 122
4.3.2. Effects of Consideration of an Expanded Form of the Mass Action Law 129
4.4. Discussions 135
4.4.1. Applicability of the Proposed Theory 135
4.4.2. Limitations and Scope of Improvement of the Proposed Theory 136
4.5. Strong Stretching Theory for pH-Responsive Polyelectrolyte Brushes in Large Salt Concentrations 138
4.5.1. Motivation and Model Description 138
4.5.2. Theory 143
4.5.3. Results 152
4.6. Conclusions 174
Chapter 5: Electrokinetic Energy Conversion in Nanochannels Grafted with pH-responsive Polyelectrolyte Brushes Modelled using Augmented Strong Stretching Theory 176
5.1. Introduction 177
5.2. Theory 182
5.2.1. Augmented Strong Stretching Theory Model for pH-responsive PE brushes 182
5.2.2. Liquid Transport in PE brush Grafted Nanochannels 186
5.3. Results 190
5.4. Conclusions 213
Chapter 6: Molecular Dynamics Simulations of Pressure-Driven Transport in Polyelectrolyte-Brush-Grafted Nanochannels 215
6.1. Introduction 216
6.2. Simulation Details 218
6.3. Results 224
6.3.1. Flow-induced Tilting of the PE Brushes 224
6.3.2. Overscreening of the Grafted PE Layer 226
6.3.3. Flow Profile and Nanoscale Energy Conversion Characteristics 229
6.4. Comparison with Continuum Predictions 235
6.5. Comparison with Prior Experimental Study 243
6.6. Conclusions 248
Chapter 7: Validation, Verification, and Summary of Contributions 250
7.1. Comparison of All-atom MD Simulations with Continuum Models 250
7.1.1. Match between All-atom MD Results of Brush Height and Scaling Laws of the Non-linear Osmotic Brush Regime 250
7.1.2. Comparison of the Theoretical Predictions of the Modified Strong Stretching Theory (MSST) to the All-atom MD Results for Brush Height 254

7.1.3. Comparison of All-atom MD Results for Pressure Driven Flow in PE Brush-grafted Nanochannels to the Continuum Predictions 258
7.2. Comparison of All-atom MD Simulations and Continuum Calculations with Prior Experiments 266
7.2.1. Comparison of All-atom MD Results for Electroosmotic Flow in PE Brush-grafted Nanochannels to Existing Experiments 266
7.2.2. Comparison of All-atom MD simulations and Continuum Calculations for Pressure-driven Transport in PE Brush-grafted Nanochannels to Prior Experimental Study 276
7.3. Summary of Contributions 281
Appendix A 285
Appendix B 288
Appendix C 290
Bibliography 292

List of Tables

Table 2.1: Variation of brush thickness <z_b>, counterion layer thickness <z_{ci}> and brush end-point height <z_e> with N and σg. 12
Table 2.2: Comparison of the solvation structure of Ca^{2+} ions (in terms of the species, namely $O_{Carboxylate}$ atoms or O_w atoms, occupying the solvation shell) in bulk and within the PE brushes for the case where the Ca^{2+} are the counterions neutralizing the charge on the PE brushes. The table also provides the weight and the volume ratios of the "salt" (Ca^{2+}-PE brush repeating unit) to the water indicating if the "salt" outnumbers water in mass and volume (and thereby leads to the "water-in-salt"-like structure). 31
Table 2.3: Equilibration time (T_{equi}), production run time (T_{prod}) and autocorrelation time (τe) for all N and σg..... 38
Table 2.4: Charge, mass and LJ parameters for all different atom types..... 41
Table 2.5: Bond parameters used in the simulations 42
Table 2.6: Angle parameters used in the simulations 43
Table 2.7: Dihedral parameters used in the simulations 44
Table 2.8: Improper dihedral parameters used in the simulations 45
Table 3.1: Equilibration time (t_{equi}), production run time (t_{prod}) and autocorrelation time scale (τe) for various degrees of ionization and grafting densities. 54
Table 3.2: Equilibrium end-point brush height for various degrees of ionization and grafting densities..... 59
Table 3.3: Charge, mass and LJ parameters for various atom types..... 97
Table 3.4: Bond parameters for all different types of bonds 98
Table 3.6: Dihedral parameters for different types of dihedrals..... 103
Table 3.7: Improper dihedral parameters for different types of improper dihedrals 103
Table 4.1: Comparison of brush heights obtained from the MSST model presented in section 4.5 and all-atom MD simulations of chapter 2 for various values of the number of carbon atoms (N) and grafting density (in units of $1/\sigma 2$), where $\sigma = 3.5$ Å is the Lennard Jones size parameter). The values of bulk salt concentration ($c\infty$ in M) used in MSST model, the equivalent average cation concentration within the brushes for the MSST model, and the average counterion concentration for the MD simulations are also provided. Please note for a given N and σg value, we consider such a value of the bulk salt concentration that yields nearly identical values of cation concentration and counterion concentration for the MSST model and the MD simulations, respectively. Only under such circumstances, we could compare that height values obtained from the present MSST model and the all-atom MD simulations. Other parameters used in the MSST model are as follow: Kuhn length, a, of 1 C-C bond length equivalent to 1.53 Å and the density of chargeable sites (γ) equal to $0.5/a3$. 173
Table 6.1: Equilibration time (t_{equi}) and production run time (t_{prod}) for different applied pressure gradients..... 223
Table 6.2: Volume flux for water transport and nanoscale energy conversion characteristics obtained from the all-atom MD simulations (for different applied pressure gradients). 234

Table 6.3: Comparison of the average cation concentration inside the grafted PE layer and equilibrium brush heights obtained from the continuum calculations and all-atom MD simulations (for the case of no applied pressure gradient). Parameters used in the MSST model are a=1.53 Å, ℓ =15.65 Å, $c\infty$=1.02 M, γ=0.5/$a3$, h=60.225 Å, N=48, pK_a=3.5, pH_∞=7. All other parameters for the MSST model are identical to that used in Fig. 4.20. 241
Table 6.4: Comparison of the volume flux for water transport and nanoscale energy conversion characteristics obtained from the continuum calculations and all-atom MD simulations (for different applied pressure gradients). Parameters used in the MSST model are a=1.53 Å, ℓ =15.65 Å, $c\infty$=1.02 M, γ=0.5/$a3$, h=60.225 Å, N=48, pK_a=3.5, pH_∞=7. All other parameters for the MSST model are identical to that used in Fig. 4.20. Parameters used in the calculations of the flow rate and nanoscale energy conversion characteristics are $\eta = 8.9 \times 10 - 4$ Pa.s, $\mu Na+= 4.98 \times 10 - 8$ m^2/Vs, $\mu Cl-= 6.88 \times 10 - 8$ m^2/Vs, L=234.75 Å, and w=93.9 Å. 242
Table 7.1: Comparison of brush heights obtained from the MSST model presented in section 4.5 and all-atom MD simulations of chapter 2 for various values of the number of carbon atoms (N) and grafting density (in units of 1/$\sigma 2$), where $\sigma = 3.5$ Å is the Lennard Jones size parameter). 257
Table 7.2: Comparison of the average cation concentration inside the grafted PE layer and equilibrium brush heights obtained from the continuum calculations and all-atom MD simulations (for the case of no applied pressure gradient). Parameters used in the MSST model are a=1.53 Å, ℓ =15.65 Å, $c\infty$=1.02 M, γ=0.5/$a3$, h=60.225 Å, N=48, pK_a=3.5, pH_∞=7. All other parameters for the MSST model are identical to that used in Fig. 4.20. 264
Table 7.3: Comparison of the volume flux for water transport and nanoscale energy conversion characteristics obtained from the continuum calculations and all-atom MD simulations (for different applied pressure gradients). Parameters used in the MSST model are a=1.53 Å, ℓ =15.65 Å, $c\infty$=1.02 M, γ=0.5/$a3$, h=60.225 Å, N=48, pK_a=3.5, pH_∞=7. All other parameters for the MSST model are identical to that used in Fig. 4.20. Parameters used in the calculations of the flow rate and nanoscale energy conversion characteristics are $\eta = 8.9 \times 10 - 4$ Pa.s, $\mu Na+= 4.98 \times 10 - 8$ m^2/Vs, $\mu Cl-= 6.88 \times 10 - 8$ m^2/Vs, L=234.75 Å, and w=93.9 Å. 265

List of Figures

Figure 2.1: Structure and Configuration of the PE Brushes 14
Figure 2.2: Distribution, Structure, and Properties of the Counterions 19
Figure 2.3: Transverse variation of net charge across the simulation domain, for different values of σg. Results are shown for N=69. The arrows indicate the position of average brush end-point height $<z_e>$. 20
Figure 2.4: Normalized probability distribution $p(r)\sigma^2$ of finding the nearest $O_{Carboxylate}$ atom at a distance r/σ from the counterions within the PE brush layer. σg=0.05/σ², 0.1/σ², 0.2/σ² and N=49. 21
Figure 2.5: Distribution, Structure, and Properties of Water 27
Figure 2.6: Transverse variation of $n_{HB,w}$ across the simulation domain for various σg. Results are shown for N=49. 28
Figure 2.7: (a) Variation in the solvation structure of divalent Ca^{2+} counterions with σg (top axis) and counterion concentration (bottom axis). (b) Variation in the salt (Ca^{2+}-PE brush repeating unit) to water ratio by weight and volume within the PE brushes with σg (top axis) and counterion concentration (bottom axis). Table 2.2 summarizes the different numbers represented in (a) and (b). (c) Comparison of counterion MSD within PE brush layer for monovalent (Na^+) and divalent (Ca^{2+}) counterions for σg=0.05/σ² and 0.2/σ², (d) Comparison of MSD of water molecules within the PE brushes for σg=0.05/σ² and 0.2/σ² (see inset). N=49 is used for all subfigures. 34
Figure 2.8: Autocorrelation function $C_e(t)$ of average end-point brush height $<z_e>$ for various σg. Results are shown for N=69. 37
Figure 2.9: Schematic representation (not to scale) of the fully ionized polyacrylic acid molecule. The arrows indicate the atom type of their respective atoms. Dashed box indicates the polyelectrolyte's (PE's) repeating unit. 39
Figure 3.1: Autocorrelation function $[Cet]$ corresponding to the average end-point brush height, plotted over the production run for various degrees of ionization for (a) $\sigma g = 0.1/\sigma 2$and (b) $\sigma g = 0.2/\sigma 2$. Only three values of degree of ionization (f) are plotted to avoid clutter. 53
Figure 3.2: Variation in the end-point brush height with degree of ionization for different grafting densities. 56
Figure 3.3: Equilibrium end-point brush height for different degrees of ionization and grafting densities obtained via MD simulations and scaling laws of the non-linear osmotic brush regime. 58
Figure 3.4: Stratification of the mean squared displacement (MSD) of backbone carbon atoms of the PE chains for various degrees of ionization at t=100ps for (a) σg=0.1/σ² and (c) σg=0.2/σ². MSD of the non-grafted terminal Carbon atom of the PE chains for various degrees of ionization for (b) σg=0.1/σ² and (d) σg=0.2/σ². ... 62
Figure 3.5: Stratification of the mean squared displacement (MSD) of backbone carbon atoms of the PE chains for various degrees of ionization at t=50ps for (a) σg=0.1/σ² and (c) σg=0.2/σ². MSD of the middle (25th) Carbon atom of the PE chains for various degrees of ionization for (b) σg=0.1/σ² and (d) σg=0.2/σ². 63

Figure 3.6: Variation of counterion concentration (expressed in terms of molarity and molality) within the PE brush layer with the degree of ionization for (a) σg=0.1/σ^2 and (b) σg=0.2/σ^2. In both (a) and (b) the markers are the results from the MD simulations. 65
Figure 3.7: Transverse counterion distribution profiles [$\rho ci(z)$] for various degrees of ionization for (a) σg=0.1/σ^2 and (b) σg=0.2/σ^2. 66
Figure 3.8: Normalized probability distribution of finding the nearest $O_{Carboxylate}$ atom around Na^+ counterions within the PE brush layer for (a) σg=0.1/σ^2 and (c) σg=0.2/σ^2. (b) and (d) show the cumulative distribution function (cdf) for scenarios depicted in (a) and (c) respectively. (e) depicts the percentage of counterions (present within the PE brush layer) condensed on $O_{Carboxylate}$ atoms for different degrees of ionization and grafting densities. 70
Figure 3.9: Variation in the solvation structure of Na^+ counterions (within the PE brush layer) with degree of ionization for (a) σg=0.1/σ^2 and (c) σg=0.2/σ^2. 'Salt'-to-water mass and volume ratios for various degrees of ionization for (b) σg=0.1/σ^2 and (d) σg=0.2/σ^2. Here "salt" refers to Na^+ $RCOO^-$ (R: -CH_2-CH-). 73
Figure 3.10: Na^+ - O_w (O_w represents Oxygen of water molecules) RDF within the PE brush layer for various degrees of ionization for (a) σg=0.1/σ^2 and (b) σg=0.2/σ^2. Bulk Na^+ - O_w RDF is also provided for comparison (dashed line). 76
Figure 3.11: Mean squared displacement (MSD) of Na^+ counterions within the PE brush layer for various degrees of ionization for (a) σg=0.1/σ^2 and (b) σg=0.2/σ^2... 78
Figure 3.12: O_w-O_w RDF of water molecules within the PE brush layer for various degrees of ionization for (a) σg=0.1/σ^2 and (b) σg=0.2/σ^2. Bulk O_w-O_w RDF is also provided for comparison. 80
Figure 3.13: Transverse variation of mass density of water molecules for various degrees of ionization for (a) σg=0.1/σ^2 and (b) σg=0.2/σ^2. 83
Figure 3.14: Left axis- Static dielectric constant of water molecules (normalized with respect to bulk value) within the brushes for various degrees of ionization. Right axis- Variation in the percentage of bound water molecules within the PE brush layer for various degrees of ionization. (a) σg=0.1/σ^2 and (b) σg=0.2/σ^2. 86
Figure 3.15: Transverse variation in number of hydrogen bonds per water molecule n_{HB} with degree of ionization for (a) σg=0.1/σ^2 and (c) σg=0.2/σ^2. Transverse variation in number of hydrogen bonds between water molecules (per water molecule) $n_{HB,w}$ with degree of ionization for (b) σg=0.1/σ^2 and (d) σg=0.2/σ^2..... 89
Figure 3.16: Probability distribution of orientational tetrahedral order parameter (q) of water molecules within the PE brushes for various degrees of ionization for (a) σg=0.1/σ^2 and (b) σg=0.2/σ^2. Probability distribution of q for bulk SPC/E water is also provided for comparison..... 91
Figure 3.17: Mean squared displacement (MSD) of water molecules within the PE brushes for various degrees of ionization for (a) σg=0.1/σ^2 and (b) σg=0.2/σ^2. 94
Figure 3.18: Schematic representation (not to scale) of a partially ionized polyacrylic acid (PAA) molecule. The arrows depict the atom types of their respective atoms. Dashed boxes indicate two different types of repeating units. 95
Figure 4.1: Schematic showing the pH-responsive PE brush layer. 111
Figure 4.2: Variation of (a) non-dimensional equilibrium brush height H_0/a (a is the PE Kuhn length) and (b) percentage increase in equilibrium brush height $\Delta H_0/H_0$

(where $\Delta H_0 = H_0 - H_{0,\nu=0,\omega=0}$) with the first virial coefficient ν for different pH_∞ and c_∞ values. The case of Ref. 14 is the one where $\nu = 0, \omega = 0$ − we recover exactly the results of Ref. 14 when $\nu = 0, \omega = 0$. Other parameters for this figure are $\omega = 0.1$, $pK_a = 3.5$, a = 1nm, $\gamma = 1/a^3$ (1 PCS per kuhn monomer), N = 662, ℓ = 40nm, $k_B = 1.38 \times 10^{-23}$ J/K, T = 298K, e = 1.6×10^{-19} C, $\epsilon 0 = 8.854 \times 10^{-12}$ F/m, $\epsilon r = 79.8$, $pK_w = 14$, $pOH_\infty = pK_w - pH_\infty$, $c_{+,\infty} = c_\infty$, $cH+,\infty = 10 - pH\infty$, $cOH-,\infty = 10 - pOH\infty$, $c_{-,\infty} = c_\infty + cH+,\infty + cOH-,\infty$. 124
Figure 4.3: Comparison of monomer distribution profiles (ϕ) as a function of the dimensionless transverse distance along the brush (x_b/a, a is the Kuhn length) obtained for different values of the first virial coefficient ν using our theory and theory of Ref. 14 for different pH_∞ and c_∞ values. All other parameters are identical to that used in Fig. 4.2. 125
Figure 4.4: Comparison of non-dimensional chain end distribution profiles (g x a, a is the Kuhn length) as a function of the dimensionless transverse distance along the brush (x_b/a) obtained for different values of the first virial coefficient ν using our theory and theory of Ref. 14 for different pH_∞ and c_∞ values. All other parameters are identical to that used in Fig. 4.2. 127
Figure 4.5: Comparison of non-dimensional electrostatic potential profiles ($\psi = e\psi/(k_BT)$) as a function of the dimensionless transverse distance along the nanochannel half height (x/a) obtained for different values of the first virial coefficient ν using our theory and theory of Ref. 14 for different pH_∞ and c_∞ values. All other parameters are identical to that used in Fig. 4.2. 128
Figure 4.6: Variation of non-dimensional equilibrium brush height H_0/a with number of PCS per kuhn monomer γa^3 for different pH_∞ and c_∞ values. ν= 0.1, ω = 0:01. All other parameters are identical to that used in Fig. 4.2. 130
Figure 4.7: Comparison of monomer distribution profiles (ϕ) as a function of the dimensionless transverse distance along the brush (x_b/a, a is the Kuhn length) obtained for different values of PCS number density using our theory and theory of Ref. 14 for different pH_∞ and c_∞ values. ν = 0.1, ω = 0.01. All other parameters are identical to that used in Fig. 4.2. 131
Figure 4.8: Comparison of non-dimensional chain end distribution profiles (g x a, a is the Kuhn length) as a function of the dimensionless transverse distance along the brush (x_b/a) obtained for different values of PCS number density γ using our theory and theory of Ref. 14 for different pH_∞ and c_∞ values. ν = 0.1, ω = 0.01. All other parameters are identical to that used in Fig. 4.2. 133
Figure 4.9: Comparison of non-dimensional electrostatic potential profiles ($\psi = e\psi/(k_BT)$) as a function of the dimensionless transverse distance along the nanochannel half height (x/a) obtained for different values of PCS number density γ using our theory and theory of Ref. 14 for different pH_∞ and c_∞ values. ν = 0.1, ω = 0.01. All other parameters are identical to that used in Fig. 4.2. 134
Figure 4.10: Schematic representing the PE brush grafted on a planar substrate. We employ an asymmetric lattice model to describe the thermodynamics of the mobile ions and solvent dipoles. 142
Figure 4.11: Variation of the equilibrium brush height, $H0$, with salt concentration ($c\infty$, expressed in M, with $c\infty = n\infty/103NA$ and $n\infty$ is the bulk number density of the salt having the units of $1/m3$) for various $pH\infty$ values. Here, "IC" refers to the

case where only the ion-ion correlations, among the different non-PB effects, have been accounted for to describe the EDL electrostatics, while the PE brushes are described using the augmented SST. On the other hand, "SST" refers to the case where the EDL electrostatics is modelled using the standard PB model (i.e., we consider no non-PB term) and the PE brushes are modelled using the augmented SST. Parameters used in this work are $kB = 1.38 \times 10 - 23\, J/K, T = 300\, K$, $pKa = 3.5$, $a = 1nm, \ell = 30nm$, $\gamma = 1/a3$ (1 polyelectrolyte chargeable site per Kuhn monomer), $N = 400$, $pKw = 14$, $p = 1$, $\nu 0 = 0.5$, $\omega 0 = 0.1$, $e = 1.6 \times 10 - 19C$, $\epsilon 0 = 8.854 \times 10 - 12F/m$, $\epsilon r = 79.8$, $pOH\infty = pKw - pH\infty$, $n+,\infty = n\infty$, $nH+,\infty = 103NA10 - pH\infty$, $nOH-,\infty = 103NA10 - pOH\infty$, $n-,\infty = n\infty + nH+,\infty - nOH-,\infty$, $nw,\infty = 103NA1000\rho w - 58.44c\infty/18$, where ρw is the density (in g/cc) of the bulk electrolyte salt solution and is expressed as a function of the salt concentration[185], and $lc = 0.3nm$. 153
Figure 4.12: Monomer density profiles for various salt concentration values for (a) $pH\infty$ = 3, and (b) $pH\infty$ = 4. Here the cases shown by solid lines (-) and dashed lines (--) represent the cases of "IC" and "SST", respectively. Please see the caption of Fig 4.11 for the definition of "IC" and "SST" cases. All other parameters are identical to those used in Fig 4.11. 156
Figure 4.13: Transverse variation of electrostatic EDL potential for various salt concentration values for (a) $pH\infty$ = 3, and (b) $pH\infty$ = 4. Here the cases shown by solid lines (-) and dashed lines (--) represent the cases of "IC" and "SST", respectively. Please see the caption of Fig 4.11 for the definition of "IC" and "SST" cases. All other parameters are identical to those used in Fig. 4.11. 156
Figure 4.14: Variation of the equilibrium brush height, $H0$, with salt concentration for various $pH\infty$ values. Here, "POL" refers to the case where only the solvent polarization effect, among the different non-PB effects, has been accounted for to describe the EDL electrostatics, while the PE brushes are described using the augmented SST. On the other hand, "SST" refers to the case where the EDL electrostatics is modelled using the standard PB model (i.e., we consider no non-PB term) and the PE brushes are modelled using the augmented SST. We consider $pw = 1.85D$, while all other parameters are identical to those used in Fig. 4.11..... 159
Figure 4.15: Monomer density profiles for various salt concentration values for (a) $pH\infty$ = 3, and (b) $pH\infty$ = 4. Here the cases shown by solid lines (-) and dashed lines (--) represent the cases of "POL" and "SST", respectively. Please see the caption of Fig. 4.14 for the definition of "POL" and "SST" cases. All other parameters are identical to those used in Fig. 4.14. 162
Figure 4.16: Transverse variation of electrostatic EDL potential for various salt concentration values for (a) $pH\infty$ = 3, and (b) $pH\infty$ = 4. Here the cases shown by solid lines (-) and dashed lines (--) represent the cases of "POL" and "SST", respectively. Please see the caption of Fig. 4.14 for the definition of "POL" and "SST" cases. All other parameters are identical to those used in Fig. 4.14. 162
Figure 4.17: Variation of equilibrium brush height, $H0$, with salt concentration for various $pH\infty$ values. Here, "Ster" refers to the case where only the finite size effect, among the different non-PB effects, has been accounted for to describe the EDL electrostatics, while the PE brushes are described using the augmented SST. On the other hand, "SST" refers to the case where the EDL electrostatics is modelled using

the standard PB model (i.e., we consider no non-PB term) and the PE brushes are modelled using the augmented SST. We consider $vH+= 3.4866 \times 10 - 30$ [187] (where $vH+$ denotes the volume of $H+$ ion, which is the smallest species in our lattice model and occupies just one lattice site), $\xi+= v+/vH+= 39.3674$, $\xi-= v-/vH+= 26.3731$, $\xi w = vw/vH+= 3.1779$, $\xi H+= 1$, and $\xi OH-= vOH-/vH+= 3.7143$ [77,187]. All other parameters are identical to those used in Fig. 4.11..... 164
Figure 4.18: Monomer density profiles for various salt concentration values for (a) $pH\infty$ = 3, and (b) $pH\infty$ = 4. Here the cases shown by solid lines (-) and dashed lines (--) represent the cases of "Ster" and "SST", respectively. Please see the caption of Fig. 4.17 for the definition of "Ster" and "SST" cases. All other parameters are identical to those used in Fig. 4.17. 165
Figure 4.19: Transverse variation of electrostatic EDL potential for various salt concentration values for (a) $pH\infty$ = 3, and (b) $pH\infty$ = 4. Here the cases shown by solid lines (-) and dashed lines (--) represent the cases of "Ster" and "SST", respectively. Please see the caption of Fig. 4.17 for the definition of "Ster" and "SST" cases. All other parameters are identical to those used in Fig. 4.17. 165
Figure 4.20: Variation of equilibrium brush height, $H0$, with salt concentration for various $pH\infty$ values. Here, "MSST" refers to the case of modified augmented SST: for this case all the three different non-PB effects (ion-ion correlation, solvent polarization, and finite ion and dipole size) have been considered simultaneously to describe the EDL electrostatics, while the PE brushes are described using the augmented SST. On the other hand, "SST" refers to the case where the EDL electrostatics is modelled using the standard PB model (i.e., we consider no non-PB term) and the PE brushes are modelled using the augmented SST. Here we use $lc = 0.3nm$, $pw = 1.85\ D$, $vH+= 3.4866 \times 10 - 30$ [187], $\xi+= v+/vH+= 39.3674$, $\xi-= v-/vH+= 26.3731$, $\xi w = vw/vH+= 3.1779$, $\xi H+= 1$, and $\xi OH-= vOH-/vH+= 3.7143$ [77,187]. All other parameters are identical to that used in Fig. 4.11..... 167
Figure 4.21: Monomer density profiles for various salt concentration values for (a) $pH\infty$ = 3, and (b) $pH\infty$ = 4. Here the cases shown by solid lines (-) and dashed lines (--) represent the cases of "MSST" and "SST", respectively. Please see the caption of Fig. 4.20 for the definition of "MSST" and "SST" cases. All other parameters are identical to those used in Fig. 4.20. 169
Figure 4.22: Transverse variation of electrostatic EDL potential for various salt concentration values for (a) $pH\infty$ = 3, and (b) $pH\infty$ = 4. Here the cases shown by solid lines (-) and dashed lines (--) represent the cases of "MSST" and "SST", respectively. Please see the caption of Fig. 4.20 for the definition of "MSST" and "SST" cases. All other parameters are identical to those used in Fig. 4.20. 169
Figure 5.1: Schematic depicting the generation of the streaming electric field (E_s) and streaming current (i_s) [the electrokinetically generated electric power P_{out} and the resultant energy conversion efficiency ξ are proportional to the product of i_s and E_s]. in a) brush-free nanochannel b) backbone charged PE brushes grafted nanochannel. In the schematic, we highlight the manner in which the presence of the brushes localizes the average EDL charge density further away from the grafting surface enforcing the EDL ions to be advected by a larger background flow velocity, which in turn will lead to an enhanced i_s, E_s, P_{out}, and ξ in brush-grafted nanochannels. 181

Figure 5.2: Variation of equilibrium brush height H_0 with bulk salt concentration c_∞ and pH_∞ for pH-responsive, PE brush grafted nanochannels with (a) $\gamma a^3 = 0.5$ and (b) $\gamma a^3 = 1$. Here N = 400, h = 100 nm, a = 1 nm (Kuhn length), $k_B = 1.38 \times 10^{-23}$ JK^{-1}, T = 298 K, e = 1.6×10^{-19} C (electronic charge), $\epsilon 0 = 8.8 \times 10^{-12}$ F m^{-1} (permittivity of free space), ϵr = 79.8 (relative permittivity of water), $pK_a = 3.5$, $\nu = 0.5$, $\omega = 0.1$. pK_w =14, $pOH_\infty = pK_w - pH_\infty$, $c_{+,\infty} = c_\infty$, $cH+,\infty = 10 - pH\infty$, $cOH-,\infty = 10 - pOH\infty$, $c_{-,\infty} = c_\infty + cH+,\infty + cOH-,\infty$..... 191
Figure 5.3: Variation of monomer distribution profile ϕ with bulk salt concentration c_∞ and pH_∞ for pH-responsive, PE brush grafted nanochannels with (a) $\gamma a^3 = 0.5$, ℓ = 60 nm, (b) $\gamma a^3 = 0{:}5$, ℓ = 10 nm, (c) $\gamma a^3 = 1$, ℓ = 60 nm and (d) $\gamma a^3 = 1$, ℓ = 10 nm. All the other parameters are same as those used in Fig. 5.2. 193
Figure 5.4: Transverse variation of the non-dimensional EDL electrostatic potential with bulk salt concentration c_∞ and pH_∞ for (a) PE brush-grafted nanochannel with $\gamma a^3 = 0.5$, ℓ = 60 nm, (b) brush-free nanochannel with equivalent charge density $\sigma c, eq$ identical to that of the brush-grafted nanochannels with $\gamma a^3 = 0.5$ and ℓ = 60 nm, (c) PE brush-grafted nanochannel with $\gamma a^3 = 0.5$, ℓ = 10 nm, (d) brush-free nanochannel with equivalent charge density $\sigma c, eq$ identical to that of the brush-grafted nanochannels with $\gamma a^3 = 0.5$ and ℓ = 10 nm, (e) PE brush-grafted nanochannel with $\gamma a^3 = 1$, ℓ = 60 nm, (f) brush-free nanochannel with equivalent charge density $\sigma c, eq$ identical to that of the brush-grafted nanochannels with $\gamma a^3 = 1$ and ℓ = 60 nm, (g) PE brush-grafted nanochannel with $\gamma a^3 = 1$, ℓ = 10 nm and (h) brush-free nanochannel with equivalent charge density $\sigma c, eq$ identical to that of the brush-grafted nanochannels with $\gamma a^3 = 1$ and ℓ = 10 nm. All the parameters are same as those mentioned in Fig. 5.2..... 196
Figure 5.5: Transverse variation of the non-dimensional velocity profile u with bulk salt concentration c_∞ and pH_∞ for (a) PE brush-grafted nanochannel with$\gamma a^3 = 0.5$, ℓ = 60 nm, (b) brush-free nanochannel with equivalent charge density $\sigma c, eq$ identical to that of the brush-grafted nanochannels with $\gamma a^3 = 0.5$ and ℓ = 60 nm, (c) PE brush-grafted nanochannel with $\gamma a^3 = 0.5$, ℓ = 10 nm, (d) brush-free nanochannel with equivalent charge density $\sigma c, eq$ identical to that of the brush-grafted nanochannels with $\gamma a^3 = 0.5$ and ℓ = 10 nm, (e) PE brush-grafted nanochannel with $\gamma a^3 = 1$, ℓ = 60 nm, (f) brush-free nanochannel with equivalent charge density $\sigma c, eq$ identical to that of the brush-grafted nanochannels with $\gamma a^3 = 1$ and ℓ = 60 nm, (g) PE brush-grafted nanochannel with $\gamma a^3 = 1$, ℓ = 10 nm and (h) brush-free nanochannel with equivalent charge density $\sigma c, eq$ identical to that of the brush-grafted nanochannels with $\gamma a^3 = 1$ and ℓ = 10 nm. Here $R_i = 1$ ($i = +, -, H+, OH-$). All other parameters are same as those mentioned in Fig. 5.2..... 202
Figure 5.6: Variation of streaming current is with bulk salt concentration c_∞ and pH_∞ for (a) brush-grafted nanochannels (with $\gamma a^3 = 0.5$, ℓ = 60 nm) and brush-free nanochannels with equivalent charge density $\sigma c, eq$ identical to that of the brush-grafted nanochannels with $\gamma a^3 = 0{:}5$ and ℓ = 60 nm, (b) brush-grafted nanochannels (with $\gamma a^3 = 0.5$, ℓ = 10 nm) and brush-free nanochannels with equivalent charge density $\sigma c, eq$ identical to that of the brush-grafted nanochannels with $\gamma a^3 = 0.5$ and ℓ = 10 nm, (c) brush-grafted nanochannels (with $\gamma a^3 = 1$, ℓ = 60 nm) and brush-free nanochannels with equivalent charge density $\sigma c, eq$ identical to that of the brush-

grafted nanochannels with $\gamma a^3 = 1$ and $\ell = 60$ nm and (d) brush-grafted nanochannels (with $\gamma a^3 = 1$, $\ell = 10$ nm) and brush-free nanochannels with equivalent charge density $\sigma c, eq$ identical to that of the brush-grafted nanochannels with $\gamma a^3 = 1$ and $\ell = 10$ nm. Here = 8.9 x 10^{-4} Pa.s, dp/dx = -5 x 10^8 Pa/m. All other parameters are identical to those used in Fig. 5.5. 203
Figure 5.7: Variation of streaming electric field E_s with bulk salt concentration c_∞ and pH_∞ for (a) brush-grafted nanochannels (with $\gamma a^3 = 0{:}5$, $\ell = 60$ nm) and brush-free nanochannels with equivalent charge density $\sigma c, eq$ identical to that of the brush-grafted nanochannels with $\gamma a^3 = 0.5$ and $\ell = 60$ nm, (b) brush-grafted nanochannels (with $\gamma a^3 = 0.5$, $\ell = 10$ nm) and brush-free nanochannels with equivalent charge density $\sigma c, eq$ identical to that of the brush-grafted nanochannels with $\gamma a^3 = 0{:}5$ and $\ell = 10$ nm, (c) brush-grafted nanochannels (with $\gamma a^3 = 1$, $\ell = 60$ nm) and brush-free nanochannels with equivalent charge density $\sigma c, eq$ identical to that of the brush-grafted nanochannels with $\gamma a^3 = 1$ and $\ell = 60$ nm and (d) brush-grafted nanochannels (with $\gamma a^3 = 1$, $\ell = 10$ nm) and brush-free nanochannels with equivalent charge density $\sigma c, eq$ identical to that of the brush-grafted nanochannels with $\gamma a^3 = 1$ and $\ell = 10$ nm. All other parameters are identical to those used in Fig. 5.6..... 206
Figure. 5.8: Variation of net power output P_{out} with bulk salt concentration c_∞ and pH_∞ for (a) brush-grafted nanochannels (with $\gamma a^3 = 0.5$, $\ell = 60$ nm) and brush-free nanochannels with equivalent charge density $\sigma c, eq$ identical to that of the brush-grafted nanochannels with $\gamma a^3 = 0{:}5$ and $\ell = 60$ nm, (b) brush-grafted nanochannels (with $\gamma a^3 = 0.5$, $\ell = 10$ nm) and brush-free nanochannels with equivalent charge density $\sigma c, eq$ identical to that of the brush-grafted nanochannels with $\gamma a^3 = 0.5$ and $\ell = 10$ nm, (c) brush-grafted nanochannels (with $\gamma a^3 = 1$, $\ell = 60$ nm) and brush-free nanochannels with equivalent charge density $\sigma c, eq$ identical to that of the brush-grafted nanochannels with $\gamma a^3 = 1$ and $\ell = 60$ nm and (d) brush-grafted nanochannels (with $\gamma a^3 = 1$, $\ell = 10$ nm) and brush-free nanochannels with equivalent charge density $\sigma c, eq$ identical to that of the brush-grafted nanochannels with $\gamma a^3 = 1$ and $\ell = 10$ nm. A microchip (with dimensions of 1mm x 10cm x 10cm and a porosity of 0.5) containing multiple nanochannels of half-height h = 100 nm is considered for the calculation of output power[1]. All other parameters are identical to those used in Fig. 5.6..... 209
Figure 5.9: Variation of electrokinetic energy efficiency ξ with bulk salt concentration c_∞ and pH_∞ for (a) brush-grafted nanochannels (with $\gamma a^3 = 0.5$, $\ell = 60$ nm) and brush-free nanochannels with equivalent charge density $\sigma c, eq$ identical to that of the brush-grafted nanochannels with$\gamma a^3 = 0.5$ and $\ell = 60$ nm, (b) brush-grafted nanochannels (with $\gamma a^3 = 0.5$, $\ell = 10$ nm) and brush-free nanochannels with equivalent charge density $\sigma c, eq$ identical to that of the brush-grafted nanochannels with $\gamma a^3 = 0.5$ and $\ell = 10$ nm, (c) brush-grafted nanochannels (with $\gamma a^3 = 1$, $\ell = 60$ nm) and brush-free nanochannels with equivalent charge density $\sigma c, eq$ identical to that of the brush-grafted nanochannels with $\gamma a^3 = 1$ and $\ell = 60$ nm and (d) brush-grafted nanochannels (with $\gamma a^3 = 1$, $\ell = 10$ nm) and brush-free nanochannels with equivalent charge density $\sigma c, eq$ identical to that of the brush-grafted nanochannels

with $\gamma a^3 = 1$ and $\ell = 10$ nm. All other parameters are identical to those used in Fig. 5.6..... 211
Figure 6.1: Snapshot of the MD simulation domain for pressure-driven transport in PE-brush grafted nanochannel. Na^+ and Cl^- ions are depicted by blue and yellow spheres, respectively. The atoms forming the discrete walls at the top and bottom of the nanochannel are depicted as black spheres. All other colors represent the various atom types of the PAA chains. Water molecules are not shown explicitly for improved visualization..... 222
Figure 6.2: (a) Reduction in average end-point brush height (H) with applied axial pressure gradient, (b) average profile of the grafted PAA chains (projected on the x-z plane) as a function of the imposed pressure gradient. In (b), the grafted ends of the PAA chains are assumed to lie at the origin (with z=0 representing the grafting plane) and the flow occurs along the positive x-direction. The equilibrium end-point brush height and average chain profile for ∇P=0 MPa/nm were first obtained in Ref. 209. 225
Figure 6.3: Transverse distribution of the number density of Na^+ and Cl^- ions inside the nanochannel for (a) ∇P=0 MPa/nm (no applied pressure gradient), (b) ∇P=1 MPa/nm, and (c) ∇P=2 MPa/nm. A zoomed view of the ionic distributions in the brush-free bulk are depicted in the insets. The transverse ionic distributions for ∇P=0 MPa/nm were first obtained in Ref. 209. 228
Figure 6.4: Axial flow profiles (obtained from our all-atom MD simulations) for the pressure-driven transport of water inside the nanochannel as a function of the applied pressure gradient. 233
Figure 6.5: Comparison of the axial flow profiles for the pressure-driven transport of water (for different applied pressure gradients) obtained from all-atom MD simulations and continuum calculations. Parameters used in the MSST model are a=1.53 Å, ℓ =15.65 Å, $c\infty$=1.02 M, γ=0.5/$a3$, h=60.225 Å, N=48, pK_a=3.5, pH_∞=7. All other parameters for the MSST model are identical to that used in Fig. 4.20. Parameters used in the continuum flow calculations are $\eta = 8.9 \times 10 - 4$ Pa.s, $\mu Na+ = 4.98 \times 10 - 8$ m^2/Vs, and $\mu Cl- = 6.88 \times 10 - 8$ m^2/Vs. 240
Figure 7.1: Equilibrium end-point height of the PE brushes. 253
Figure 7.2: Comparison of the axial flow profiles for the pressure-driven transport of water (for different applied pressure gradients) obtained from all-atom MD simulations and continuum calculations. Parameters used in the MSST model are a=1.53 Å, ℓ =15.65 Å, $c\infty$=1.02 M, γ=0.5/$a3$, h=60.225 Å, N=48, pK_a=3.5, pH_∞=7. All other parameters for the MSST model are identical to that used in Fig. 4.20. Parameters used in the continuum flow calculations are $\eta = 8.9 \times 10 - 4$ Pa.s, $\mu Na+ = 4.98 \times 10 - 8$ m^2/Vs, and $\mu Cl- = 6.88 \times 10 - 8$ m^2/Vs. 263
Figure 7.3: A snapshot of the PE brush grafted nanochannel system..... 269
Figure 7.4: Excess of the positive charges $\Delta e = (e_+ - e_-)$ inside brush and in brush-free bulk as a function of the electric field (E). e_+ and e_- indicate total number of positive charges (Na^+) and negative charges (Cl^- and PE charges) respectively. 271
Figure 7.5: (A) Simulation setup of the PE brush grafted nanochannel with the nanochannel being connected to two reservoirs at its two ends. (B) Ion distribution profile in the nanochannel. Yellow shaded region in (A) is considered for calculating the ion distribution profile [reported in (B)] within the nanochannel..... 275

List of Abbreviations

Polyelectrolyte (PE)

Molecular Dynamics (MD)

Strong Stretching Theory (SST)

Electric Double Layer (EDL)

Modified Strong Stretching Theory (MSST)

Polyacrylic Acid (PAA)

Excluded Volume (EV)

Water in Salt Electrolyte (WISE)

Radial Distribution Function (RDF)

Mean Squared Displacement (MSD)

Poisson Boltzmann (PB)

Electroosmotic (EOS)

Chapter 1: Background and Motivation

1.1. Structure and Configuration of Polyelectrolyte Brushes

Polyelectrolytes (or PEs) are macromolecules whose repeating unit is an electrolyte. PE chains grafted close enough vicinity of each other extend in the direction perpendicular to the substrate (in order to avoid each other), thereby attaining a brush-like configuration, due to electrostatic repulsion between the charged segments as well as the excluded volume interactions between the monomers. PE brushes have been employed in a myriad of applications such as electrokinetic energy conversion[1], biosensing[2-4], colloidal stabilization[5], drug delivery[6-7], oil recovery[8], etc. The wide-spread use of PE brushes can be attributed to their stimuli-responsive behavior, i.e., their configuration can be tuned by changing the characteristics of the surrounding medium like bulk salt concentration, pH, solvent quality, temperature, etc. Therefore, it is vital to understand the thermodynamics of such PE brush systems.

The literature consists of several Molecular Dynamics (MD) studies probing the structure of PE brushes[9-13]. However, these studies suffer from two major drawbacks. Firstly, they have not employed a fully atomistic description of the PE brush system. Instead, most studies have utilized major approximations such as coarse-grained models of the PEs and consideration of an implicit solvent. Secondly, most MD studies have focused their attention to the overall configuration or macrostructure of the PE brushes such as the variation in brush height and monomer distribution profile. On the contrary, there are virtually no studies that investigate the local structure of ions and

solvent molecules within the brushes at the atomistic length scales (microstructure). In Chapter 2, we overcome both these limitations by performing MD simulations of planar polyacrylic acid (PAA) brushes with an all-atom framework. We investigate the distribution and local arrangement of Na^+ counterions and water molecules within the brushes for various chain lengths and grafting densities.

In Chapter 3, we utilize our all-atom MD framework to study the effects of variation in degree of ionization of the PE brushes on the brush properties such as end-to-end height and chain mobility as well as the local structure of the counterions and water molecules within the brushes. This is the first fully atomistic study to probe the effects of variation in charge density on the microstructure of densely grafted weak polyionic brushes.

Several analytical models have been developed over the past few decades to capture the behavior of PE brushes. The state-of-the-art theoretical model for planar PE brushes is the Strong Stretching Theory (SST)[14]. This theory assumes that the brushes are in a strongly extended conformation and thereby models the PE chains as a 1D arrangement of monomers in the direction perpendicular to the grafting surface. However, this model ignores several important factors such as the effects of excluded volume (EV) interactions between the monomers and variation of charge density of the PE chains. In Chapter 4, we modify the existing SST model to incorporate the effects of EV interactions and an extended form of the mass action law, and thereby come up with the most exhaustive analytical model for pH-responsive PE brushes, called the augmented SST.

Another major drawback of the existing theoretical models is that they do not account for the non-Poisson Boltzmann (PB) effects on the configuration of PE brushes. Such non-PB effects become increasingly significant at high bulk salt concentrations. We further modify our augmented SST model in conjunction with the theory of 'water-in-salt' electrolytes (WISE)[15] to develop the modified augmented Strong Stretching Theory (MSST). Our theory can incorporate non-PB effects such as ion-ion correlations, solvent polarization and finite size effects. We go on to obtain an excellent match between the predictions of our model and the results of the all-atom MD simulations of Chapter 2.

1.2. Flows in Polyelectrolyte Brush-grafted Nanochannels

Liquid transport in nanochannels has received significant scientific attention due to its vast number of applications. One key problem in nanofluidic transport is the tremendous retarding effect of the viscous drag due to the large surface area to volume ratios of the nanochannels. Electrolytes in nanochannels are often driven through electrokinetic transport which involves charging of the nanochannel walls to generate an imbalance of mobile charges or Electric Double Layer (EDL) and the interaction of the charge density gradient of this EDL with an applied or an induced electric field. One commonly employed electrokinetic flow is the pressure-driven flow which involves the application of an axial pressure gradient across a charged nanochannel containing an electrolyte. The pressure gradient leads to a downstream migration of the ions within the EDL, resulting in an ionic current and a streaming electric field. This leads to the generation of electric power and can be used for nanofluidic energy

conversion. Das and coworkers[1] recently proposed that grafting the surface of the nanochannels with end-charged PE brushes (under appropriate parameter combinations) can increase the power output and nanofluidic conversion efficiency by shifting the location of the EDL away from the retarding effects of the nanochannel walls. However, they considered a very primitive model for the PE brushes. They employed the Alexander de Gennes model which assumes a uniform monomer distribution throughout the brushes. This is a major limitation, since the proper modeling of the brushes is critical to obtain the correct brush-induced drag force on the fluid flow and EDL potential which ultimately dictates the flow profile and energy conversion efficiency. In Chapter 5, we overcome this drawback by employing our augmented Strong Stretching Theory (developed in Chapter 4) to obtain a thermodynamically self-consistent description of the brushes and using this description to capture the correct pressure-driven flow profile and the associated power generation characteristics. Moreover, we consider the case of backbone-charged PE brushes instead of the less practical end-charged brushes considered in Ref. 1.

A few existing MD studies[16-18] have probed electrokinetics in PE brush-grafted nanochannels. However, these studies are severely limited in their accuracy due to the use of coarse-grained models for the brushes. In Chapter 6, we report all-atom MD simulations for investigating the pressure-driven transport of water in a PE brush-grafted nanochannel. In addition to obtaining the velocity profiles and nanoscale energy conversion characteristics, we also uncover some highly interesting phenomenon such as the overscreening of the grafted PE layer and the tilting of the brushes due to the

flow-induced drag forces. Our results indicate that the tilting of the brushes can be significant at large values of imposed pressure gradients and leads to a reduction in the average height of the grafted PE layers. This reduction in brush height manifests as a reduction in the extent of overscreening of the brushes. Furthermore, we show that our all-atom MD results are in reasonable agreement with the predictions of our continuum framework (Chapters 4 and 5). This is followed by a thorough discussion of the reasons for the observed discrepancy in the all-atom MD results and the continuum models. We conclude by showing that one of the quantities (namely streaming conductance) obtained from our study lies within the range of values reported by a prior experimental study,[19] providing a sense of feasibility of the numbers obtained from our methods.

Finally, in Chapter 7, we provide several comparisons of our all-atom MD results with continuum calculations to validate/verify our methods. These comparisons are made for the equilibrium configuration of PE brushes grafted on a substrate as well as flows in nanochannels decorated with PE brushes. In addition, we also provide a comparison of our all-atom MD simulations for probing electrokinetics in PE brush-grafted nanochannels to the findings of prior experimental studies and establish that our results are within the span of values observed in these experiments. We end with a summary of the contributions of our work to the existing body of knowledge.

Chapter 2: Densely Grafted Polyelectrolyte Brushes Trigger "Water-in-Salt" like Scenarios and Ultraconfinement Effect*

Abstract: *In this chapter, we conduct an all-atom molecular dynamics (MD) simulation of highly charged and densely grafted polyelectrolyte (PE) brushes on a flat surface. Simulation findings for the variation of brush height with polymer size and grafting density are explained by the scaling laws for brushes in the non-linear osmotic regime. More importantly, this study establishes the triggering of an ultraconfinement effect by the densely grafted brushes. This effect leads to significant changes in the distribution, structure, and properties and a massive mobility reduction of both the counterions and water. Furthermore, the interplay of the ultraconfinement effect and the large counterion-PE electrostatic interactions trigger "water-in-salt"-like scenario (witnessed in highly concentrated aqueous electrolyte solutions), which is characterized by the counterion-PE-functional group serving as the "salt" with the "salt" overwhelming the water in both mass and volume and affecting the solvation structure of the counterion by replacing the solvation water with the PE-functional group.*

2.1. Introduction

Densely grafted charged polymer molecules (or polyelectrolytes or PEs) form a "brush"-like structure (known as PE brushes) dictated by the balance of the elastic,

* The contents of this Chapter have been published as the following journal article: Sachar, H. S.; Pial, T. H..; Desai, P. R.; Etha, S. A.; Wang, Y.; Chung, P. W.; Das, S. "Densely Grafted Polyelectrolyte Brushes Trigger "Water-in-Salt"-like Scenarios and Ultraconfinement Effect." *Matter* **2020**, *2*, 1509-1521.

excluded volume, and electrostatic interactions.[20-24] Functionalizing surfaces by grafting them with PE brushes has been extensively used for a host of applications such as ion and bioanlayte sensing in a nanochannel/nanopore,[2,4] nanofluidic current rectification[25,26] and diode action,[27,28] nanoparticle-based targeted drug and gene delivery,[6,7] *in-vivo* imaging,[29] oil recovery,[8] emulsion stabilization,[5] water harvesting,[30] and many more. Understanding the detailed structure of the PE brushes and their responses to external stimuli (such as salt concentration, pH, etc.) is critical to better control all these applications as well as to gain fundamental insight on one of the most interesting polymer states (namely the "brush"-like state). Motivated by these prospects, there have been several decades of theoretical,[14,31-39] simulation-based,[9-13,40-44] and experimental[45-54] research unraveling a myriad of information on the structure and properties of PE brushes. Several of these studies on PE brushes have been partly based simulation models and frameworks developed for other polyelectrolyte related systems such as polyelectrolyte gels,[55-58] polyelectrolyte solutions,[59-61] polyelectrolyte nanofilms,[62-63] etc.

In this chapter, we conduct an *all-atom Molecular Dynamics* (MD) *simulation* of the PE brushes. We consider a fully ionized polyacrylic acid (PAA) brush, which is neutralized by the Na^+ counterions, in an explicitly resolved water system [modeled using SPC/E water molecules[64]] in presence of a finite concentration of NaCl salt. The results provide an atomistic level elucidation of the PE brush properties. We study the variation of brush height with size of the polymer and grafting density and explain the results using scaling laws for PE brushes in non-linear osmotic regime.[65-67] Subsequently, we study the distribution of the monomers and the brush ends, and the

results demonstrate close resemblance to that predicted from coarse-grained MD simulations.[9]

More importantly, we unravel a hitherto unknown ultraconfinement effect and the development of "water-in-salt"-like scenarios triggered by densely grafted PE brushes. Here by "ultraconfinement", we signify the tremendous confinement created by the PE brushes as would be evident from the orders of magnitude reduction in the mobilities of counterions and water molecules (as described later). Of course, given the nanoscopic length of the system, this ultraconfinement is a form of nanoconfinement. The dense grafting of the PE brushes affords lesser space to the water molecules and the counterions enforcing this confinement effect. This effect becomes so pronounced that it leads to significant changes in the structure and properties of the counterions (quantified by the water-oxygen−counterion radial distribution function or RDF) and the water molecules (quantified by the water-oxygen−water-oxygen RDF, water tetrahedral order parameter, and water density and hydrogen bond distribution). Furthermore, this confinement leads to an extreme reduction in the mobility of the counterions (also contributed by the large electrostatic attraction between the densely grafted and fully ionized brushes and the counterions) and the water molecules, quantified by orders of magnitude reduction in their mobilities within the brushes as compared to their bulk values. Most importantly, this atomistic quantification of the brush behavior leads us to a situation where the counterion, PE brush functional group, and the water together leads to the development of "water-in-salt"-like scenarios. "Water-in-salt" systems, referring to the highly concentrated aqueous electrolyte solutions (of a typical electrolyte with a small cation and a bulky anion) where the salt

overwhelms the water in mass and volume,[15,68-73] have seen a massive recent surge in interests owing to its widespread use in fabricating Li-ion and Na-ion batteries with broad electrochemical stability window.[68,69,72,73] For the present case, we hypothesize that the combination of the confinement effect and the large electrostatic attraction between the brushes and the counterions enforce a situation where the counterion-PE-functional-group serves as a "salt" that overwhelms the water in terms of mass and volume beyond a certain grafting density. Also, analogous to the case of the standard "water-in-salt" systems, here we find that the PE-functional group (serving as "coion") replaces the water molecules from the solvation shell of the counterion. In fact, several of these effects characterizing the "water-in-salt" scenarios occur at a counterion concentration that is significantly lower than the salt concentration where these effects occur for standard "water-in-salt" systems.

2.2. Results

2.2.1 All-atom MD Simulation Results for the PE Brush Configuration

Fig. 2.1(a) provides a representative snapshot for the *all-atom MD simulation* (the 'Simulation Details' section details the MD simulation procedure). We investigate the brush height, the monomer distribution profile, and the end distribution of the PE chains. Figure 2.1(b) depicts the variation of the end-point brush height $< z_e >$ with *N*, which denotes the number of backbone carbon atoms of the PE brush molecule. We observe $< z_e >$~*N*. On the other hand, in Fig. 2.1(c), we provide the variation of $< z_e >$ with the grafting density σ_g. In order to explain the trends of $< z_e >$ with *N* and

σ_g, we invoke the scaling prediction on the brush height ($H_{osm,nl}$) for PE brushes in the *non-linear* osmotic regime.[65,66] This regime improves the predictions of the standard osmotic brush regime (in osmotic regime, the brush height is obtained by balancing the elastic energy of the brushes with the entropic energy of the counterions) by additionally accounting for the effects of self-volume of the polyelectrolyte chains on the counterion entropy. Following refs 65-66, we can write:

$$H_{osm,nl} = nb\frac{f+\sigma_{eff}^2\sigma_g}{1+f}, \quad (2.1)$$

where *n* is the number of repeating units [in our case n=(N-1)/2], *b* is the length of each repeating unit [in our case *b* is equal to 2 backbone C-C bond lengths. i.e. 3.058 Å], f is the fraction of charged monomers (f=1 for a fully ionized brush), and $\sigma_{eff} = \sqrt{2}\sigma$ (σ=3.5 Å is the LJ distance parameter for backbone carbon atoms on the PE chains) is the effective monomer diameter (i.e., the diameter of the monomer accounting for the condensed counterions). Eq. (2.1) and n=(N-1)/2 explains the linear variation of $< z_e >$ with *N*. Also, we compute the variation of $H_{osm,nl}$ with σ_g from eq. (2.1) and compare the theoretical results with the MD predictions [see Fig. 2.1(c)]. The theoretical result accurately captures the rate of increase of $<z_e>$ with σ_g, although it under predicts the values of $<z_e>$ for all combinations of *N* and σ_g, which can be attributed to different factors such as the lateral inhomogeneity in counterion distribution, improper consideration of σ_{eff} (possibly due to the presence of pendant groups attached to the PE backbone), short-range excluded volume interactions between the PE chains, etc. In Table 2.1, we also provide the variation of $<z_e>$, the average brush thickness $< z_b >$ and the counterion layer thickness $< z_{ci} >$ [where $< z_b >= \frac{\int_0^\infty z\rho_b(z)dz}{\int_0^\infty \rho_b(z)dz}$ and $\rho_b(z)$ is

the number density of backbone carbon atoms normalized such that $\frac{1}{\sigma_g}\int_0^\infty \rho_b(z)\,dz = N$ and $< z_{ci} >= \frac{\int_0^\infty z\rho_{ci}(z)dz}{\int_0^\infty \rho_{ci}(z)dz}$ such that $\frac{1}{\sigma_g}\int_0^\infty \rho_{ci}(z)\,dz = N_{ci} = (N-1)/2]$ with N and σ_g. Here ρ_b and ρ_{ci} are the number densities of backbone carbon atoms and counterions, respectively.

N	σ_g ($1/\sigma^2$)	$\langle z_b \rangle$ (Å)	$\langle z_{ci} \rangle$ (Å)	$\langle z_e \rangle$ (Å)
29	0.05	13.70	15.00	25.58
29	0.1	15.06	19.39	28.90
29	0.15	15.71	16.19	30.68
29	0.2	17.83	20.08	34.12
39	0.05	17.83	19.17	33.95
39	0.1	20.33	21.02	38.83
39	0.15	21.20	21.53	41.15
39	0.2	23.25	23.58	45.32
49	0.05	23.30	24.26	44.34
49	0.1	26.03	26.63	50.52
49	0.15	27.18	27.46	53.31
49	0.2	29.32	29.61	57.39
69	0.05	32.07	32.59	61.99
69	0.1	36.15	36.38	70.53
69	0.15	38.45	38.51	75.67
69	0.2	41.01	40.87	81.39

Table 2.1: *Variation of brush thickness $\langle z_b \rangle$, counterion layer thickness $\langle z_{ci} \rangle$ and brush end-point height $\langle z_e \rangle$ with N and σ_g.*

In figure 2.1(d), we plot the transverse distribution profiles of the backbone carbon atoms on the PE brushes. These profiles are analogous to the monomer distribution

profiles for coarse-grained PE brush models.[9] We observe that the backbone carbon distribution approximately follows a step-like profile especially at high grafting density. There is a slight deviation from the step-like behavior near the tail of the brush at lower values of grafting density. Very similar monomer distribution profiles were obtained by Csajka et al,[9] who reported a nearly constant monomer density at high grafting densities. In Fig. 2.1(e), we plot the backbone carbon distribution profiles with respect to the reduced z coordinate (z/Nσ) for σ_g=0.1/σ^2. A collapse of the profiles is observed, and it indicates that there is no significant finite size effect due to chain size for any of the studied values of *N*. Finally, in Fig. 2.1(f), we plot the normalized distribution of the brush ends for the PE chains. At higher grafting density, the brushes are very strongly stretched resulting in severely restricted mobility of the chain ends ensuring that they are localized within a small *z* range. This is confirmed by the very sharp and narrow distribution profile corresponding to σ_g =0.2/σ^2. As grafting density decreases, however, the chain ends become more mobile and the end-point distribution profile spreads out (becomes flatter). Such distributions of the brush ends, as a function of the grafting density, are very similar to those reported previously in coarse-grained MD simulation-based studies.[74]

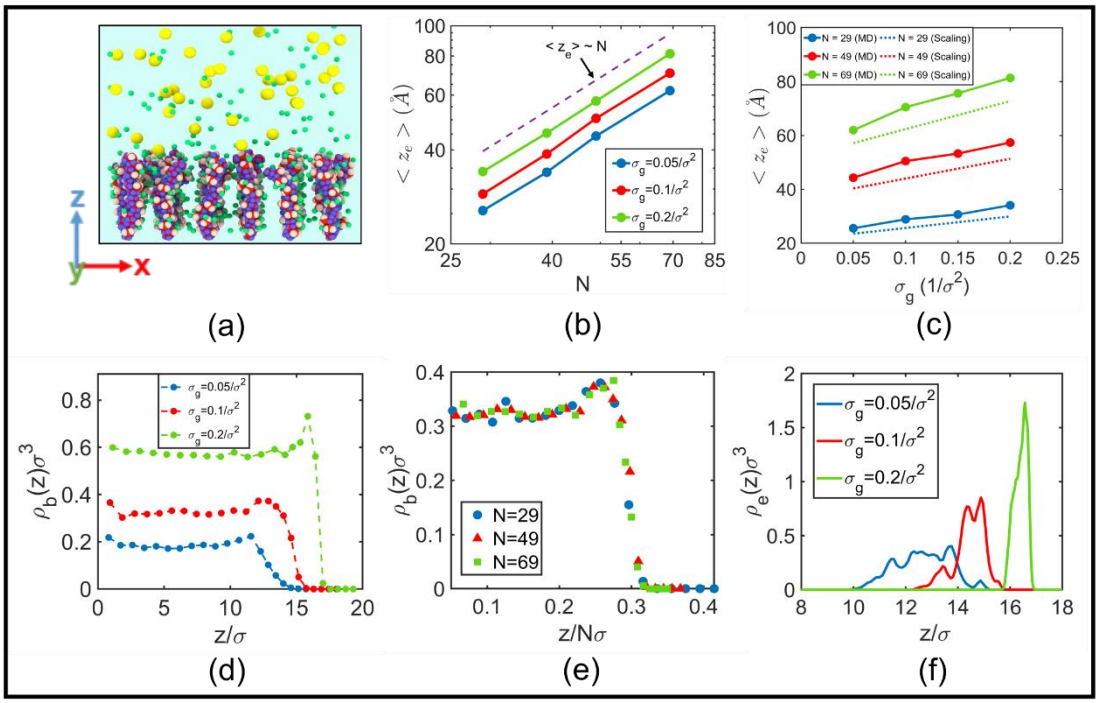

Figure 2.1: *Structure and Configuration of the PE Brushes*

(a) Snapshot of the all-atom PE brush MD simulations. In this schematic, Na^+ ions are shown as dark green spheres, Cl^- ions are shown as yellow spheres, and the other colors represent atoms of the PE brushes. Also, the water molecules have not been explicitly shown for better visualization. (b) Variation of the end-point brush height with N for different grafting densities. The dashed line denotes the $< z_e >$~N scaling as also confirmed by eq. (1). (c) Variation of the end point brush height with grafting density (σ_g) for different N. The dotted lines provide the result of the theoretical calculation of brush height obtained by employing eq. (1). (d) Variation of backbone carbon distribution profiles with grafting density for N=49. (e) Backbone carbon distribution profiles plotted against the reduced z coordinate (z/Nσ) for $\sigma_g=0.1/\sigma^2$. (f) Variation of the chain end-point distribution profiles with grafting density for N=49.

2.2.2 Counterion Distribution, Structure, and Properties: Brush-induced "Water-in-Salt" Like Scenario and Counterion Confinement

Here we investigate the behavior of the counterions inside and outside the PE brush layer. Fig. 2.2(a) shows the counterion distribution profiles for different PE brush grafting densities. As anticipated, the counterion distribution profiles closely resemble (qualitatively) the PE brush backbone carbon distribution profiles [see Fig. 2.1(d)]. This is also evident in the corresponding electroneutrality behavior of the system (see Fig. 2.3). Therefore, the counterion distribution shows an approximately step-like profile at higher brush grafting densities and deviates from the step-like behavior near the tail of the brush for low grafting densities. We also witness a lateral inhomogeneity in the counterion distribution within the PE brush layer as a result of counterion condensation around the $O_{Carboxylate}$ groups. In Figure 2.2(b), we quantify the solvation structure of the counterions (Na^+ ions) inside the brush layer for different values of the PE brush grafting density, which corresponds to different values of the counterion concentration (expressed in molality). An increase in the grafting density leads to a smaller accessible space for the same number of counterions (the number of counterions is dictated by the charge on the PE brush) enforcing an increase in the counterion molality. *The solvation structure of the counterions within the PE brush layer is characterized by a decrease in the number of water molecules (or the number of oxygen atoms of the water molecules) occupying the first solvation shell ($r \leq 3.2$ Å) of the Na^+ ion with an increase in the PE brush grafting density (i.e., an increase in the counterion molality).* This decrease is compensated by an equivalent increase in the number of $O_{Carboxylate}$ (oxygen atoms in the carboxylate groups of PE chains) in the first

solvation shell of the Na^+ ion [see Fig. 2.2(c) for a schematic illustration]. However, the total coordination number remains almost invariant of grafting density (~6), which is very close to that of the Na^+ ion in bulk [in our simulations, we obtain the bulk Na^+ coordination number of 5.84, which is very similar to that reported by the existing literature[75-76]]. This is the *first key result* of this chapter. The above finding points to a most remarkable situation where the confinement effect of the densely grafted PE brushes, along with the strong PE-counterion electrostatic interactions, trigger *water-in-salt* like scenarios. Such "water-in-salt" systems refer to highly concentrated aqueous electrolytes containing an electrolyte salt (e.g., Li-TFSI) that has a small cation (e.g., Li^+) and a large and bulky anion (e.g., $TFSI^-$).[15,68,71] In our study, the Na^+ counterion is serving the role of this small cation, while $–R\text{-}COO^-$ (R: CH_2-CH) on the PE brush is serving the role of this heavy anion. In standard Li-TFSI electrolyte solution, beyond a certain Li-TFSI concentration (>10 molal), the Li^+ ion solvation structure is disturbed with some of the water molecules getting replaced by the $TFSI^-$ ion. For a Li-TFSI concentration of 20 molals, the first Li^+ ion solvation shell has as many as two $TFSI^-$ ions and only 2.5 water molecules. On the other hand, in the present study, we find that such replacement of the water molecules by the anion (here $–R\text{-}COO^-$) starts to occur at a significantly lesser equivalent molality (as small as 4 molal) [see Fig. 2(b)] and in the solvation shell, both the number of water molecules and $R\text{-}COO^-$ become equal to 3 for an equivalent molality of ~20. Therefore, we refer to this behavior as a PE-brush-induced-confinement driven *water-in-salt* like behavior of the entrapped water-counterion system. We can explain this radical alteration in the counterion solvation structure within the brush layer for small molalities considering

Gibbs free energy of solvation. Typically, solvation is aided by the associated favorable entropic change of the cation and anion: solvation lowers the attraction between the cation and anion and in the process frees them to become more mobile, i.e., become entropically more favorable. In the present case, the anion (-R-COO^-) is fixed on the PE backbone. Hence the solvation will not be that entropically favorable since with solvation the mobility of the -R-COO^- will not change drastically. This reduced tendency of solvation ensures that the brush-entrapped counterions will demonstrate a much larger tendency to have the water molecules in their first solvation shell get replaced by -R-COO^-. Standard water-in-salt systems (highly concentrated aqueous Li-TFSI electrolyte solution) are also characterized by the fact that beyond a particular molality, the salt overwhelms the solvent (in volume and weight). For Li-TFSI, this effect is witnessed for a concentration of ~5 molals.[68] In the present study, we witness such a scenario (i.e., when the weight and volume of the Na^+-R-COO^- becomes larger than the brush-confined water) for a counterion molality of 11 molals (for weight) and 7 molals (for volume), which is equivalent to a grafting density of $\frac{0.13}{\sigma^2}$ and $\frac{0.09}{\sigma^2}$ respectively [see Fig. 2.2(d)].

Figure 2.2(e) provides a comparison of the cation-water RDFs both inside and outside the PE brush layer. Our RDF in the bulk matches with the RDF for aqueous sodium ion reported in the literature.[77] On the other hand, the RDFs inside and outside the PE brushes are significantly deviated from each other. For the RDF within the brushes, the peak corresponding to the first solvation shell decreases. This can be directly attributed to the reduction in the number of water molecules within the counterion solvation structure [see Figure 2.2(b)].

Finally, we examine the mobility of the counterions within the brush layer by quantifying their mean square displacements (MSDs) [see Fig. 2.2(f)]. Fig. 2.2(f) compares the MSD values of the counterions both inside and outside the PE brush layer. The displacement in the bulk is isotropic (i.e., $D_x=D_y=D_z$), as expected. We obtain a self-diffusivity value of $D=4.52 \times 10^{-10}$ m^2/s, which is much lesser than the value cited in literature (approx. $D=1.2 \times 10^{-9}$ m^2/s).[78-80] This lower value of self-diffusivity can be attributed to the use of Langevin thermostat,[81] which adds random forces to the atoms for maintaining a constant temperature. As a result, the MSD decreases (at sufficiently long time scale) and the self-diffusivity goes down. In figure 2.2(f), we also plot the MSD profile for the counterions trapped within the PE brush layer. We observe a drastic reduction as compared to the bulk MSD and the MSD within the brushes plateaus after some time. Both these effects can be attributed to the combined influence of the steric effects (or the brush-induced confinement) and the large brush-counterion electrostatic attraction.

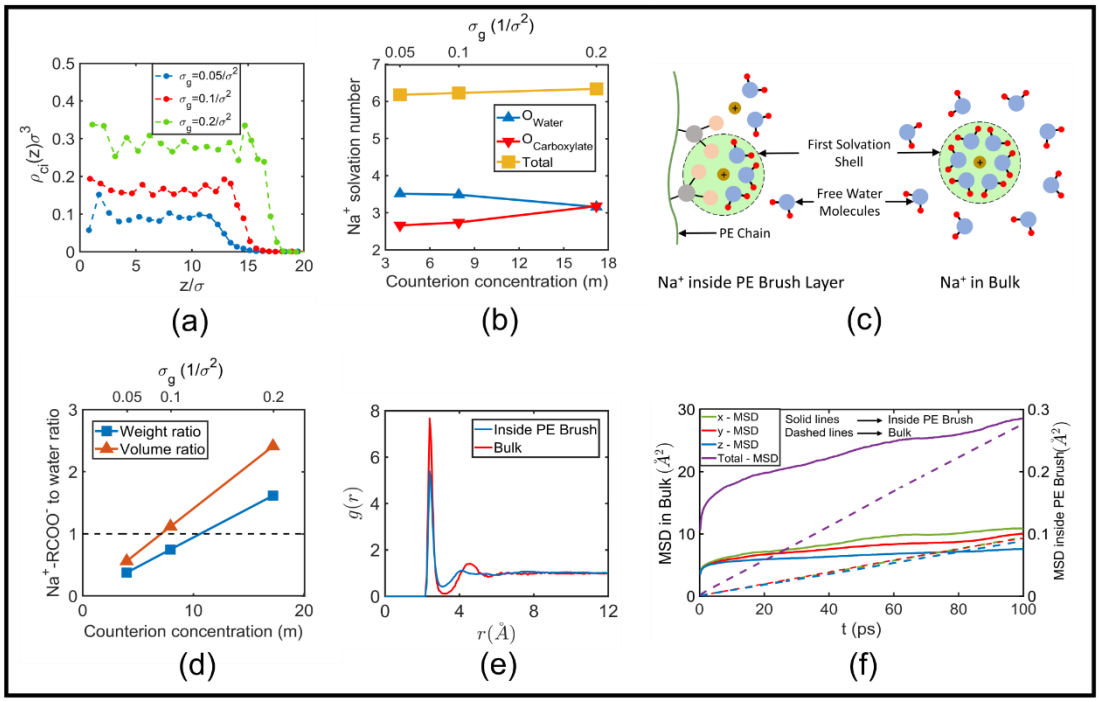

Figure 2.2: *Distribution, Structure, and Properties of the Counterions (a) Variation of the dimensionless counterion distribution* $\rho_{ci}(z)\sigma^3$ *with grafting density, where* ρ_{ci} *is the number density of counterions normalized such that* $\frac{1}{\sigma_g}\int_0^\infty \rho_{ci}(z)\,dz = N_{ci}$ *[*N_{ci} *= (N-1)/2 is the number of counterions per PE chain] (b) Solvation structure of* Na^+ *ions within the PE brush layer with different PE brush grafting density (shown on the top axis) or equivalently, with different counterion concentration (shown on the bottom axis). (c) Schematic depicting the replacement of water molecules by* $O_{Carboxylate}$ *inside the first solvation shell of* Na^+ *ions within the PE brushes. Here the grey and pink spheres respectively represent the carbon and oxygen of the* COO^- *of the PE chain and the brown sphere represents the* Na^+ *ion. Here the schematic provides a 2D representation of the 3D solvation structure. (d) Variation of salt (*Na^+*-*$RCOO^-$*; R:* CH_2*-CH) to water weight and volume ratios with different PE brush grafting density (shown on the top axis) or equivalently, with different counterion concentration (shown on the bottom axis). (e)* Na^+*-*O_w *(*O_w*: oxygen of the water molecule) RDF in bulk and inside the PE brush layer for* $\sigma_g = 0.2/\sigma^2$*. (f) MSD of counterions in bulk (see left axis) and inside the PE brush*

layer (see right axis) for $\sigma_g=0.2/\sigma^2$. In (f), solid and dashed lines indicate MSD inside the brushes and in bulk respectively. N=49 is used for (a), (b), (d), (e) and (f).

In Figure 2.3, we plot the net charge of the PE's and counterions over the simulation domain (for N=69). We observe that local electroneutrality is satisfied everywhere except in the vicinity of the graft and the average brush end-point height $\langle z_e \rangle$. The variation near the grafted end is a result of short ranged ordering of the backbone carbon atoms near the graft. We witness an abundance of counterions, just above the average end-point height of the brush, especially at high grafting density. This can be attributed to the clustering of counterions above the brush ends within the Gouy-Chapman length scale.

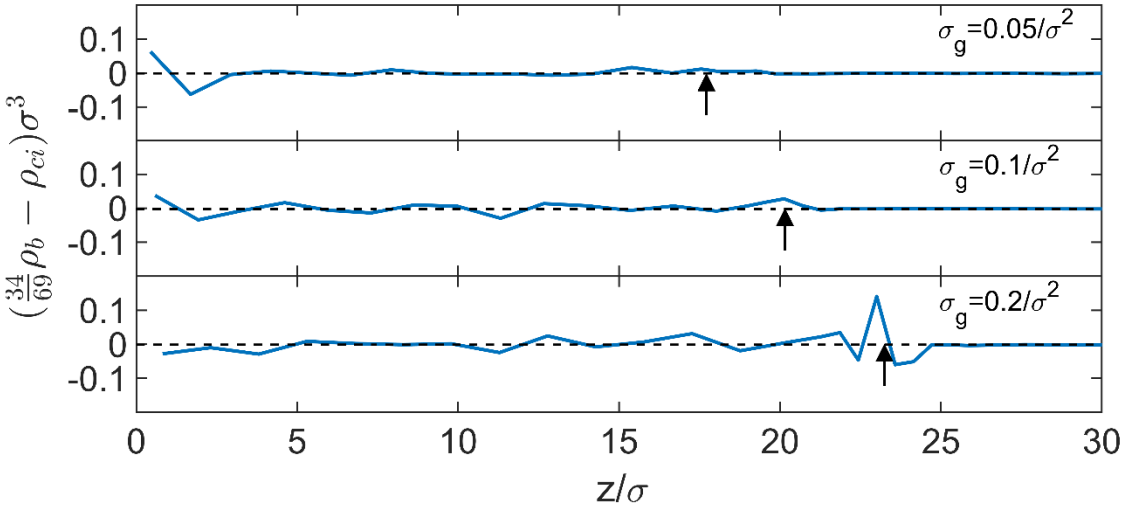

Figure 2.3: *Transverse variation of net charge across the simulation domain, for different values of σ_g. Results are shown for N=69. The arrows indicate the position of average brush end-point height $\langle z_e \rangle$.*

In Fig. 2.3, each fully ionized PE chain carries 69 backbone carbon atoms and a net charge of -34 e (e is the electronic charge). Hence, each backbone carbon atom can be

attributed an average charge of $-\frac{34}{69}$ e, thereby justifying the use of $\frac{34}{69}\rho_b$ to evaluate the net charge.

Figure 2.4 shows the probability distribution p(r) of finding the nearest $O_{Carboxylate}$ atom at a distance r from a given counterion within the brushes. p(r) is normalized such that $\int_0^\infty 2\pi r p(r) dr = 1$. We witness a huge peak in p(r) at ~0.63σ or 2.2 Å, which is very close to the LJ diameter of Na^+ (2.1595 Å) used in the simulations. This peak is observed for all values of σ_g and confirms the presence of counterion condensation in our system. The local electroneutrality expressed in Fig. 2.3 is a direct consequence of this counterion condensation.

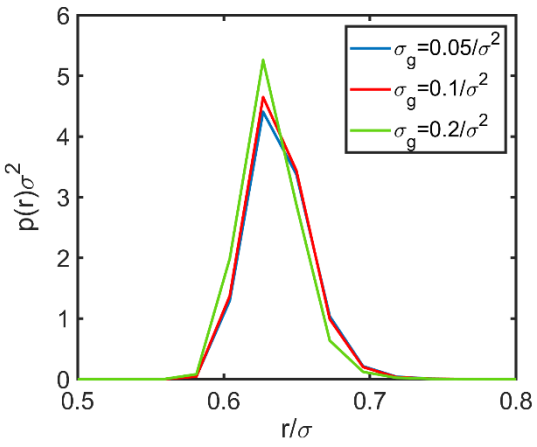

Figure 2.4: *Normalized probability distribution $p(r)\sigma^2$ of finding the nearest $O_{Carboxylate}$ atom at a distance r/σ from the counterions within the PE brush layer. σ_g=0.05/σ², 0.1/σ², 0.2/σ² and N=49.*

2.2.3 Water Structure, and Properties: Brush-induced Confinement

Here we investigate the brush-induced alteration in water structure and properties. In Figure 2.5(a), we plot the variation of the O_w-O_w (O_w represents oxygen of the water molecule) RDFs both inside and outside the brushes. Our bulk RDF (RDF outside the brushes) matches precisely with that predicted in the literature.[82] However, the structure of the water changes within the PE brush layer as revealed by the corresponding O_w-O_w RDF within the brushes (for σ_g =0.2/σ^2). For the O_w-O_w RDF within the brushes, the first hydration shell becomes more diffuse and the entire RDF curve shifts towards the right. This rightward shift can be explained by the presence of counterions and brush atoms in between the water molecules causing them to move further apart from each other. More importantly, this O_w-O_w RDF profile within the brushes is commensurate with our hypothesis of brush-induced generation of the "water-in-salt"-like scenarios, where the Na^+- R-COO^- system acts like a "salt". Han et al.[83] has demonstrated exactly similar shift of the O_w-O_w RDF profile for a highly concentrated aqueous Li-TFSI salt solution for a concentration range of 1-20 M. We report such a shift for σ_g =0.2/σ^2, which corresponds to a "salt" concentration of 17 m. In figure 2.5(b), we plot the probability distribution of the orientational tetrahedral order parameter (q) for water molecules.[84] q=1 corresponds to a perfect tetrahedron structure with lower values of q indicating higher deviations from the tetrahedral structure. We observe that the distribution shifts towards lower values of q inside the PE brush layer. The extent of the shift can be understood in terms of the mean value of q which falls from 0.62 in bulk to 0.33 inside PE layer with σ_g=0.2/σ^2 (approximately a 50% decrease). This is an indicator of the fact that the water structure gets distorted from its

usual tetrahedron packing due to the presence of PE brushes and counterions. This finding is in agreement with the fact that the average hydrogen bonding between water molecules decreases within the PE brush layer (discussed later). Figure 2.5(c) plots the static dielectric constant of water, normalized to its bulk value as a function of σ_g for N=49. This normalized form can be expressed as:

$$\bar{\epsilon_r} = \frac{\varepsilon(0)}{[\varepsilon(0)]_{bulk,w}}, \quad (2.2)$$

where $\varepsilon(0) = \varepsilon_\infty + \frac{1}{3k_BT\epsilon_0 V}(\langle \mathbf{M}^2 \rangle - \langle \mathbf{M} \rangle^2)$ is the static dielectric constant [obtained using the linear response equation[85]], $[\varepsilon(0)]_{bulk,w}$ is the static dielectric constant of bulk water, ε_∞ is the dielectric constant at infinite frequency which is equal to 1 for our case, k_BT is the thermal energy, ϵ_0 is the permittivity of free space, V is the volume, and **M** is the net dipole moment of the volume under consideration. We observe a dramatic decrease in the dielectric constant with values dropping to less than 15% of the bulk value at σ_g =0.2/σ^2. Most water molecules inside the PE brushes are strongly bound to the counterions due to ion-dipole interactions. These bound water molecules have a lower ability to polarize and thereby do not contribute much to the dielectric constant.[15] The percentage of such bound water molecules increases with σ_g [see Fig. 2.5(c)], leading to the observed reduction in dielectric constant with σ_g.

In figure 2.5(d), we plot the mass density of water across the simulation domain. The water density inside the PE brushes decreases monotonically with an increase in grafting density. This is due to the reduced lateral spacing between the brushes at a high grafting density coupled with the excluded volume effects of the PE brushes and counterions, which eventually leaves a lesser space for the inclusion of the water

molecules. We witness a significant reduction in the density (by 1/3rd of the bulk value) within the PE brush layer at $\sigma_g = 0.2/\sigma^2$. There is a sharp gradient in density across the PE-brush-water interface especially for high values of the grafting density. Of course, the mass density approaches its bulk value of 1 g/cm^3 far away from the brushes.

In Figure 2.5(e), we further investigate the structure of water by studying the hydrogen bond network of the water. We have considered hydrogen bonding between neighboring water molecules, between water and oxygen on the PAA brushes (within the PE brush layer), as well as between water and Cl^- anions. The conditions for the existence of hydrogen bond are taken as: distance between O_w and X < 3.4 Å, distance between X and H_w < 2.425 Å, and the angle H_w–O_w–X < 30°, where X = {O_w, $O_{Carboxylate}$, Cl^-} and H_w represents the hydrogen of water molecules.[86,87] We plot the variation of the average number of hydrogen bonds per water molecule (n_{HB}) along *z* direction. n_{HB} is reduced to ~ 2.7 within the PE layer (for $\sigma_g = 0.2/\sigma^2$) as a result of the severing of the hydrogen bond network in the presence of brushes and counterions. The decrease in n_{HB} is a direct consequence of the decline in average number of hydrogen bonds per water molecule with other water molecules $n_{HB,w}$ (see Fig. 2.6). Just like density, there is a steep rise in n_{HB} across the PE brush-water interface, indicating that water quickly reestablishes its bulk structure/arrangement outside the PE brush layer. The bulk value of n_{HB} (far away from the brushes) is about 3.5. Such bulk value of n_{HB} has been obtained in previous experimental, theoretical, and simulation studies. For example, Smith *et al*.[88] experimentally reported the bulk value of n_{HB} as 3.3 at 284 K using oxygen K-edge x-ray adsorption technique. Muscatello *et al*.,[89] in their MD simulation study of water transport through graphene-based membranes, reported the

number of hydrogen bonds in the bulk as ~ 3.5. Finally, Haggis *et al*.[90] calculated the percentage of water molecules (n_i) forming *i* hydrogen bonds for i=0, 1, 2, 3, 4: a simple calculation revealed that in the bulk, $n_{HB} = \frac{\sum_{i=0}^{4} i n_i}{100} \approx 3.55$ at 298 K.

It is important to investigate the effects of PE brushes on hydrogen bonding of water molecules with each other. This will help shed light on the local structure of water molecules within the PE brushes. Figure 2.6 plots the transverse variation of the average number of hydrogen bonds per water molecule with other water molecules ($n_{HB,w}$), for different values of σ_g.

The decrease in $n_{HB,w}$ inside the PE brushes is consistent with the findings of Han et al[83], who reported a reduction in hydrogen bonding between water molecules with increasing salt concentration for superconcentrated aqueous LiTFSI solution. An increase in σ_g increases the counterion molality within the brushes due to confinement of the counterions within a smaller volume. This enhancement in counterion molality with σ_g reduces the value of $n_{HB,w}$, as evident from Figure 2.6. The reduction in $n_{HB,w}$ with σ_g is partly compensated by an increase in the number of hydrogen bonds between water and $O_{Carboxylate}$. The overall decrease of n_{HB} with σ_g [witnessed in Figure 2.5(e)] is therefore the resultant of a decrease in hydrogen bonding between water molecules and an increase in hydrogen bonding between water and $O_{Carboxylate}$.

Finally, Figure 2.5(f) depicts the MSD for water molecules present in the bulk. Just like counterions, the MSD for water molecules is isotropic within the bulk. However, the value of self-diffusivity obtained by fitting the bulk MSD is D=1.24 x 10^{-9} m^2/s, which is about half the reported literature value of D=2.7 x 10^{-9} m^2/s for SPC/E water.[91] This

is again an artifact associated with the use of the Langevin thermostat (as explained earlier). We confirmed this hypothesis by separately calculating the self-diffusivity of pristine water simulated using the Nosé-Hoover thermostat[92,93] and recovering the value reported in the literature. Figure 2.5(f) also quantifies the MSD of water molecules within the PE brush layer. The MSD plateaus out after a few picoseconds, just like it did for the counterions. Also, we observe a massive lowering in the MSD confirming a severe reduction in the mobility of the water molecules. This is due to the steric effects (or the confinement effect induced by the brushes) as well as ion-dipole interactions binding the water molecules to the neighboring polyelectrolytes and counterions. We observe a slightly higher MSD in z-direction as compared to the x and y directions possibly due to the lateral confinement (i.e., confinement in x and y directions) imposed by the densely grafted brushes.

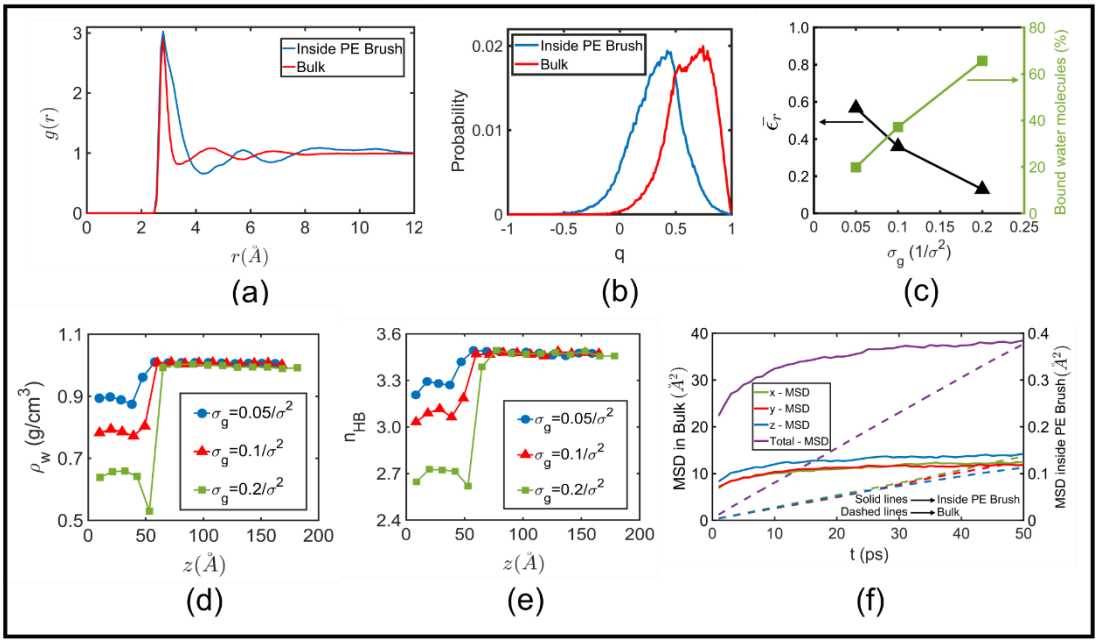

Figure 2.5: *Distribution, Structure, and Properties of Water*

(a) O_w-O_w RDF in bulk and inside the PE brushes for $\sigma_g=0.2/\sigma^2$. (b) Probability distribution of the orientational tetrahedral order parameter q in bulk and inside PE brushes for $\sigma_g=0.2/\sigma^2$. (c) Variation of the static dielectric constant (normalized by its bulk value) of water, within the brushes (left axis) and the percentage of water molecules within the brushes, bound to the counterions (right axis), with PE brush grafting density. (d) Transverse distribution of mass density of water for various grafting densities. (e) Transverse distribution of the number of hydrogen bonds per water molecule (n_{HB}) for various grafting densities. (f) MSD of water molecules in bulk (see left axis) and inside the PE brush layer (see right axis) for $\sigma_g=0.2/\sigma^2$. In (f), solid and dashed lines indicate MSD inside the brushes and in bulk respectively. N=49 is used for all the subfigures.

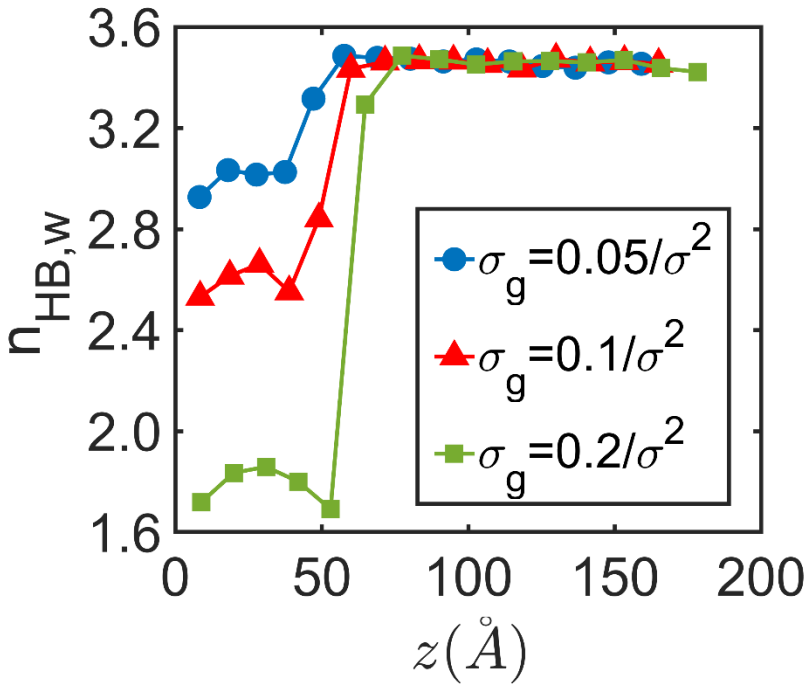

Figure 2.6: *Transverse variation of $n_{HB,w}$ across the simulation domain for various σ_g. Results are shown for N=49.*

2.3. Implications for Continuum Models

Our simulations report a massive decrease in the dielectric constant of water within the PE brush layer, particularly at high grafting densities [see figure 2.5(c)]. This has tremendous implications for several continuum models involving PE brush systems. A number of sophisticated continuum theories like the augmented Strong stretching theory,[39] Self-consistent field theory[94] etc. assume that the dielectric constant of water remains unaltered (same as bulk) within the PE brush layer. Our study clearly indicates that such an assumption might not be accurate especially at high grafting density of the brushes. Thus, the presence of brushes not only changes water structure and arrangement at the molecular level, but also leads to a radical change in water properties at the macroscopic length scale.

Mean field-based continuum models for the PE brushes neglect the effects of ion-ion correlations. Such ion-ion correlations become prominent at high ionic concentrations like that observed in our simulations for larger values of σ_g. For better predictions of the PE brush configuration, these correlations need to be explicitly considered in the total free energy of the system. McEldrew et al[15] recently proposed the first continuum model for EDL description of water-in-salt electrolytes. Extending these calculations to PE brush systems can be an interesting problem for future research.

2.4. Effect of Multivalent Counterions

We ran simulations for the case where the brush charge was neutralized by the Ca^{2+} counterions for N=49 and σ_g=0.05/σ^2, 0.2/σ^2. The simulations for this case followed the same methodology as the case of the PE brushes neutralized by the Na^+ counterions (see section 2.5) except for the addition of an external salt. No salt was added for the Ca^{2+} counterion case, while for the case of the PE brushes neutralized by the Na^+ counterions 0.1 M of added NaCl salt was considered. We believe that at such a small concentration, salt should not have any significant effect on the local counterion and water structure within the brushes. The force field parameters for Ca^{2+} counterions were taken from Li et al[102].

Significant changes in the counterion solvation structure were observed within the PE brushes when compared to the bulk [see Table 2.2 and Figure 2.7(a)]. Inside the PE brushes, we witness a drastic replacement of hydration water with $O_{Carboxylate}$ atoms within the first solvation shell [$r \leq 3.4$ Å[103]] of Ca^{2+}. However, the total coordination number of Ca^{2+} ions remains almost invariant within the brushes, similar to the case of Na^+ counterions. Of course, the molality for Ca^{2+} counterions is much lesser than that of Na^+ counterions at the same σ_g because fewer Ca^{2+} counterions are required to neutralize the PE brush charge.

Case	Counterion concentration (m)	Number of $O_{Carboxylate}$ atoms	Number of O_w atoms	Coordination number ($O_{Carboxylate}$+O_w)	Weight ratio	Volume ratio
Bulk[97]	-	-	7.1	7.1	-	-
Inside PE brush (N=49, σ_g=0.2/σ^2)	7.685	4.20	3.16	7.36	1.414	2.183
Inside PE brush (N=49, σ_g=0.05/σ^2)	1.905	3.07	4.25	7.32	0.353	0.546

Table 2.2: *Comparison of the solvation structure of Ca^{2+} ions (in terms of the species, namely $O_{Carboxylate}$ atoms or O_w atoms, occupying the solvation shell) in bulk and within the PE brushes for the case where the Ca^{2+} are the counterions neutralizing the charge on the PE brushes. The table also provides the weight and the volume ratios of the "salt" (Ca^{2+}-PE brush repeating unit) to the water indicating if the "salt" outnumbers water in mass and volume (and thereby leads to the "water-in-salt"-like structure).*

Table 2.2 enlists the variation in the mass and the volume ratio of Ca^{2+}-R-COO^- complex (serving as the "salt") to water for different σ_g (i.e., for different counterion concentration). The counterion-PE brush repeating unit complex overwhelms the water at a counterion concentration of 5.4 m (by mass) and 3.5 m (by volume), which correspond to a grafting density of 0.14/σ^2 and 0.09/σ^2 respectively [see Figure 2.7(b)]. The crossover grafting density to 'water-in-salt' system (by both weight and volume)

is remarkably similar for both Na^+ and Ca^{2+} counterions. Hence, we are confident that our results for monovalent counterions can be extended to multivalent counterions.

We also investigated the effects of counterion valence on their mobility within the brushes. Our results indicate a reduced mobility (quantified by a reduced mean square displacement) for the divalent Ca^{2+} counterions as compared to the monovalent Na^+ counterions [see Fig. 2.7(c)] for all σ_g. This is due to the enhanced electrostatic binding between the divalent ions and PE brush segments as compared to their monovalent counterparts.

Figure 2.7(d) depicts the mean square displacement (MSD) of water molecules within the brushes. At high grafting density ($\sigma_g = 0.2/\sigma^2$), the MSD of water molecules is greater for the case of the PE brushes neutralized by the Ca^{2+} counterions. This can be explained using the concept of 'free water' molecules. We define the water molecules present inside the first solvation shell of a counterion as 'bound water'. Conversely, any water molecule that is not located inside the first solvation shell of a counterion is termed as 'free water'. At high grafting density, there is a huge difference in the percentage of free water molecules between the cases of monovalent and multivalent counterions. Our analysis reveals that at $\sigma_g = 0.2/\sigma^2$, the percentage of 'free water' is ~34% for the case of Na^+ counterions case and ~62% for the case of Ca^{2+} counterions. This is because fewer Ca^{2+} counterions are required to neutralize the PE brush charge, resulting in a lower number of total water molecules present within the first solvation shell of the Ca^{2+} ions. The bound water molecules are significantly less mobile and are

responsible for the reduction in the MSD of water for the case of monovalent counterions at high σ_g. On the other hand, at low grafting density ($\sigma_g = 0.05/\sigma^2$), we witness a reduction in the MSD of water molecules for the multivalent counterion case. This is because at low σ_g, most of the water molecules are 'free water'. In fact, the percentage of 'free water' is ~80% for the case of Na^+ counterions and ~86% for the case of Ca^{2+} counterions at $\sigma_g = 0.05/\sigma^2$. As most of the water is unbound, the enhanced ion-dipole interactions with the multivalent counterions (and thereby an enhanced electrostatic binding) leads to a reduction in the MSD of water molecules.

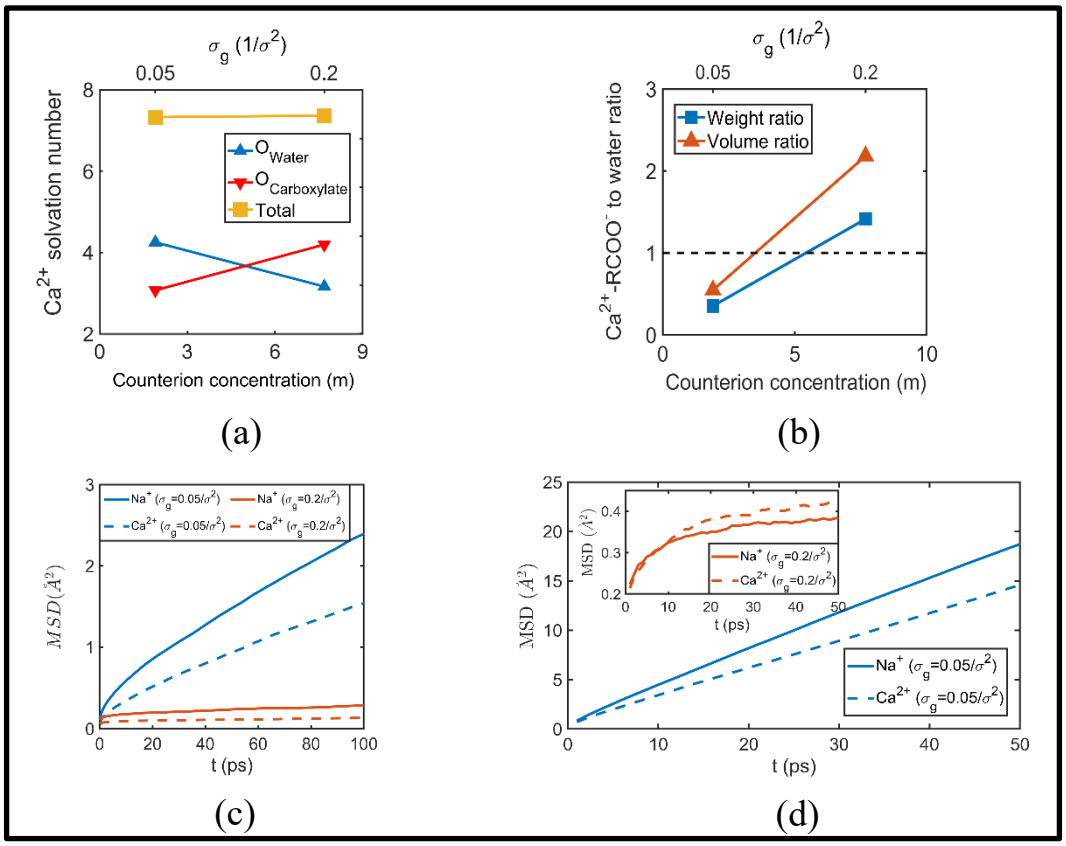

Figure 2.7: *(a) Variation in the solvation structure of divalent Ca^{2+} counterions with σ_g (top axis) and counterion concentration (bottom axis). (b) Variation in the salt (Ca^{2+}-PE brush repeating unit) to water ratio by weight and volume within the PE brushes with σ_g (top axis) and counterion concentration (bottom axis). Table 2.2 summarizes the different numbers represented in (a) and (b). (c) Comparison of counterion MSD within PE brush layer for monovalent (Na^+) and divalent (Ca^{2+}) counterions for $\sigma_g=0.05/\sigma^2$ and $0.2/\sigma^2$, (d) Comparison of MSD of water molecules within the PE brushes for $\sigma_g=0.05/\sigma^2$ and $0.2/\sigma^2$ (see inset). N=49 is used for all subfigures.*

2.5. Simulation Details

We simulate backbone-charged PE brushes using an explicit all-atom model on the Molecular Dynamics (MD) simulation package LAMMPS.[95] 36 fully ionized PAA chains H[-CH_2-$CH(COO^-)$-]$_n$$CH_3$ (neutralized by Na^+ counterions) were grafted in a 6 x 6 square array by fixing their lowermost terminal carbon on the x-y plane. Simulations are performed for four values of grafting density ($\sigma_g = 0.05/\sigma^2$, $0.1/\sigma^2, 0.15/\sigma^2,\ 0.2/\sigma^2$), and four values of the number of backbone carbon atoms (N=29, 39, 49, 69). A continuous purely repulsive LJ wall and a uniform reflective wall are placed below the grafting surface and at the top of the simulation domain respectively, to prevent the mobile ions and water molecules from escaping. The brushes are modelled using the OPLS-AA force field[96] and the bonded/non-bonded interaction parameters for the PEs have been taken from the OPLS database. The 3-site SPC/E model[64] is used for water molecules. 0.1 M NaCl is added to the system in addition to the Na^+ counterions neutralizing the fully ionized brushes.

Non-bonded interactions are modelled as the sum of a Coulombic potential (U_{Coul}) with a cut-off of 10.5Å and a shifted-truncated 12-6 Lennard-Jones potential (U_{LJ}) with a cut-off of 13Å. Long-range Coulombic interactions were calculated using a PPPM (particle-particle particle-mesh) algorithm[97] with periodic boundary conditions in x and y directions, and a fixed boundary condition in the z direction. The LJ interaction parameters for all mobile ions are taken from Joung et al.[98] Geometric mixing rules are used for LJ interactions between dissimilar atoms, except for the ion-ion and ion-water interactions, which use the Lorentz-Berthelot mixing rules in order to be consistent

with ref 98. All bonded (bonds, angles, dihedrals, impropers) and non-bonded interaction parameters are provided in section 2.6.

The initial configuration involved an array of fully extended polyelectrolyte chains with a line of counterions adjacent to them. Salt ions were added randomly above the polyelectrolyte layer while water was present throughout the simulation domain (both inside and outside the PE brush layer). The bonds and angles of water molecules were preserved by using the SHAKE algorithm.[99] The system is first run under the NP_zT ensemble (where the subscript z denotes that only the vertical gap is allowed to change) to maintain pressure and temperature at 1 atm and 300 K, respectively. Nose-Hoover thermostat and barostat[92,93] were used with relaxation times of 0.1 ps and 1 ps for temperature and pressure respectively. Subsequently, the system is equilibrated under the NVT ensemble. The polyelectrolytes and water (including the mobile ions) were thermostated separately at 300 K using the Langevin thermostat[81] with a relaxation time of 0.1 ps. It was ensured that the height of the simulation domain is always greater than or equal to Nσ. The particle trajectories were calculated by using the Velocity Verlet algorithm, with a timestep of 2 fs. The simulations were carried out on parallel processors in the HPC cluster Deepthought2. Coordinates of all atoms were dumped every 1000 fs, while coordinates of atoms in polyelectrolytes, water molecules and mobile ions were dumped in separate files every 200 fs. The simulation results were visualized using OVITO.[100]

Average end point height $<z_e>$ of the brushes was monitored to check for equilibration. The autocorrelation function for a variable Y is given by $C_Y(t) = \frac{<(Y(t)-\langle Y\rangle)(Y(0)-\langle Y\rangle)>}{<Y^2>-<Y>^2}$, where $\langle Y\rangle$ denotes the mean value of Y. We plot the autocorrelation function for

average end-point brush height $C_e(t)$ in Figure 2.8. The corresponding autocorrelation time scale is calculated as $\tau_e = \int_0^{t_0} C_e(t)dt\,/(1 - C_e(t_0))$, where t_0 is the time at which $C_e(t) = 1/e$. [101]

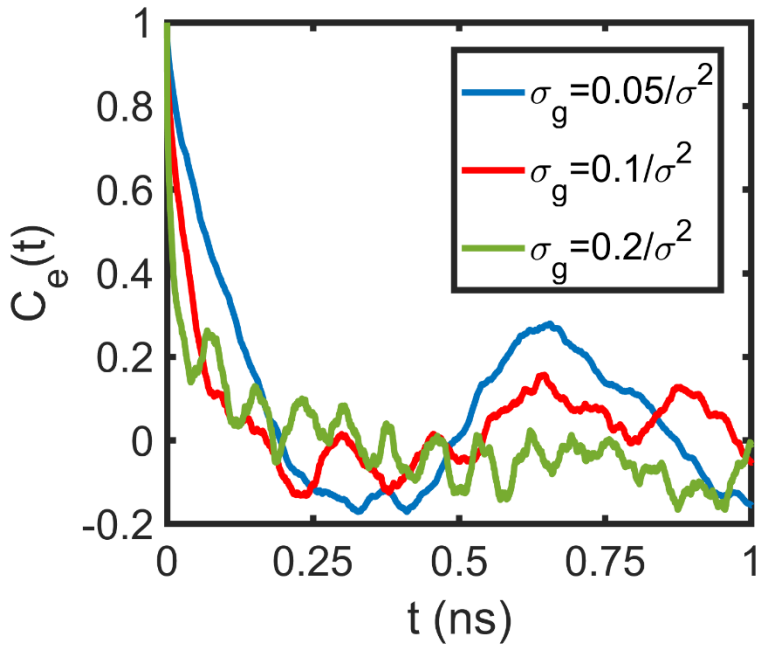

Figure 2.8: *Autocorrelation function $C_e(t)$ of average end-point brush height $\langle z_e \rangle$ for various σ_g. Results are shown for N=69.*

Table 2.3 summarizes the equilibration time (T_{equi}), production run time (T_{prod}) and autocorrelation time (τ_e) for all values of N and σ_g. The production run time for each case is more than one order of magnitude larger than the autocorrelation time, ensuring proper statistical sampling. Convergence was further checked by simulating the cases with N=49 for longer times (≥2 ns). No significant changes in the results were observed for these longer runs, with less than 2% error in the brush end-point height and less than 4% error in the solvation structure of Na^+ ions.

N	σ_g ($1/\sigma^2$)	T_{equi} (ns)	T_{prod} (ns)	τ_e (ps)
29	0.05	4	2	167.71
29	0.1	4	2	52.11
29	0.15	8	2	19.63
29	0.2	8	2	6.12
39	0.05	12	2	353.65
39	0.1	10	2	227.20
39	0.15	8	2	28.10
39	0.2	6	2	81.69
49	0.05	8	2	138.80
49	0.1	6	2	131.86
49	0.15	8	2	9.53
49	0.2	4	2	4.60
69	0.05	10	2	92.82
69	0.1	8	2	38.21
69	0.15	10	2	48.21
69	0.2	6	2	11.19

Table 2.3: *Equilibration time (T_{equi}), production run time (T_{prod}) and autocorrelation time (τ_e) for all N and σ_g.*

2.6. Force Field Parameters

In Fig. 2.9, we provide a schematic representation of the fully ionized polyacrylic acid molecule.

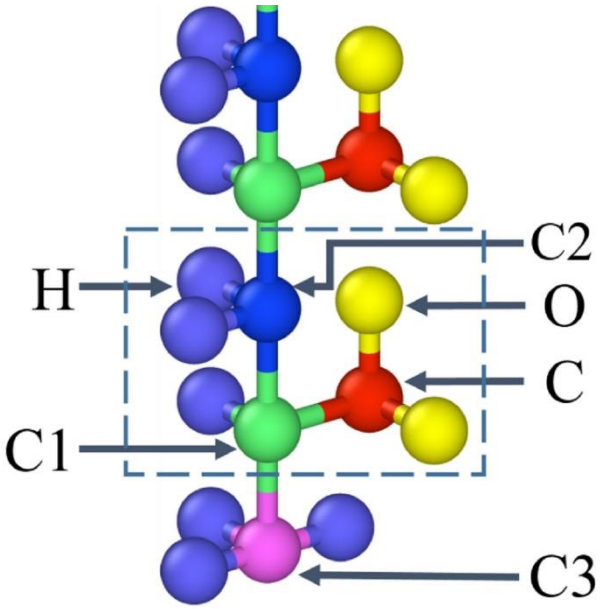

Figure 2.9: *Schematic representation (not to scale) of the fully ionized polyacrylic acid molecule. The arrows indicate the atom type of their respective atoms. Dashed box indicates the polyelectrolyte's (PE's) repeating unit.*

Nonbonded Potentials and Corresponding Parameters

The Lennard-Jones (LJ) potential (U_{LJ}) used in the simulations is expressed as:

$$U_{LJ} = 4\epsilon_{ij}\left[\left(\frac{\sigma_{ij}}{r_{ij}}\right)^{12} - \left(\frac{\sigma_{ij}}{r_{ij}}\right)^{6}\right], \quad (2.3)$$

while the Coulombic pairwise interaction (U_{Coul}) used in the simulation is expressed as:

$$U_{Coul} = \frac{q_i q_j}{4\pi \in_0 \in_1 r_{ij}}. \quad (2.4)$$

In the above equations, ϵ_{ij} is the depth of the LJ potential well between atoms i and j, σ_{ij} is the distance where the LJ potential between atoms i and j becomes zero, q_i and q_j are charges of i^{th} and j^{th} atoms, r_{ij} is the distance between atoms i and j, $\in_0$ is the permittivity of free space and $\in_1$ the relative permittivity of the background (taken to be 1).

The values for these parameters [appearing in eqs.(2.3,2.4)] for all the different atom types, depicted in Fig. 2.9, have been summarized in Table 2.4.

Atom Type	**Charge (e)**	**Mass (amu)**	**ϵ (Kcal/mole)**	**σ (Å)**
C3 (CH_3)	-0.18	12.011	0.066	3.50
C2 (CH_2)	-0.12	12.011	0.066	3.50
C1 (CH, Attached to COO-)	-0.16	12.011	0.066	3.50
C (COO-)	0.70	12.011	0.105	3.75
H	0.06	1.008	0.03	2.50
O (COO-)	-0.80	15.999	0.210	2.96
O_w (H_2O)	-0.8476	15.999	0.155354	3.166
H_w (H_2O)	0.4238	1.008	0	0
Na	1.00	22.99	0.3526418	2.1595
Cl	-1.00	35.453	0.012785	4.83
Ca	2.00	40.078	0.04560206	2.7083
Continuous LJ Wall (Parameters remain unchanged for interaction with all atom types)	0.00	15.00794	0.1947	3.00 (LJ cut off length is 3.36 Å)

Table 2.4: *Charge, mass and LJ parameters for all different atom types*

Bonded Potentials and Corresponding Parameters

The potential energy for harmonic bond style is expressed as:

$U_{bond} = K_b(r - r_0)^2$ (2.5)

Here, r_0 is the equilibrium bond length and K_b is bond stiffness. The values for r_0 and K_b for different bonds are provided in Table 2.5.

Bond Type	$\boldsymbol{K_b}$, $(\frac{\boldsymbol{Kcal}}{\boldsymbol{mol}.\text{Å}^2})$	$\boldsymbol{r_0}$, (Å)
C2-H	340.0	1.09
C2-C1	268.0	1.529
C1-H	340.0	1.09
C3-H	340.0	1.09
C-C1	317.0	1.522
C1-C3	268.0	1.529
C-O	656.0	1.25
O_w-H_w	-	1.00

Table 2.5: *Bond parameters used in the simulations*

The potential energy associated with the finite angle between different bonds is calculated using the following equation:

$U_{angle} = K_a(\theta - \theta_0)^2$ (2.6)

Here, θ_0 is the equilibrium value of the angle and K_a represents the angle stiffness. The values for θ_0 and K_a for different bonds are provided in Table 2.6.

Angle Type	$K_a, (\frac{Kcal}{mol.rad^2})$	$\theta_0(deg)$
H-C2-H	33.00	107.8
H-C2-C1	37.5	110.7
C2-C1-H	37.5	110.7
C1-C3-H	37.5	110.7
H-C3-H	33.00	107.8
H-C1-C	35.0	109.5
O-C-O	80.0	126.00
C2-C1-C	63.0	111.1
C3-C1-C	63.0	111.1
H_w-O_w-H_w	-	109.47
C2-C1-C2	58.35	112.7
C2-C1-C3	58.35	112.7
C1-C-O	70.0	117.0
C3-C1-H	37.5	110.7
C1-C2-C1	58.35	112.7

Table 2.6: *Angle parameters used in the simulations*

The potential energy associated with the dihedral interactions is given by

$$U_{dihedral} = \frac{1}{2}K_1[1 + \cos(\emptyset)] + \frac{1}{2}K_2[1 - \cos(2\emptyset)] + \frac{1}{2}K_3[1 + \cos(3\emptyset)] + \frac{1}{2}K_4[1 - \cos(4\emptyset)] \qquad (2.7)$$

Here, K_1, K_2, K_3 and K_4 are the Fourier coefficients for torsional interactions, and $\emptyset$ is the torsional angle. Values of K_1, K_2, K_3 and K_4 are provided in Table 2.7.

Dihedral type	$\boldsymbol{K_1}$, $(\boldsymbol{Kcal/mole})$	$\boldsymbol{K_2}$, $(\boldsymbol{Kcal/mole})$	$\boldsymbol{K_3}$, $(\boldsymbol{Kcal/mole})$	$\boldsymbol{K_4}$, $(\boldsymbol{Kcal/mole})$
H-C2-C1-H	0.0	0.0	0.30	0.0
H-C2-C1-C	0.0	0.0	-0.10	0.0
H-C2-C1-C2	0.0	0.0	0.30	0.0
H-C2-C1-C3	0.0	0.0	0.30	0.0
H-C1-C-O	0.0	0.0	0.00	0.0
H-C1-C3-H	0.0	0.0	0.30	0.0
C2-C1-C-O	0.0	0.82	0.00	0.0
C2-C1-C2-C1	1.30	-0.05	0.20	0.0
H-C3-C1-C2	0.0	0.0	0.30	0.0
C3-C1-C-O	0.0	0.82	0. 0	0.0
C1-C2-C1-C	-3.185	-0.825	0.493	0.0
C1-C2-C1-C3	1.30	-0.05	0.20	0.0
H-C1-C2-C1	0.0	0.0	0.30	0.0
H-C3-C1-C	0.0	0.0	-0.10	0.0

Table 2.7: *Dihedral parameters used in the simulations*

Improper torsional dihedrals are modelled using the harmonic function:

$U_{improper} = K_i(\varphi - \varphi_0)^2$ (2.8)

Here, φ_0 is the equilibrium value of the improper torsional angle and K_i represents the improper torsional stiffness. Their values for the C1-O-C-O system is provided in Table 2.8.

Improper Type	$\boldsymbol{K_i}$ $(\frac{\boldsymbol{Kcal}}{\boldsymbol{mol.rad^2}})$	$\boldsymbol{\varphi_0(deg)}$
C1-O-C-O	10.5	180

Table 2.8: *Improper dihedral parameters used in the simulations*

2.7. Conclusions

In this chapter, we have employed all-atom MD simulations to study the behavior of densely grafted PE brushes on a flat surface. The findings describe PE brush configuration and properties in unprecedented atomistic details. More importantly, the chapter establishes a unique nanoconfinement-triggering role of the PE brushes. Such nanoconfinement effect, coupled with the large electrostatic attraction between the brush and the counterion usher in a most remarkable water-in-salt like scenario with the counterion-PE complex serving as the "salt". Similar to the existing water-in-salt electrolyte systems, here too one observes that the water gets replaced by "anion" (here the PE segment serves as the "anion") in the first solvation shell of the counterion (serving as the cation). Also, analogous to the standard water-in-salt systems, the counterion-PE complex overwhelms the water in mass and volume beyond a certain grafting density. Qualitatively similar findings are obtained for multivalent (Ca^{2+}) counterions. Furthermore, the Na^{+} counterions experience a severe confinement effect and large electrostatic attraction to the brushes enforcing a drastic reduction in their diffusivity (quantified by the corresponding lowering of the MSD) within the brushes. Such brush-induced-confinement triggered reduced diffusivity (or reduced MSD) is also witnessed for the water molecules. Also, the water molecules bind to the counterions within the brush layer enforcing a significant reduction in the dielectric constant of the solution within the brushes. Other water properties, such as mass density and average number of hydrogen bonds per water molecule, also undergo a significant reduction due to the brush-induced confinement.

Chapter 3: All-atom Molecular Dynamics Simulations of Weak Polyionic Brushes: Influence of Charge Density on the Properties of Polyelectrolyte Chains, Brush-Supported Counterions, and Water Molecules*

Abstract: *All atom Molecular Dynamics (MD) simulations of planar Na^+-counterion-neutralized Polyacrylic Acid (PAA) brushes are performed for varying degrees of ionization (and thereby varying charge density) and varying grafting density. Variation in the PE charge density (or degree of ionization) and grafting density leads to massive changes on the properties of the PE molecules (quantified by the changes in the height and the mobility of the PE brushes) as well as the local arrangement and distribution of the brush-supported counterions and water molecules within the brushes. The effect on the counterions is manifested by the corresponding variation of the counterion mobility, counterion concentration, extent of counterion binding to the charged site of the PE brushes, water-in-salt-like structure formation, and counterion-water-oxygen radial distribution function within the PE brushes. On the other hand, the effect on water molecules is manifested by the corresponding variation of water-oxygen-water-oxygen RDF, local water density, water-water and water-PE functional group hydrogen bond networks, static dielectric constant of water molecules, orientational tetrahedral order parameter, and water mobility. Enforcing such varying degree of*

* The contents of this Chapter have been published as the following journal article: Sachar, H. S.; Pial, T. H.; Chava, B. S.; Das, S. "All-atom Molecular Dynamics Simulations of Weak Polyionic Brushes: Influence of Charge Density on the Properties of Polyelectrolyte Chains, Brush-Supported Counterions, and Water Molecules" *Soft Matter* **2020**, *16*, 7808-7822.

ionization of weak polyelectrolytes is possible by changing the pH of the surrounding medium. Thus, our results provide insights into the changes in microstructure (at the atomistic level) of weak polyionic brushes at varying pH. We anticipate that this knowledge will prove to be vital for the efficient design of several nano-scale systems employing PE brushes such as nanomechanical gates, current rectifiers, etc.

3.1. Introduction

Charge bearing polymer molecules or polyelectrolytes (or PEs) are undoubtedly one of the pillars of modern-day material science due to their widespread use in day-to-day life. PEs are used for synthesizing a variety of materials ranging from gels[104-106] to solutions[107-109] to blends[110-112]. One of the most intriguing architectures involving PEs is the "brush-like" form, where one end of the individual PE chains is grafted to a substrate. When grafted in close proximity to each other in a good solvent, the PE chains tend to stretch in the direction perpendicular to the substrate in order to avoid monomer-monomer contacts and reduce electrostatic repulsion between the charged segments and in the process attain such "brush-like" configuration. PE brushes find use in a multitude of applications such as nanofluidic energy conversion[1,113], biosensing[2,4], colloidal stabilization[5], oil recovery[8], drug delivery[6-7], etc. This has inspired several theoretical[14,31-39], computational[9-13,40-44] as well as experimental[45-54] studies to probe the structure and configuration of PE brushes.

One of the most exciting prospects about PE brushes is their ability to respond to changes in the surrounding medium like solvent quality, pH, salt concentration, etc. This structural transition of the brushes in response to their environment renders a sense of "smartness" to PE brush grafted interfaces, and forms the basis for several

application such as nanomechanical gates[114], current rectifiers[25-26], etc. One key reason for the responsiveness of weak polyanionic or polycationic PE brushes is a change in the degree of ionization of the titration sites. This is typically induced by variation in the pH of the surrounding medium, shifting the equilibrium of the acid-base reaction responsible for charging of the PE chains. Several studies have investigated the effects of changes in degree of ionization (and thereby the charge density) of PEs in solution[115-119] as well as PE brushes[120-123]. However, most of these studies have focused on the overall structural changes (macrostructure) of the PE molecules rather than the changes occurring at the atomistic length scales (microstructure). Recently, we published the first molecular dynamics (MD) simulation study probing the local arrangement of counterions and water molecules within the planar PE brushes using an all-atom framework[124]. In the current chapter, we take a similar approach to probe the changes in the microstructure of densely grafted Polyacrylic acid (PAA) brushes *with varying degree of ionization*. The charges on the brushes are neutralized by adding an appropriate number of Na^+ counterions to the system (depending on the degree of ionization). A 3-site SPC/E model[64] is used to explicitly resolve the water molecules. Analysis of the microstructure of the brushes is anticipated to provide us fundamental insights into their behavior and thereby envision new applications of PE brushes in the fields of nanotechnology and tribology.

This chapter is organized in the following sections. We begin with a detailed description of our MD simulation setup. Subsequently, we present our results for the brush height and chain mobility, followed by the local arrangement and distribution of the counterions and water molecules respectively. The effect on the counterions is

investigated by quantifying the brush-induced changes in counterion concentration, condensation, solvation structure (and the resultant propensity to form water-in-salt like structure[124]), radial distribution function (RDF), and mobility. On the other hand, the effect on the water molecules is identified by probing the corresponding brush-induced changes in the water-oxygen-water-oxygen RDF, water-water and water-PE functional group hydrogen bond networks, water mass density, static dielectric constant, orientational tetrahedral order parameter[84], and mobility. The results demonstrate massive impact of the changes of the degree of ionization as well as the grafting density. Given that such variation in the degree of ionization can be brought about by the corresponding changes in the pH of the surrounding medium, the findings shed light to the possible impact of the pH-responsiveness of densely grafted brushes on its properties as well as the properties and distributions of the brush-supported counterions and water molecules in an unprecedented atomistically resolved fashion.

3.2. Simulation Details

MD simulations were conducted using an all-atom framework. We considered 36 Polyacrylic acid (PAA) chains having N=49 backbone Carbon atoms. Each chain was end-grafted on a 6 X 6 square lattice by fixing one of their terminal Carbons in the x-y plane (z=0). Each chain consisted of 24 functional groups that could exist either in the protonated state (COOH) or the deprotonated state (COO^-). The degree of ionization of the brushes *f* (ratio of deprotonated functional groups to total number of functional groups) was varied from no charge (f=0) to completely ionized (f=1) in steps of 0.25 i.e. *f*=0, 0.25, 0.5, 0.75, 1. For a given degree of ionization, 24**f* functional groups were randomly ionized along the length of each chain. An equal number of Na^+ counterions

were added in the simulation box to ensure charge neutrality. No external salt was added to the system (salt-free brushes). 3-site SPC/E water molecules[64] were used as the explicit solvent. Two different values of brush grafting densities σ_g = 0.1/σ^2 and 0.2/σ^2 (where σ=3.5 Å is the LJ distance parameter for backbone Carbon atoms) were probed. Enough water molecules were added to ensure that the simulation box height was always greater than or equal to 1.5Nσ to eliminate finite size effects. Continuous LJ and reflective walls were placed at the bottom and top of the simulation box respectively to prevent counterions and water molecules from leaving the system. All simulations were performed on the MD platform LAMMPS[95] (Large-scale Atomic/Molecular Massively Parallel Simulator).

We used the OPLS-AA force field[96] to model the brushes. All bonded (bonds, angles, dihedrals, impropers) and non-bonded parameters (charge, LJ diameter, LJ well-depth) were taken from the OPLS database and provided in section 3.4. A shifted truncated 12-6 Lennard Jones (LJ) potential with a 13 Å cut-off was used to model short-range interactions. The LJ parameters for the Na^+ counterions were taken from Joung et al[98]. LJ interactions between dissimilar atoms were calculated using geometric mixing rules, with the only exception being interactions between Na^+ counterions and water molecules. These interactions were modeled using the Lorentz-Berthelot mixing rules (similar to Joung et al[98]). A modified Particle-Particle Particle-Mesh (PPPM) solver[97] was used to calculate long-range electrostatic interactions with periodic boundary condition in the x and y directions, and fixed boundary condition in z direction.

Our initial configuration consisted of an array of counterions placed adjacent to fully extended PAA chains. Water molecules were added throughout the simulation domain.

The SHAKE algorithm[99] was used to fix the bonds and angles of the SPC/E water molecules. Firstly, the system was run in a NP_zT (the subscript z indicates that only the simulation box height is allowed to change) ensemble using the Nose-Hoover thermostat and barostat[92-93] in order to obtain the correct height of the simulation domain. The system temperature and pressure were maintained at 300K and 1 atmosphere respectively. The relaxation time for temperature and pressure were set to 0.1 ps and 1 ps respectively. This was followed by equilibration in the NVT ensemble using the Langevin thermostat[81]. The temperature of the PE chains and the mobile species (water molecules and counterions) were separately maintained at 300K with a relaxation time of 0.1 ps for the thermostat. The atomic trajectories are calculated using the velocity-Verlet integrator with a time step of 2 fs. A production run of 2 ns was performed for each case and the coordinates of each atom were dumped at intervals of 200 fs and 1000 fs in separate files. The open source software OVITO[100] was used for visualization of the atomic trajectories. We monitored the autocorrelation function for average end-point height of the brushes $<z_e>$ to check for equilibration. The equilibration times as well as the autocorrelation time scale for all simulations are provided in Table 3.1.

The autocorrelation function corresponding to the average end-point brush height was monitored throughout the simulations to check for convergence. The autocorrelation function for a given variable Z can be expressed as:

$$C_Z(t) = \frac{<(Z(t)-\langle Z\rangle)(Z(0)-\langle Z\rangle)>}{<Z^2>-<Z>^2}, \quad (3.1)$$

where the angular brackets denote time average and $\langle Z \rangle$ is the mean value of variable Z over the sampling interval. Figure 3.1 plots the autocorrelation function for the average end-point height of the brushes $[C_e(t)]$.

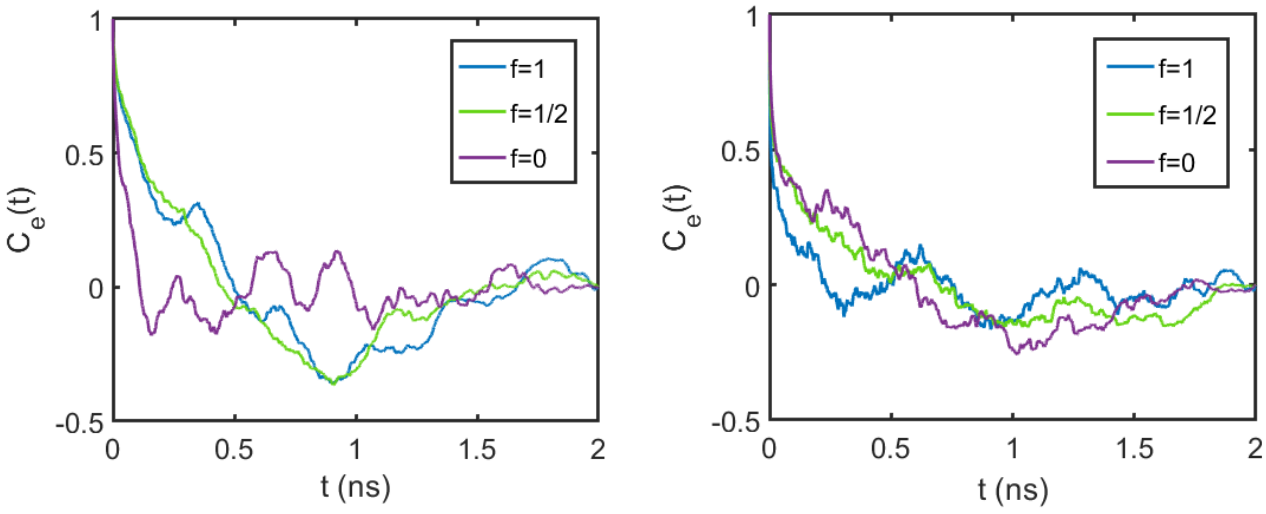

Figure 3.1: *Autocorrelation function* $[C_e(t)]$ *corresponding to the average end-point brush height, plotted over the production run for various degrees of ionization for (a)* $\sigma_g = 0.1/\sigma^2$ *and (b)* $\sigma_g = 0.2/\sigma^2$. *Only three values of degree of ionization (f) are plotted to avoid clutter.*

The time scale corresponding to the autocorrelation function (τ_e) was calculated as:

$$\tau_e = \int_0^{t_0} C_e(t)dt \,/(1 - C_e(t_0)), \quad (3.2)$$

where t_0 is the time when $C_e(t) = 1/e$. [101]

σ_g ($1/\sigma^2$)	f	t_{equi} (ns)	t_{prod} (ns)	τ_e (ps)
0.1	0	14	2	42.37
0.1	0.25	16	2	137.07
0.1	0.5	16	2	158.19
0.1	0.75	12	2	44.76
0.1	1	12	2	136.92
0.2	0	10	2	54.38
0.2	0.25	10	2	12.94
0.2	0.5	8	2	72.60
0.2	0.75	6	2	7.06
0.2	1	8	2	13.44

Table 3.1: *Equilibration time (t_{equi}), production run time (t_{prod}) and autocorrelation time scale (τ_e) for various degrees of ionization and grafting densities.*

3.3. Results

3.3.1 PE Molecules: Brush Height and Chain Mobility

Figure 3.2 plots the end-to-end brush height (<z_e>) for various degrees of ionization (*f*) and grafting densities (σ_g) of the PAA brushes. For a given value of σ_g, we observe only a slight increase in the brush height with the degree of ionization (*f*) due to enhanced electrostatic repulsion between the chain segments as the effective charge of the brush segments increases with an increase in *f*. The brush height begins to saturate at higher values of *f*. On the other hand, an increase in the grafting density implies that the brushes are forced to stretch out more in a direction perpendicular to the grafting surface, enforcing a larger value of the end-to-end brush height for a larger σ_g for a given *f*.

Fig. 3.2 also points that the brushes always remain in the swollen state for all values of *f*, since <z_e> >> ℓ (where $\ell=\sigma_g^{-1/2}$ is the lateral separation between adjacent chains). This behavior is consistent with the experiments of Swift et al[125], who reported no coil-to-globule transition for the PAA chains (in aqueous solution) below a molar mass of 16.5 kDa (corresponding to a degree of polymerization ≈230). They postulated that this behavior was a consequence of the inefficacy of the small chains to participate in intra-chain hydrogen bonding due to a lack of monomer-monomer contacts.

In a previous publication[124], we demonstrated that our all-atom MD-simulation predicted variation of the endpoint brush height (for the fully ionized brushes) with grafting density could be excellently recovered from the scaling laws of the non-linear osmotic brush regime[65-67]. However, in the present chapter, the variation of the end-to-

end brush height with respect to the degree of ionization does not follow the scaling results of the non-linear osmotic brush regime. The scaling law massively overpredicts the change in brush height with respect to the degree of ionization (see Figure 3.3). In fact, the mismatch between the scaling theory and the MD simulation results increases for lower degrees of ionization. This could be due to the lack of the consideration of excluded volume interactions between the PE segments in the scaling law of the non-linear osmotic brush regime, which becomes increasingly important at lower degrees of ionization.

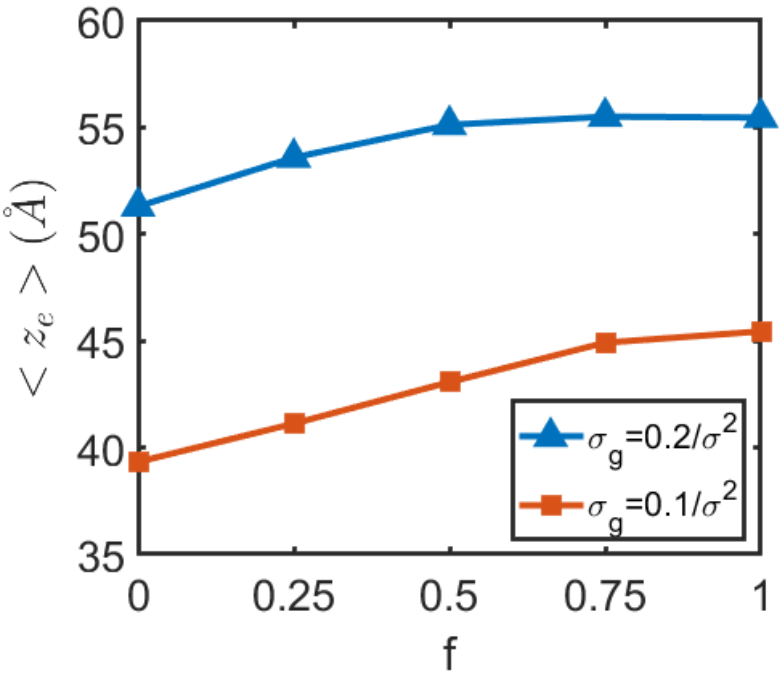

Figure 3.2: *Variation in the end-point brush height with degree of ionization for different grafting densities.*

Now we compare our equilibrium end-point brush height with the scaling predictions of the non-linear osmotic brush regime[65-67]. In this regime, the brush height is dictated by a balance between the elastic energy of the brushes and the entropy of the counterions. However, contrary to the osmotic brush regime, the counterion entropy in non-linear osmotic brush regime is calculated after removing the volume occupied by the PE chains (along with the condensed counterions).

The brush height for the non-linear osmotic brush regime is given by:

$$H_{osm,nl} = nb\frac{f+\sigma_{eff}^2\sigma_g}{1+f}, \quad (3.3)$$

Here, n=(N-1)/2 is the number of repeating units (neutral or ionized) where N is the total number of backbone Carbon atoms, b=3.058 Å is equal to 2 C-C bond lengths, f is the degree of ionization, σ_g is the grafting density and $\sigma_{eff} = \sqrt{2}\sigma$ is the effective monomer diameter after considering the volume of the condensed counterions.

Figure 3.3 compares the end-point brush heights obtained by MD simulations and the scaling laws of the non-linear osmotic brush regime for various degrees of ionization and grafting densities.

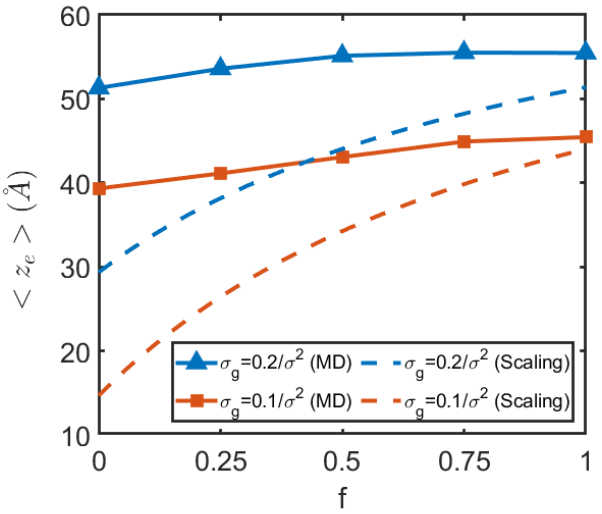

Figure 3.3: *Equilibrium end-point brush height for different degrees of ionization and grafting densities obtained via MD simulations and scaling laws of the non-linear osmotic brush regime.*

Table 3.2 lists the equilibrium end-point brush height obtained via MD simulations for all degrees of ionization and grafting densities.

σ_g ($1/\sigma^2$)	f	$\langle z_e \rangle$ (Å)
0.1	0	39.33
0.1	0.25	41.12
0.1	0.5	43.07
0.1	0.75	44.92
0.1	1	45.44
0.2	0	51.30
0.2	0.25	53.59
0.2	0.5	55.12
0.2	0.75	55.50
0.2	1	55.46

Table 3.2: *Equilibrium end-point brush height for various degrees of ionization and grafting densities.*

Figure 3.4 quantifies the mobility of the PE brushes as functions of the grafting density and degree of ionization. Accordingly, in Figs. 3.4 (a) and (c), we plot the mean squared displacement (MSD) of the backbone Carbon atoms (numbered sequentially from 1 to 49 with 1 being the grafted Carbon atom and 49 being the non-grafted terminal Carbon atom) at t=100ps for different degrees of ionization and grafting densities. We can clearly observe the stratification in the mobility of the backbone Carbon atoms, with

an increase in the mobility along the length of the chain (away from the grafting site). This behavior is expected, as the effect of the topological constraint due to grafting diminishes as one moves away from the grafting site. We see a sharp increase in the MSD of the last few Carbon atoms (near the non-grafted chain end) for all values of degree of ionization. This is due to a reduction in the steric effects from neighboring chains near the non-grafted chain ends. The thermal fluctuations near the chain ends cause different chains to attain different vertical heights and hence reduce the steric effects near the chain ends. The MSD of backbone carbon atoms decreases with an increase in the degree of ionization. This can be attributed to an enhancement in the average number of counterions condensed per PE chain. The condensed counterions form a sheath around the PE chains, like a jacket around a cylinder. The columbic repulsion between the condensed counterions of neighboring chains restricts the motion of the PE segments and thereby reduces the MSD of backbone atoms. Similar trend is observed at t=50ps (see Figure 3.5). On the other hand, an increase in the grafting density forces the PE brushes to be even closer to one another enforcing a reduced mobility (or a smaller MSD) of a particular carbon atom for a given f [compare the findings of Figs. 3.4(a) and 3.4(c)].

Figures 3.4 (b) and (d) depict the MSD of the non-grafted terminal Carbon atoms of the PE chains for different degrees of ionization and grafting densities. The slope of the MSD-vs-time curve decreases due to the topological restrictions resulting from chain connectivity. Here too, we observe a reduction in MSD with an increase in the degree of ionization and an increase in the grafting density (for reasons as explained

before). Similar observations were made for the middle Carbon atom (the 25^{th} Carbon atom) of each chain (see Figure 3.5).

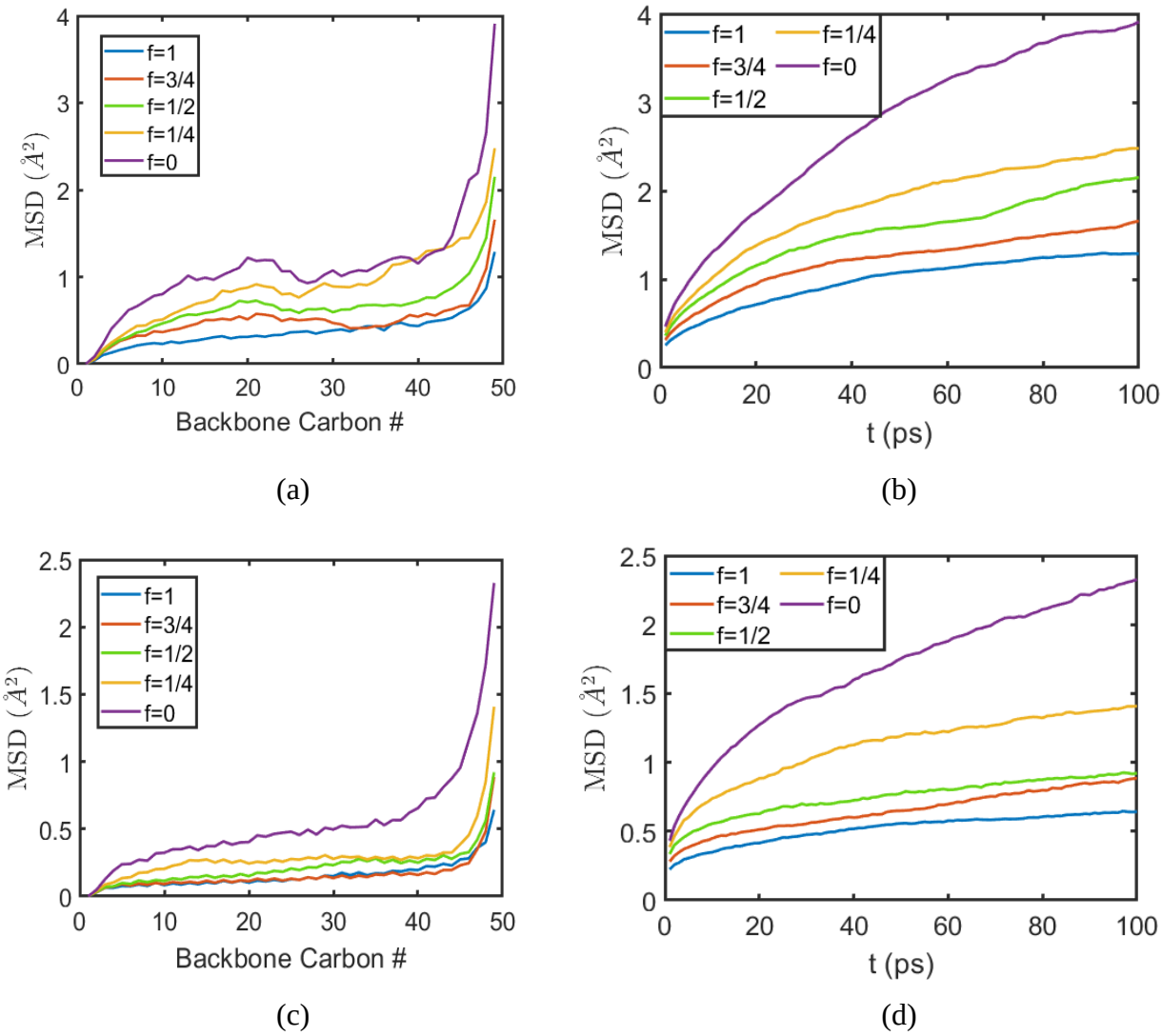

Figure 3.4: *Stratification of the mean squared displacement (MSD) of backbone carbon atoms of the PE chains for various degrees of ionization at t=100ps for (a) $\sigma_g=0.1/\sigma^2$ and (c) $\sigma_g=0.2/\sigma^2$. MSD of the non-grafted terminal Carbon atom of the PE chains for various degrees of ionization for (b) $\sigma_g=0.1/\sigma^2$ and (d) $\sigma_g=0.2/\sigma^2$.*

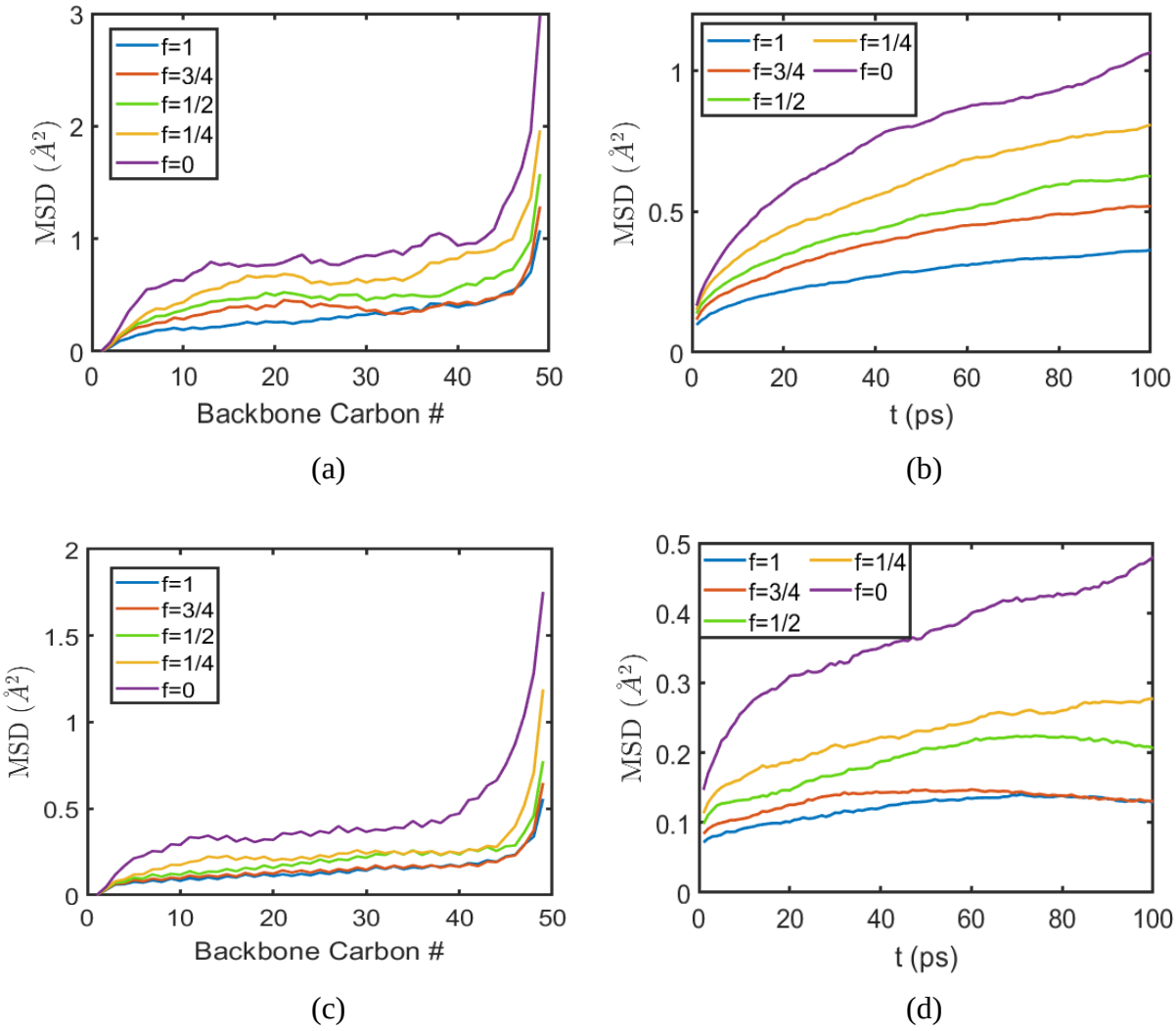

Figure 3.5: *Stratification of the mean squared displacement (MSD) of backbone carbon atoms of the PE chains for various degrees of ionization at t=50ps for (a) $\sigma_g=0.1/\sigma^2$ and (c) $\sigma_g=0.2/\sigma^2$. MSD of the middle (25^{th}) Carbon atom of the PE chains for various degrees of ionization for (b) $\sigma_g=0.1/\sigma^2$ and (d) $\sigma_g=0.2/\sigma^2$.*

3.3.2 Counterions: Local Arrangement and Distribution

Figure 3.6 depicts the counterion concentration (quantified by the corresponding molarity and molality values) within the brushes for various degrees of ionization (*f*) and grafting densities. The total number of counterions released by the ionization of the brushes is proportional to *f*. We observe that almost all the counterions are trapped within the PE brush layer, irrespective of the degree of ionization and grafting density (see Figure 3.7). Thus, the number of moles of counterions within the brushes varies linearly with *f*. The increase in the volume of PE brush layer (due to an increase in brush height) with *f* is rather small (see Figure 3.2). Hence, the counterion molarity has a scaling exponent slightly less than 1 (0.97 for $\sigma_g = 0.1/\sigma^2$ and 0.99 for $\sigma_g = 0.2/\sigma^2$) with respect to the degree of ionization. The counterion molality, on the other hand, follows a scaling of $f^{0.87}$ for both the values of grating density. Counterion molality depends on the ratio of the number of counterions to the number of water molecules i.e. the number density of counterions to that of water molecules. The number density of counterions within the brushes varies almost linearly with f (as explained previously). However, we observe an increase in the mass density (and hence the number density) of water molecules within the brushes with the degree of ionization (see Figure 3.13). This results in a sub-linear scaling exponent (0.87) for both $\sigma_g = 0.1/\sigma^2$ and $0.2/\sigma^2$ for counterion molality within the brushes with respect to *f*.

Of course, both molarity and molality of the counterions increase with the grafting density as a larger grafting density implies a larger number of charged monomers within a given volume, which will lead to a larger number of charged counterions within a fixed volume causing a larger molality and molarity.

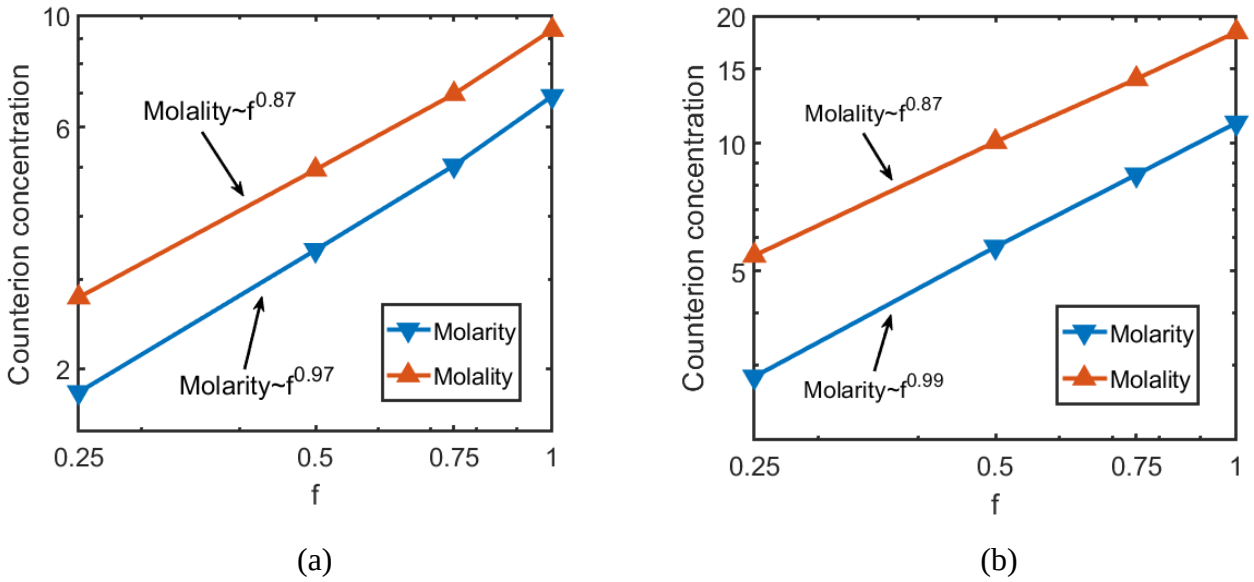

Figure 3.6: *Variation of counterion concentration (expressed in terms of molarity and molality) within the PE brush layer with the degree of ionization for (a)* $\sigma_g = 0.1/\sigma^2$ *and (b)* $\sigma_g = 0.2/\sigma^2$*. In both (a) and (b) the markers are the results from the MD simulations.*

In Figure 3.7, we plot the transverse counterion distribution profiles $\rho_{ci}(z)$, normalized such that $\frac{1}{\sigma_g}\int_0^\infty \rho_{ci}(z)dz = N_{ci}f$, where $N_{ci} = (N-1)/2 = 24$ is the number of counterions associated with each fully ionized PE chain.

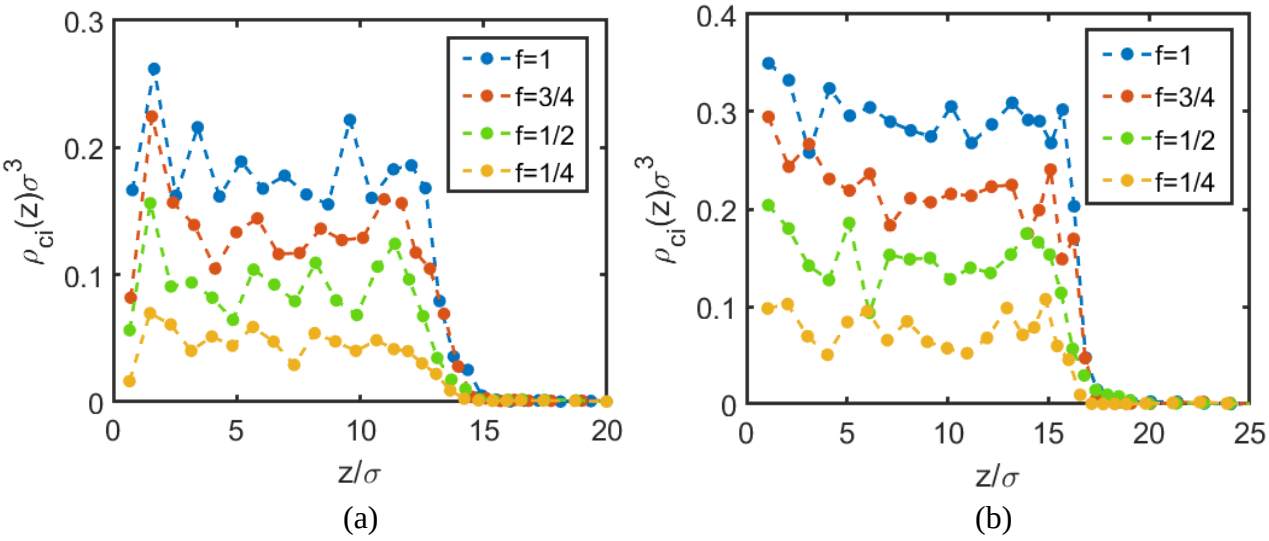

Figure 3.7: *Transverse counterion distribution profiles* $[\rho_{ci}(z)]$ *for various degrees of ionization for (a)* $\sigma_g = 0.1/\sigma^2$ *and (b)* $\sigma_g = 0.2/\sigma^2$.

We can observe that most of the counterions are present within the PE brush layer (see Table 3.2 for the equilibrium end-point brush heights) for all degrees of ionization and grafting densities. This is a characteristic behavior of densely grafted brushes[31].

In addition to the gross description of the change in the concentration of the PE-brush-supported counterions as functions of the grafting density and degree of ionization [see Figs. 3.6(a,b)], we intend to provide a more thorough understanding of the behavior, properties, and distributions of the counterions within the brushes as functions of *f* and σ_g. Accordingly, in Figures 3.8 (a) and (c), we depict the probability density [p(r)] of finding the nearest $O_{Carbocylate}$ atom at a distance *r* from a given counterion within the

brushes for various degrees of ionization and grafting densities. This result will help to quantify the extent of counterion condensation on oxygen atoms of the COO^- groups ($O_{Carbocylate}$ atoms) of the PAA brushes. For all combinations of *f* and σ_g, we observe a peak in the probability density at r~0.64σ (2.24 Å). This value is very close to the LJ diameter of Na^+ counterion (2.1595 Å), indicating counterion condensation. The peak value of probability density increases with degree of ionization, leading to a reduction in the probability density for higher values of r. This indicates a reduction in the average distance between the counterions and the nearest $O_{Carbocylate}$ atom (manifesting, as expected, in higher counterion condensation) with an increase in *f* or an increase in the charge of the PE brushes.

Next, in Figures 3.8 (b) and (d), we plot the cumulative distribution function (cdf) by integrating the probability density over a sphere of radius r [$\text{cdf}(r) = \int_0^r 4\pi r^2 p(r) dr$]. This gives us the overall probability of finding the nearest $O_{Carboxylate}$ atom within a distance r from a given counterion. We observe that the cdf plateaus at a distance of r~0.75σ for all degrees of ionization and grafting density (depicted by black dashed line in the cdf plots). The value of the cdf at this location corresponds to the fraction of counterions condensed on the $O_{Carboxylate}$ atoms. We see a larger cdf plateau value corresponding to a larger *f* (or larger ionization), which is a consequence of the larger peak values in the probability density distribution [see Figures 3.8 (a) and (c)].

Figure 3.8(e) depicts the percentage of condensed counterions within the PE brush layer for various degrees of ionization and grafting densities. Most of the counterions (>90%) are condensed for the explored parametric range. We observe that the percentage of condensed counterions decreases for lower degrees of ionization. This is because the

entropic cost of binding counterions to $O_{Carboxylate}$ atoms increases with a reduction in the degree of ionization. As a result, some of the counterions are able to break free of the enthalpically favorable electrostatic binding with the $O_{Carboxylate}$ atoms in order to reduce the net free energy of the system. Typically, the percentage of condensed counterions is larger at a higher grafting density, with the only exception at f=0.5.

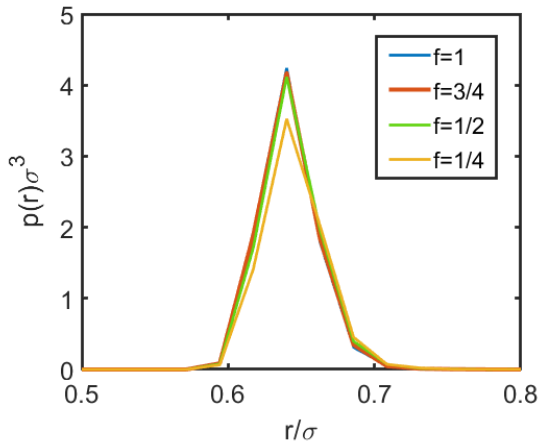
f=1
f=3/4
f=1/2
f=1/4
p(r)σ^3
r/σ

(a)

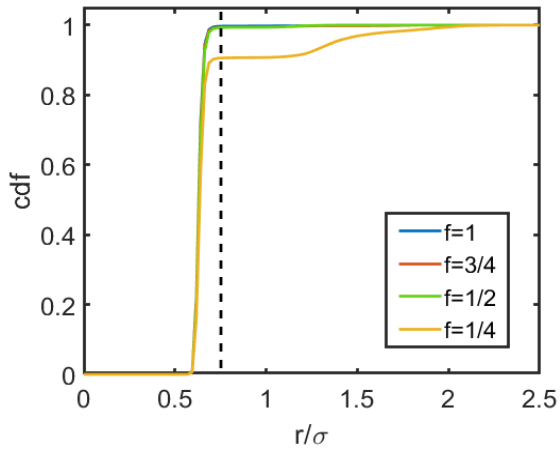
f=1
f=3/4
f=1/2
f=1/4
cdf
r/σ

(b)

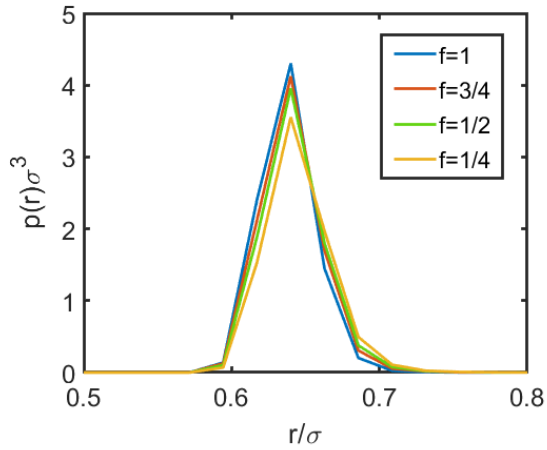
f=1
f=3/4
f=1/2
f=1/4
p(r)σ^3
r/σ

(c)

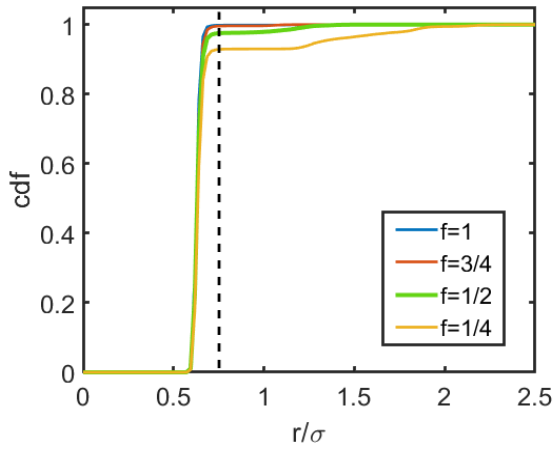
f=1
f=3/4
f=1/2
f=1/4
cdf
r/σ

(d)

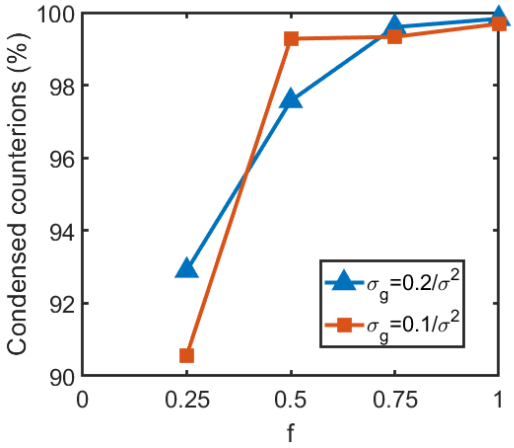
σg=0.2/σ^2
σg=0.1/σ^2
Condensed counterions (%)
f

(e)

Figure 3.8: *Normalized probability distribution of finding the nearest $O_{Carboxylate}$ atom around Na^+ counterions within the PE brush layer for (a) $\sigma_g=0.1/\sigma^2$ and (c) $\sigma_g=0.2/\sigma^2$. (b) and (d) show the cumulative distribution function (cdf) for scenarios depicted in (a) and (c) respectively. (e) depicts the percentage of counterions (present within the PE brush layer) condensed on $O_{Carboxylate}$ atoms for different degrees of ionization and grafting densities.*

In our previous paper considering the all-atom MD simulations of fully ionized PAA brushes, we had established a unique *water-in-salt-like* scenario within the PE brushes, where the solvation water of the brush-supported counterions got replaced by the COO^- functional group of the PE[124]. This *water-in-salt-like* scenario was quantified by studying the solvation structure of the counterions (that gave a sense to what extent the solvation water was replaced by the PE functional group) and the condition where the counterion-PE-functional-group complex (acting as the effective "salt") overwhelmed water in terms of volume and weight[124].

Here we quantify the similar *water-in-salt-like* scenarios as a function of the degree of ionization of the PE brushes and the grafting density. Accordingly, in Figures 3.9 (a) and (c), we depict the solvation structure of the counterions within the PE brushes for different degrees of ionization and grafting densities. Inside the brushes, the solvation water of the counterions (Oxygen of water molecules or O_{Water} atoms to be specific) can be partially replaced by $O_{Carboxylate}$ atoms (Oxygen of COO^- group), $O_{Carbonyl}$ atoms (double bonded Oxygen of COOH group) as well as $O_{Hydroxyl}$ atoms (single bonded Oxygen of COOH group). Such a replacement of the solvation water by the $O_{Carbonyl}$ or $O_{Hydroxyl}$ atoms, which is not relevant for the case of fully ionized PE brushes[124], is only

relevant when the PE brushes are only partially ionized and contains non-dissociated COOH group. The contribution of $O_{Carbonyl}$ and $O_{Hydroxyl}$ atoms in replacing the water from the solvation shell of counterion is much smaller than that of $O_{Carboxylate}$ atoms, for all degrees of ionization. This happens because the carboxylate group (COO^-) has a net negative charge whereas the oxygens on the carboxylic acid group (COOH) only carry partial charges (carboxylic acid group is neutral as a whole), thereby ensuring a much larger attraction between the carboxylate group and the counterions as compared to that between the oxygen of the COOH and counterions. This enhanced attraction allows the COO^- group to show a much larger tendency to bind strongly with the counterion and in the process lead to a much more effective replacement of the solvation water of the counterion. Of course, the replacement of water molecules always occurs in a way that preserves the total solvation number of the Na^+ counterions (~6). The contribution of $O_{Carboxylate}$ atoms increases with *f*, whereas that of $O_{Carbonyl}$ and $O_{Hydroxyl}$ atoms decreases with *f*. This is simply due to the increase in the ratio of ionized groups (COO^-) to protonated groups (COOH) at higher degrees of ionization. The total number of water molecules within the first solvation shell ($r \leq 3.2$ Å) of Na^+ ions shows different trends with respect to the degree of ionization, depending on the grafting density. At lower grafting density ($\sigma_g = 0.1/\sigma^2$), the number of solvation water molecules first decreases with *f* ($0.25 \leq f \leq 0.5$) and then becomes almost invariant with f ($0.5 \leq f \leq 1$). However, this invariance is not witnessed at high grafting density ($\sigma_g = 0.2/\sigma^2$), where the number of solvation water molecules monotonically decreases with the degree of ionization.

Figures 3.9 (b) and (d) depict the mass and volume ratios of the "salt" to water molecules within the PE brushes for various degrees of ionization and grafting density. Very similar to our previous paper[124], in our system, the "salt" is formed by the counterions and the charged PE segments. Therefore, the Na^+ counterions act as the cations and the ionized monomers [-CH_2-CH(COO^-)-] act as the anions. As expected, the "salt" to water ratios (by mass and volume) increase monotonically with the degree of ionization since larger *f* implies the presence of a larger number of ionized segments (-COO^-) that can form the "salt" with the counterions. For the higher grafting density ($\sigma_g = 0.2/\sigma^2$), we observe that both the mass and volume ratios cross 1 at approximately *f*=0.5. Thus, beyond *f*=0.5, the "salt" supersedes water by both mass and volume, giving rise to water in salt like scenarios. However, such a scenario is not witnessed for the lower grafting density ($\sigma_g = 0.1/\sigma^2$), where the mass ratio remains less than 1, even at full ionization of the brushes (*f*=1). This is because of the smaller counterion concentrations (and hence "salt" concentration) witnessed at lower grafting density (see Fig. 3.6).

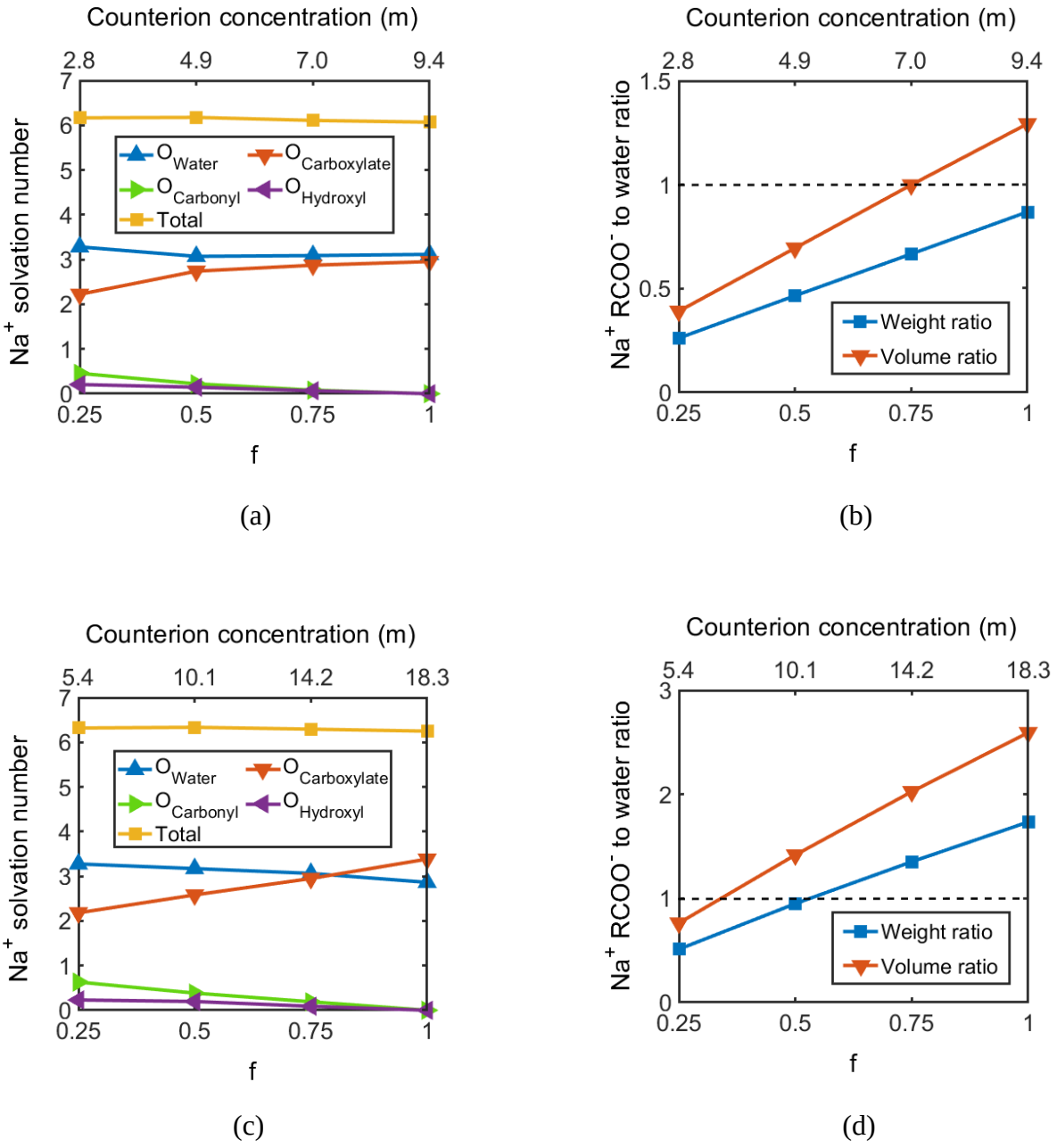

Figure 3.9: *Variation in the solvation structure of Na^+ counterions (within the PE brush layer) with degree of ionization for (a) $\sigma_g=0.1/\sigma^2$ and (c) $\sigma_g=0.2/\sigma^2$. 'Salt'-to-water mass and volume ratios for various degrees of ionization for (b) $\sigma_g=0.1/\sigma^2$ and (d) $\sigma_g=0.2/\sigma^2$. Here "salt" refers to Na^+ $RCOO^-$ (R: $-CH_2-CH-$).*

Figures 3.10 (a) and (b) plot the Na^+ - O_w RDF (O_w represents Oxygen of water molecules) of counterions within the brushes for various degrees of ionization and grafting densities. We also provide the Na^+ - O_w RDF in bulk for comparison. The height of the peak corresponding to the first solvation shell of the counterions reduces inside the brushes (compared to bulk). This is due to the partial replacement of water molecules within the first solvation shell of the counterions by $O_{Carboxylate}$, $O_{Carbonyl}$ and $O_{Hydroxyl}$ atoms.

At higher grafting density ($\sigma_g = 0.2/\sigma^2$) [see Fig. 3.10(b)], the height of this peak, corresponding to the first solvation shell, reduces monotonically with an increasing degree of ionization. This can be explained as follows: Firstly, there is a reduction in the number of water molecules within the first solvation shell of the Na^+ counterions with an increase in *f* [see Fig. 3.9(c) and the related discussions]. Secondly, the overall density of water within the brushes itself increases with the degree of ionization (see Figure 3.13). This reduces the height of the peak even further as the RDF is normalized with respect to the overall density of water within the brushes.

At lower grafting density ($\sigma_g = 0.1/\sigma^2$), the height of this peak, corresponding to the first solvation shell, initially decreases with an increase in the degree of ionization ($0.25 \leq f \leq 0.5$). Again, this is due to the depletion of water molecules within the first solvation shell of Na^+ in this range of *f* ($0.25 \leq f \leq 0.5$) [see Fig. 3.9(a)] coupled with an increase in the overall density of water molecules (within the brushes) with *f*. However, beyond $f=0.5$, the number of water molecules within the first solvation shell of the counterions becomes almost invariant of the degree of ionization (increases very slightly with increase in *f*) [see Fig. 3.9(a)]. Of course, the water density within the

brushes still increases with *f*. The resultant of these two effects is that the peaks heights corresponding to the first solvation shell of Na^+ become very close and vary non-monotonically with respect to *f* for $0.5 \leq f \leq 1$.

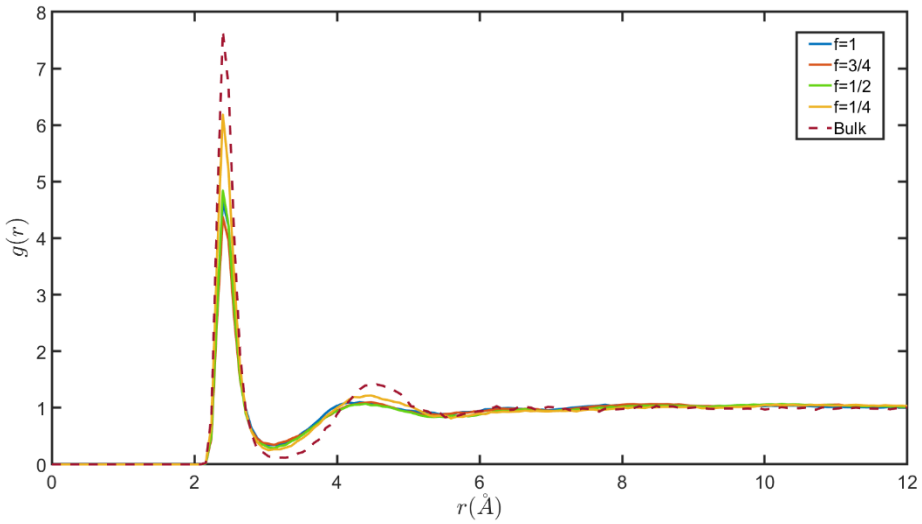

(a)

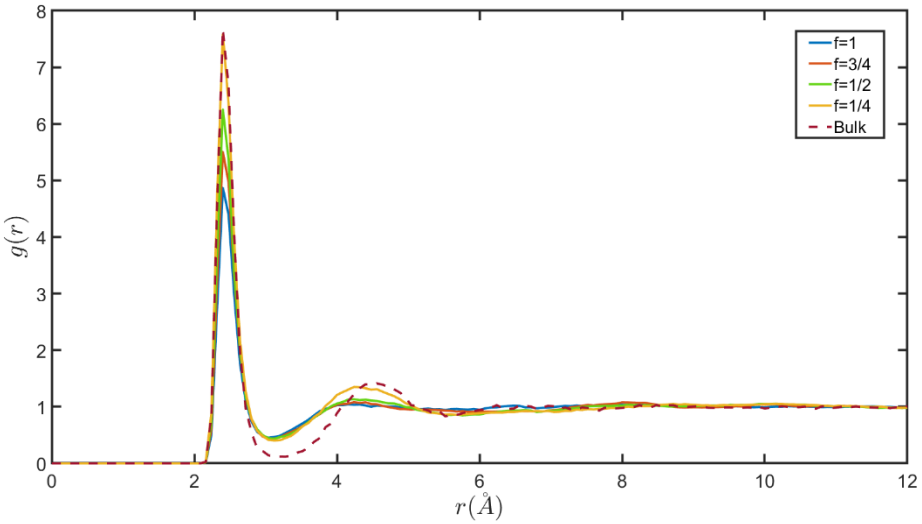

(b)

Figure 3.10: *Na^+ - O_w (O_w represents Oxygen of water molecules) RDF within the PE brush layer for various degrees of ionization for (a) $\sigma_g=0.1/\sigma^2$ and (b) $\sigma_g=0.2/\sigma^2$. Bulk Na^+ - O_w RDF is also provided for comparison (dashed line).*

Our previous all-atom MD simulation paper had identified a significant reduction in the mobility (quantified through the corresponding mean squared displacements or MSDs) of the counterions within the densely grafted PE brushes owing to the large confinement effect introduced by the densely grafted brushes as well as the strong electrostatic attraction between the completely ionized PE brushes and the counterions[124]. Here we study the effect of the varying degree of ionization for different grafting densities on the counterion mobility. For that purpose, in Figures 3.11 (a) and (b) we depict the MSDs of the Na^+ counterions within the brushes for different degrees of ionization and grafting densities. The slope of the MSD-vs-time curves decreases with time and the MSD eventually saturates to a constant value. This indicates that the counterions are unable to diffuse freely. This happens due to a combination of electrostatic binding with the PE segments and brush-induced nanoconfinement. For a given grafting density, the counterion mobility increases with decrease in the degree of ionization due to a decrease in the percentage of bound counterions (see Figure 3.8). Bound counterions are condensed on the $O_{Carboxylate}$ atoms and lose much of their mobility due to strong coulombic interactions. The counterion mobility is much smaller at a higher grafting density ($\sigma_g = 0.2/\sigma^2$) due to enhancement in the percentage of bound counterions (typically) and a stronger brush induced confinement.

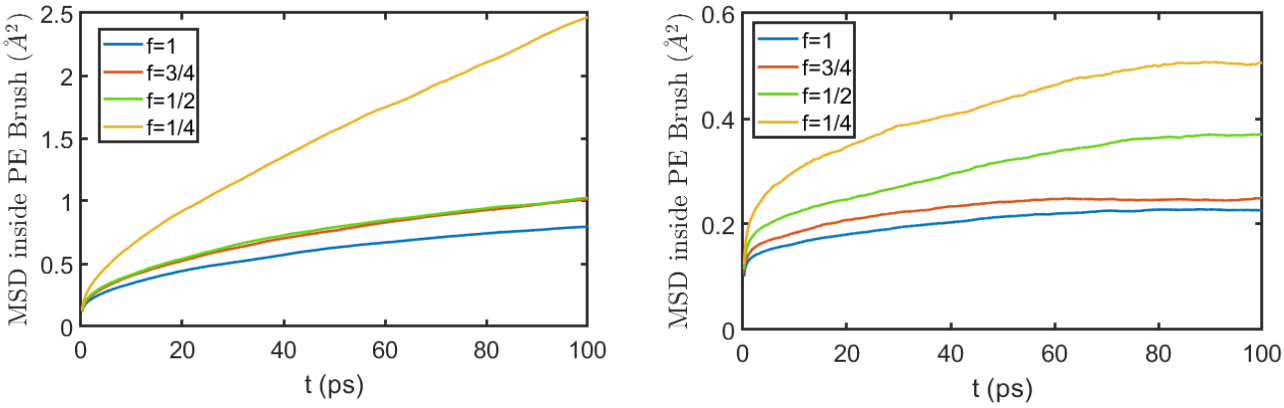

Figure 3.11: *Mean squared displacement (MSD) of Na^+ counterions within the PE brush layer for various degrees of ionization for (a) $\sigma_g=0.1/\sigma^2$ and (b) $\sigma_g=0.2/\sigma^2$.*

3.3.3 Water: Local Arrangement and Distribution

Figure 3.12 depicts the $O_w - O_w$ (water-oxygen-water-oxygen) RDF of water molecules inside the brushes for various degrees of ionization and grafting densities. $O_w - O_w$ RDF of bulk water is also provided for comparison. The peak height corresponding to the first solvation shell increases drastically within the uncharged brushes (f=0) as compared to bulk. This is because the overall density of water molecules within the uncharged brushes is significantly smaller as compared to bulk (see Figure 3.13) and the RDF is normalized with respect to the overall water density.

The RDF shifts towards the right within the brushes as compared to bulk. This is because the PE chains and counterions occupy spaces between the water molecules causing them to drift further away from each other. The rightward shift in RDF is more prominent at higher degrees of ionization due to the corresponding enhanced counterion concentration within the brushes.

The peak height corresponding to the first solvation shell decreases with an increase in the degree of ionization. This is because of the partial replacement of water molecules by counterions inside the first solvation shell of water. Increase in degree of ionization increases the counterion concentration within the brushes, resulting in a more enhanced replacement of water molecules within the first solvation shell of water. Moreover, the overall water density within the brushes increases with the degree of ionization, also resulting in lowering of the first peak height with f (the RDF is normalized with respect to the overall density of water molecules).

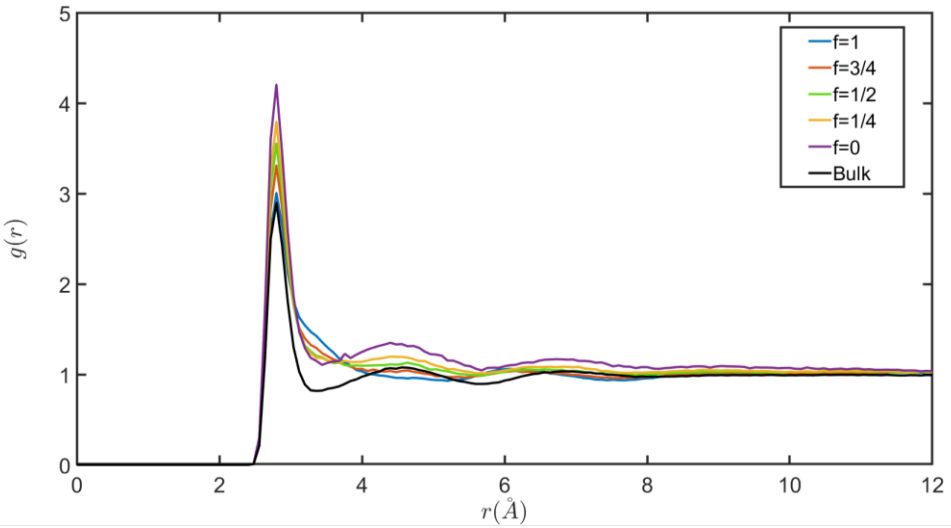

(a)

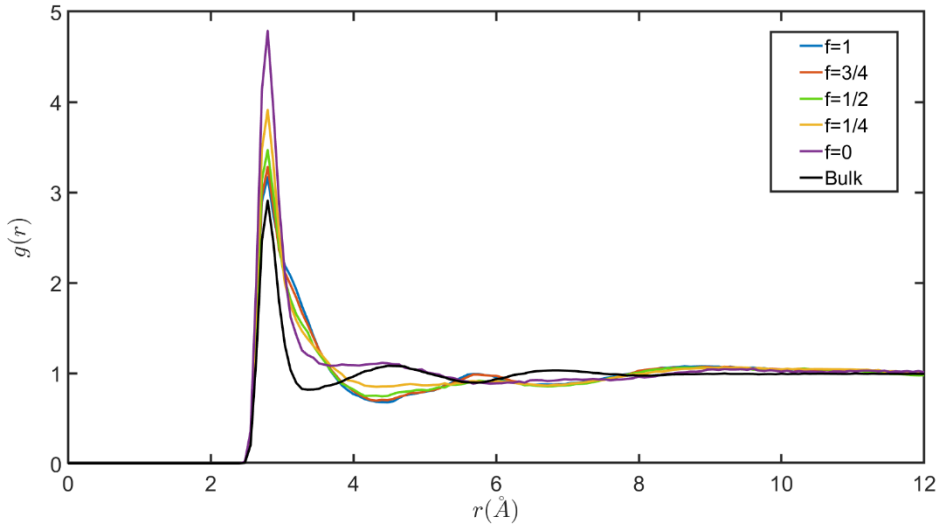

(b)

Figure 3.12: *O_w-O_w RDF of water molecules within the PE brush layer for various degrees of ionization for (a) $\sigma_g=0.1/\sigma^2$ and (b) $\sigma_g=0.2/\sigma^2$. Bulk O_w-O_w RDF is also provided for comparison.*

In Figure 3.13, we plot the local mass density of water molecules as a function of the z coordinate (z=0 is the grafting plane) for various degrees of ionization (*f*) and grafting densities. The water mass density drastically decreases within the brushes as compared to that in the bulk, as has been reported in our previous paper[124]. Interestingly, inside the brushes, the mass density of water increases with f for both the grafting densities. Two factors are at play here. On one hand, increasing the degree of ionization leads to a significant increase in the number of counterions trapped within the brushes, as evident by the much larger values of counterion concentration for such degrees of ionization (see Figure 3.6). For example, the counterion concentration for $\sigma_g = 0.2/\sigma^2$ at f=1 is 18.33 m i.e. there is 1 counterion for approximately every 3 water molecules. Such a massive increase in counterion concentration leads to steric effects ensuring that there is lesser space available for the water molecules. On the other hand, an increase in the degree of ionization increases the number of water molecules required to solvate the counterions. Thus, more water molecules get trapped inside the brushes to cater to the solvation requirements of the counterions.

These two effects counter each other. While steric effects tend to reduce the number of water molecules by reducing the space available for the water molecules, the enhanced counterion solvation requirements warrant an increase in the number of water molecules present inside the brushes. We observe that the counterion solvation requirements dominate the steric effects for both values of grafting densities and dictate an enhancement in the mass density of water inside the brushes with an increase in the degree of ionization. This establishes a highly fascinating scenario: a progressive increase in the degree of ionization effectively pulls in more amounts of species in a

given available volume as manifested by the simultaneous increase in the counterion concentration and water mass density. In other words, this suggests that a charged PE brush is capable of "packing" more amounts of species (counterions and water) within the layer that it forms as compared to the layer formed by an uncharged (or weakly charged) polymer brush.

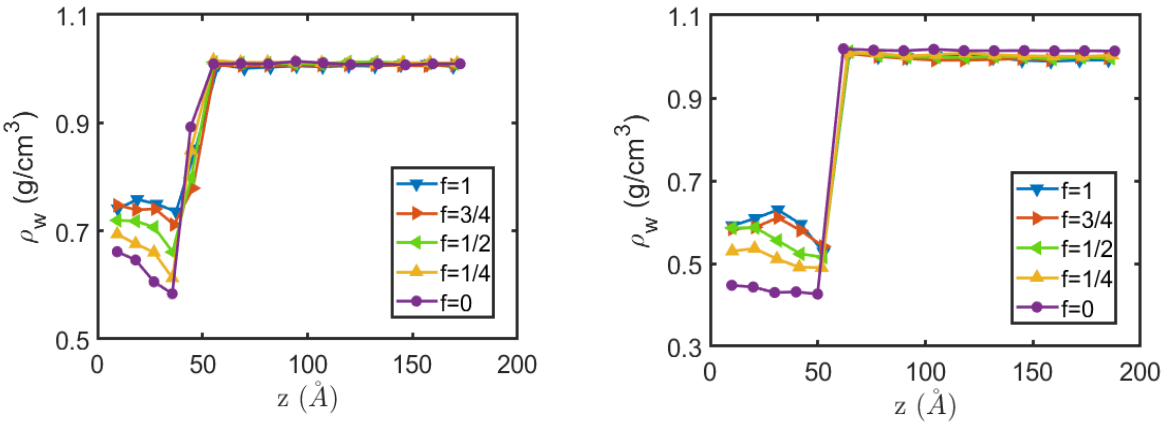

(a) (b)

Figure 3.13: *Transverse variation of mass density of water molecules for various degrees of ionization for (a) $\sigma_g=0.1/\sigma^2$ and (b) $\sigma_g=0.2/\sigma^2$.*

Figure 3.14 plots the static dielectric constant of water molecules (normalized by its bulk value), $\bar{\epsilon_r} = \frac{\epsilon_r(0)}{[\epsilon_r(0)]_{Bulk}}$ within the brushes for various values of degrees of ionization (f) and grafting densities. Here $\epsilon_r(0)$ is the dielectric constant of water molecules within the brushes at zero frequency and $[\epsilon_r(0)]_{Bulk}$ is the dielectric constant of bulk water at zero frequency. Our previous study had reported a significant decrease in $\bar{\epsilon_r}$ within the brushes for the fully ionized brushes[124]. Here we study the role of *f* and σ_g in this reduction of $\bar{\epsilon_r}$. The static dielectric constant of water molecules was calculated using the linear response theory[85] as:

$$\epsilon_r(0) = 1 + \frac{1}{3k_BT\epsilon_0 V}(< \mathbf{M}^2 > - < \mathbf{M} >^2), \quad (3.4)$$

where k_BT is the thermal energy, ϵ_0 is the permittivity of free space, V is the volume under consideration and **M** is the total dipole moment of water molecules in volume V.

A non-monotonic variation in the dielectric constant of water with *f* is observed for both values of grafting density probed. There are two factors at play here. Firstly, the mass density (and hence the number density) of water molecules within the brushes increases with the degree of ionization (see Figure 3.13). This increases the dielectric polarization density in the presence of an electric field as there are greater number of water molecules (per unit volume) available to be polarized in the first place. Secondly, the percentage of bound water molecules also increases with the degree of ionization. A water molecule is considered to be bound if it is present within the first solvation shell ($r \leq 3.2$ Å) of a Na^+ counterion. This trend is depicted on the right axis in Figures 3.14 (a) and (b). An increase in the percentage of bound water molecules decreases the dielectric constant of water due to the inability of bound water molecules to polarize freely in the presence of an electric field.

Clearly, the two effects oppose each other. The resultant of the two effects leads to the observed non-monotonic variation in the dielectric constant of water (within the brushes) with the degree of ionization. At lower grafting density ($\sigma_g = 0.1/\sigma^2$), the mass density effects dominate at lower values of f ($0 \leq f \leq 0.75$), while the enhancement in fraction of bound water molecules dominates at higher values of f ($0.75 \leq f \leq 1$). This leads to an initial enhancement in the dielectric constant of water followed by a reduction with increase in the degree of ionization. However, we observe a completely opposite trend at higher grafting density. For $\sigma_g = 0.2/\sigma^2$, we witness a decrease in the dielectric constant of water at low to moderate degrees of ionization followed by a slight increase at high degrees of ionization.

This finding points to a most interesting scenario where a fundamental property of water such as *static dielectric constant* could be regulated in a most unique fashion within a layer of PE brushes by tuning the degree of ionization and the grafting density of the brushes.

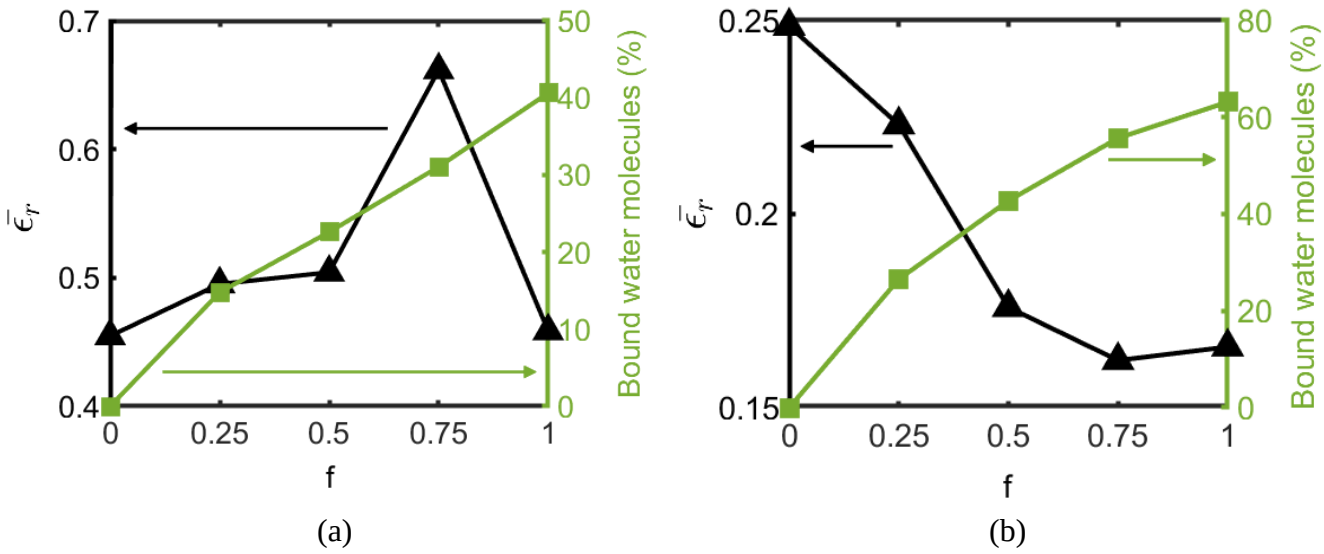

Figure 3.14: *Left axis- Static dielectric constant of water molecules (normalized with respect to bulk value) within the brushes for various degrees of ionization. Right axis- Variation in the percentage of bound water molecules within the PE brush layer for various degrees of ionization. (a) $\sigma_g=0.1/\sigma^2$ and (b) $\sigma_g=0.2/\sigma^2$.*

Figure 3.15 plots the transverse variation in average number of hydrogen bonds formed by water molecules (per water molecule) (n_{HB}) for various degrees of ionization and grafting densities. The transverse variation in average number of hydrogen bonds formed by water molecules with other water molecules (per water molecule) ($n_{HB,w}$) is also plotted. Water molecules can form hydrogen bonds with other water molecules as well as the polyelectrolyte chains. Various atoms on the pendant groups of the PAA chains can form hydrogen bonds with water molecules. These include the $O_{Carboxylate}$, $O_{Carbonyl}$, $O_{Hydroxyl}$ and $H_{Hydroxyl}$ (Hydrogen of COOH group) atoms. Thus, PAA functional groups can behave like hydrogen bond acceptors (via $O_{Carboxylate}$, $O_{Carbonyl}$ and $O_{Hydroxyl}$ atoms) as well as hydrogen bond donors (via $H_{Hydroxyl}$ atoms). A hydrogen bond (between water-water or water-PE functional group) is considered to exist if the distance between the donor and acceptor Oxygen atoms is less than 3.4 Å, the distance between the participating Hydrogen atom and acceptor Oxygen atom is less than 2.425 Å, and the angle between participating Hydrogen atom−donor Oxygen atom−acceptor Oxygen atom is less than 30°. [86-87]

There is a significant reduction in hydrogen bonding between water molecules within the brushes (as compared to bulk) even for the case of uncharged brushes (f=0). This is because water molecules form hydrogen bonds with the PE chains at the expense of water-water hydrogen bonds. We observe that increasing the degree of ionization typically increases the average number of hydrogen bonds between water molecules and PE chains (per water molecule). The only exception to this was witnessed while increasing degree of ionization from 0 to 0.25 at $\sigma_g = 0.2/\sigma^2$, where the average hydrogen bonding between water and PE chains decreased due to a significant

reduction in the hydrogen bonds formed with $H_{Hydroxyl}$ atoms. We witness a decrease in $n_{HB,w}$ with increasing degree of ionization. This can be attributed to the increase in counterion concentration within the brushes. The Na^+ counterions act as structure breakers and undermine the hydrogen bond network between the water molecules.

The aforementioned effects compete with each other. On one hand, an increase in the degree of ionization increases the hydrogen bonding between water and PE chains (typically). On the other hand, it leads to a reduction in the hydrogen bonding between water molecules ($n_{HB,w}$). However, the change in number of hydrogen bonds between water molecules and PE chains (with the degree of ionization) is much smaller as compared to the change in number of hydrogen bonds formed by water molecules with each other. Therefore, the resultant of the two effects is an overall decrease in the number of hydrogen bonds per water molecule (n_{HB}) with increasing degree of ionization (for both values of σ_g).

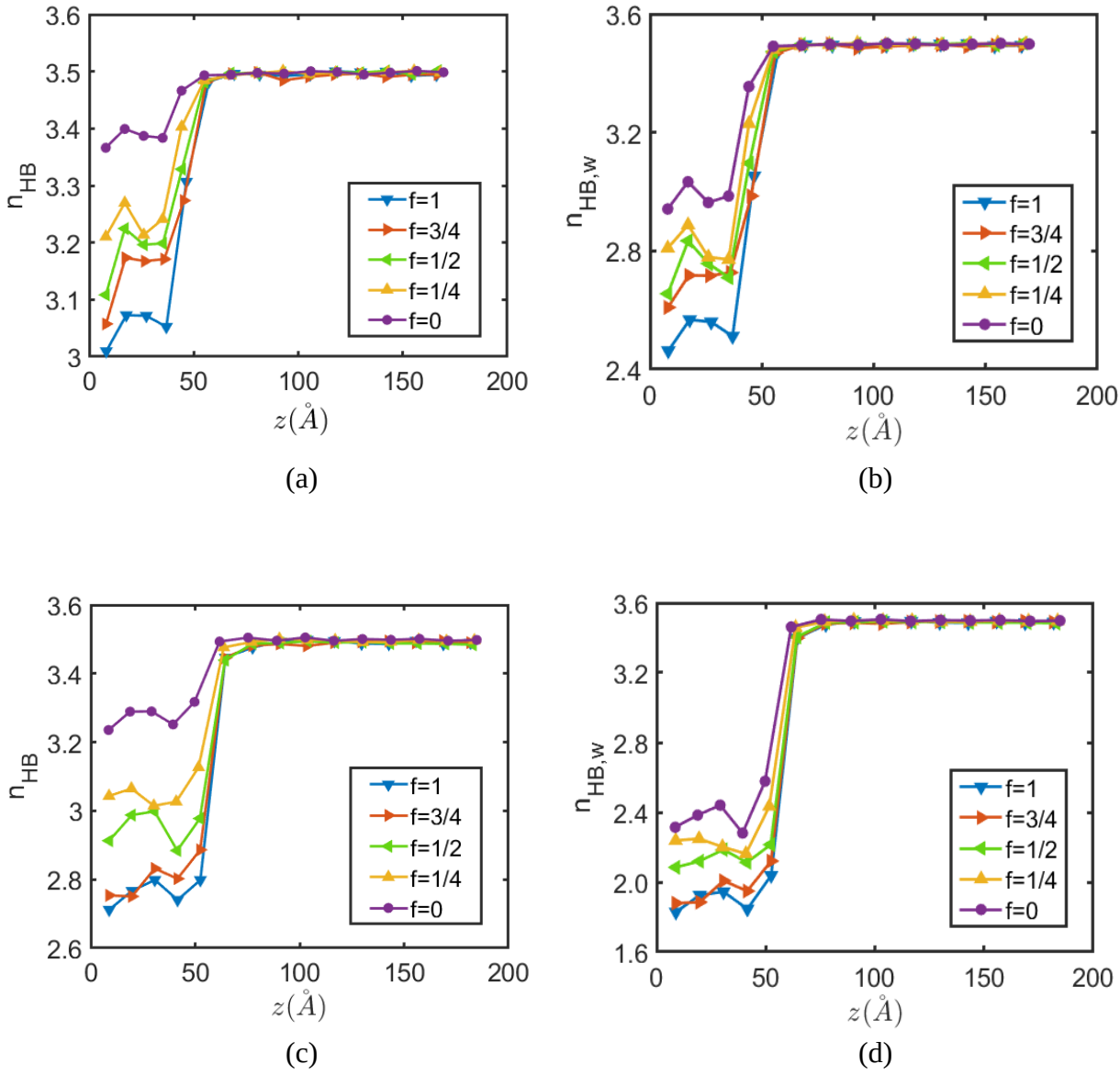

Figure 3.15: *Transverse variation in number of hydrogen bonds per water molecule n_{HB} with degree of ionization for (a) $\sigma_g=0.1/\sigma^2$ and (c) $\sigma_g=0.2/\sigma^2$. Transverse variation in number of hydrogen bonds between water molecules (per water molecule) $n_{HB,w}$ with degree of ionization for (b) $\sigma_g=0.1/\sigma^2$ and (d) $\sigma_g=0.2/\sigma^2$.*

Figure 3.16 plots the probability distribution of the orientational tetrahedral order parameter (q) of water molecules[84] within the brushes for various degrees of ionization and grafting densities. q=1 corresponds to a perfectly tetrahedral arrangement of water molecules. Smaller values of q represent larger deviations from the local tetrahedral arrangement. We observe that the presence of brushes causes a significant change in the probability distribution. This happens even if the brushes are uncharged (f=0). The presence of brushes causes a reduction in the hydrogen bonding (as compared to bulk) between water molecules ($n_{HB,w}$), thereby significantly distorting the local tetrahedral arrangement of water. This shifts the probability distribution towards lower values of q within the brushes. The shift towards lower values of q is more pronounced at higher grafting density, as the hydrogen bond network between water molecules is much more severely affected at higher values of σ_g.

The mean value of q remains relatively unaffected with the degree of ionization. However, the height of the probability distribution peak increases with an increase in the degree of ionization. As a result, the distribution becomes narrower and its variance decreases. This suggests that there is a higher energy penalty to fluctuations away from the mean local arrangement of water molecules at higher degrees of ionization. Such penalties could result from the presence of strong electric fields generated by the enormous counterion concentration within the brushes.

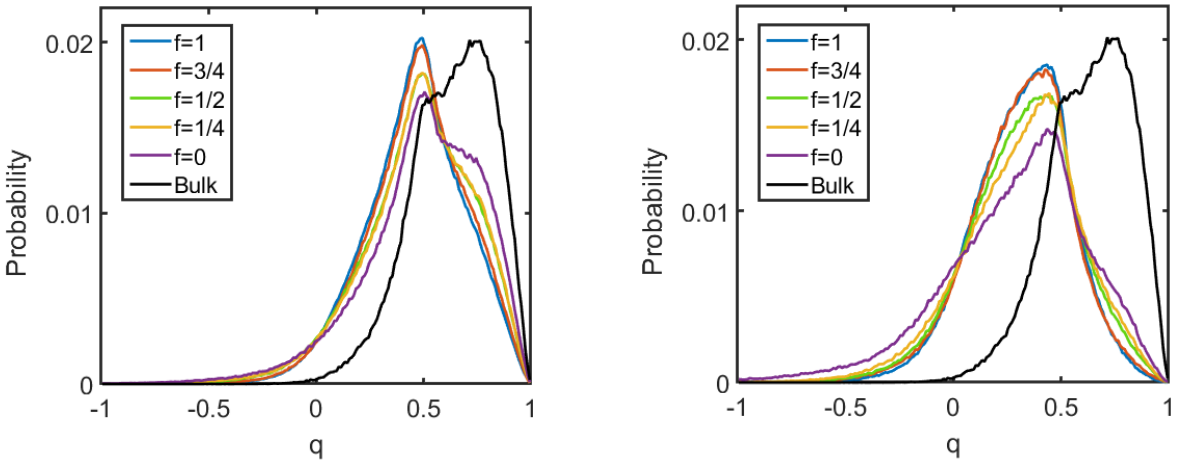

Figure 3.16: *Probability distribution of orientational tetrahedral order parameter (q) of water molecules within the PE brushes for various degrees of ionization for (a)* $\sigma_g = 0.1/\sigma^2$ *and (b)* $\sigma_g = 0.2/\sigma^2$*. Probability distribution of q for bulk SPC/E water is also provided for comparison.*

Our previous paper had identified a significant reduction of the mobility of the water molecules (quantified by the corresponding MSDs) within the fully-ionized PE brushes owing to the large confinement effect induced by the densely grafted PE brushes as well as the significant dipolar interactions between water molecules and the charged PE brushes[124]. Here we quantify the water mobility within the PE brushes as functions of the degree of ionization and the grafting density of the PE brushes. For that purpose, in Figure 3.17 we depict MSDs of water molecules within the brushes as a function of time for various degrees of ionization and grafting densities. The long-time slope of the MSD vs time curves decreases with an increase in the degree of ionization and grafting density, indicating some form of confinement effect that is hindering the water molecules from diffusing freely. The reduction in water mobility with increasing degree of ionization can be explained via electrostatic interactions. With an increase in f, the percentage of water molecules bound to the counterions increases (see Figure 3.14). A majority of these counterions are in turn condensed on the $O_{Carboxylate}$ atoms of the PAA brushes. In fact, the percentage of condensed counterions itself increases with *f* (see Figure 3.8). As a result, the water molecules become much less mobile with increased ionization of the PE chains.

We witness a significant reduction in MSD of water molecules within the brushes (as compared to bulk) even for f=0. This indicates that electrostatic binding to the counterions is not the only reason for reduction in water mobility within the brushes. There is a tremendous nanoconfinement effect created by the presence of the brushes alone (even if they are uncharged). The reason for this is twofold. Firstly, the brushes create a form of lateral confinement due to their unique topology. Secondly, the water

molecules form hydrogen bonds with the pendant groups attached to the PE backbone. This further restricts their mobility as the PE chains are tethered to a substrate and cannot move freely (see Figures 3.4 and 3.5).

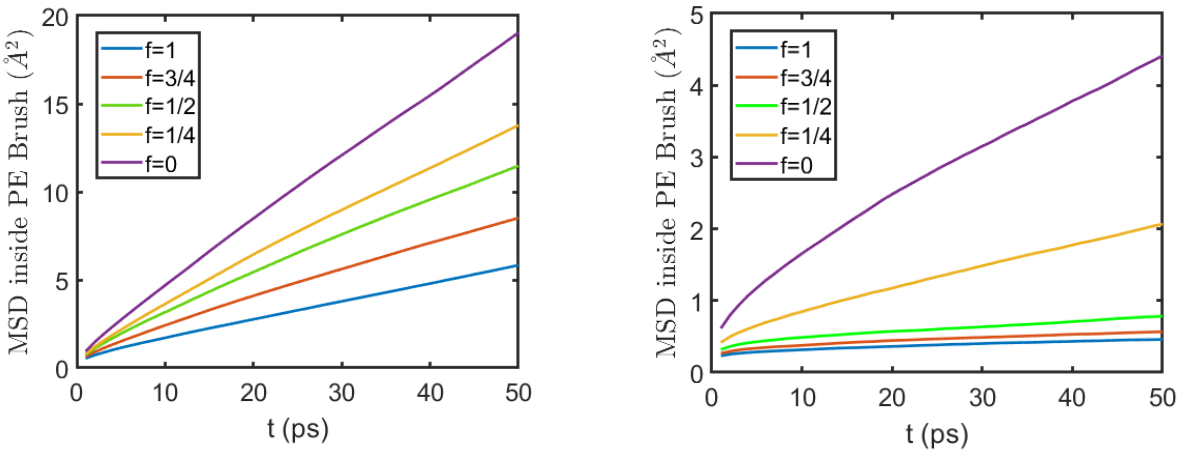

(a) (b)

Figure 3.17: *Mean squared displacement (MSD) of water molecules within the PE brushes for various degrees of ionization for (a) $\sigma_g=0.1/\sigma^2$ and (b) $\sigma_g=0.2/\sigma^2$.*

3.4. Force Field Parameters

In Figure 3.18, we provide a schematic representation of a partially ionized polyacrylic acid (PAA) molecule.

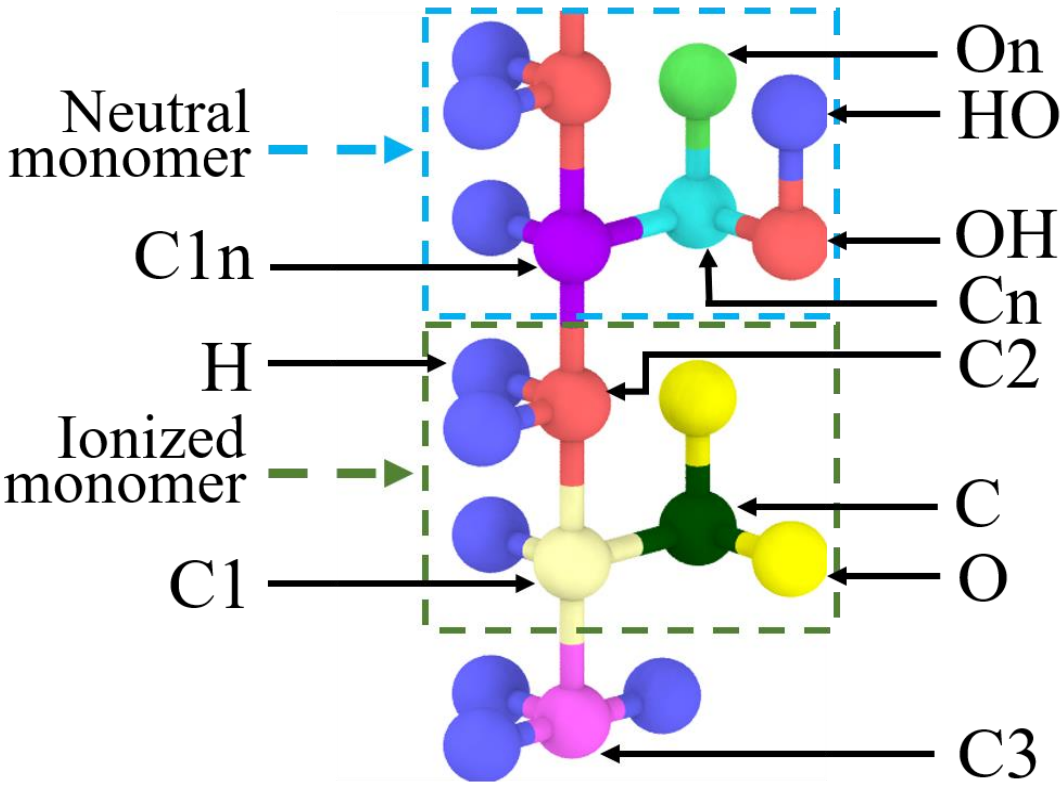

Figure 3.18: *Schematic representation (not to scale) of a partially ionized polyacrylic acid (PAA) molecule. The arrows depict the atom types of their respective atoms. Dashed boxes indicate two different types of repeating units.*

Non-bonded Potentials and Associated Parameters

The Coulombic pairwise interactions (U_{Coul}) between charged atoms are given by:

$$U_{Coul} = \frac{q_i q_j}{4\pi \in_0 \in_1 r_{ij}}. \quad (3.5)$$

and the 12-6 Lennard-Jones (LJ) potential (U_{LJ}) used in the simulations can be represented as:

$$U_{LJ} = 4\epsilon_{ij}\left[\left(\frac{\sigma_{ij}}{r_{ij}}\right)^{12} - \left(\frac{\sigma_{ij}}{r_{ij}}\right)^{6}\right], \quad (3.6)$$

In the above equations, q_i and q_j are the charges on i^{th} and j^{th} atoms respectively, r_{ij} is the Euclidian distance between atoms i and j, $\in_0$ is the permittivity of free space (vacuum), $\in_1$ is the relative permittivity of the background (equal to 1), ϵ_{ij} is the well depth for LJ interactions between atoms i and j and σ_{ij} is the distance corresponding to zero LJ potential between atoms i and j.

The values of these parameters for the various atom types shown in Figure 3.18 along with water and mobile ions are listed below in Table 3.3.

Atom Type	**Charge (e)**	**Mass (amu)**	**ϵ (Kcal/mole)**	**σ (Å)**
C3 (CH_3)	-0.18	12.011	0.066	3.50
C2 (CH_2)	-0.12	12.011	0.066	3.50
C1 (CH, Attached to COO^-)	-0.16	12.011	0.066	3.50
C (COO^-)	0.70	12.011	0.105	3.75
C1n (CH, Attached to COOH)	-0.06	12.011	0.066	3.50
Cn (COOH)	0.52	12.011	0.105	3.75
H	0.06	1.008	0.03	2.50
HO (H in COOH)	0.45	1.008	0.00	0.00
O (COO^-)	-0.80	15.999	0.210	2.96
On (O, Attached to C in COOH)	-0.44	15.999	0.210	2.96
OH (O, Attached to C and H in COOH)	-0.53	15.999	0.170	3.00
O_w (H_2O)	-0.8476	15.999	0.155354	3.166
H_w (H_2O)	0.4238	1.008	0	0
Na	1.00	22.99	0.3526418	2.1595
Continuous LJ Wall (Parameters remain unchanged for interaction with all atom types)	0.00	15.00794	0.1947	3.00 (LJ cut off length is 3.36 Å)

Table 3.3: *Charge, mass and LJ parameters for various atom types*

Bonded Potentials and Associated Parameters

The potential energy for bonds is considered in harmonic form, which is expressed as:

$U_{bond} = K_b(r - r_0)^2$, (3.7)

where r_0 is the equilibrium bond length and K_b is bond stiffness. The values of r_0 and K_b for different bond types are summarized below in Table 3.4.

Bond Type	$\boldsymbol{K_b}$, $(\frac{\boldsymbol{Kcal}}{\boldsymbol{mol}.\text{Å}^2})$	$\boldsymbol{r_0}$, (Å)
C2-H	340.0	1.09
C2-C1	268.0	1.529
C1-H	340.0	1.09
C3-H	340.0	1.09
C-C1	317.0	1.522
C1-C3	268.0	1.529
C-O	656.0	1.25
C1n-H	340.0	1.09
C1n-C2	268.0	1.529
C1n-Cn	317.0	1.522
Cn-On	570.0	1.229
Cn-OH	450.0	1.364
OH-HO	553.0	0.945
C1n-C3	268.0	1.529
O_w-H_w	-	1.00

Table 3.4: *Bond parameters for all different types of bonds*

The potential energy for the angles between different bonds is considered in harmonic form and expressed as:

$U_{angle} = K_a(\theta - \theta_0)^2,$ (3.8)

where θ_0 is the equilibrium angle value and K_a is the angle stiffness. The values of θ_0 and K_a for different angle types are listed in Table 3.5.

Angle Type	$\boldsymbol{K_a, (\frac{Kcal}{mol.rad^2})}$	$\boldsymbol{\theta_0(deg)}$
H-C2-H	33.00	107.8
H-C2-C1	37.5	110.7
C2-C1-H	37.5	110.7
C1-C3-H	37.5	110.7
H-C3-H	33.00	107.8
H-C1-C	35.0	109.5
O-C-O	80.0	126.00
C2-C1-C	63.0	111.1
C3-C1-C	63.0	111.1
H_w-O_w-H_w	-	109.47
C2-C1-C2	58.35	112.7
C2-C1-C3	58.35	112.7
C1-C-O	70.0	117.0
C3-C1-H	37.5	110.7
C1-C2-C1	58.35	112.7
C3-C1n-C2	58.35	112.7
H-C3-C1n	37.5	110.7

H-C1n-Cn	35.0	109.5
C2-C1n-C2	58.35	112.7
H-C2-C1n	37.5	110.7
C2-C1n-Cn	63.0	111.1
C1n-C2-C1n	58.35	112.7
C1n-Cn-On	80.0	120.4
C1n-Cn-OH	70.0	108.0
On-Cn-OH	80.0	121.0
Cn-OH-HO	35.0	113.0
C1-C2-C1n	58.35	112.7
C3-C1n-H	37.5	110.7
C3-C1n-Cn	63.0	111.1
H-C1n-C2	37.5	110.7

Table 3.5: *Angle parameters for all different types of angles*

The potential energy corresponding to proper dihedral interactions is expressed as:

$$U_{dihedral} = \frac{1}{2}K_1[1 + \cos(\emptyset)] + \frac{1}{2}K_2[1 - \cos(2\emptyset)] + \frac{1}{2}K_3[1 + \cos(3\emptyset)] + \frac{1}{2}K_4[1 - \cos(4\emptyset)], \quad (3.9)$$

where K_1, K_2, K_3 and K_4 are the Fourier coefficients associated with torsional interactions, and $\emptyset$ is the value of the torsional angle. Values of K_1, K_2, K_3 and K_4 are listed in Table 3.6.

Dihedral type	$\boldsymbol{K_1}$, $(\boldsymbol{Kcal/mole})$	$\boldsymbol{K_2}$, $(\boldsymbol{Kcal/mole})$	$\boldsymbol{K_3}$, $(\boldsymbol{Kcal/mole})$	$\boldsymbol{K_4}$, $(\boldsymbol{Kcal/mole})$
H-C2-C1-H	0.0	0.0	0.30	0.0
H-C2-C1-C	0.0	0.0	-0.10	0.0
H-C2-C1-C2	0.0	0.0	0.30	0.0
H-C2-C1-C3	0.0	0.0	0.30	0.0
H-C1-C-O	0.0	0.0	0.00	0.0
H-C1-C3-H	0.0	0.0	0.30	0.0
C2-C1-C-O	0.0	0.82	0.00	0.0
C2-C1-C2-C1	1.30	-0.05	0.20	0.0
H-C3-C1-C2	0.0	0.0	0.30	0.0
C3-C1-C-O	0.0	0.82	0. 0	0.0
C1-C2-C1-C	-3.185	-0.825	0.493	0.0
C1-C2-C1-C3	1.30	-0.05	0.20	0.0
H-C1-C2-C1	0.0	0.0	0.30	0.0
H-C3-C1-C	0.0	0.0	-0.10	0.0

On-Cn-OH-HO	0.0	5.50	0.0	0.0
C1n-Cn-OH-HO	1.50	5.50	0.0	0.0
H-C1n-Cn-OH	0.0	0.0	0.0	0.0
C2-C1n-Cn-OH	1.0	0.546	0.45	0.0
C3-C1n-Cn-OH	1.0	0.546	0.45	0.0
H-C1n-Cn-On	0.0	0.0	0.00	0.0
C2-C1n-Cn-On	0.0	0.546	0.0	0.0
C3-C1n-Cn-On	0.0	0.546	0.0	0.0
H-C2-C1n-Cn	0.0	0.0	-0.10	0.0
C1-C2-C1n-Cn	-3.185	-0.825	0.493	0.0
C1n-C2-C1n-Cn	-3.185	-0.825	0.493	0.0
H-C3-C1n-Cn	0.0	0.0	-0.10	0.0
H-C1-C2-C1n	0.0	0.0	0.30	0.0
C1n-C2-C1-C	-3.185	-0.825	0.493	0.0
C1n-C2-C1-C2	1.30	-0.05	0.20	0.0
H-C1n-C2-C1n	0.0	0.0	0.30	0.0
C1n-C2-C1n-C2	1.30	-0.05	0.20	0.0
C1n-C2-C1-C3	1.30	-0.05	0.20	0.0
C1n-C2-C1n-C3	1.30	-0.05	0.20	0.0
H-C1n-C2-H	0.0	0.0	0.30	0.0
H-C1n-C2-H	0.0	0.0	0.30	0.0
H-C1n-C3-H	0.0	0.0	0.30	0.0
C2-C1n-C2-H	0.0	0.0	0.30	0.0

C2-C1n-C2-C1	1.30	-0.05	0.20	0.0
C3-C1n-C2-C1	1.30	-0.05	0.20	0.0
C3-C1n-C2-H	0.0	0.0	0.30	0.0
C2-C1n-C3-H	0.0	0.0	0.30	0.0

Table 3.6: *Dihedral parameters for different types of dihedrals*

Improper torsional dihedrals are considered in the harmonic form and expressed as:

$U_{improper} = K_i(\varphi - \varphi_0)^2,$ (3.10)

where φ_0 is the equilibrium improper torsional angle value and K_i is the associated improper torsional stiffness. The values of the improper dihedral parameters are listed below in Table 3.7.

Improper Type	$\boldsymbol{K_i}$ $(\frac{\boldsymbol{Kcal}}{\boldsymbol{mol.rad^2}})$	$\boldsymbol{\varphi_0(deg)}$
C1-O-C-O	10.5	180
C1n-On-Cn-OH	10.5	180

Table 3.7: *Improper dihedral parameters for different types of improper dihedrals*

3.5. Conclusions

Changes in the properties of PE brushes along with the local arrangement and distribution of counterions and water molecules with the degree of ionization of the brushes are quantified via an all-atom MD framework elucidating the effects of the variation of degree of ionization and the grafting density of the PE brushes. The brush height shows a weak increase with the degree of ionization due to enhanced electrostatic repulsion between the chain segments. The chain mobility, quantified via MSD of the backbone Carbon atoms, decreases with an increase in the degree of ionization, due to an enhancement in the number of condensed counterions per PE chain. We witness an enhancement in the percentage of condensed condensation along with a reduction in the counterion mobility with increase in the degree of ionization. This is accompanied by an increase in the mass density of water within the brushes and a reduction in the water mobility and hydrogen bonding between water molecules (per water molecule). Several other changes in the PE brush microstructure are quantified via shift in the counterion-water and water-water RDFs as well as the probability distribution of the orientational tetrahedral order parameter of water. Moreover, the static dielectric constant of water molecules shows a non-monotonic trend with respect to the degree of ionization, depending on the grafting density of the brushes.

Chapter 4: Revisiting the Strong Stretching Theory for pH-responsive Polyelectrolyte Brushes: Effects of Consideration of Excluded Volume Interactions and an Expanded Form of the Mass Action Law[†]

Abstract: *In this chapter, we develop a theory to account for the effect of the excluded volume (EV) interactions in the Strong Stretching Theory (SST) based description of the pH-responsive polyelectrolyte (PE) brushes. The existing studies have considered the PE brushes to be present in a Θ-solvent and hence have neglected the EV interactions; however, such a consideration cannot describe the situations where the pH-responsive brushes are in a "good" solvent. Secondly, we consider a more expanded form of the mass action law, governing the pH-dependent ionization of the PE molecules, in the SST description of the PE brushes. This expanded form of the mass action law considers different values of* γa^3 *(*γ *is the density of the chargeable sites on the PE molecule and a is the PE Kuhn length) and therefore is an improvement over the existing SST models of PE brushes as well as other theories involving pH-responsive PE molecules that always consider* $\gamma a^3 = 1$*. Our results demonstrate that the EV effects enhance the brush height by inducing additional PE inter-segmental*

[†] The contents of this Chapter (except Section 4.5) have been published as the following journal article: Sachar, H. S.; Sivasankar, V. S.; Das, S. "Revisiting the Strong Stretching Theory for pH-responsive Polyelectrolyte Brushes: Effects of Consideration of Excluded Volume Interactions and an Expanded Form of the Mass Action Law." *Soft Matter* **2019**, *15*, 559-574.

The contents of Section 4.5 were primarily developed by a fellow Ph.D. student Sai Ankit Etha and have been published as the following journal article: Etha, S. A.; Sivasankar, V. S.; Sachar, H. S.; Das, S. "Strong Stretching Theory for pH-responsive Polyelectrolyte Brushes in Large Salt Concentrations." *Physical Chemistry Chemical Physics* **2020**, *22*, 13536-13553.

repulsion. Similarly, the consideration of the expanded form of the mass action law would lead to a reduced (enhanced) brush height for $\gamma a^3 < 1$ ($\gamma a^3 > 1$). We also quantify the variables such as the monomer density distribution, distribution of the ends of the PE brush, and the EDL electrostatic potential and explain their differences with respect to those obtained with no EV interactions or $\gamma a^3 = 1$.

We also develop a model to describe the thermodynamics, configuration, and electrostatics of strongly stretched, pH-responsive polyelectrolyte brushes in the presence of large salt concentrations. The brushes are modelled using the augmented SST, while the effect of the presence of the large salt concentration is accounted for by including the contributions of three different types of non-Poisson-Boltzmann (non-PB) effects in the free energy description of the PE brush induced EDL. These non-PB effects are ionic non-mean-field ion-ion correlations, solvent polarization, and finite size effect of the ions and water dipoles. We study the individual influences of these different effects and show that the ion-ion correlations and solvent polarization effect reduce the brush height and consequentially enhance the monomer density and lead to an electrostatic potential distribution of the brush induced EDL that has a larger magnitude at near-wall locations and becomes zero at shorter distances from the wall. The finite size effect, on the other hand, increases the brush height and therefore, weakens the monomer density and leads to a smaller near-wall magnitude of the EDL potential that becomes zero at larger distances from the wall. Eventually, we consider the impact of all the three non-PB effects simultaneously and show that the ion-ion correlation and solvent polarization effect dominate the size effects and dictate the overall brush configuration and the EDL electrostatics. We also point out that the

influence of all the three non-PB effects becomes largest for larger salt concentration and smaller bulk pH. Finally, we compare our theoretical predictions with those obtained from our recently developed all-atom MD simulation model and obtain an excellent match.

4.1. Introduction

Grafting charged, polyelectrolyte (PE) brushes on solid-liquid interfaces have proven to be an excellent way of functionalizing such interfaces for applications such as nano fluidic ion and biosensing[2-4,26,126], fabrication of nanofluidic diodes[27-28], current rectifiers[25], and nano-actuators[127], designing surfaces of desired wettability[128], engineering nanoparticles for targeted drug delivery[129], oil recovery[8], and many more. The key to several of these applications is the responsiveness of these brushes to environmental cues (e.g., a change in pH or a change in salt concentration) − as a response to these cues, the PE brushes undergo a change in some of its properties (e.g., configuration, height, etc.) thereby enabling most of these above applications. pH-responsive (or annealed) PE brushes refer to brushes whose ionization and hence the charging depends on the local pH[14,130−133]. For example, poly(meth)acrylic brush is an example of a pH-responsive anionic brush. On the other hand, there are brushes (also known as quenched brushes) whose degree of ionization and hence the charging is independent of pH (e.g., partially sulfonated polystyrene brushes). The purpose of this chapter is to provide a detailed thermodynamic self-consistent theoretical model for quantifying such pH-responsive PE brushes.

PE brushes have been modelled extensively. For example, there have been significant efforts aimed at developing scaling laws by balancing the different energies (elastic, electrostatic, and excluded volume) and yielded the brush height as scaled functions of variables such as the grafting density and charge density of the brushes, number of monomers, and the concentration of the added salt[31-36,134-137]. Subsequently, a more involved calculation procedure was also attempted where the electrostatics of the induced electric double layer (EDL) was described using the Poisson-Boltzmann (PB) equation[1,34,131,133,138−141]. Such studies varied in complexity and rigor depending on the manner in which the monomer interactions were described − there have been several approaches ranging from the use of simple Alexander-de-Gennes model[1,138−140] to a more involved parabolic model[34,141] for the brushes. The most complete analytically tractable approach till date, however, has been proposed in a series of seminal papers that employed the Strong Stretching Theory (SST) to describe the PE brushes while the resulting EDL electrostatics was described by the classical PB equation[14,37,94,142−143].

The same self-consistent SST and the PB equation have also been employed to study the configuration of the pH-responsive PE brushes[14]. This study is the state-of-the-art in the SST calculation of the pH-responsive PE brushes. However, this paper considers the PE brushes to be in a *Θ*-solvent and hence neglects all the possible excluded volume (EV) interactions. On the other hand, a vast number of experimental studies involving pH-responsive PE brushes invariably consider the solvent to be a "good" solvent (i.e., a solvent that makes the considerations of the EV interactions between the segments of the PE molecule mandatory) with respect to the PE brush[52,144−150]. Obviously, for such

problems, the theory of Ref. 14 will be inadequate. In order to fill this void, in this chapter, we modify the SST for the pH-responsive PE brushes by accounting for the EV interactions between the PE brush segments. Therefore, this is the first study for the SST of the pH-responsive PE brushes accounting for the effect of the EV interactions. EV interactions have been considered for other theoretical calculations of the PE brushes[151–153], but not in this SST framework used to quantify the behavior of the pH-responsive PE brushes. As a second improvement to the SST model of the pH-responsive PE brushes, we consider a more expanded form of the mass action law for the pH-dependent ionization of the PE molecules valid for all values of γa^3 (γ is the density of the chargeable sites on the PE molecule and a is the PE Kuhn length) and study the effect of this more expanded form of the mass action law in the SST calculations of PE brushes. Both Ref. 14 as well as other papers describing the pH-responsive PE molecules (not necessarily PE "brushes")[154–158] have considered only a special form of the mass action law where $\gamma a^3 = 1$. Our calculations, therefore, ensure a more generic description of the pH-responsive PE brushes within the general ambit of the SST model.

Our results demonstrate distinct contributions of the EV interactions and the expanded form of the mass action law in the SST description of the PE brushes. Consideration of the EV interactions imply consideration of additional inter-segmental repulsion for a particular PE brush molecule. Accordingly, the EV effect enhances the brush height. This enhancement is most magnified for large salt concentration (which leads to an enhanced screening of the PE brush charges) and small pH_∞ (i.e., a large bulk H^+ ion concentration that weakens the ionization of the brushes). On the other hand,

consideration of the generic mass action law implies that one witnesses a decrease (increase) of the PE brush height for $\gamma a^3 < 1$ ($\gamma a^3 > 1$) owing to a reduced (enhanced) charge density of the PE brushes causing a reduced (enhanced) counterion-induced brush swelling[44,67,159]. We complete the description of the problem by accounting for the effects of the EV interactions and the expanded form of the mass action law in dictating the monomer density distribution, distribution of the end location of the PE brushes, and the EDL electrostatics. In summary, this chapter establishes the theory for a much more generic SST-based description of the pH-responsive PE brushes and the resultant EDL electrostatics.

Moreover, we present our model for describing the thermodynamics, configuration, and electrostatics of PE brushes in large salt concentrations. This model accounts for the non-PB effects encountered at high salt concentrations such as the ion-ion correlations, finite size effects and solvent polarization. Finally, we present the results of this model and compare them to our all-atom MD simulations. A remarkable match between the results is observed, even at extremely high ionic concentrations within the PE brushes.

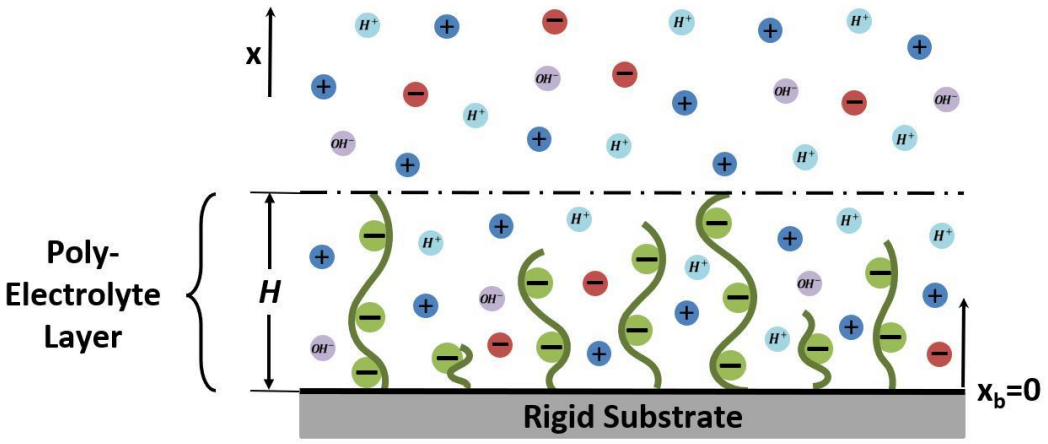

Figure 4.1: *Schematic showing the pH-responsive PE brush layer.*

4.2. Self-Consistent Field Approach

4.2.1. Free Energy Equations

We consider a rigid, impenetrable substrate grafted with pH-responsive, weakly poly-acidic (anionic) PE brushes immersed in an electrolyte solution (see Fig. 4.1). The separation between adjacent grafted PE molecules ℓ is assumed to be small enough such that the system attains a brush like configuration. Here we would discuss the free energies that dictate the brush equilibrium in a self-consistent field approach. These equations have already been discussed by several previous papers[14,37,151]; we repeat them here for the sake of continuity.

The net free energy functional (F) of a given PE molecule can be expressed as:

$$\frac{F}{k_BT} = \frac{F_{els}}{k_BT} + \frac{F_{EV}}{k_BT} + \frac{F_{elec}}{k_BT} + \frac{F_{EDL}}{k_BT} + \frac{F_{ion}}{k_BT}, \tag{4.1}$$

where F_{els}, F_{EV}, F_{elec}, F_{EDL} and F_{ion} are the elastic (entropic), excluded volume, electrostatic, electric double layer and ionization contributions to the free energy (per PE molecule) respectively.

In this model, the equilibrium brush height H (to be determined self-consistently later) refers to the maxi-mum distance of the monomers of the PE brush from the substrate. In order to express the free energy, the system is divided into two regions: region 1 ($0 \leq x \leq H$) forms the interior of the brush and comprises of all the PE chains whereas the region 2 ($H \leq x \leq \infty$) lies exterior to the brush. We consider the case where the electrostatic repulsion between the charged monomers is large enough to ensure that the brush is in a strongly stretched configuration. Therefore, this free energy description is the same as the Strong Stretching Theory description of the PE brushes.

Following the notation of Zhulina et al.[151], we write:

$$\frac{F_{els}}{k_B T} = \frac{3}{2pa^2} \int_0^H g(x')dx' \int_0^{x'} E(x, x')dx, \tag{4.2}$$

$$\frac{F_{EV}}{k_B T} = \frac{\sigma}{a^3} \int_0^H f_{conc}[\phi(x)]dx, \tag{4.3}$$

where p is the chain rigidity, a is the Kuhn length, and $\sigma \sim \ell^2$ is the grafted area per chain. Also, $E(x, x') = dx/dn$ is the local stretching at a distance x from the surface for a chain whose end is located at a distance of x'. Furthermore, $g(x')$ is the normalized chain end distribution function, such that

$$\int_0^H g(x')dx' = 1. \tag{4.4}$$

Finally, $\phi(x)$ is the dimensionless monomer distribution profile of a given PE chain and $f_{conc}[\phi(x)]$ is the non-dimensionalized per unit-volume free energy for the excluded volume interactions.

Following Ref. 133, $F_{elec} + F_{EDL}$ can be expressed as:

$$\frac{F_{elec}}{k_BT}+\frac{F_{EDL}}{k_BT}=\frac{\sigma}{k_BT}\int_0^{\infty}[-\frac{\epsilon_0\epsilon_r}{2}\left|\frac{\mathrm{d}\psi}{\mathrm{dx}}\right|^2+e\psi(n_+-n_-+n_{H^+}-n_{OH^-})]dx$$
$$-\frac{\sigma}{k_BT}\int_0^{H}[e\psi n_{A^-}\phi]dx+\sigma\int_0^{\infty}[n_+(ln(\frac{n_+}{n_{+,\infty}})-1)+n_-(ln(\frac{n_-}{n_{-,\infty}})$$
$$-1)+n_{H^+}(ln(\frac{n_{H^+}}{n_{H^+,\infty}})-1)+n_{OH^-}(ln(\frac{n_{OH^-}}{n_{OH^-,\infty}})-1)$$
$$+(n_{+,\infty}+n_{-,\infty}+n_{H^+,\infty}+n_{OH^-,\infty})]dx \tag{4.5}$$

where ψ is the electrostatic potential, n_i is the number density of the ion *i* [where *i* = ±; H^+; OH^-], $n_{i,\infty}$ is the bulk number density of the ion *i*, n_{A-} is the local number density of the A^- ion, *e* is the electronic charge, k_BT is the thermal energy, ϵ_0 is the permittivity of free space, and ϵ_r is the relative permittivity of the solution.

The PE brush ionizes via dissociation of an acid HA producing H^+ and A^- ions. n_{A-} is a function of the hydrogen ion concentration (n_{H^+}) as given by the expanded form of the mass action law (see the derivation later).

Following Ref. 14, F_{ion} can be expressed as:

$$\frac{F_{ion}}{k_BT}=\frac{\sigma}{a^3}\int_0^{H}\phi\,[(1-\frac{n_{A^-}}{\gamma})ln(1-\frac{n_{A^-}}{\gamma})+\frac{n_{A^-}}{\gamma}ln(\frac{n_{A^-}}{\gamma})$$
$$+\frac{n_{A^-}}{\gamma}(\frac{\mu^0_{H^+}+\mu^0_{A^-}-\mu^0_{AH}}{k_BT}+ln(c_{H^+,\infty}))]dx$$
$$\Longrightarrow\frac{F_{ion}}{k_BT}=\frac{\sigma}{a^3}\int_0^{H}\phi\,[(1-\frac{n_{A^-}}{\gamma})ln(1-\frac{n_{A^-}}{\gamma})+\frac{n_{A^-}}{\gamma}ln(\frac{n_{A^-}}{\gamma})+\frac{n_{A^-}}{\gamma}ln(\frac{n_{H^+,\infty}}{K_a'})]dx \tag{4.6}$$

where $K_a{}' = 10^3 N_A\, K_a$, N_A is the Avogadro number and K_a is the ionization constant of the reaction $HA \rightarrow H^+ + A^-$. Also $K_a = exp\left(-\frac{\mu^0_{H^+}+\mu^0_{A^-}-\mu^0_{AH}}{k_BT}\right)$, where μ_i^0

represents the standard chemical potential of species i. $n_{H^+,\infty} = 10^3 N_A\, c_{H^+,\infty}$ and γ ($1/m^3$) is the maximum density of polyelectrolyte chargeable sites (PCS).

Substituting eqs.(4.2, 4.3 ,4.5 ,4.6) in eq.(4.1), F can be written as:

$$\frac{F}{k_B T} = \frac{3}{2pa^2}\int_0^H g(x')dx' \int_0^{x'} E(x,x')dx + \frac{\sigma}{a^3}\int_0^H f_{conc}[\phi(x)]dx + \frac{\sigma}{k_B T}\int_0^\infty [$$
$$- \frac{\epsilon_0 \epsilon_r}{2}\left|\frac{\mathrm{d}\psi}{\mathrm{dx}}\right|^2 + e\psi(n_+ - n_- + n_{H^+} - n_{OH^-})]dx$$
$$- \frac{\sigma}{k_B T}\int_0^H [\, e\psi n_{A^-}\phi]dx + \sigma\int_0^\infty [\, n_+(ln(\frac{n_+}{n_{+,\infty}}) - 1) \; + n_-(ln(\frac{n_-}{n_{-,\infty}})$$
$$- 1) + n_{H^+}(ln(\frac{n_{H^+}}{n_{H^+,\infty}}) - 1) + n_{OH^-}(ln(\frac{n_{OH^-}}{n_{OH^-,\infty}}) - 1) + (n_{+,\infty}$$
$$+ n_{-,\infty} + n_{H^+,\infty} + n_{OH^-,\infty})]dx + \frac{\sigma}{a^3}\int_0^H \phi\,[(1 - \frac{n_{A^-}}{\gamma})ln(1 - \frac{n_{A^-}}{\gamma})$$
$$+ \frac{n_{A^-}}{\gamma} ln(\frac{n_{A^-}}{\gamma}) + \frac{n_{A^-}}{\gamma} ln(\frac{n_{H^+,\infty}}{K_a'})]dx \tag{4.7}$$

This energy needs to be minimized in presence of the following conditions (constraints):

$$N = \int_0^{x'} \frac{dx}{E(x,x')}, \tag{4.8}$$

$$N = \frac{\sigma}{a^3}\int_0^H \phi(x)dx, \tag{4.9}$$

where N is the number of monomers per chain.

Also ϕ(x) is related to the functions g and E as:

$$\phi(x) = \frac{a^3}{\sigma}\int_x^H \frac{g(x')dx'}{E(x,x')}.$$

(4.10)

Accounting for the constraints, the elastic component of free energy can be expressed in terms of Lagrange multipliers [λ_1 and $\lambda_2(x')$] as:

$$\frac{F'_{els}}{k_BT} = \frac{3}{2pa^2}\int_0^H g(x')dx' \int_0^{x'} E(x,x')dx + \lambda_1\left[\frac{\sigma}{a^3}\int_0^H \phi(x)dx - N\right] + \int_0^H \lambda_2(x')dx'\left[\int_0^{x'} \frac{dx}{E(x,x')} - N\right].$$

(4.11)

Therefore, the net free energy (F') accounting for all the constraints is:

$$\frac{F'}{k_BT} = \frac{F'_{els}}{k_BT} + \frac{F_{EV}}{k_BT} + \frac{F_{elec}}{k_BT} + \frac{F_{EDL}}{k_BT} + \frac{F_{ion}}{k_BT}$$

(4.12)

4.2.2. Variational Formalism

We would like to obtain the governing equations dictating the problem by carrying a variational minimization of eq.(4.12). Variation of eq.(4.12), i.e.,

$$\frac{\delta F'}{k_BT} = \frac{\delta F'_{els}}{k_BT} + \frac{\delta F_{EV}}{k_BT} + \frac{\delta F_{elec}}{k_BT} + \frac{\delta F_{EDL}}{k_BT} + \frac{\delta F_{ion}}{k_BT} = 0.$$

(4.13)

The condition $\delta F' = 0$ leads to the following equations (see appendix A for the detailed derivation), which stem from the fact that $\delta E(x,x') \neq 0, \delta g(x') \neq 0, \delta\psi \neq 0, \delta n_{A^-} \neq 0, \delta n_{\pm} \neq 0, \delta n_{H^+} \neq 0, \delta n_{OH^-} \neq 0$:

$$\frac{3g(x')}{2a^2} - \frac{\lambda_2(x')}{E^2(x,x')} - (\frac{\delta f_{conc}}{\delta \phi} + \lambda_1 - \frac{ea^3\psi}{k_BT} n_{A^-} + (1 - \frac{n_{A^-}}{\gamma}) ln(1 - \frac{n_{A^-}}{\gamma}) + \frac{n_{A^-}}{\gamma} ln(\frac{n_{A^-}}{\gamma}) + \frac{n_{A^-}}{\gamma} ln(\frac{n_{H^+,\infty}}{K_a'})) \frac{g(x')}{E^2(x,x')} = 0,$$

(4.14)

$$\int_0^{x'} [\frac{3E(x,x')}{2a^2} + (\frac{\delta f_{conc}}{\delta \phi} + \lambda_1 - \frac{ea^3\psi}{k_BT} n_{A^-} + (1 - \frac{n_{A^-}}{\gamma}) ln(1 - \frac{n_{A^-}}{\gamma}) + \frac{n_{A^-}}{\gamma} ln(\frac{n_{A^-}}{\gamma}) + \frac{n_{A^-}}{\gamma} ln(\frac{n_{H^+,\infty}}{K_a'})) \frac{1}{E(x,x')}] dx = 0,$$

(4.15)

$$-\gamma a^3 \frac{e\psi}{k_BT} - ln(1 - \frac{n_{A^-}}{\gamma}) + ln(\frac{n_{A^-}}{\gamma}) + ln(\frac{n_{H^+,\infty}}{K_a'}) = 0$$

$$\Longrightarrow n_{A^-} = \frac{K_a'\gamma}{K_a' + n_{H^+,\infty} \exp(-\gamma a^3 \frac{e\psi}{k_BT})}$$

(4.16)

$$\epsilon_0 \epsilon_r (\frac{d^2\psi}{dx^2}) + e(n_+ - n_- + n_{H^+} - n_{OH^-} - n_{A^-} \phi) = 0 \quad (0 \le x \le H)$$

$$\epsilon_0 \epsilon_r (\frac{d^2\psi}{dx^2}) + e(n_+ - n_- + n_{H^+} - n_{OH^-}) = 0 \quad (H \le x \le \infty),$$

(4.17)

$$n_\pm = n_{\pm,\infty} exp(\mp \frac{e\psi}{k_BT}),$$

(4.18)

$$n_{H^+} = n_{H^+,\infty} exp(-\frac{e\psi}{k_BT}),$$

(4.19)

$$n_{OH^-} = n_{OH^-,\infty} exp(\frac{e\psi}{k_BT}),$$

(4.20)

Eq. (4.16) is the expanded form of the mass action law that we shall use here. On the other hand, all the existing studies have invariably considered $\gamma = 1/a^3$ and accordingly, have considered a form of the mass action law expressed as[14]:

$$n_{A^-} = \frac{K_a'\gamma}{K_a' + n_{H^+,\infty}\exp\left(-\frac{e\psi}{k_B T}\right)}.$$

(4.21)

This study, therefore, will reveal for the first time the effect of consideration of the mass action law in dictating the strong stretching behavior of the pH-responsive PE brushes. Now, from eq.(4.14), we get:

$$E(x, x') = \sqrt{U_1(x') - U_2(x)},$$

(4.22)

where

$$U_1(x') = \frac{2a^2}{3}\frac{\lambda_2(x')}{g(x')},$$

(4.23)

$$U_2(x) = \frac{2a^2}{3}\left(-\frac{\delta f_{conc}}{\delta\phi} - \lambda_1 + \frac{ea^3\psi}{k_B T}n_{A^-} - \left(1 - \frac{n_{A^-}}{\gamma}\right)ln\left(1 - \frac{n_{A^-}}{\gamma}\right) - \frac{n_{A^-}}{\gamma}ln\left(\frac{n_{A^-}}{\gamma}\right) - \frac{n_{A^-}}{\gamma}ln\left(\frac{n_{H^+,\infty}}{K_a'}\right)\right).$$

(4.24)

Since there is no extension at the brush ends, $E(x, x) = 0$. Therefore, $U_1(x) = U_2(x) = U(x)$. Hence,

$$E(x, x') = \sqrt{U(x') - U(x)}.$$

(4.25)

The normalization condition of eq.(4.8) serves as an integral equation for U(x′). One can check that this integral equation is satisfied if:

$$U(x) = \frac{\pi^2 x^2}{4N^2} \tag{4.26}$$

Consequently,

$$E(x, x') = \frac{\pi}{2N}\sqrt{x'^2 - x^2}. \tag{4.27}$$

Now we can re-write eq.(4.15) as:

$$\int_0^{x'} [\, E(x, x') - \frac{U(x)}{E(x, x')}]dx = 0. \tag{4.28}$$

Eq.(4.28) is equally satisfied with these stated forms of U(x) and $E(x, x')$. To obtain ϕ(x) we can employ eq.(4.24), but prior to that we would need the functional dependence of f on ϕ. Considering the virial expansion for the non-dimensionalised per-unit volume free energy of volume interactions, we can write[151]:

$$f_{conc}[\phi(x)] \approx \nu\phi^2 + \omega\phi^3 + \ldots, \tag{4.29}$$

where ν and ω are the virial coefficients.

Considering the first two terms of the expansion of $f_{conc}[\phi(x)]$, we can use eq. (4.24) to obtain ϕ(x) in terms of ψ(x) by solving a quadratic equation:

$$\phi(x) = \frac{\nu}{3\omega}[\{1+\kappa^2(\lambda - x^2 + \beta\frac{K_a'\gamma}{K_a' + n_{H^+,\infty}\exp(-\gamma a^3\frac{e\psi}{k_BT})}\psi$$
$$-\rho(1-\frac{K_a'}{K_a' + n_{H^+,\infty}\exp(-\gamma a^3\frac{e\psi}{k_BT})})ln(1-\frac{K_a'}{K_a' + n_{H^+,\infty}\exp(-\gamma a^3\frac{e\psi}{k_BT})})$$
$$-\rho\frac{K_a'}{K_a' + n_{H^+,\infty}\exp(-\gamma a^3\frac{e\psi}{k_BT})}ln(\frac{K_a'}{K_a' + n_{H^+,\infty}\exp(-\gamma a^3\frac{e\psi}{k_BT})})$$
$$-\rho\frac{K_a'}{K_a' + n_{H^+,\infty}\exp(-\gamma a^3\frac{e\psi}{k_BT})}ln(\frac{n_{H^+,\infty}}{K_a'}))\}^{1/2} - 1], \tag{4.30}$$

where,

$$\kappa^2 = \frac{9\pi^2\omega}{8N^2a^2\nu^2}, \tag{4.31}$$

$$\rho = \frac{8a^2N^2}{3\pi^2}, \tag{4.32}$$

$$\lambda = -\lambda_1\rho = -\lambda_1\frac{8a^2N^2}{3\pi^2}, \tag{4.33}$$

$$\beta = \frac{8N^2ea^5}{3\pi^2k_BT}. \tag{4.34}$$

Using eqs. (4.16), (4.18), (4.19), (4.20) and (4.30), we can re-write the equations governing ψ as:

$$\epsilon_0\epsilon_r\left(\frac{d^2\psi}{dx^2}\right) + e\left(n_{+,\infty}\exp\left(-\frac{e\psi}{k_BT}\right) - n_{-,\infty}\exp\left(\frac{e\psi}{k_BT}\right) + n_{H^+,\infty}\exp\left(-\frac{e\psi}{k_BT}\right)\right.$$
$$\left. - n_{OH^-,\infty}\exp\left(\frac{e\psi}{k_BT}\right) - \frac{K_a'\gamma}{K_a' + n_{H^+,\infty}\exp\left(-\gamma a^3\frac{e\psi}{k_BT}\right)}\frac{\nu}{3\omega}\left[\{1 + \kappa^2(\lambda\right.\right.$$
$$\left. - x^2 + \beta\frac{K_a'\gamma}{K_a' + n_{H^+,\infty}\exp\left(-\gamma a^3\frac{e\psi}{k_BT}\right)}\psi - \rho(1\right.$$
$$\left. - \frac{K_a'}{K_a' + n_{H^+,\infty}\exp\left(-\gamma a^3\frac{e\psi}{k_BT}\right)}\right)ln\left(1 - \frac{K_a'}{K_a' + n_{H^+,\infty}\exp\left(-\gamma a^3\frac{e\psi}{k_BT}\right)}\right)$$
$$\left. - \rho\frac{K_a'}{K_a' + n_{H^+,\infty}\exp\left(-\gamma a^3\frac{e\psi}{k_BT}\right)}ln\left(\frac{K_a'}{K_a' + n_{H^+,\infty}\exp\left(-\gamma a^3\frac{e\psi}{k_BT}\right)}\right)\right.$$
$$\left. - \rho\frac{K_a'}{K_a' + n_{H^+,\infty}\exp\left(-\gamma a^3\frac{e\psi}{k_BT}\right)}ln\left(\frac{n_{H^+,\infty}}{K_a'}\right)\right)\}^{1/2} - 1\Big] = 0 \qquad (0 \le x \le H),$$

$$\epsilon_0\epsilon_r\left(\frac{d^2\psi}{dx^2}\right) + e\left(n_{+,\infty}\exp\left(-\frac{e\psi}{k_BT}\right) - n_{-,\infty}\exp\left(\frac{e\psi}{k_BT}\right) + n_{H^+,\infty}\exp\left(-\frac{e\psi}{k_BT}\right)\right.$$
$$\left. - n_{OH^-,\infty}\exp\left(\frac{e\psi}{k_BT}\right)\right) = 0 \qquad (H \le x \le \infty). \tag{4.35}$$

Eqs.(4.29, 4.35) establish that the equations governing the monomer distribution and the EDL electrostatic potential involve the parameters (ν, ω) dictating the excluded volume interactions enabling for the first time the inclusion of the excluded volume interactions in the SST description of the pH-responsive PE brushes. As has been already discussed, the state of the art SST invariably neglect the EV effects, i.e., consider the brushes to be always in a Θ-solvent, which might be scenario far from reality.

The boundary conditions for solving ψ are:

$$(\psi)_{x=H^-} = (\psi)_{x=H^+}, \left(\frac{d\psi}{dx}\right)_{x=H^-} = \left(\frac{d\psi}{dx}\right)_{x=H^+}, \left(\frac{d\psi}{dx}\right)_{x=0} = 0, (\psi)_{x\to\infty} = 0.$$

(4.36)

From eq.(4.35) we can solve for ψ for a given H, provided we know λ. λ is obtained by using the normalization condition provided by eq.(4.9). In other words, we shall need to solve eqs.(4.35, 4.9) simultaneously, as well as employ eq.(4.30) to obtain ϕ, ψ and λ. Now that we have ϕ(x), ψ(x), , $n_{A^-}(\psi)$, $n_{\pm} = n_{\pm}(\psi)$, $n_{H^+} = n_{H^+}(\psi)$, $n_{OH^-} = n_{OH^-}(\psi)$ we can obtain the net unbalanced charge (q_{net}) in the system as a function of H.

$$q_{net} = e\sigma \int_0^{\infty} (n_+ - n_- + n_{H^+} - n_{OH^-} - \phi n_{A^-}) dx$$

(4.37)

In order to obtain the equilibrium brush height H, which is H_0, we will obtain the resulting equation (in terms of H_0) by writing:

$$(q_{net})_{H=H_0} = 0$$

(4.38)

Finally, we can obtain g(x) by inverting the integral equation provided by eq.(4.10) in presence of eq.(4.27) as:

$$g(x) = \frac{x\sigma}{Na^3}\left[\frac{\phi(H)}{\sqrt{H^2 - x^2}} - \int_x^H \frac{d\phi(x')}{dx'}\frac{dx'}{\sqrt{x'^2 - x^2}}\right]$$

(4.39)

4.3. Results

4.3.1. Effects of Consideration of Excluded Volume Interactions

The state-of-the-art SST calculations for describing the pH-responsive PE brushes neglect the EV interactions, i.e., assume that the brushes are in a Θ-solvent. However, a more generic consideration must account for the possibilities that the brushes might be present in a "good" solvent, so that there are finite EV interactions between brush segments. In the present case, we account for such a generic consideration and consider varying extent of the "goodness" of the solvent, quantified by the different values of the parameters ν and ω. For simplicity, we de ne a given solvent using different values of ν and a given value of ω. Obviously, the results corresponding to $\nu = 0$, $\omega = 0$ represent the case of the Θ-solvent[14].

In Fig. 4.2(a), we elucidate the variation of the brush height as a function of the extent of the EV interactions (quantified by different values of ν and a given value of ω). Larger EV interactions, characterized by larger values of ν and ω, would enforce a larger separation between the segments of the PE brushes, and accordingly lead to a larger value of the brush height [see Fig. 4.2(a)]. Of course, the case of $\nu = 0$, $\omega = 0$ is the case where the EV interactions have been ignored. We have checked that the results $\nu = 0$, $\omega = 0$ from our calculations is exactly identical to that obtained by Zhulina and Borisov[14], who consider a Θ-solvent (no EV interactions). An increase in the salt concentration reduces the brush height for all the values of ν and ω. A larger salt concentration leads to a smaller EDL thickness and hence there is a screening of the electrostatic repulsion over much shorter distance, eventually reducing the brush height with the salt concentration, as has been revealed previously[36,138]. On the other hand, a larger pH_∞ or a smaller value of bulk H^+ ion concentration leads to a stronger ionization reaction (i.e., there is an enhancement of the reaction that produces H^+ ions) and hence a larger charge of the PE brushes ensuring a larger counterion-induced osmotic swelling[44,67,159] causing to a larger brush height for all values of ν and ω. The relative contribution of the EV interactions in altering the brush height (quantified by the ratio

$\Delta H_0/H_0$) has been probed in Fig. 4.2(b). We find that the maximum percentage difference occurs for the case of larger salt concentration and smaller pH_∞. Larger salt concentration (or a smaller EDL thickness) and smaller pH_∞ (or a larger H^+ ion concentration leading to a weakened PE ionization) ensure weakened charging of the PE brushes and hence weakened counterion-induced osmotic swelling of the brushes. Under such circumstances, therefore, the relative contribution of the EV-interactions (and the resulting inter segment repulsions) in enhancing the brush height becomes more important as reflected by the larger values of $\Delta H_0/H_0$ for such concentration and pH_∞ values. This is the first key finding of the chapter: the EV interactions, neglected in all previous studies of SST for pH-responsive PE brushes[14], become extremely important in dictating the brush height for large salt concentration and small pH_∞ values.

Figure 4.3 provides the variation of the monomer distribution (ϕ) along the brush height modelled considering finite EV interactions of varying magnitude (quantified by different values of and a given value of ω) and no EV interactions (i.e., $\nu = \omega = 0$). This latter case is exactly identical to the predictions by Zhulina et al[14]. Smaller H_0 for the case where EV effects have been neglected ensure a denser monomer concentration near to the wall, and accordingly, driven by the need to ensure a constant N, a smaller monomer concentration away from the wall. Deviation of the brush height due to the consideration of the EV interactions is maximum for larger c_∞ and smaller pH_∞ [see Fig. 4.2(b)]. Accordingly, for such $c_\infty - pH_\infty$ combinations, the variation in ϕ with and without the EV effects is maximum. Therefore, this variation in ϕ between the cases of with and without the EV effects is witnessed to the largest extent in Fig. 4.3(d) (c_∞ = 0.1 M and pH_∞ = 3) and to the least extent in Fig. 4.3(a) (c_∞ = 0.01 M and pH_∞ = 4).

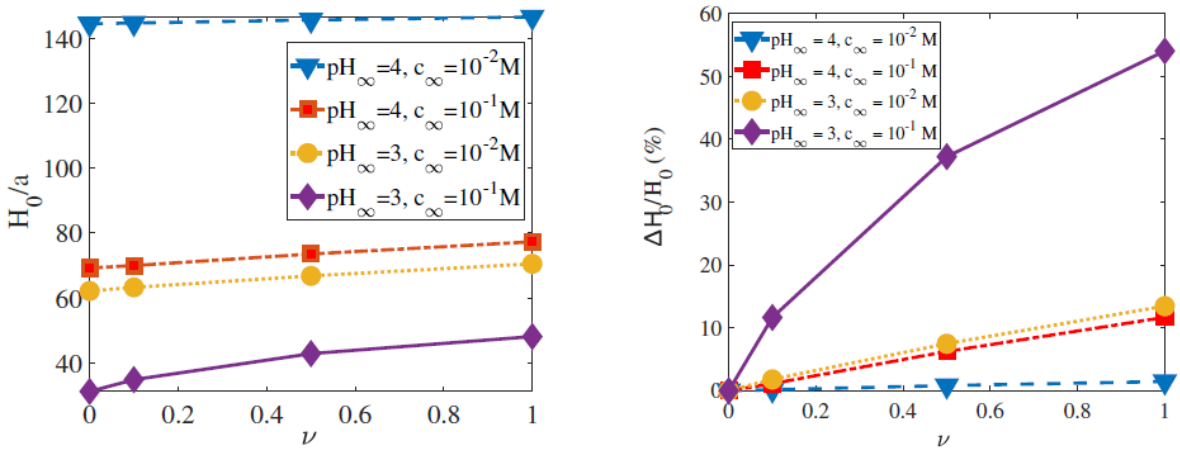

(a) (b)

Figure 4.2: *Variation of (a) non-dimensional equilibrium brush height H_0/a (a is the PE Kuhn length) and (b) percentage increase in equilibrium brush height $\Delta H_0/H_0$ (where $\Delta H_0 = H_0 - H_{0,\nu=0,\omega=0}$) with the first virial coefficient ν for different pH_∞ and c_∞ values. The case of Ref. 14 is the one where $\nu = 0, \omega = 0$ − we recover exactly the results of Ref. 14 when $\nu = 0, \omega = 0$. Other parameters for this figure are $\omega = 0.1$, $pK_a = 3.5$, $a = 1nm$, $\gamma = 1/a^3$ (1 PCS per kuhn monomer), $N = 662$, $\ell = 40nm$, $k_B = 1.38 \times 10^{-23}$ J/K, $T = 298K$, $e = 1.6 \times 10^{-19}$ C, $\epsilon_0 = 8.854 \times 10^{-12}$ F/m, $\epsilon_r = 79.8$, $pK_w = 14$, $pOH_\infty = pK_w - pH_\infty$, $c_{+,\infty} = c_\infty$, $c_{H^+,\infty} = 10^{-pH_\infty}$, $c_{OH^-,\infty} = 10^{-pOH_\infty}$, $c_{-,\infty} = c_\infty + c_{H^+,\infty} + c_{OH^-,\infty}$.*

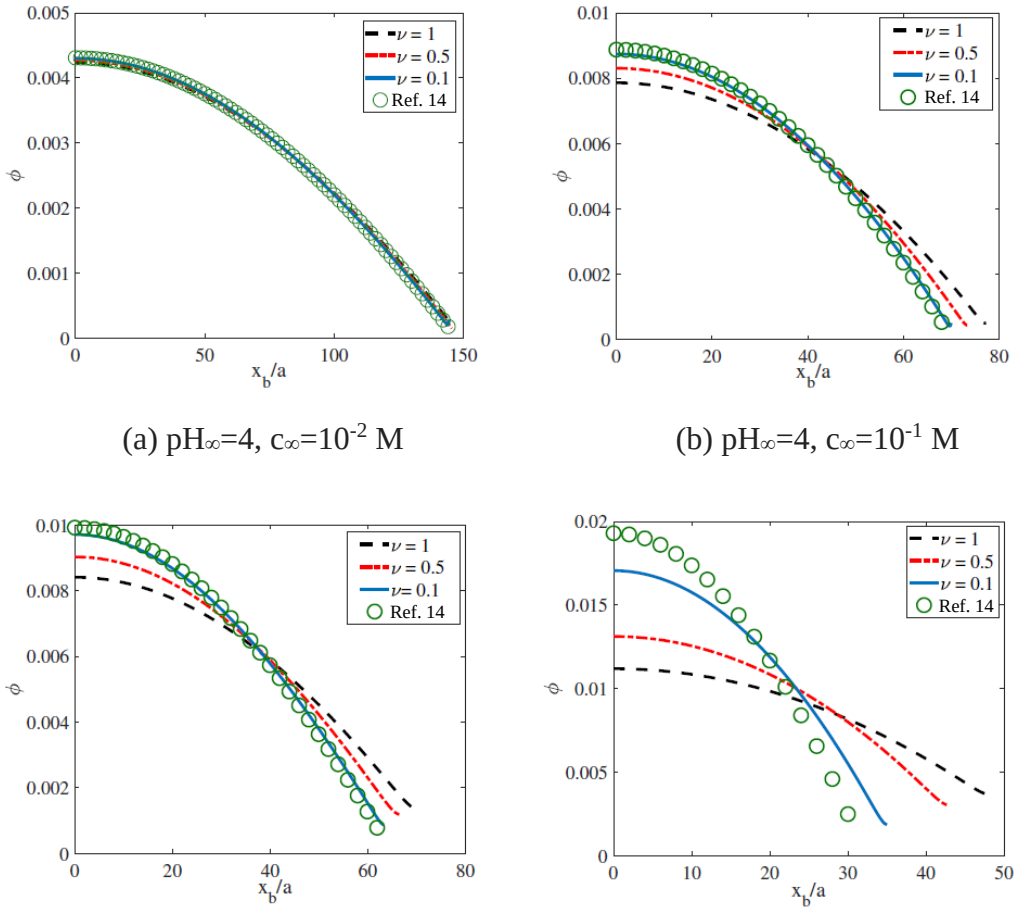

(a) pH_∞=4, c_∞=10^{-2} M

(b) pH_∞=4, c_∞=10^{-1} M

(c) pH_∞=3, c_∞=10^{-2} M

(d) pH_∞=3, c_∞=10^{-1} M

Figure 4.3: *Comparison of monomer distribution profiles (ϕ) as a function of the dimensionless transverse distance along the brush (x_b/a, a is the Kuhn length) obtained for different values of the first virial coefficient ν using our theory and theory of Ref. 14 for different pH_∞ and c_∞ values. All other parameters are identical to that used in Fig. 4.2.*

Fig. 4.4 provides the variation of the end distribution g of the PE brushes considering finite EV interactions of varying magnitude (quantified by different values of ν and a given value of ω) and no EV interactions (i.e., $\nu = \omega = 0$; this case is that of Ref. 14). Given that the case without the EV effects lead to a larger concentration of the monomers at near-wall locations, we witness a larger value of g at such near wall locations for the case without the EV effects. On the other hand, an increase in the EV effects, leading to a flatter distribution of ϕ (see Fig. 4.3), ensures a larger g value much away from the wall. Very much like Figs. 4.2 and 4.3, here too the maximum difference between the cases of with and without the EV interactions is witnessed for the condition of large c_∞ and small pH_∞.

Fig. 4.5 provides the transverse variation of the EDL electrostatic potential considering both finite EV interactions of varying magnitude between the PE brush segments (quantified by different values of ν and a given value of ω) as well as no EV interactions (i.e., $\nu = \omega = 0$; this case is that of Ref. 14). The case of no EV interactions correspond to a shorter height of the brush implying a larger per unit volume charge density of the monomers, which in turn would ensure a larger magnitude of the EDL electrostatic potential at near-wall locations. At the same time, the presence of the shorter brushes imply that the brushes extend to smaller distances away from the grafting wall. Accordingly, there is no longer any charge from the brush at some finite distance away from the wall. These two factors simultaneously ensure that the electrostatic potential at near-wall locations is much larger and steeper for the case without the EV effects. The consideration of the EV effects makes the electrostatic potential much smaller and flatter. Here too this difference between the cases that consider or neglect the EV interactions is primarily manifested for large c_∞ and small pH_∞.

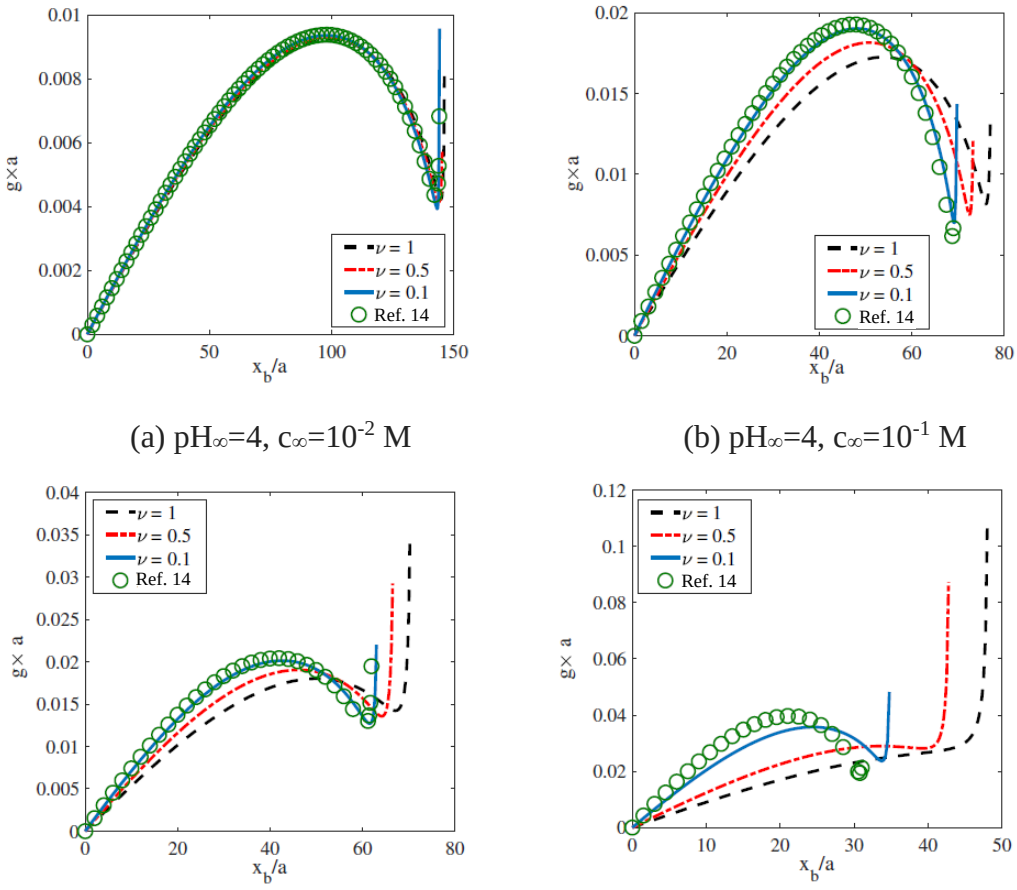

(a) pH_∞=4, c_∞=10^{-2} M

(b) pH_∞=4, c_∞=10^{-1} M

(c) pH_∞=3, c_∞=10^{-2} M

(d) pH_∞=3, c_∞=10^{-1} M

Figure 4.4: *Comparison of non-dimensional chain end distribution profiles (g* x *a, a is the Kuhn length) as a function of the dimensionless transverse distance along the brush (x_b/a) obtained for different values of the first virial coefficient ν using our theory and theory of Ref. 14 for different pH_∞ and c_∞ values. All other parameters are identical to that used in Fig. 4.2.*

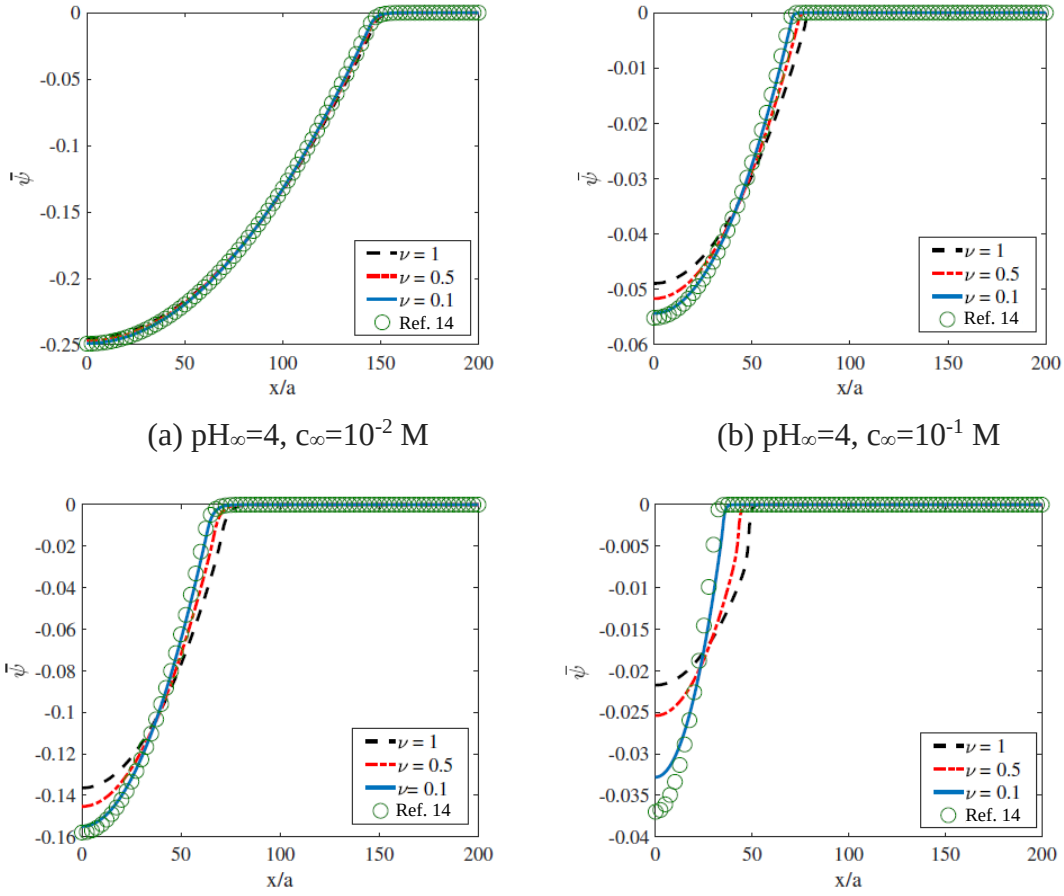

(a) pH_∞=4, c_∞=10^{-2} M

(b) pH_∞=4, c_∞=10^{-1} M

(c) pH_∞=3, c_∞=10^{-2} M

(d) pH_∞=3, c_∞=10^{-1} M

Figure 4.5: *Comparison of non-dimensional electrostatic potential profiles ($\bar{\psi}$ = $e\psi/(k_BT)$) as a function of the dimensionless transverse distance along the nanochannel half height (x/a) obtained for different values of the first virial coefficient ν using our theory and theory of Ref. 14 for different pH_∞ and c_∞ values. All other parameters are identical to that used in Fig. 4.2.*

4.3.2. Effects of Consideration of an Expanded Form of the Mass Action Law

We have discussed previously that eq.(4.16) represents the expanded form of the mass action law and not eq.(4.21), which has been invariably used in most of the existing studies, but is only a special case of the expanded form of the mass action law obtain for the specific condition of $\gamma=1/a^3$. In this subsection, we provide results dictating the PE brush configuration and the resultant EDL electrostatics for different values of γ, i.e., study the effect of the consideration of the expanded form of the mass action law. Fig. 4.6 shows the variation of the equilibrium brush height as a function of γa^3. Increase in γ or γa^3 implies that the PE molecules has a larger backbone charge density. As a consequence, a larger number of counterions will get localized within the brush in order to screen the larger magnitude of the PE charge. This, in turn, will lead to a larger counterion-induced osmotic swelling of the brushes (reflecting the tendency of the counterions to maximize their entropy by increasing the brush volume), eventually leading to a larger brush height[44,67,159]. Also, here too, the lowering of the salt concentration (i.e., increasing the EDL thickness, which in turn would lead to a screening of the PE backbone charge over a larger length) and an increase in the pH_∞ (leading to a larger ionization and hence a greater charging of the PE molecule inducing a larger counterion-induced osmotic swelling) will cause an increase of the PE brush height. Here we also account for the EV interactions quantified by ν = 0.1 and ω = 0.01.

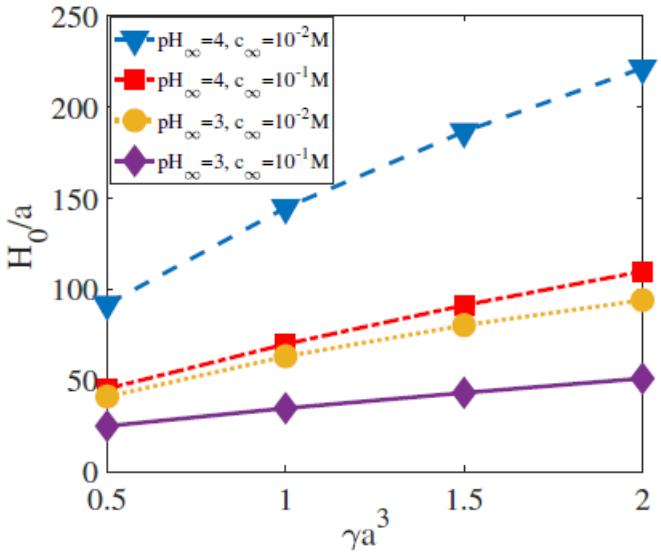

Figure 4.6: *Variation of non-dimensional equilibrium brush height H_0/a with number of PCS per kuhn monomer γa^3 for different pH_∞ and c_∞ values. $\nu = 0.1$, $\omega = 0:01$. All other parameters are identical to that used in Fig. 4.2.*

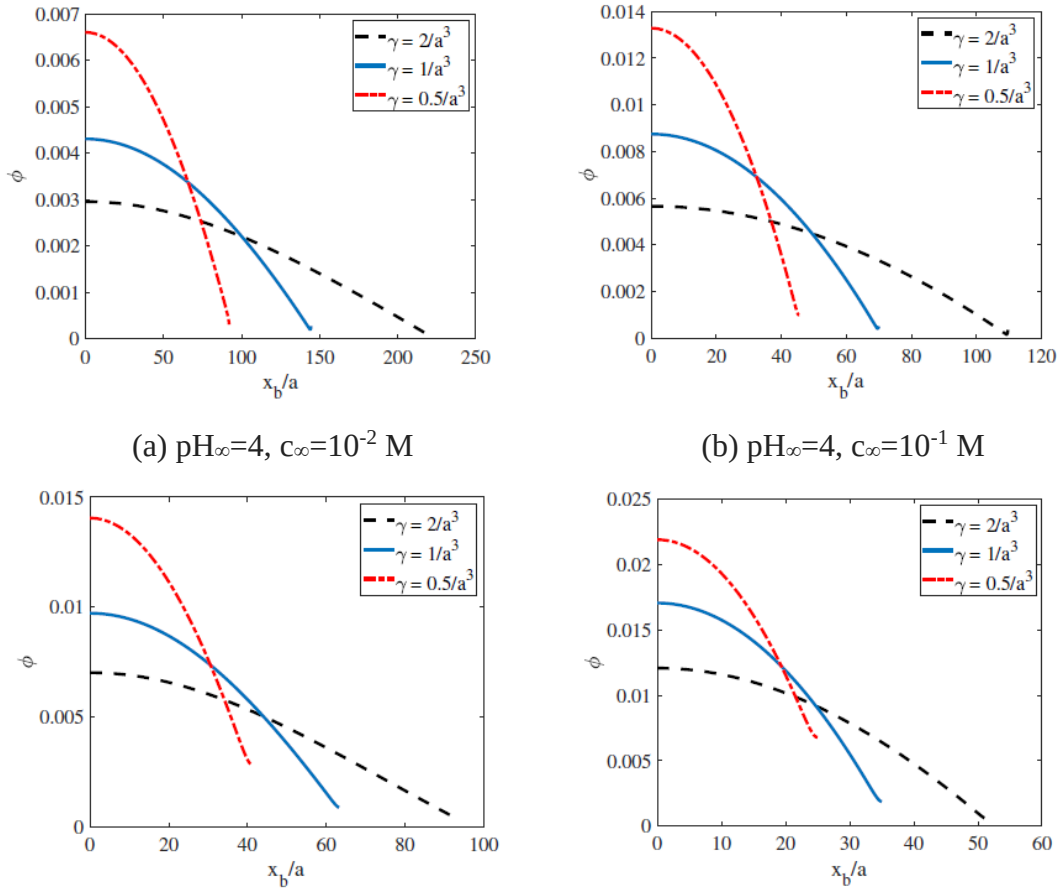

(a) pH_∞=4, c_∞=10^{-2} M

(b) pH_∞=4, c_∞=10^{-1} M

(c) pH_∞=3, c_∞=10^{-2} M

(d) pH_∞=3, c_∞=10^{-1} M

Figure 4.7: *Comparison of monomer distribution profiles (ϕ) as a function of the dimensionless transverse distance along the brush (x_b/a, a is the Kuhn length) obtained for different values of PCS number density using our theory and theory of Ref. 14 for different pH_∞ and c_∞ values. ν = 0.1, ω = 0.01. All other parameters are identical to that used in Fig. 4.2.*

Fig. 4.7 provides the variation of the monomer density along the brush height for different values of γ. As was discussed Fig. 4.3, a shorter brush would imply a larger (smaller) monomer density close to (away from) the wall in comparison to the cases with larger brush height. This is also the case here − hence we witness a larger (smaller) monomer density close to (away from) the wall for smaller values as well as the cases for larger salt concentration and smaller pH_∞ values.

Fig. 4.8 provides the variation of the end distribution g along the brush height for different values of γ. It was revealed in Fig. 4.4 that the case of smaller brush height leads to a larger concentration of the monomers close to the wall and results in a larger value of g close to the wall and it decays quickly away from the wall. On the other hand, for the case of larger brush height, g is much smaller at near wall locations and decays much more slowly away from the wall. This is the case here as well − hence we witness a larger (at near wall locations) and a steeply decaying g for the case with small γ (i.e., the case that corresponds to smaller brush height, see Fig. 4.5), but a smaller and more weakly decaying g for larger γ (i.e., the condition that leads to taller brushes).

Finally, Fig. 4.9 provides the transverse variation of the EDL electrostatic potential for different values of γ. Smaller γ implies both weakened charge density of the brushes as well as shorter brushes. Accordingly, for smaller γ, the EDL electrostatic potential is also weak and also decays quickly (since the brush height is small). Of course, for a given γ, a larger EDL electrostatic potential (magnitude) is invariably witnessed for lower c_∞ (weakened screening of the charge of the PE brushes) and larger pH_∞ (more enhanced ionization of the PE brushes).

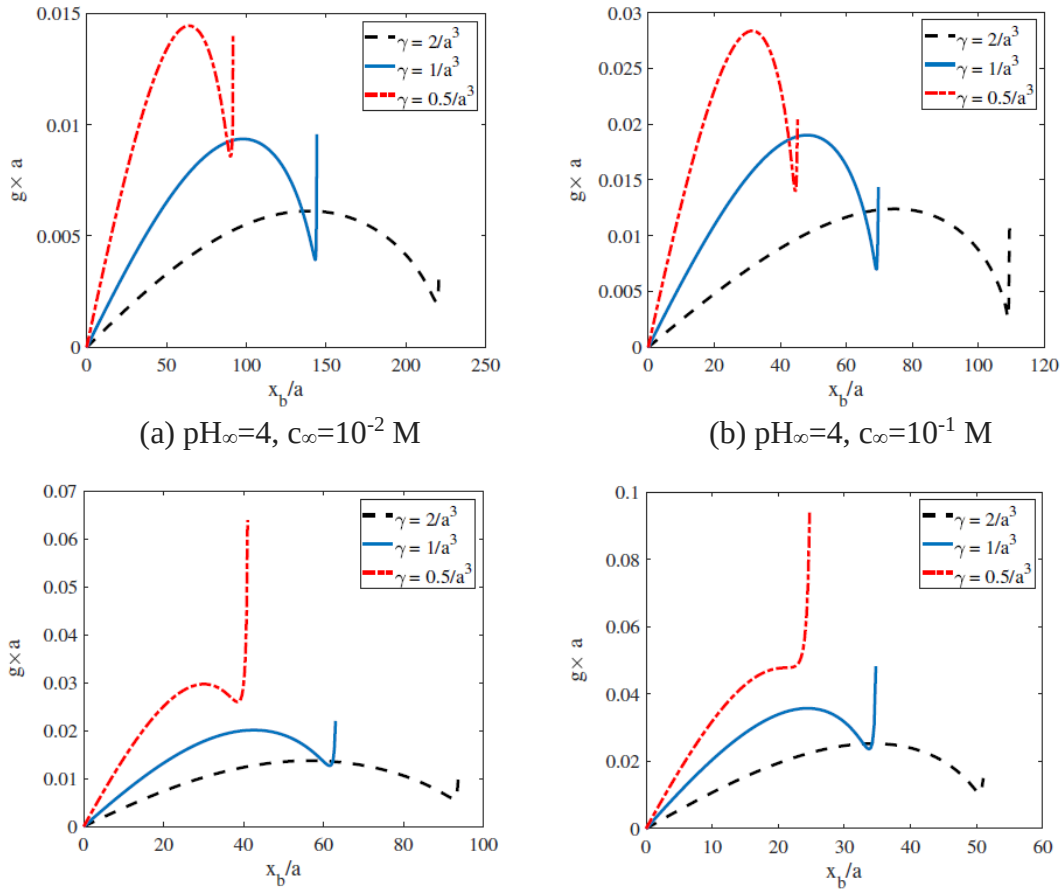

(a) pH_∞=4, c_∞=10^{-2} M (b) pH_∞=4, c_∞=10^{-1} M

(c) pH_∞=3, c_∞=10^{-2} M (d) pH_∞=3, c_∞=10^{-1} M

Figure 4.8: *Comparison of non-dimensional chain end distribution profiles (g* x *a, a is the Kuhn length) as a function of the dimensionless transverse distance along the brush (x_b/a) obtained for different values of PCS number density γ using our theory and theory of Ref. 14 for different pH_∞ and c_∞ values. ν = 0.1, ω = 0.01. All other parameters are identical to that used in Fig. 4.2.*

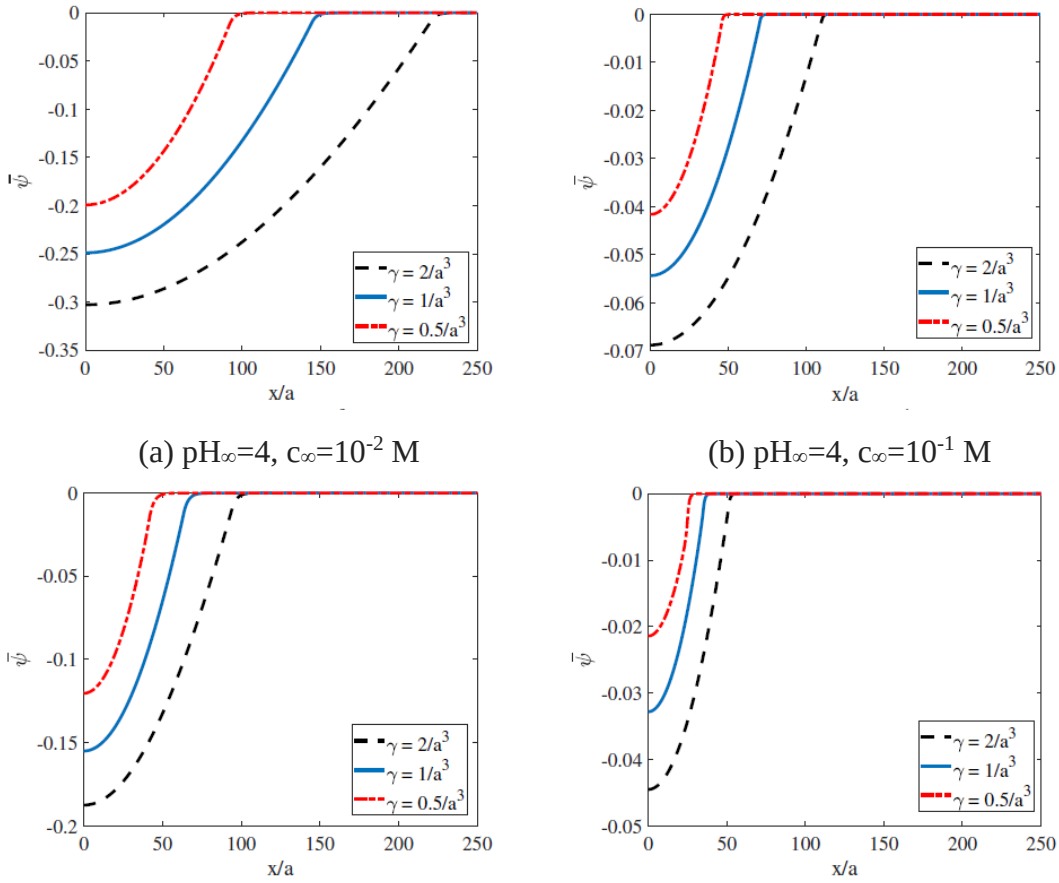

(a) pH_∞=4, c_∞=10^{-2} M (b) pH_∞=4, c_∞=10^{-1} M

(c) pH_∞=3, c_∞=10^{-2} M (d) pH_∞=3, c_∞=10^{-1} M

Figure 4.9: *Comparison of non-dimensional electrostatic potential profiles ($\bar{\psi}$ = $e\psi/(k_BT)$) as a function of the dimensionless transverse distance along the nanochannel half height (x/a) obtained for different values of PCS number density γ using our theory and theory of Ref. 14 for different pH_∞ and c_∞ values. ν = 0.1, ω = 0.01. All other parameters are identical to that used in Fig. 4.2.*

4.4. Discussions

4.4.1. Applicability of the Proposed Theory

The proposed theory is directly applicable to all the systems that involve planar, pH-responsive PE brushes. Such brushes have been extensively employed for several applications such as nanochannel ion selectivity[160] and ion detection[161], fabrication of ionic valves[162,163], nanofluidic diodes[164], and surfaces of controllable wetting properties[165], and many more. The theory provides a new prediction of the EDL electrostatic potential distribution and consequently a new prediction for the number density distribution of the electrolyte, hydrogen, and hydroxyl ions for cases where the EV interactions between the PE segments become important and the PE brushes are so charged that $\gamma a^3 \neq 1$. This would imply that the corresponding changes in the ionic current or the current-voltage characteristics (in presence of an applied voltage), which in turn would dictate several of these applications[160−164], would be significantly different as compared to that obtained with the existing theory[14]. Similarly, the prediction of a new monomer distribution would critically affect the drag and the resulting fluid flow in brush-grafted nanochannels, which would impact the problems dictated by such fluid flows in brush-grafted nanochannels[130,132,166].

The present model, while describes the planar brushes, would also motivate developing models that account for the appropriate EV interactions and the expanded form of the mass action law for the pH-responsive spherical[167] or cylindrical PE brushes (i.e., PE brushes grafted to spheres and cylinders) that have been employed in many applications such as the use of nanoparticles grafted with pH-responsive brushes for targeted drug

delivery[168], protein binding[169], synthesis of magnetic nanoparticles[170], etc. Finally, the use of the generic mass action law would be useful to improve the theoretical predictions of not only the pH-responsive planar and curved PE brushes, but also all those calculations that involve generic pH-responsive PE molecules and gels[154–158].

4.4.2. Limitations and Scope of Improvement of the Proposed Theory

In this chapter, we employ the strong stretching theory (SST) framework which assumes the brushes to be in a strongly stretched configuration. Hence, we ignore the effects of lateral variation of monomer distribution pro le and bending back of chain ends. The approximation holds good for systems with high grafting density. For other systems, an advanced numerical self-consistent field theory (SCFT) model[171] needs to be implemented.

The second important issue is that we invariably assume that the EDLs are always thin enough to ensure that $\ell > 2\lambda_D$ (ℓ is the distance between the adjacent grafted chains and λ_D is the EDL thickness) and there is no overlap between the EDLs formed by the adjacent brushes. In case such an approximation does not hold, one would need to assume a 2D (and not a 1D) model for the brush EDL electrostatics and alter the SST accordingly[172].

Thirdly, no non-PB component (e.g. finite ion size effect[173,174], solvent polarization effect[175], or ion-ion correlation effect[176]) has been considered in the description of the

EDL. These effects would become important for large and large salt concentration and would significantly impact the overall self-consistent field approach.

Fourthly, our theory also does not consider the correlations due to the connectivity of the polymer charges. Such correlations can be especially significant for pH-responsive systems (like pH-responsive PE brushes). For example, there are chances that the effective pK_a of the polymer chain might get significantly altered due to the connected charges of the pH-responsive PE chain[177]. Such alteration of the pK_a and its resulting connotations in all the presented results have been obviously neglected in the present study.

Finally, we shall like to emphasize that given the fact that we have used mean-field calculations in this chapter, the capability of the present model to quantify the exact influence of the EV effects will be limited. This stems from the fact that the mean field assumptions extend to the EV effect consideration as well. This has been described in detail by Alexander-Katz et al[178]. In this paper[178], the authors studied confined polymer solutions and used the density profiles to obtain the effective correlation length ξ_{eff} quantifying the non-mean-field polymer correlations and obtained the results to the mean field theory predictions. While for small EV parameters, the ξ_{eff} was well described by the mean-field theory results, for larger EV parameters $\xi_{eff} \sim C^{-3/4}$ (C is the polymer solution concentration), a result that the mean-field theory could not predict. In essence, therefore, chances are that the inherently mean-field approach of

our calculations would imply that some of the predictions of the effect of considering the EV interactions will be limited.

4.5. Strong Stretching Theory for pH-Responsive Polyelectrolyte Brushes in Large Salt Concentrations[*]

4.5.1. Motivation and Model Description

Developing scaling laws, describing the brush height as functions of the various parameters PE brushes have formed a critical component of many theoretical approaches. Also, much more detailed calculations, providing explicit description of the PE brush-induced electric double layers (EDLs) through Poisson-Boltzmann (PB) equations that can also account for the pH-responsiveness of the PE brushes, have been attempted for modelling the PE brushes. Most of these theoretical studies, however, do not consider the cases where the concentration of the salt in the medium is significantly large (i.e., several Molars). It is well established that for such large salt concentration, the standard Poisson-Boltzmann description of the electric double layer (EDL) breaks down[15,173,176,179] and one needs to account for the contributions of other non-Poisson-Boltzmann elements such as the finite ion size effect[173], solvent polarization effect[175], and the effect of ion-ion correlations[176,179]. A recent all-atom molecular dynamics (MD) simulation study from our group (see chapter 2) probing the behavior of the densely grafted PE brushes has shown that the concentration of the counterions surrounding the

[*] The contents of this section were primarily developed by a fellow Ph.D. student Sai Ankit Etha and have been published as the following journal article: Etha, S. A.; Sivasankar, V. S.; Sachar, H. S.; Das, S. "Strong Stretching Theory for pH-responsive Polyelectrolyte Brushes in Large Salt Concentrations." *Physical Chemistry Chemical Physics* **2020**, *22*, 13536-13553.

PE brushes can reach several molars/molals, confirming the need to develop a model to quantify the behavior of the PE brushes in presence of large salt concentration.

Here, we present a theory for describing the thermodynamics, configuration, and the electrostatics of the PE brushes in large salt concentrations. For this purpose, we invoke the recent theoretical model of McEldrew et al.[15] for describing the thermodynamics of the electrolytes with very large salt concentrations (or effectively, the free energy of the EDL induced by the PE brushes). This study by McEldrew et al.[15], which accounts for three different non-Poisson-Boltzmann (non-PB) effects (namely, the ionic non-mean-field ion-ion correlations, the solvent polarization, and the finite size effect of the ions and water dipoles) is intended to model the water-in-salt electrolyte (WISE) systems. In such WISE systems, the added salt is present in such a large concentration that it outnumbers water by both weight and volume[68,69]. The model proposed by McEldrew et al.[15] was developed from the prior theoretical studies on ionic liquids[179,180,181]. On the other hand, the PE brushes are described by our augmented SST model (see section 4.2). The augmented SST model improves the widely employed SST model for the PE brushes[14] by accounting for two additional effects namely, (a) the excluded volume interactions between the PE brush segments and (b) an expanded form of the mass action law that allows the PE chargeable site density to take different values (and not just a fixed value as in the case of the SST model). These two approaches, one for describing the electrolyte with large salt concentration and another for describing the PE brushes, are integrated to obtain a semi-analytically tractable free energy functional describing the PE brushes in large salt concentration. This functional

is subsequently minimized to obtain the governing equations that provide a thermodynamically self-consistent and coupled description of the PE brush configuration (PE brush height and PE monomer distribution) and the electrostatics of the PE brush induced EDL for the case where the PE brushes are in a large salt concentration. A few prior studies had attempted to incorporate the effect of the mean-field non-PB factors (e.g. finite ion size effect or the solvent polarization effect) in description of the PE brushes[183,184]; however, these studies suffered from considering a very primitive description of the PE brushes (for example, the brush-free energies have been totally neglected in these studies).

In our results, we first show the individual influence of the three different non-PB effects in the brush configuration (brush height and the brush monomer distribution) and the electrostatics of the brush-induced EDL. The ion-ion correlation effect tends to create local electroneutrality around the brushes: this reduces the bush inter-segmental repulsion thereby reducing the brush height. The solvent polarization effect, on the other hand, causes additional screening of the PE charge by ensuring a preferential alignment of the water dipoles: this effect too, therefore, reduces the PE-brush inter-segmental repulsion and hence decreases the brush height. Since the brush height reduces for the cases considering ion-ion correlations and solvent polarization effect, the monomer density increases and the EDL electrostatic potential shows a large magnitude at near-wall locations and becomes zero at much shorter distances from the wall. On the other hand, the consideration of the finite size effect leads to a smaller available space for the counterions thereby lowering their entropy; this enforces the

brushes, in order to counter this effect, to stretch out more (i.e., the brush height increases) so as to provide a larger volume to the counterions. Accordingly, with the finite size effect, the monomer density decreases and the EDL electrostatic potential shows a smaller magnitude at near-wall locations and becomes zero at much greater distances from the wall. Finally, we consider all the three effects simultaneously and establish that for the chosen system parameters, the effects of the ion-ion correlation and solvent polarization overwhelm the effect of the finite sizes and therefore the brush configuration and the EDL electrostatics obey the same behavior as witnessed for the cases where the ion-ion correlation and solvent polarization effects are considered. We also point out that the effects of these non-PB factors are maximum for the cases of large salt concentration and small bulk pH. Furthermore, we demonstrate that for the cases of smaller salt concentration, the present model recovers the prediction of that of the augmented SST model that does not consider the effect of large salt concentration. Finally, we compare the findings from the present model with those obtained from our recent all-atom MD simulation study (see chapter 2) probing the behavior of densely grafted PE brushes in presence of large concentration of the ions (counterions) and achieve an excellent match. Overall, to the best of our knowledge, this study provides the first theory for the behavior of the strongly stretched PE brushes in large salt concentration.

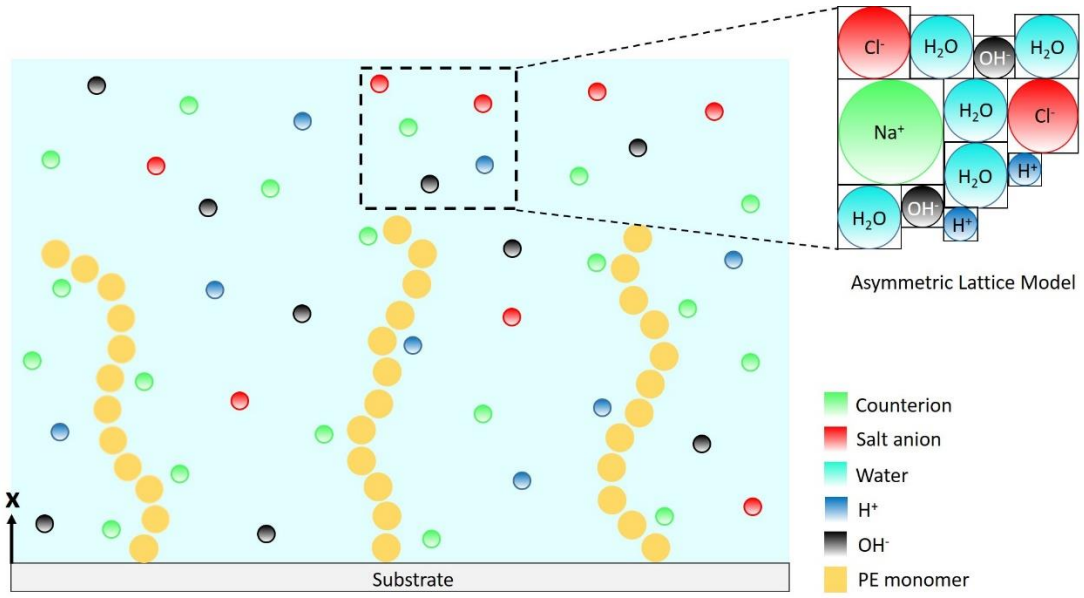

Figure 4.10: *Schematic representing the PE brush grafted on a planar substrate. We employ an asymmetric lattice model to describe the thermodynamics of the mobile ions and solvent dipoles.*

4.5.2. Theory

We consider pH-responsive, polyelectrolyte (PE) brushes present in a highly concentrated electrolytic solution. The PE molecules are grafted to a planar substrate with a small-enough lateral separation ($\ell = 30nm$ between the adjacent grafted PE chains) that ensure that the PE molecules attain a "brush"-like configuration, as shown in Fig. 4.10. In this study, we attempt to develop for the first time a theoretical model for the thermodynamics, configuration, and the electrostatics of the PE brushes in such large salt concentration. Accordingly, our model will combine the formulation of McEldrew et al.[15] (who employed the asymmetric lattice model for studying the thermodynamics of large-concentration electrolytes) and our augmented SST for the PE brushes (section 4.2).

We start by expressing the grand canonical free energy functional (Ω) of the system (assuming that the system is in a thermal and a chemical equilibrium with the bulk)

$$\Omega = \int_V \left(f_e + f_{brush} + f_{ion} - \sum_i n_i \mu_i \right) dV, \tag{4.40}$$

where V is the volume, f_e is the electrostatic energy density associated with the electric field developed around the charged PE brushes, f_{brush} is the PE brush free energy density, f_{ion} is the free energy density of all the mobile ionic species surrounding the PE brushes, n_i (i=+, -, H^+, OH^-, and w, representing the electrolyte cation, electrolyte anion, H^+ ion, OH^- ion, and water dipoles, respectively) is the number density of the

mobile species i, and μ_i is the corresponding chemical potential (obtained from the chemical configuration of the bulk).

As a next step, following McEldrew et al[15], we make use of the Legendre transform for replacing the free energy density of the mobile ions and water dipoles and the contribution due to their chemical potentials with an equivalent thermodynamic pressure (P) as:

$$P = \sum_i n_i \mu_i - f_{ion}.$$

(4.41)

As a result, eq.(4.40) reduces to:

$$\Omega = \int_V (f_e + f_{brush} - P)\ dV.$$

(4.42)

Henceforth, we shall consider that there is no variation of any quantity parallel to the planar substrate. Therefore, the above integral gets expressed as:

$$\Omega = A \int (f_e + f_{brush} - P)\ dx,$$

(4.43)

where A is the area of the substrate and x denotes the direction perpendicular to the substrate. Below, we shall derive the expressions of the individual free energy (or free energy density) terms.

Electrostatic free energy of the electric field developed around the PE brush system

This differential form of this energy (δF_e) can be expressed in terms of the corresponding free energy density (f_e) as:

$$\delta F_e = \delta \int_V f_e \, dV = \int_V \boldsymbol{E} \cdot \delta \boldsymbol{D} \, dV,$$

(4.44)

where $\boldsymbol{E} = -\nabla\psi$ (ψ is the induced EDL electrostatic potential) and $\boldsymbol{D}$ are the electric field and the displacement field, respectively.

Following McEldrew et al[15], one can express the displacement field as:

$$\boldsymbol{D} = \varepsilon_0 \varepsilon_r \boldsymbol{E} + \boldsymbol{P}_{pol} + \boldsymbol{P}_{BSK},$$

(4.45)

where, ε_0 is the permittivity of vacuum, ε_r is the permittivity of the solvent, $\boldsymbol{P}_{pol}$ represents the contribution associated with the polarization of the dipoles in the developed electric field, and $\boldsymbol{P}_{BSK}$ (described by the Bazant-Storey-Kornyshev theory[179]) is the contribution associated with the polarization field induced by the presence of the correlated ions in the system. $\boldsymbol{P}_{pol}$ and $\boldsymbol{P}_{BSK}$ can be expressed as [15]:

$$\mathbf{P}_{pol} = n_w p_w \mathcal{L}(\beta p_w \boldsymbol{E}),$$

(4.46)

$$\mathbf{P}_{BSK} = -\varepsilon_0 \varepsilon_r l_c^2 \nabla^2 \boldsymbol{E},$$

(4.47)

where n_w is the number density of the water dipoles, p_w is the dipolar moment of the free dipoles, $\mathcal{L}$ is the Langevin function, $\beta = 1/k_BT$ is the inverse of thermal energy, and ℓ_c is a lengthscale associated with the ion-ion correlations effect[179]. Finally, using eqs.(4.45,4.46,4.47) in eq.(4.44) and obtaining a variational integral of δF_e from 0 to F_e under the constraint $\nabla . D = \rho_e$ [where $\rho_e = e(n_+ - n_- + n_{H^+} - n_{OH^-})$ is the volume charge density of mobile ions], we can write (the detailed steps are provided in McEldrew et al[15]; we repeat them in Appendix B for the ease of understanding):

$$F_e = \int_V f_e dV = \int_V \left[\rho_e \psi - \frac{\varepsilon_0 \varepsilon_r}{2} (|\nabla \psi|^2 + l_c^2 |\nabla^2 \psi|^2) - \frac{n_w}{\beta} \ln\left(\frac{sinh(\beta p_w \nabla \psi)}{\beta p_w \nabla \psi} \right) \right] dV. \tag{4.48}$$

Expression for the thermodynamic pressure P defined in eq.(4.41)

For obtaining the thermodynamic pressure function (P) of the electrolyte system, we consider an asymmetric lattice model for the electrolyte[15]. Accordingly, we use a grand canonical partition function to represent a 5-component system (4 species of mobile ions and water)

$$\Xi = \sum_{\chi_+=0}^{\infty} \sum_{\chi_-=0}^{\infty} \sum_{\chi_{H^+}=0}^{\infty} \sum_{\chi_{OH^-}=0}^{\infty} \sum_{\chi_w=0}^{\infty} e^{\beta \mu_+ \chi_+} e^{\beta \mu_- \chi_-} e^{\beta \mu_{H^+} \chi_{H^+}} e^{\beta \mu_{OH^-} \chi_{OH^-}} e^{\beta \mu_w \chi_w} Q(\chi_+) Q(\chi_-) Q(\chi_{H^+}) Q(\chi_{OH^-}) Q(\chi_w). \tag{4.49}$$

Here, Q represents the canonical partition function of each species, and can be expressed as, $Q(\chi_j) = \omega_j e^{-\beta \epsilon_j \chi_j}$, with the energy given by $E_j = \epsilon_j \chi_j$ [15] and χ_j represents the number of lattice sites occupied by species j. In line with the models of Han et al[182] and McEldrew et al[15], we assume that the different species/components fill the lattice in a manner such that the configuration of each species is equivalent to the

occupation of χ_j lattice sites out of a total of N_t available sites (per unit volume), so that $\omega_j = \frac{N_t!}{\chi_j!(N_t-\chi_j)!}$. Finally, using the fact that the pressure P in a grand canonical ensemble is related to the partition function as, $PV_L = k_B T ln\Xi$ (where $V_L = N_t v_{H^+}$ is the total available lattice volume), we can obtain (see Appendix C for the detailed derivation):

$$P = \frac{k_B T}{v_{H^+}} ln\left[\left(\left(\left(\left\{1+\xi_{OH^-}e^{\beta\tilde{\mu}_{OH^-}}\right\}^{\xi_{H^+}/\xi_{OH^-}} + \xi_{H^+}e^{\beta\tilde{\mu}_{H^+}}\right)^{\xi_+/\xi_{H^+}} + \xi_+ e^{\beta\tilde{\mu}_+}\right)^{\xi_-/\xi_+} + \xi_- e^{\beta\tilde{\mu}_-}\right)^{\xi_w/\xi_-} + \xi_w e^{\beta\tilde{\mu}_w}\right]^{1/\xi_w},$$

(4.50)

where, $\xi_j = v_j/v_{H^+}$ (v_j is the volume of an individual element of species j and we non-dimensionalize with the volume of smallest species, v_{H^+}) and $\tilde{\mu_j} = \mu_j - \epsilon_j$.

Expression for the free energy of the PE brushes

The brushes are modeled using the augmented Strong Stretching Theory (SST) (see section 4.2 for the detailed derivation). The total free energy associated with the PE brushes can be expressed as:

$$\int_V f_{brush}\, dV = \frac{3k_BT}{2pa^2}\int_0^H g(x')dx' \int_0^{x'} E(x,x')dx + \frac{k_BT\sigma}{a^3}\int_0^H f_{conc}[\phi(x)]dx - \sigma\int_0^H e\psi n_{A^-}\phi\, dx + \frac{k_BT\sigma}{a^3}\int_0^H \phi\left[\left(1-\frac{n_{A^-}}{\gamma}\right)ln\left(1-\frac{n_{A^-}}{\gamma}\right) + \frac{n_{A^-}}{\gamma}ln\left(\frac{n_{A^-}}{\gamma}\right) + \frac{n_{A^-}}{\gamma}ln\left(\frac{n_{H^+,\infty}}{K_a'}\right)\right]dx.$$

(4.51)

We would like to reiterate that the free energy of the brushes should be minimized in the presence of constraints (4.8) and (4.9).

Final expression of the grand canonical free energy functional Ω expressed in eq.(4.43)

Using eqs.(4.48,4.50,4.51,4.8,4.9) in eq.(4.43), we get the final expression for the grand canonical free energy functional Ω as:

$$\Omega = A\int_V \left[e\psi(n_+ - n_- + n_{H^+} - n_{OH^-}) - \frac{\varepsilon_0\varepsilon_r}{2}(|\nabla\psi|^2 + l_c^2|\nabla^2\psi|^2) - \frac{n_w}{\beta}\ln\left(\frac{sinh(\beta p_w \nabla\psi)}{\beta p_w \nabla\psi}\right) - P\right] dx$$
$$+ \frac{3k_BT}{2pa^2}\int_0^H g(x')dx' \int_0^{x'} E(x,x')dx + \frac{k_BT\sigma}{a^3}\int_0^H f_{conc}[\phi(x)]dx - \sigma\int_0^H e\psi n_{A^-}\phi\, dx$$
$$+ \frac{k_BT\sigma}{a^3}\int_0^H \phi\left[\left(1-\frac{n_{A^-}}{\gamma}\right)ln\left(1-\frac{n_{A^-}}{\gamma}\right) + \frac{n_{A^-}}{\gamma}ln\left(\frac{n_{A^-}}{\gamma}\right) + \frac{n_{A^-}}{\gamma}ln\left(\frac{n_{H^+,\infty}}{K_a'}\right)\right]dx$$
$$+ \lambda_1\left[\frac{\sigma}{a^3}\int_0^H \phi(x)dx - N\right] + \int_0^H \lambda_2(x')dx'\left[\int_0^{x'}\frac{dx}{E(x,x')} - N\right],$$

(4.52)

where λ_2 and λ_1 serve as the Lagrange multipliers accounting for the constraints expressed in eq.(4.8) and eq.(4.9), respectively.

Minimization Procedure

In order to get the differential equations governing the problem, we first need to find the PE brush equilibrium state. For that purpose, we employ variational calculus and minimize the free energy terms for the PE brushes (w.r.t $E(x,x')$, $g(x')$, and n_{A^-}) in eq.(4.52). This minimization (the procedure has been described in detail in section 4.2) yields equations (4.27), (4.15), (4.16) and (4.30).

We now, have all variables in terms of ψ (except the equilibrium brush height, H_0 and $\lambda_3 = -\lambda_1\frac{8a^2N^2p}{3\pi^2}$). Hence, all of this culminates with the governing equation for the ψ, that is obtained by taking the variation of eq.(4.52) with respect to ψ and setting it to zero, yielding (with $\psi' = d\psi/dx$):

$$\epsilon_0\epsilon_r\Big(1-l_c^2\frac{d^2}{dx^2}\Big)\frac{d^2\psi}{dx^2}+\frac{d}{dx}(n_w p_w\mathcal{L}(\beta p_w\psi'))+e\Bigg(n_+-n_-+n_{H^+}-n_{OH^-}$$
$$-\frac{K_a'\gamma}{K_a'+n_{H^+,\infty}\exp\big(-\gamma a^3\frac{e\psi}{k_BT}\big)}\frac{\nu}{3\omega}\Bigg[\Bigg\{1+\kappa^2\Bigg(\lambda_3-x^2+\alpha\frac{K_a'\gamma}{K_a'+n_{H^+,\infty}\exp\big(-\gamma a^3\frac{e\psi}{k_BT}\big)}\psi$$
$$-\rho\Big(1-\frac{K_a'}{K_a'+n_{H^+,\infty}\exp\big(-\gamma a^3\frac{e\psi}{k_BT}\big)}\Big)ln\Big(1-\frac{K_a'}{K_a'+n_{H^+,\infty}\exp\big(-\gamma a^3\frac{e\psi}{k_BT}\big)}\Big)$$
$$-\rho\frac{K_a'}{K_a'+n_{H^+,\infty}\exp\big(-\gamma a^3\frac{e\psi}{k_BT}\big)}ln\Big(\frac{K_a'}{K_a'+n_{H^+,\infty}\exp\big(-\gamma a^3\frac{e\psi}{k_BT}\big)}\Big)$$
$$-\rho\frac{K_a'}{K_a'+n_{H^+,\infty}\exp\big(-\gamma a^3\frac{e\psi}{k_BT}\big)}ln\Big(\frac{n_{H^+,\infty}}{K_a'}\Big)\Bigg)\Bigg\}^{1/2}-1\Bigg]\Bigg)=0 \qquad (0\le x\le H),$$

$$\epsilon_0\epsilon_r\Big(1-l_c^2\frac{d^2}{dx^2}\Big)\frac{d^2\psi}{dx^2}+\frac{d}{dx}(n_w p_w\mathcal{L}(\beta p_w\psi'))+e\,(n_+-n_-+n_{H^+}-n_{OH^-})=0 \qquad (H\le x\le\infty).$$

(4.53)

To solve these ODE's we need to first find an expression for the number density (n_j) of each of the mobile species (we already have the concentration of the PE charge, n_{A^-}). For this purpose, we shall use $n_j=\left.\frac{\partial P}{\partial\mu_j}\right|_{T,\mu_{i\neq j}}$. [where P is defined in eq.(4.50)], yielding:

$$n_w=\frac{1}{v_{H^+}}\frac{e^{\beta(\mu_w+\Lambda)}}{D_1},$$
$$n_-=\frac{1}{v_{H^+}}\frac{e^{\beta(\mu_-+e\psi)}(D_2)^{\xi_w/\xi_--1}}{D_1},$$
$$n_+=\frac{1}{v_{H^+}}\frac{e^{\beta(\mu_+-e\psi)}(D_2)^{\xi_w/\xi_--1}(D_3)^{\xi_-/\xi_+-1}}{D_1},$$
$$n_{H^+}=\frac{1}{v_{H^+}}\frac{e^{\beta(\mu_{H^+}-e\psi)}(D_2)^{\xi_w/\xi_--1}(D_3)^{\xi_-/\xi_+-1}(D_4)^{\xi_+/\xi_{H^+}-1}}{D_1},$$
$$n_{OH^-}=\frac{1}{v_{H^+}}\frac{e^{\beta(\mu_{OH^-}+e\psi)}(D_2)^{\xi_w/\xi_--1}(D_3)^{\xi_-/\xi_+-1}(D_4)^{\xi_+/\xi_{H^+}-1}(D_5)^{\xi_{H^+}/\xi_{OH^-}-1}}{D_1}.$$

(4.54)

In the above equations, $\Lambda=k_BTln(sinh(\beta p_w\psi')/\beta p_w\psi')$ is the free energy associated with the dipolar fluctuations in an electric field and

$$
\begin{aligned}
D_5 &= 1 + \xi_{OH^-} e^{\beta(\mu_{OH^-} + e\psi)}, \\
D_4 &= D_5^{\xi_{H^+}/\xi_{OH^-}} + \xi_{H^+} e^{\beta(\mu_{H^+} - e\psi)}, \\
D_3 &= D_4^{\xi_+/\xi_{H^+}} + \xi_+ e^{\beta(\mu_+ - e\psi)}, \\
D_2 &= D_3^{\xi_-/\xi_+} + \xi_- e^{\beta(\mu_- + e\psi)}, \\
D_1 &= D_2^{\xi_w/\xi_-} + \xi_w e^{\beta(\mu_w + \Lambda)}.
\end{aligned}
$$

(4.55)

To use the above equations, we need to know the values of the chemical potential of the mobile species, μ_j. This is obtained by forcing the ion distributions to be equal to the bulk concentrations in the limit of $x \to \infty$, yielding:

$$
\begin{aligned}
\mu_{OH^-} &= \frac{1}{\beta} ln \left[\frac{n_{OH^-,\infty} v_{H^+}}{1 - \xi_w n_{w,\infty} v_{H^+} - \xi_- n_{-,\infty} v_{H^+} - \xi_+ n_{+,\infty} v_{H^+} - \xi_{H^+} n_{H^+,\infty} v_{H^+} - \xi_{OH^-} n_{OH^-,\infty} v_{H^+}} \right], \\
\mu_{H^+} &= \frac{1}{\beta} ln \left[\frac{n_{H^+,\infty} v_{H^+}}{1 - \xi_w n_{w,\infty} v_{H^+} - \xi_- n_{-,\infty} v_{H^+} - \xi_+ n_{+,\infty} v_{H^+} - \xi_{H^+} n_{H^+,\infty} v_{H^+}} \right] + \\
&\quad \frac{\xi_{H^+}}{\xi_{OH^-}} ln \left[\frac{1 - \xi_w n_{w,\infty} v_{H^+} - \xi_- n_{-,\infty} v_{H^+} - \xi_+ n_{+,\infty} v_{H^+} - \xi_{H^+} n_{H^+,\infty} v_{H^+}}{1 - \xi_w n_{w,\infty} v_{H^+} - \xi_- n_{-,\infty} v_{H^+} - \xi_+ n_{+,\infty} v_{H^+} - \xi_{H^+} n_{H^+,\infty} v_{H^+} - \xi_{OH^-} n_{OH^-,\infty} v_{H^+}} \right], \\
\mu_+ &= \frac{1}{\beta} ln \left[\frac{n_{+,\infty} v_{H^+}}{1 - \xi_w n_{w,\infty} v_{H^+} - \xi_- n_{-,\infty} v_{H^+} - \xi_+ n_{+,\infty} v_{H^+}} \right] + \\
&\quad \frac{\xi_+}{\xi_{OH^-}} ln \left[\frac{1 - \xi_w n_{w,\infty} v_{H^+} - \xi_- n_{-,\infty} v_{H^+} - \xi_+ n_{+,\infty} v_{H^+} - \xi_{H^+} n_{H^+,\infty} v_{H^+}}{1 - \xi_w n_{w,\infty} v_{H^+} - \xi_- n_{-,\infty} v_{H^+} - \xi_+ n_{+,\infty} v_{H^+} - \xi_{H^+} n_{H^+,\infty} v_{H^+} - \xi_{OH^-} n_{OH^-,\infty} v_{H^+}} \right] + \\
&\quad \frac{\xi_+}{\xi_{H^+}} ln \left[\frac{1 - \xi_w n_{w,\infty} v_{H^+} - \xi_- n_{-,\infty} v_{H^+} - \xi_+ n_{+,\infty} v_{H^+}}{1 - \xi_w n_{w,\infty} v_{H^+} - \xi_- n_{-,\infty} v_{H^+} - \xi_+ n_{+,\infty} v_{H^+} - \xi_{H^+} n_{H^+,\infty} v_{H^+}} \right], \\
\mu_- &= \frac{1}{\beta} ln \left[\frac{n_{-,\infty} v_{H^+}}{1 - \xi_w n_{w,\infty} v_{H^+} - \xi_- n_{-,\infty} v_{H^+}} \right] + \\
&\quad \frac{\xi_-}{\xi_{OH^-}} ln \left[\frac{1 - \xi_w n_{w,\infty} v_{H^+} - \xi_- n_{-,\infty} v_{H^+} - \xi_+ n_{+,\infty} v_{H^+} - \xi_{H^+} n_{H^+,\infty} v_{H^+}}{1 - \xi_w n_{w,\infty} v_{H^+} - \xi_- n_{-,\infty} v_{H^+} - \xi_+ n_{+,\infty} v_{H^+} - \xi_{H^+} n_{H^+,\infty} v_{H^+} - \xi_{OH^-} n_{OH^-,\infty} v_{H^+}} \right] + \\
&\quad \frac{\xi_-}{\xi_{H^+}} ln \left[\frac{1 - \xi_w n_{w,\infty} v_{H^+} - \xi_- n_{-,\infty} v_{H^+} - \xi_+ n_{+,\infty} v_{H^+}}{1 - \xi_w n_{w,\infty} v_{H^+} - \xi_- n_{-,\infty} v_{H^+} - \xi_+ n_{+,\infty} v_{H^+} - \xi_{H^+} n_{H^+,\infty} v_{H^+}} \right] + \\
&\quad \frac{\xi_-}{\xi_+} ln \left[\frac{1 - \xi_w n_{w,\infty} v_{H^+} - \xi_- n_{-,\infty} v_{H^+}}{1 - \xi_w n_{w,\infty} v_{H^+} - \xi_- n_{-,\infty} v_{H^+} - \xi_+ n_{+,\infty} v_{H^+}} \right], \\
\mu_w &= \frac{1}{\beta} ln \left[\frac{n_{w,\infty} v_{H^+}}{1 - \xi_w n_{w,\infty} v_{H^+}} \right] + \\
&\quad \frac{\xi_w}{\xi_{OH^-}} ln \left[\frac{1 - \xi_w n_{w,\infty} v_{H^+} - \xi_- n_{-,\infty} v_{H^+} - \xi_+ n_{+,\infty} v_{H^+} - \xi_{H^+} n_{H^+,\infty} v_{H^+}}{1 - \xi_w n_{w,\infty} v_{H^+} - \xi_- n_{-,\infty} v_{H^+} - \xi_+ n_{+,\infty} v_{H^+} - \xi_{H^+} n_{H^+,\infty} v_{H^+} - \xi_{OH^-} n_{OH^-,\infty} v_{H^+}} \right] + \\
&\quad \frac{\xi_w}{\xi_{H^+}} ln \left[\frac{1 - \xi_w n_{w,\infty} v_{H^+} - \xi_- n_{-,\infty} v_{H^+} - \xi_+ n_{+,\infty} v_{H^+}}{1 - \xi_w n_{w,\infty} v_{H^+} - \xi_- n_{-,\infty} v_{H^+} - \xi_+ n_{+,\infty} v_{H^+} - \xi_{H^+} n_{H^+,\infty} v_{H^+}} \right] + \\
&\quad \frac{\xi_w}{\xi_+} ln \left[\frac{1 - \xi_w n_{w,\infty} v_{H^+} - \xi_- n_{-,\infty} v_{H^+}}{1 - \xi_w n_{w,\infty} v_{H^+} - \xi_- n_{-,\infty} v_{H^+} - \xi_+ n_{+,\infty} v_{H^+}} \right] + \\
&\quad \frac{\xi_w}{\xi_-} ln \left[\frac{1 - \xi_w n_{w,\infty} v_{H^+}}{1 - \xi_w n_{w,\infty} v_{H^+} - \xi_- n_{-,\infty} v_{H^+}} \right].
\end{aligned}
$$

(4.56)

where, $n_{j,\infty}$ represents the bulk number density of the species j.

In order to solve the governing ODEs, we need to know the boundary conditions for our problem. We use the following boundary conditions for ψ:

$$(\psi)_{x=H^-} = (\psi)_{x=H^+},\ \left(\frac{d\psi}{dx}\right)_{x=H^-} = \left(\frac{d\psi}{dx}\right)_{x=H^+},\ \left(\frac{d\psi}{dx}\right)_{x=0} = 0,\ \left(\frac{d^3\psi}{dx^3}\right)_{x=0} = 0,\ (\psi)_{x\to\infty} = 0,\ \left(\frac{d^3\psi}{dx^3}\right)_{x\to\infty} = 0. \tag{4.57}$$

The last thing we require is to find the equilibrium structure of the PE brushes themselves (equilibrium height H_0). This requires that we know λ_3, which can be obtained by substituting eq.(4.30) in eq.(4.9). Hence, we use the following procedure: For a given guess of the equilibrium height (H_0), we use our set of equations to obtain ϕ, ψ, and λ_3. This gives us the distribution of all charged species in our system (n_j), which can then be used to calculate the net charge (q_{net}) in the system using $q_{net} = e\sigma\int_0^\infty (n_\pm n_\mp n_{H^+} - n_{OH^-} - \phi n_{A^-})dx$. The true equilibrium brush height, H_0, can then be obtained by enforcing the condition that $(q_{net})_{H=H_0} = 0$.

4.5.3. Results

Having established a more generic formulation for describing the thermodynamics, configuration, and electrostatics of the PE brushes in large salt concentrations, we now provide a few results to understand the effects of the different non-PB terms (employed to account for the effects of the large salt concentrations) on the electrostatics and the resulting brush structure. We first point out the effect of each of the non-PB effects individually (this is ensured by mathematically "turning on" only one of the non-PB effect at a time) on the PE brush structure (quantified by the brush height and the monomer distribution) and the induced EDL (characterized by the variation of the corresponding EDL electrostatic potential) and compare these results with those obtained from the case where the PE brushes are described by the augmented SST without any non-PB term. Finally, we study the influence of all the different non-PB effects "turned on" simultaneously.

Effect of ion-ion correlation

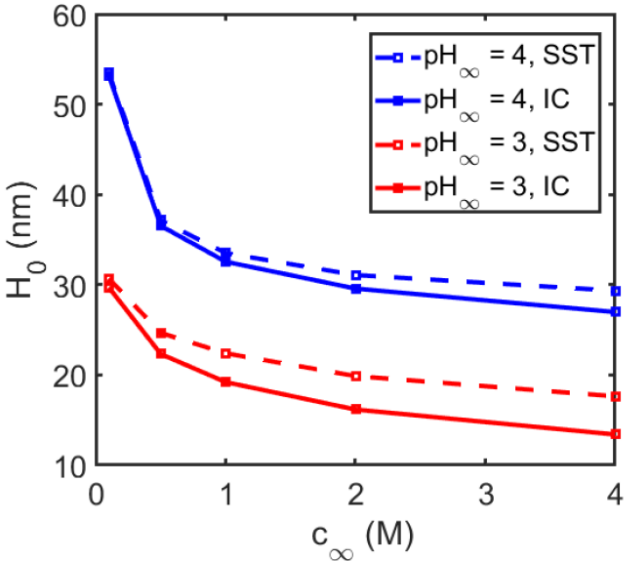

Figure 4.11: *Variation of the equilibrium brush height, H_0, with salt concentration (c_∞, expressed in M, with $c_\infty = n_\infty/(10^3 N_A)$ and n_∞ is the bulk number density of the salt having the units of $1/m^3$) for various pH_∞ values. Here, "IC" refers to the case where only the ion-ion correlations, among the different non-PB effects, have been accounted for to describe the EDL electrostatics, while the PE brushes are described using the augmented SST. On the other hand, "SST" refers to the case where the EDL electrostatics is modelled using the standard PB model (i.e., we consider no non-PB term) and the PE brushes are modelled using the augmented SST. Parameters used in this work are $k_B = 1.38 \times 10^{-23}\, J/K, T = 300\, K$, $pK_a = 3.5$, $a = 1nm, \ell = 30nm$, $\gamma = 1/a^3$ (1 polyelectrolyte chargeable site per Kuhn monomer), $N = 400$, $pK_w = 14$, $p = 1$, $\nu_0 = 0.5$, $\omega_0 = 0.1$, $e = 1.6 \times 10^{-19} C$, $\epsilon_0 = 8.854 \times 10^{-12} F/m$, $\epsilon_r = 79.8$, $pOH_\infty = pK_w - pH_\infty$, $n_{+,\infty} = n_\infty$, $n_{H^+,\infty} = 10^3 N_A 10^{-pH_\infty}$, $n_{OH^-,\infty} = 10^3 N_A 10^{-pOH_\infty}$, $n_{-,\infty} = n_\infty + n_{H^+,\infty} - n_{OH^-,\infty}$, $n_{w,\infty} = 10^3 N_A (1000\rho_w - 58.44 c_\infty)/18$, where ρ_w is the density (in g/cc) of the bulk electrolyte salt solution and is expressed as a function of the salt concentration[185], and $l_c = 0.3nm$.*

We first investigate the effect of the ion-ion correlations (IC) on the brush configuration and the induced EDL electrostatics. The extent of influence of these interactions are determined by the length scale l_c dictating the correlation. In our case, since we consider relatively large salt concentrations, we chose l_c to be of the order of the radius of the ions that are correlated. We choose NaCl as the salt; accordingly, we choose $l_c = 0.3nm$, which is similar to the size of the first hydration shell of these ions species[77,186]. Fig. 4.11 shows the variation of equilibrium PE brush height with the bulk salt concentration for two different bulk values of pH: 3 and 4. The brush height decreases in presence of ion-ion correlations and the extent of this decrease becomes more severe at larger salt concentration and smaller bulk pH (or pH_∞). Ion-ion correlations tend to create local electroneutrality around the charged segments of the PE brush owing to the localization of more counterions near the brush segments. This leads to effectively lower inter-segmental electrostatic repulsions in the brushes over longer distances (~ greater than Kuhn length) causing a shorter brush height. At larger salt concentration, there are more counterions localized near the brushes: the ion-ion correlation effect affects a larger number of ions in the vicinity of the brushes triggering a more enhanced electroneutrality effect. This justifies why the effect of ion-ion correlation in reducing the brush height (for a given pH_∞) is more prominent at a larger salt concentration. On the other hand, for a smaller pH_∞, there is a larger concentration of H^+ ions both in the bulk as well as near the PE brushes; therefore, the ion-ion correlation effect now acts on a larger number of H^+ ions. Hence the ion-ion correlation induced creation of local electroneutrality effect in the vicinity of the brushes becomes more prominent for a smaller pH_∞ at a given value of salt concentration, leading to a more prominent

decrease in the brush height. Also, for a larger pH_{∞}, the brush is almost completely ionized, which implies that the effect of brush ionization is quite large as compared to the ion-ion correlations thereby reducing the difference between the cases of with and without the ion-ion correlation.

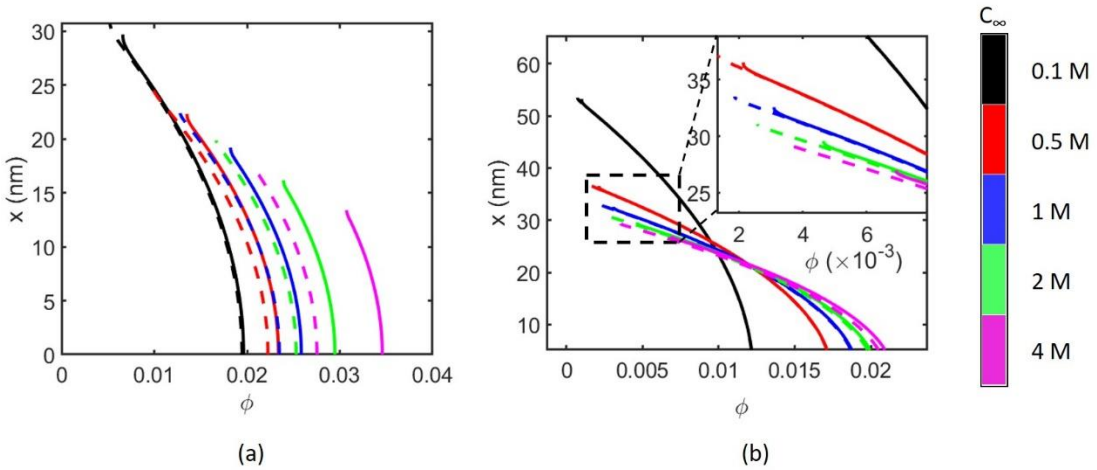

Figure 4.12: *Monomer density profiles for various salt concentration values for (a) pH_∞ = 3, and (b) pH_∞ = 4. Here the cases shown by solid lines (-) and dashed lines (--) represent the cases of "IC" and "SST", respectively. Please see the caption of Fig 4.11 for the definition of "IC" and "SST" cases. All other parameters are identical to those used in Fig 4.11.*

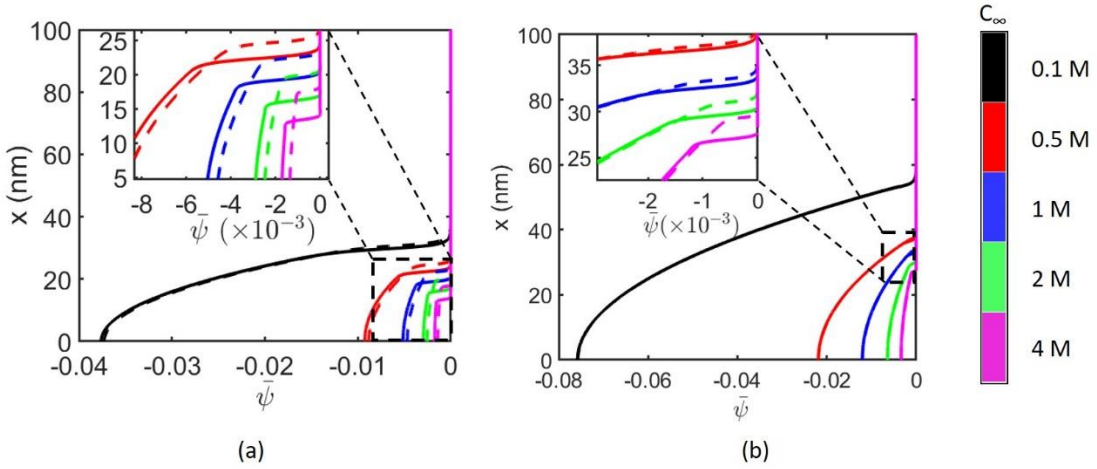

Figure 4.13: *Transverse variation of electrostatic EDL potential for various salt concentration values for (a) pH_∞ = 3, and (b) pH_∞ = 4. Here the cases shown by solid lines (-) and dashed lines (--) represent the cases of "IC" and "SST", respectively. Please see the caption of Fig 4.11 for the definition of "IC" and "SST" cases. All other parameters are identical to those used in Fig. 4.11.*

In Fig. 4.12, we elucidate the effect of the ion-ion correlation in affecting the monomer distribution (ϕ) as a function of the salt concentration and pH_∞. Commensurate with the fact that the brush height with the consideration of the ion-ion correlation effects show the maximum difference for the cases of large salt concentration and small pH_∞ (i.e., the conditions that ensure larger number of ions), the effect of the ion-ion correlations in altering ϕ is most prominent for larger salt concentration and smaller pH_∞. Incorporating the ion-ion correlation effect yields smaller brushes (or denser brushes, i.e., brushes with less heights) as compared to those from the SST (without ion-ion correlation effects). A smaller brush height implies that the monomers are denser locally. This trend (showing larger monomer concentration for the case that accounts for the ion-ion correlation effect, particularly for the condition of larger salt concentration) is readily witnessed in Figure 3. Insets to the figures have been provided to quantify the small differences in the ϕ variations for the cases of with and without the ion-ion correlation for $pH_\infty = 4$ [see Fig. 4.12(b)].

Fig. 4.13 provides the dimensionless electrostatic potential ($\bar{\psi}$) of the PE brush induced EDL. Variation of $\bar{\psi}$ for the case considering the ion-ion correlations show significant difference with respect to the case without the ion-ion correlations for pH_∞=3 and for larger salt concentrations; this difference is much smaller for smaller salt concentration and pH_∞=4. The smaller brush heights for the case considering ion-ion correlations (an effect that is augmented for large salt concentration and small pH_∞) implies that that the corresponding electrostatic potential becomes zero at shorter distances from the wall. A smaller brush height also means that the charge density of the monomer per

unit volume increase, leading to a larger magnitude of $\bar{\psi}$ near the wall. For the case of pH_{∞}=4, the electrostatic potentials are almost indistinguishable between the cases of with and without the ion correlation effect.

Effect of solvent polarization

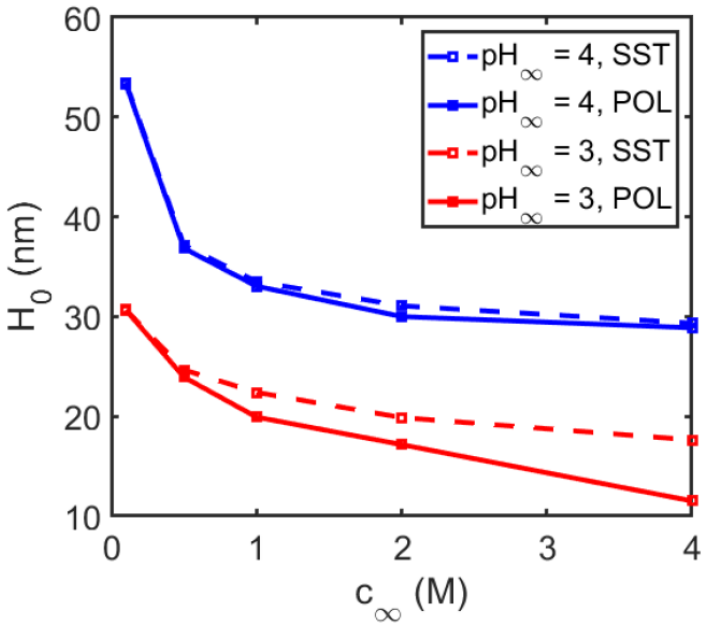

Figure 4.14: *Variation of the equilibrium brush height, H_0, with salt concentration for various pH_∞ values. Here, "POL" refers to the case where only the solvent polarization effect, among the different non-PB effects, has been accounted for to describe the EDL electrostatics, while the PE brushes are described using the augmented SST. On the other hand, "SST" refers to the case where the EDL electrostatics is modelled using the standard PB model (i.e., we consider no non-PB term) and the PE brushes are modelled using the augmented SST. We consider $p_w = 1.85D$, while all other parameters are identical to those used in Fig. 4.11.*

We next consider the effect of the solvent polarization. We choose water with a dipolar moment of $p_w = 1.85D$ as our solvent. Polarization of the solvent molecules acts as a mechanism for the solvent molecules to realign and hence be better able to screen the PE charges. Therefore, by considering the effect of the solvent polarization one would expect a more enhanced screening effect of the EDL (in terms of the screening of the charges on the PE brushes). This is equivalent to considering a more compressed EDL, or equivalent to considering that the PE brush inter-segmental repulsions are screened over much shorter distances. Such screening would obviously imply a significant lowering of the impact of the PE brush inter-segmental electrostatic repulsion (in particular for the case of a smaller pH_∞). This, in turn, would lead to much smaller brush height as compared to the case where the solvent polarization effects have not been considered (see Fig. 4.14). Such solvent polarization effect induced lowering of the brush height is also enhanced for the cases of large salt concentration and low pH_∞. At a larger pH_∞, the more enhanced ionization of the PE brushes leading to a larger brush charge and hence a large PE brush inter-segmental repulsion dominates the effect of the solvent polarization, leading to a weakened effect of the solvent polarization at a larger pH_∞. At large salt concentration, where the existing EDL screening effect is already magnified, the effect of solvent polarization in further enhancing the screening effect becomes larger leading to such augmented solvent-polarization-driven reduction of the brush height.

We next plot the monomer distribution profiles in Fig 4.15 for different bulk salt concentrations and pH_{∞}, elucidating the effect of the solvent polarization. Just like in Fig. 4.12, we observe an increase in the dimensionless monomer density, owing to the reduction in brush height for the case that considers the solvent polarization effect. Also, the insignificant impact of the effect of the solvent polarization for larger pH and smaller salt concentration makes the difference in the monomer distribution (between the cases of with and without the solvent polarization) negligible.

Finally, Fig. 4.16 provides the normalized electrostatic potential, $\bar{\psi}$, and we observe that for pH_{∞}=3 and higher salt concentrations, $\bar{\psi}$ for the case considering solvent polarization effect diverges from that not considering this effect; on the other hand, for pH_{∞}=4, the variation of $\bar{\psi}$ for these two cases (cases with and without considering the effect of solvent polarization) are indistinguishable. Also stemming from the fact that the brush height is smaller for the cases of $pH_{\infty} = 3$ and large salt concentration, we find $\bar{\psi}$ becoming zero at shorter distances from the wall and showing a large magnitude at near-wall locations (where, due to the compression of the brushes, there is a larger concentration of the charged monomers).

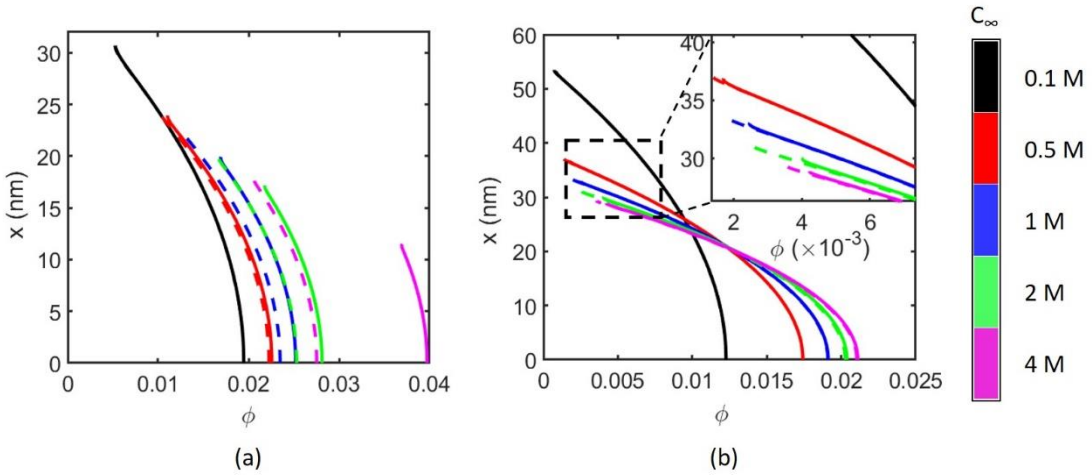

Figure 4.15: *Monomer density profiles for various salt concentration values for (a) pH_∞ = 3, and (b) pH_∞ = 4. Here the cases shown by solid lines (-) and dashed lines (--) represent the cases of "POL" and "SST", respectively. Please see the caption of Fig. 4.14 for the definition of "POL" and "SST" cases. All other parameters are identical to those used in Fig. 4.14.*

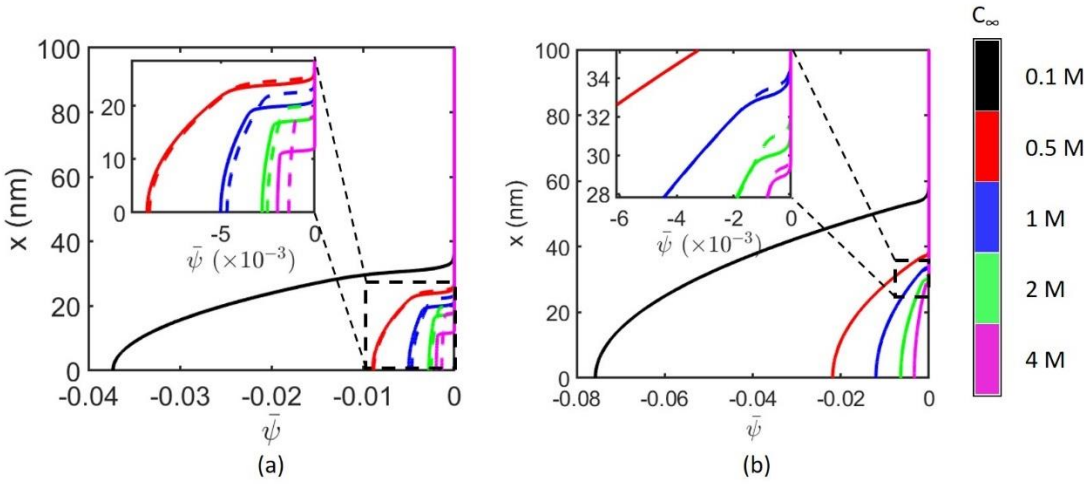

Figure 4.16: *Transverse variation of electrostatic EDL potential for various salt concentration values for (a) pH_∞ = 3, and (b) pH_∞ = 4. Here the cases shown by solid lines (-) and dashed lines (--) represent the cases of "POL" and "SST", respectively. Please see the caption of Fig. 4.14 for the definition of "POL" and "SST" cases. All other parameters are identical to those used in Fig. 4.14.*

Effect of finite sizes of the ions and dipoles

The final non-PB effect that we consider is the finite size effect for all mobile species (ions and water dipoles) in the system. For us to include the finite size effect by using the model described in the theory section of this paper, we first need to obtain certain parameters (which are summarized in the caption of Fig. 4.17). We expect that the consideration of the finite size effect will enforce a lesser available volume to accommodate the counterions, which in turn decreases the entropy of the counterions; to counter this effect, the brushes stretch out more (and hence undergoes an increase in height) so that a larger space can be provided to the counterions. We indeed observe such an effect of the consideration of the finite ion and dipole sizes (see Fig. 4.17). Here, unlike the cases that consider either the ion-ion correlations (see Fig. 4.11) or solvent polarization (see Fig. 4.14), the difference between the cases with and without the non-PB effect (namely, the finite size effect of the ions and dipoles) is not significantly large even for larger salt concentration and small pH_∞. A possible reason for this could be that the bulk salt concentration is still not large enough to cause a massive size effect.

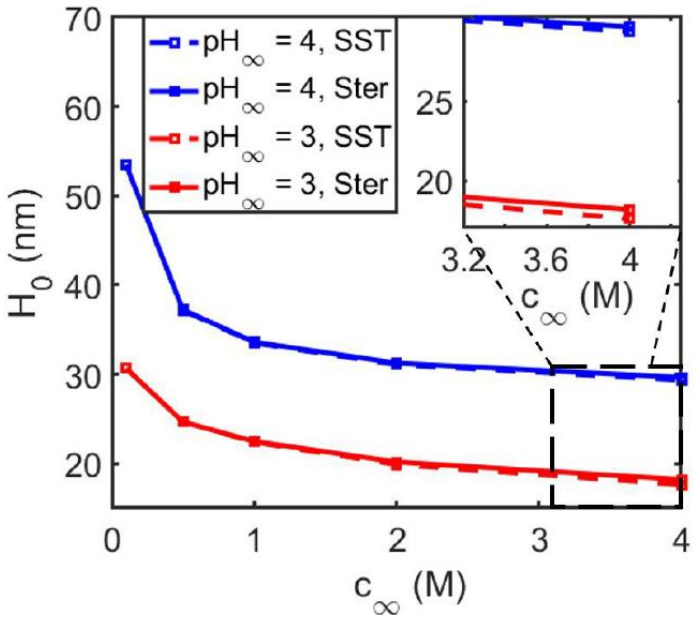

Figure 4.17: *Variation of equilibrium brush height, H_0, with salt concentration for various pH_∞ values. Here, "Ster" refers to the case where only the finite size effect, among the different non-PB effects, has been accounted for to describe the EDL electrostatics, while the PE brushes are described using the augmented SST. On the other hand, "SST" refers to the case where the EDL electrostatics is modelled using the standard PB model (i.e., we consider no non-PB term) and the PE brushes are modelled using the augmented SST. We consider $v_{H^+} = 3.4866 \times 10^{-30}$ [187] (where v_{H^+} denotes the volume of H^+ ion, which is the smallest species in our lattice model and occupies just one lattice site), $\xi_+ = v_+/v_{H^+} = 39.3674$, $\xi_- = v_-/v_{H^+} = 26.3731$, $\xi_w = v_w/v_{H^+} = 3.1779$, $\xi_{H^+} = 1$, and $\xi_{OH^-} = v_{OH^-}/v_{H^+} = 3.7143$ [77,187]. All other parameters are identical to those used in Fig. 4.11.*

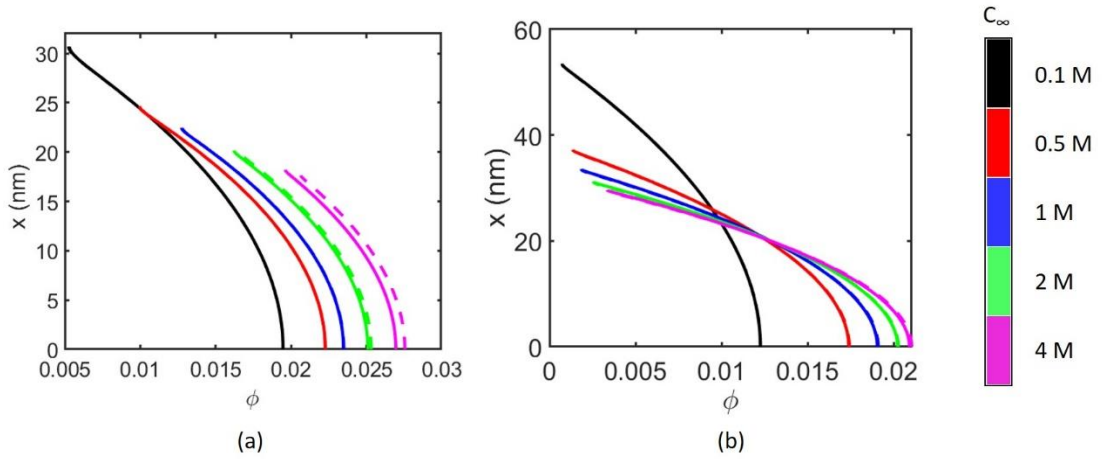

Figure 4.18: *Monomer density profiles for various salt concentration values for (a) pH_∞ = 3, and (b) pH_∞ = 4. Here the cases shown by solid lines (-) and dashed lines (--) represent the cases of "Ster" and "SST", respectively. Please see the caption of Fig. 4.17 for the definition of "Ster" and "SST" cases. All other parameters are identical to those used in Fig. 4.17.*

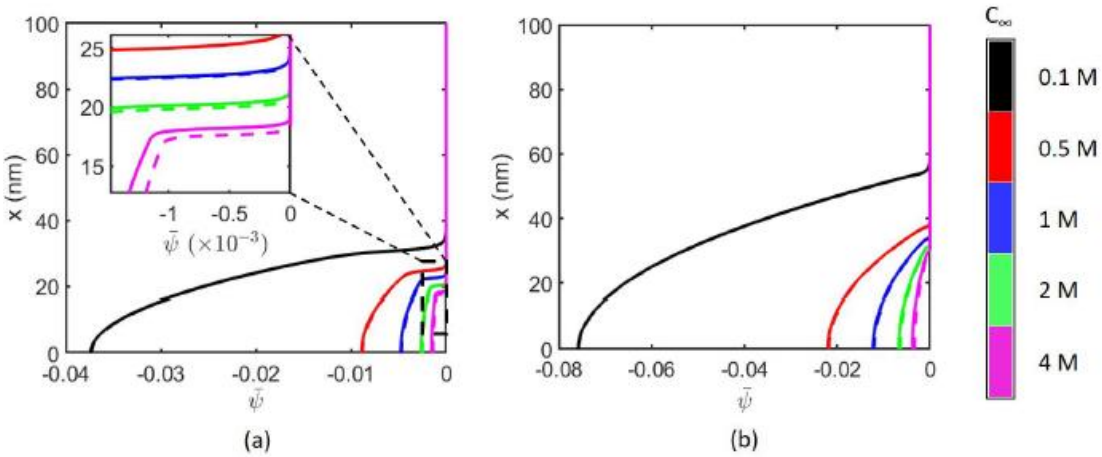

Figure 4.19: *Transverse variation of electrostatic EDL potential for various salt concentration values for (a) pH_∞ = 3, and (b) pH_∞ = 4. Here the cases shown by solid lines (-) and dashed lines (--) represent the cases of "Ster" and "SST", respectively. Please see the caption of Fig. 4.17 for the definition of "Ster" and "SST" cases. All other parameters are identical to those used in Fig. 4.17.*

Figures 4.18 and 4.19 show respectively the dimensionless monomer density and the electrostatic potential ($\bar{\psi}$), elucidating the effect of considering the finite size effect. The monomer distribution has smaller magnitude, since the brush heights were slightly larger, for the case with finite ion sizes. Of course, only for the cases of largest bulk salt concentration ($2M, 4M$) and $pH_{\infty} = 3$, we see some difference in the monomer distribution between the cases of with and without the finite size effect. For other salt concentration and pH_{∞} combinations, this difference between the cases of with and without the finite size effect becomes insignificant. On the other hand, the larger brush size and the weaker monomer distribution implies that for the case that considers the finite size effect, the electrostatic potential goes to zero at distances further away from the wall and has a weaker magnitude at near-wall locations (see Fig. 4.19).

Effect of all the different non-PB contributions considered simultaneously

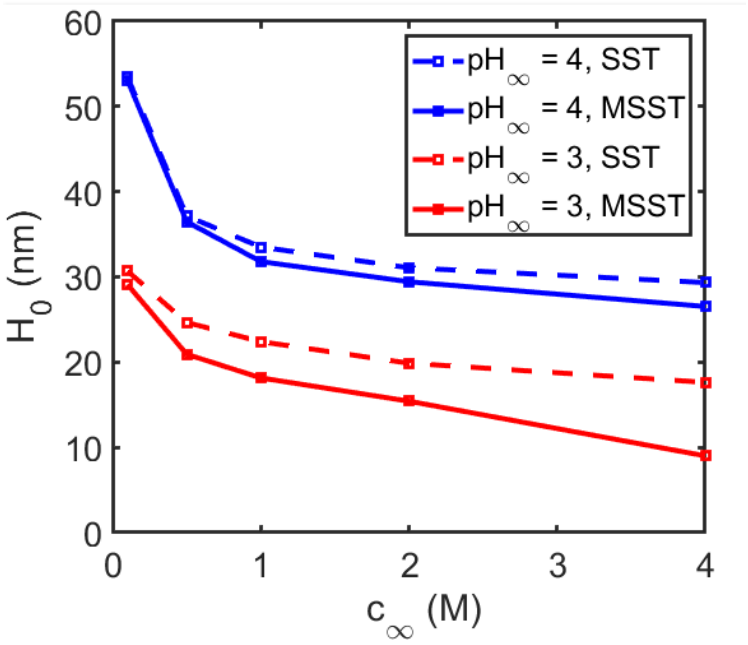

Figure 4.20: *Variation of equilibrium brush height, H_0, with salt concentration for various pH_∞ values. Here, "MSST" refers to the case of modified augmented SST: for this case all the three different non-PB effects (ion-ion correlation, solvent polarization, and finite ion and dipole size) have been considered simultaneously to describe the EDL electrostatics, while the PE brushes are described using the augmented SST. On the other hand, "SST" refers to the case where the EDL electrostatics is modelled using the standard PB model (i.e., we consider no non-PB term) and the PE brushes are modelled using the augmented SST. Here we use* $l_c = 0.3nm$, $p_w = 1.85\ D$, $v_{H^+} = 3.4866 \times 10^{-30}$ [187], $\xi_+ = v_+/v_{H^+} = 39.3674$, $\xi_- = v_-/v_{H^+} = 26.3731$, $\xi_w = v_w/v_{H^+} = 3.1779$, $\xi_{H^+} = 1$, *and* $\xi_{OH^-} = v_{OH^-}/v_{H^+} = 3.7143$ [77,187]. *All other parameters are identical to that used in Fig. 4.11.*

Finally, we provide the results showcasing the impact of all the three different non-PB effects (ion-ion correlation, solvent polarization, and finite ion and dipole size) considered simultaneously on the brush configuration (quantified through the variation of the brush height and the monomer distribution) and the brush-induced EDL (quantified through the variation of the EDL electrostatic potential). We denote this case (the one that considers all the three different non-PB effects) as the modified augmented SST (or MSST). The equilibrium brush height shows a net reduction due to the consideration of the non-PB effects: both the ion-ion correlation as well as the solvent polarizability effect cause a significant reduction in the brush height and dominate the effect of the consideration of finite sizes (that only causes a weak increase in the brush height). Commensurate with the variation where the individual effects were considered in isolation, we find that the reduction in the brush height is maximum for the cases of larger salt concentration and smaller pH_{∞}. This in turn translates to a larger magnitude of dimensionless monomer densities (see Fig. 4.21) and an electrostatic potential distribution (see Fig. 4.22) that has a large magnitude at near-wall locations and becomes zero at shorter distances from the wall. Also, very much like the case of the height variation, these distinct trends in the monomer and electrostatic potential distribution become observable for the cases of large salt concentration and small pH_{∞}.

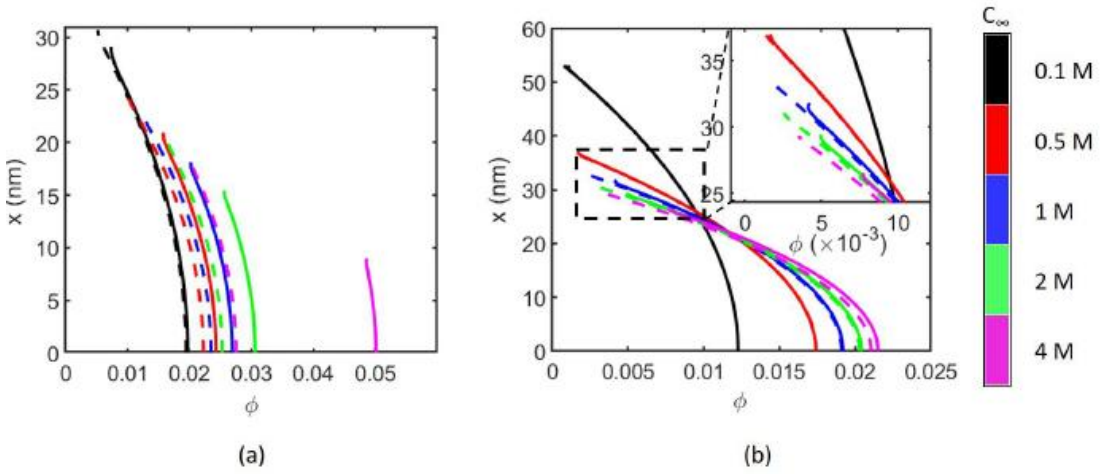

Figure 4.21: *Monomer density profiles for various salt concentration values for (a) pH_∞ = 3, and (b) pH_∞ = 4. Here the cases shown by solid lines (-) and dashed lines (--) represent the cases of "MSST" and "SST", respectively. Please see the caption of Fig. 4.20 for the definition of "MSST" and "SST" cases. All other parameters are identical to those used in Fig. 4.20.*

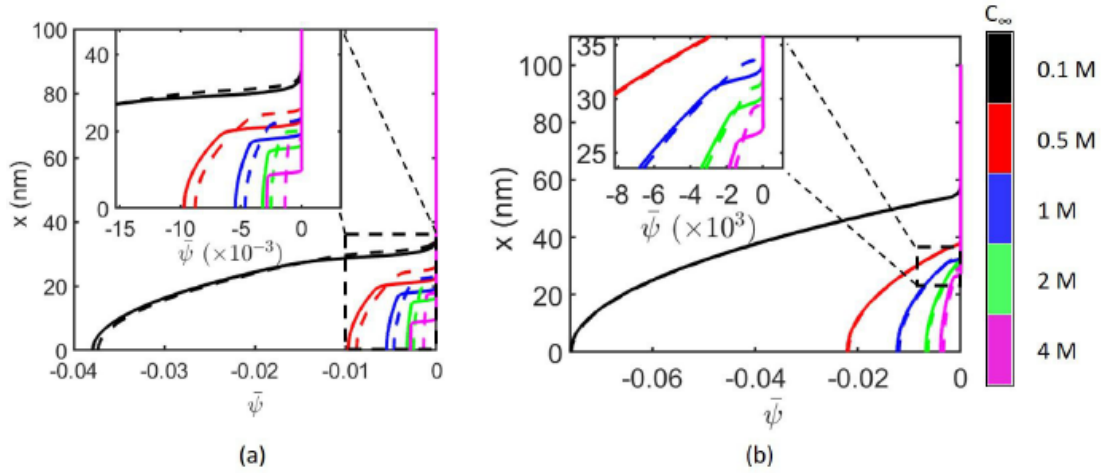

Figure 4.22: *Transverse variation of electrostatic EDL potential for various salt concentration values for (a) pH_∞ = 3, and (b) pH_∞ = 4. Here the cases shown by solid lines (-) and dashed lines (--) represent the cases of "MSST" and "SST", respectively. Please see the caption of Fig. 4.20 for the definition of "MSST" and "SST" cases. All other parameters are identical to those used in Fig. 4.20.*

Comparison with all-atom MD simulation results

In this section, we compare the results (the brush height) from our present theoretical model with those obtained from our all-atom molecular dynamics (MD) simulation study on PE brushes (see chapter 2). The system probed by the all-atom simulations consist of fully ionized Polyacrylic acid (PAA) brushes neutralized by Na^+ counterions. The MD simulations probed different values of chain lengths (quantified by the number of backbone Carbon atoms) and grafting densities (quantified by the lateral separation between adjacent chains). We provide results for the brush height predicted from our MSST model and that obtained from the atomistic simulations (see Table 4.1) and we observe a most outstanding match (discussed in more details later).

In order to make a one-to-one comparison of our theoretical results with the simulations, we make a few assumptions. Firstly, we consider each C-C bond in the PAA backbone (along with the attached pendant groups) (as represented in the all-atom MD model) as one Kuhn segment in the present theoretical model. This gives us a Kuhn length of a=1.53 Å and the number of Kuhn segments equal to the number of C-C bonds (along the backbone of the individual PAA chains) for using in our theoretical model. For example, a chain having 29 backbone Carbon atoms in the MD simulation will contain 28 backbone C-C bonds and thus 28 Kuhn segments. Of course, with considerations we neglect the effect of the strong angular and torsional constraints along the PAA backbone; despite that, as we shall see later, we obtain an excellent match between the theory and simulation results. Moreover, since fully ionized PAA

chains contain a carboxylate group on every alternate backbone carbon atom, we set the density of polyelectrolyte chargeable sites to $\gamma = 0.5/a^3$.

Our second assumption relates to the quantification of an equivalent bulk salt concentration for the MD simulations. The simulations have some fundamental differences from the theoretical model as they consider the effects of the counterions explicitly. In fact, most of the cation concentration within the brushes in our MD simulations was due to the presence of the explicit counterions. We had added 0.1 M NaCl salt in the simulation box as well (for our MD simulation study), but its concentration within the brushes was negligible in comparison to the counterions. On the other hand, our theoretical model involves the effects of a bulk salt concentration but does not consider the counterions (in the vicinity of the PE brushes) separately. Thus, in order to make an appropriate comparison between the two systems, we have ensured that the cation (or counterion) concentration within the brushes is equal for the two cases (i.e., the case studied by the MD simulations and the present case). This was achieved by varying the bulk salt concentration in our theoretical model (for each value of chain length and grafting density) until we obtained a nearly identical average cation concentration within the brushes to that obtained from the simulations. Of course, the anion concentration within the brushes is negligible due to the presence of negative charges on the PE functional groups and the fact that the brushes are extremely densely grafted and hence can be ignored. The final bulk salt concentration values used in the theoretical model as well as the average cation concentration within the brushes (for

both theory and simulations) are provided in Table 4.1 and as one could see, we work with almost identical concentration values (for the two cases).

Finally, in order to enforce complete ionization of the PE functional groups in our model, we set $pH_{\infty} \gg pK_a$. This was done to be consistent with the MD simulations that considered fully ionized PAA chains.

From Table 4.1, we observe an excellent match between the brush heights predicted by our MSST model and the all-atom MD simulations. In fact, the brush heights differ by less than 5% for all the different combinations of parameters that were considered. This level of agreement with the MD simulation results is remarkable, considering the sophistication involved in such atomistic simulations that considered an all-atom framework where each atom of the brushes, water and the mobile ions was modelled explicitly. This allows the simulations to attain levels of accuracy that are beyond the capabilities of any mean field continuum model. Despite that, our theoretical results are in outstanding agreement with the MD simulation results. This not only verifies our model but also testifies its potential in capturing non-PB effects to an extent that is unprecedented in the continuum modelling of PE brushes.

Number of Carbon atoms (N)	Grafting Density (σ_g) ($1/\sigma^2$)	Bulk salt concentration used for the MSST model [c_∞ (M)]	Average counterion concentration within PE brushes for MD study (M)	Average cation concentration within PE brushes for the MSST model (M)	Brush Height (Å) obtained in MD study	Brush Height (Å) obtained using the MSST model
29	0.05	0.1	3.38	3.43	25.56	24.92
29	0.1	0.6	6.04	6.00	28.99	29.50
49	0.05	0.3	3.47	3.46	44.25	45.40
49	0.1	1.25	6.19	6.21	50.43	50.91
69	0.05	0.5	3.57	3.62	61.98	62.86
69	0.1	1.5	6.32	6.30	70.53	72.86

Table 4.1: *Comparison of brush heights obtained from the MSST model presented in section 4.5 and all-atom MD simulations of chapter 2 for various values of the number of carbon atoms (N) and grafting density (in units of $1/\sigma^2$), where $\sigma = 3.5$ Å is the Lennard Jones size parameter). The values of bulk salt concentration (c_∞ in M) used in MSST model, the equivalent average cation concentration within the brushes for the MSST model, and the average counterion concentration for the MD simulations are also provided. Please note for a given N and σ_g value, we consider such a value of the bulk salt concentration that yields nearly identical values of cation concentration and counterion concentration for the MSST model and the MD simulations, respectively. Only under such circumstances, we could compare that height values obtained from the present MSST model and the all-atom MD simulations. Other parameters used in the MSST model are as follow: Kuhn length, a, of 1 C-C bond length equivalent to 1.53 Å and the density of chargeable sites (γ) equal to $0.5/a^3$.*

4.6. Conclusions

In this chapter, we develop a self-consistent field approach (modified SST) to probe the behavior of the pH-responsive brush system by accounting for (a) the EV interactions between the PE segments and (b) a more expanded form of the mass action law valid for $\gamma a^3 \neq 1$. Results indicate an enhancement of the brush height due to the consideration of the EV interaction driven PE inter-segmental repulsion and an increase (decrease) of the brush height for $\gamma a^3 > 1$ ($\gamma a^3 < 1$) due to increased (decreased) counterion-induced osmotic swelling of the brushes. We also establish that these typical height variations get reflected in the corresponding variations of the monomer density profile, distributions of the PE brush ends, and the corresponding EDL electrostatic potential distribution. This model, which can be considered as the most generic SST model for the pH-responsive PE brushes, will not only be critical for explaining several experiments that invariably consider the PE brushes to be in a "good" solvent, but will also help to better interpret a large number of problems that involve pH-responsive PE molecules (not necessarily in a "brush" configuration) and gels and where a more expanded form of the mass action law with $\gamma a^3 \neq 1$ may be more applicable.

In addition, we develop for the first time a detailed theoretical model for describing the thermodynamics, configurations, and electrostatics of the pH-responsive, PE brushes in presence of a large salt concentration. The theory combines our augmented SST for describing the PE brushes with the model proposed by McEldrew et al[15] that accounts for the appropriate non-PB effects [non-mean-field electrostatic ion-ion correlations, solvent polarization, and the finite size (ion and water dipole) effects] for describing

the free energy of the large-concentration electrolytes. Our results point out that these different non-PB effects compete with each other and eventually ensure, in a scenario where the ion-ion correlation and the solvent polarization effects outweigh the influence of the finite size effect, the PE brush height decreases, thereby increasing the monomer density and inducing an EDL electrostatic potential distribution that has a larger magnitude at near-wall locations and becomes zero at shorter distances away from the wall. Furthermore, we also discover that the influence of the non-PB effects are maximum at large salt concentrations and small bulk pH. Finally, we are able to validate our model by comparing its findings with those of our recent all-atom MD simulation study. In the end, we would like to point out a few limitations of the model. We account for the ion-ion correlations only between the mobile ions (i.e., the EDL ions). Such a consideration overlooks the effect of the possible correlation between the static charged functional groups of the PE brushes and the EDL ions (especially the counterions). To the best of our knowledge, no theory exists that accounts for such a correlation; however, it is definitely worthwhile to investigate in future if such a correlation between the charges of the PE brushes and the counterions can be of any consequence in the thermodynamics, configuration, and electrostatics of densely grafted brushes in large salt concentrations. Secondly, we do not consider the ion-partitioning effect, which stems from a possible mismatch between the solvent permittivities inside and outside the PE brushes and have been known to have some effect on the overall electrostatics of the brush-induced EDL[188].

Chapter 5: Electrokinetic Energy Conversion in Nanochannels Grafted with pH-responsive Polyelectrolyte Brushes Modelled using Augmented Strong Stretching Theory*

Abstract: *In this chapter, we develop a theory to quantify the electrokinetic energy conversion in electrolyte-filled nanochannels grafted with pH-responsive polyelectrolyte (PE) brushes. A pressure-driven flow drives the mobile electrolyte ions of the electric double layer (EDL) supported by the charged PE brushes leading to the generation of a streaming current, a streaming electric field and eventually an electrical energy. The salient feature of this study is that the brushes are described using our recently developed augmented Strong Stretching Theory (SST) model. In all the previous theoretical studies on liquid transport in PE-brush-grafted nanochannels, the brushes have either been assumed to be of constant height (independent of salt concentration or pH) or modelled using the Alexander-de-Gennes model that considers uniform monomer distribution along the brush height. Such simplifications have meant that the salt and the pH dependence of the brush height, the monomer distribution, and the resulting electrostatics have not been appropriately accounted for in the transport calculations. This chapter addresses these limitations and provides a much more detailed description of the brushes while capturing the corresponding electrokinetic*

* The contents of this Chapter have been published as the following journal article: Sachar, H. S.; Sivasankar, V. S.; Das, S. "Electrokinetic Energy Conversion in Nanochannels Grafted with pH-responsive Polyelectrolyte Brushes Modelled using Augmented Strong Stretching Theory" *Soft Matter* **2019**, *15*, 5973-5986.

energy conversion. The results establish that the presence of the PE brushes ensures a localization of the average EDL charge density away from the grafting surface, thereby enabling the migration of the EDL ions with a larger background flow velocity; as a consequence, there is an enhancement of the streaming current, streaming electric field, and the resulting electrical energy generation under certain grafting densities of the PE brushes.

5.1. Introduction

Functionalizing nanoscale surfaces (e.g., inner walls of a nanochannel or the surface of a nanoparticle) by grafting them with polyelectrolyte (PE) brushes that are sensitive to environmental stimuli (e.g., pH, salt concentration, etc.) has been widely employed for applications such as nanoscale sensing of ions, analytes, and biomolecules[2-4,26,126], fabrication of devices like nanofluidic diodes, current rectifiers, and nano-actuators[25,27-28,127], nanoparticle-based targeted drug delivery[129,189−191], oil recovery[8], water harvesting[30], emulsion stabilization[192], and many more. All these applications rely on the changes in the configurations and structures of the PE brushes in response to these environ-mental stimuli and the manner in which these changes affect the quantities dictated by the brushes (e.g., the ionic current, mobility of the brush-grafted nanoparticles, etc.). On the other hand, the liquid transport in PE-brush-grafted nanochannels has rarely been considered as the basis of any application. This has stemmed from the universal notion that the presence of the brushes will invariably reduce the flow in PE-brush-grafted nanochannels due to the enhanced drag imparted by the brushes[132].

A recent set of papers by Das and co-workers have led to a paradigm shift in this universal notion of reduced transport in brush-grafted nanochannels[1,139-140,193]. In these papers, the authors studied the transport of an electrolyte solution in nanochannels grafted with end-charged PE brushes containing charges at their non-grafted ends, which localized the electric double layer (EDL) at locations away from the grafting surface. Under such conditions, the effect of the body force on water resulting from the interaction of the EDL charge density with the applied electric field gets augmented, leading to an augmented electroosmotic transport in PE-brush-grafted nanochannels under certain conditions of the PE grafting density[139]. Similarly, this condition of the EDL being localized away from the nanochannel wall meant that the background velocity with which the counterions of the EDL are advected is also enhanced. This, in turn, was responsible for enhanced electrokinetic energy conversion in presence of a background pressure-driven flow[1] and enhanced diffusioosmotic[140] and thermoosmotic transport[193]. A key limitation of these papers[1,139-140,193] is that they consider a somewhat idealistic system where the charge is localized at the non-grafted end of the brushes, while the rest of the brush is uncharged and hence likely to be hydrophobic due to the alkane chain. Such a system will make the penetration of the flow within the brushes difficult, which implies that there is rarely any interaction between the brushes and the flow. These papers[1,139-140,193], however, in addition to being studies that demonstrate a positive influence of the brushes on the liquid transport, are also among the first studies that have considered a thermodynamic description of the brushes, albeit through the simplified Alexander-de-Gennes model that considers a uniform monomer distribution,

in the calculation of the liquid transport in PE-brush-grafted nanochannels. In such a thermodynamic description, the brush height is quantified by the balance of the energy of a brush (consisting of the elastic, excluded volume, and the electrostatic contributions) and the electrostatic energy of the EDL. Accordingly, these calculations are far more rigorous than a large number of previous studies, including those by the present authors, where the brush height has been assumed to be an apriori constant and independent of the salt concentration[16,130,132,166,188,194-204].

In this chapter, we make two major advancements over and above the calculations of the papers by Das and coworkers[1,139-140,193]. First, we consider a much more realizable and practical set up where a pressure-driven water flow is occurring in a nanochannel grafted with backbone-charged, pH-responsive PE brushes (i.e., the ionization of the brushes depends on the local pH). More importantly, such a configuration ensures that the entire PE brush is hydrophilic (that supports a charge and an EDL) and accordingly, will be completely wetted by the flow enforcing a ow-PE-brush interaction that might be absent for the cases of end-charged brushes[1,139-140,193]. Second, the brushes are modelled by the augmented Strong Stretching Theory or SST model. The SST model is a much more improved and complete model for describing the polymer and the PE brushes[37,94,142-143] that does not require enforcing a restrictive condition like the uniform monomer distribution along the length of the polymer brush. Very recently, the present authors provided an improvement of the SST model where the effects of the PE excluded volume interactions and an expanded form of the mass action law were considered[39]. In this chapter, by employing such augmented SST for modelling the brushes, we ensure that we are developing possibly the most rigorous continuum

description of liquid transport in PE-brush-grafted nanochannels till date. For the sake of completeness, we first describe the thermodynamics of the problem, where the brush height, the monomer density and the EDL electrostatics are quantified. The EDL variation clearly points out that the presence of the brushes localizes the EDL charge density away from the walls. Accordingly, in presence of the background pressure-driven transport, the presence of the brushes ensure that the average flow velocity with which the EDL ions are getting advected is much larger as compared to the brush-free nanochannels (this is illustrated in Fig. 5.1) leading to an enhanced streaming current and streaming electric field. As a consequence, the output power as well as the efficiency of the electrokinetic energy conversion is significantly enhanced in comparison to the brush-free nanochannels, despite the presence of the brush-induced enhanced drag. We report efficiency values of as large as 5% for brush-grafted nanochannels and establish that the efficiency improves (in comparison to the brush-free nanochannels) by several folds for both the cases of nanochannels with weakly and densely grafted pH-responsive, PE brushes. In summary, therefore, through the most rigorous theoretical description for studying electrokinetic transport in brush-grafted nanochannels till date, we establish that the functionalization by pH-responsive, charged PE brushes can significantly enhance the electrokinetic energy conversion efficiency in nanochannels.

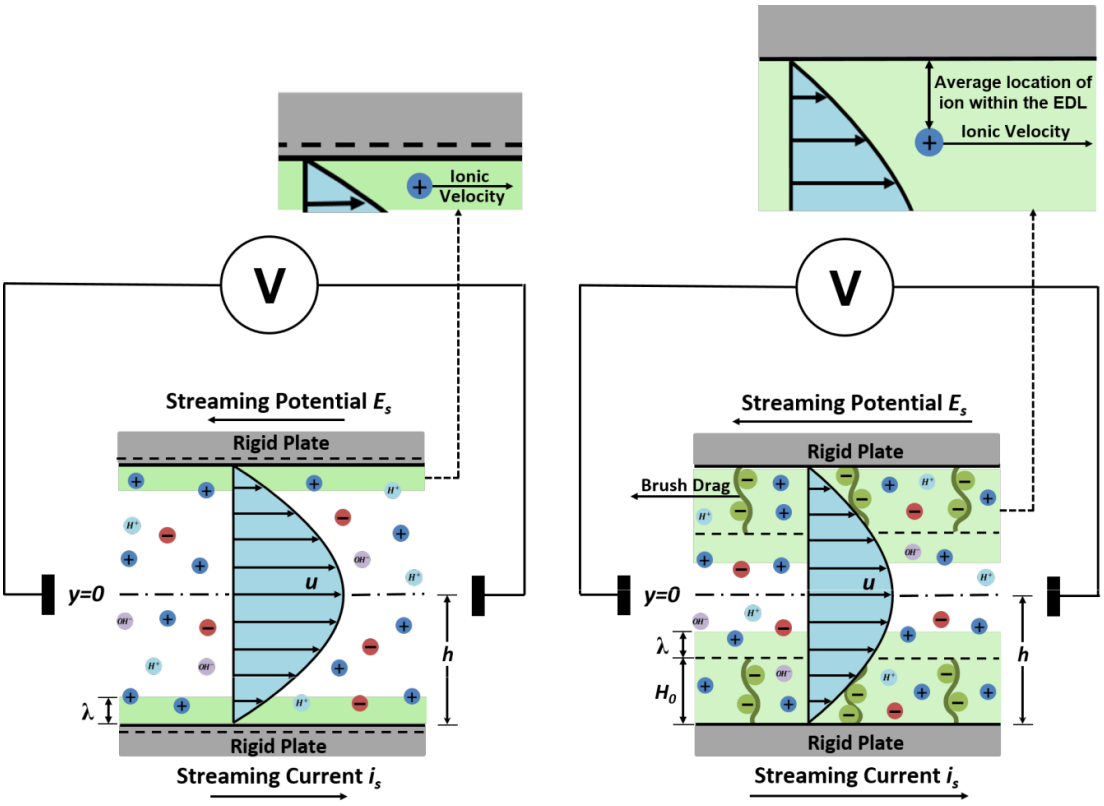

Figure 5.1: *Schematic depicting the generation of the streaming electric field (E_s) and streaming current (i_s) [the electrokinetically generated electric power P_{out} and the resultant energy conversion efficiency ξ are proportional to the product of i_s and E_s]. in a) brush-free nanochannel b) backbone charged PE brushes grafted nanochannel. In the schematic, we highlight the manner in which the presence of the brushes localizes the average EDL charge density further away from the grafting surface enforcing the EDL ions to be advected by a larger background flow velocity, which in turn will lead to an enhanced i_s, E_s, P_{out}, and ξ in brush-grafted nanochannels.*

5.2. Theory

We consider a pressure driven flow in a nanochannel with half-channel height h grafted with backbone-charged, pH-responsive polyelectrolyte (PE) brushes [see Fig.5.1(b)]. The brushes are negatively charged, have a degree of polymerization N, a Kuhn length a, a grafting density (number of chains per unit area) of $\sigma = 1/\ell^2$ (where ℓ is the lateral space between two adjacently grafted PE brushes), and a polyelectrolyte chargeable sites (PCS) density of γ. The surrounding fluid has a dielectric constant ϵ_r, a bulk salt number density n_∞ and a bulk pH value of pH_∞. Here the PE brushes are described by our recently developed augmented Strong Stretching Theory (SST) model[39]. Below we summarize the key equations of this model.

5.2.1. Augmented Strong Stretching Theory Model for pH-responsive PE brushes

Our augmented SST model for the PE brushes improves the existing SST models for the PE brushes[37,94,142-143] by considering the excluded volume effects and a generic value of γ (with $\gamma a^3 \neq 1$, where a is the Kuhn length). Here we summarize the key findings of this augmented SST model; for details, kindly refer to our previous paper[39]. In this theory, we first express the energy functional (F) of a given PE molecule as:

$$\frac{F}{k_BT} = \frac{F_{els}}{k_BT} + \frac{F_{EV}}{k_BT} + \frac{F_{elec}}{k_BT} + \frac{F_{EDL}}{k_BT} + \frac{F_{ion}}{k_BT}, \tag{5.1}$$

where F_{els}, F_{EV}, F_{elec}, F_{EDL} and F_{ion} are the elastic (entropic), excluded volume, electrostatic, electric double layer and ionization free energies (per PE molecule),

respectively. For the expressions of these different energy components please refer to our previous paper[39].

We carry out a variational minimization of the above energy functional in presence of the following constraints:

$$N = \int_{-\mathrm{h}}^{y'} \frac{dy}{E(y, y')}, \tag{5.2}$$

$$N = \frac{1}{\sigma a^3} \int_{-h}^{-h+H} \phi(y) dx, \tag{5.3}$$

where N is the PE size (i.e., number of monomer per PE chain), E(y, y′) = dy/dn quantifies the local stretching of the PE chain at a location y with the end of the PE chain being located at a location y′, ϕ(y) is the dimensionless monomer distribution, and H is the brush height. This minimization eventually yields the following governing equations that dictate the brush thermodynamics. These equations are:

$$n_{A^-} = \frac{K_a' \gamma}{K_a' + n_{H^+,\infty} \exp\left(-\frac{e\psi}{k_B T}\right)}. \tag{5.4}$$

$$\begin{aligned} &\epsilon_0 \epsilon_r \left(\frac{d^2\psi}{dy^2}\right) + e(n_+ - n_- + n_{H^+} - n_{OH^-} - n_{A^-}\phi) = 0 \quad (-\mathrm{h} \le y \le -\mathrm{h} + H) \\ &\epsilon_0 \epsilon_r \left(\frac{d^2\psi}{dy^2}\right) + e(n_+ - n_- + n_{H^+} - n_{OH^-}) = 0 \qquad\qquad (-\mathrm{h} + H \le y \le 0), \end{aligned} \tag{5.5}$$

$$n_\pm = n_{\pm,\infty} exp\left(\mp \frac{e\psi}{k_B T}\right), \tag{5.6}$$

$$n_{H^+} = n_{H^+,\infty} exp(-\frac{e\psi}{k_B T}),$$

(5.7)

$$n_{OH^-} = n_{OH^-,\infty} exp(\frac{e\psi}{k_B T}),$$

(5.8)

$$\begin{aligned}\phi(y) = \quad & \frac{\nu}{3\omega}[\{1 + \kappa^2(\lambda - (y+h)^2 + \beta \frac{K_a'\gamma}{K_a' + n_{H^+,\infty}\exp(-\gamma a^3 \frac{e\psi}{k_B T})}\psi \\ & -\rho(1 - \frac{K_a'}{K_a' + n_{H^+,\infty}\exp(-\gamma a^3 \frac{e\psi}{k_B T})})ln(1 - \frac{K_a'}{K_a' + n_{H^+,\infty}\exp(-\gamma a^3 \frac{e\psi}{k_B T})}) \\ & -\rho \frac{K_a'}{K_a' + n_{H^+,\infty}\exp(-\gamma a^3 \frac{e\psi}{k_B T})} ln(\frac{K_a'}{K_a' + n_{H^+,\infty}\exp(-\gamma a^3 \frac{e\psi}{k_B T})}) \\ & -\rho \frac{K_a'}{K_a' + n_{H^+,\infty}\exp(-\gamma a^3 \frac{e\psi}{k_B T})} ln(\frac{n_{H^+,\infty}}{K_a'}))\}^{1/2} - 1],\end{aligned}$$

(5.9)

$$E(y, y') = \frac{\pi}{2N}\sqrt{(y'+h)^2 - (y+h)^2}.$$

(5.10)

$$(q_{net})_{H=H_0} = 0$$

(5.11)

$$q_{net} = \frac{e}{\sigma}\int_{-h}^{0}(n_+ - n_- + n_{H^+} - n_{OH^-} - \phi n_{A^-})dy$$

(5.12)

$$g(y) = \frac{(y+h)}{\sigma N a^3}\left[\frac{\phi(-h+H)}{\sqrt{H^2-(y+h)^2}} - \int_y^{-h+H} \frac{d\phi(y')}{dy'}\frac{dy'}{\sqrt{(y'+h)^2-(y+h)^2}}\right] \quad (5.13)$$

Eq.(5.4) expresses the number density (n_{A^-}) of the A^- ion − the PE brush becomes negatively charged by producing A^- ions on their backbone via the acid-like dissociation, i.e., $HA \rightarrow H^+ + A^-$. In eq.(5.4), $K_a{}' = 10^3 N_A K_a$ (where N_A is the Avogadro number and K_a is the ionization constant for the reaction $HA \rightarrow H^+ + A^-$), $n_{H^+,\infty}$ is the bulk number density of the hydrogen ion concentration, k_BT is the thermal energy, e is the electronic charge, and ψ is the EDL electrostatic potential. Eq.(5.5) is the Poisson equation expressing the distribution of the EDL electrostatic potential ψ. While expressing this equation, we consider only the bottom half of the nanochannel ($-h \leq y \leq 0$). Also, in eq.(5.5), ϵ_0 is the permittivity of free space, ϵ_r is the relative permittivity of the electrolyte solution (assumed identical for locations within the brushes and outside the brushes) and n_i is the number density of ion *i* ($i = \pm; H^+; OH^-$). Eqs.(5.6, 5.7, 5.8) provide the Boltzmann distributions expressing the ion number densities n_i in terms of the corresponding bulk number densities $n_{i,\infty}$ ($i = \pm; H^+; OH^-$). Eq.(5.9) expresses the monomer distribution profile. In eq.(5.9), ν and ω are the virial coefficients quantifying the excluded volume effects, $\kappa^2 = \frac{9\pi^2\omega}{8N^2a^2\nu^2}$, $\rho = \frac{8a^2N^2}{3\pi^2}$, $\lambda = -\lambda_1\rho = -\lambda_1\frac{8a^2N^2}{3\pi^2}$ [λ_1 is the Lagrange multiplier associated with the constraint expressed in eq.(5.3)], and $\beta = \frac{8N^2ea^5}{3\pi^2k_BT}$. Eq.(5.10) expresses the profile of the local stretching. Eq.(5.11) helps to obtain the equilibrium brush height H_0. Eq.(5.11) is based

on the net unbalanced charge q_{net} in the system, which in turn is expressed through eq.(5.12). Finally, eq.(5.13) expresses the normalized chain end distribution function that can be written as $\int_{-h}^{-h+H} g(y')dy' = 1$. The brush thermodynamics, configuration and electrostatics are obtained by solving eqs.(5.4 – 5.13) in a coupled fashion in presence the following boundary conditions for the EDL electrostatics (assuming an uncharged grafting surface):

$$(\psi)_{y=(-h+H)^-} = (\psi)_{y=(-h+H)^+}, \left(\frac{d\psi}{dy}\right)_{y=(-h+H)^-} = \left(\frac{d\psi}{dy}\right)_{y=(-h+H)^+}, \left(\frac{d\psi}{dy}\right)_{y=-\mathrm{h}} = 0, (\psi)_{y=0} = 0. \tag{5.14}$$

5.2.2. Liquid Transport in PE brush Grafted Nanochannels

We apply a pressure gradient along the length of the nanochannel to drive the flow. The flow is assumed to be steady, fully developed, and one-dimensional. Due to the pressure driven flow, there is a downstream advection of the charged mobile ions present within the EDL, which in turn results in the generation of a streaming current i_s and a streaming electric field E_s. The velocity profile for the bottom half of the nanochannel (due to the pressure driven flow described above) is governed by the following incompressible, steady-state Stokes equations:

$$\eta\frac{d^2u}{dy^2} - \frac{dp}{dx} + eE_s(n_+ - n_- + n_{H^+} - n_{OH^-}) - \frac{\eta}{\kappa_d}u = \quad 0(-h \le y \le -h + H_0),$$
$$\eta\frac{d^2u}{dy^2} - \frac{dp}{dx} + eE_s(n_+ - n_- + n_{H^+} - n_{OH^-}) = \qquad 0(-h + H_0 \le y \le 0).$$

(5.15)

In eq.(5.15), h is the nanochannel half-height, u is the velocity profile, η is the dynamic viscosity of the fluid, $-\frac{dp}{dx}$ the applied pressure gradient, E_s is the induced streaming electric field, $\kappa_d = a^2\left(\frac{H_0}{\sigma a^3 N\bar{\phi}}\right)^2$, and $\bar{\phi} = \frac{\phi H_0}{\sigma a^3 N}$ [$\bar{\phi}$ is the normalized monomer distribution profile and ϕ is the monomer distribution profile expressed through eq.(5.9) in our augmented SST formulation]. Eq.(5.15) can be expressed in non-dimensional form as:

$$\frac{d^2\overline{u}}{d\overline{y}^2} + 1 + \frac{\overline{E_s}}{2\overline{\lambda}_D^2}[\overline{n}_{+,\infty}\exp(-\overline{\psi}) - \overline{n}_{-,\infty}\exp(\overline{\psi}) + \overline{n}_{H^+,\infty}\exp(-\overline{\psi}) - \overline{n}_{OH^-,\infty}\exp(\overline{\psi})]$$

$$- (\frac{\sigma a^2 N\overline{\phi}}{\overline{H}_0})^2\overline{u} = 0 \qquad (-1 \le y \le -1 + \overline{H}_0),$$

$$\frac{d^2\overline{u}}{d\overline{y}^2} + 1 + \frac{\overline{E_s}}{2\overline{\lambda}_D^2}[\overline{n}_{+,\infty}\exp(-\overline{\psi}) - \overline{n}_{-,\infty}\exp(\overline{\psi}) + \overline{n}_{H^+,\infty}\exp(-\overline{\psi}) - \overline{n}_{OH^-,\infty}\exp(\overline{\psi})]$$

$$= 0 \qquad (-1 + \overline{H}_0 \le y \le 0).$$

(5.16)

In eq.(5.16), $\overline{\psi} = \frac{e\psi}{k_B T}, \overline{u} = \frac{u}{u_{p,0}}, \overline{E}_s = \frac{E_s}{E_0}, \overline{n}_{i,\infty} = \frac{n_{i,\infty}}{n_\infty}(i = \pm, H^+, OH^-), \overline{y} = \frac{y}{h}, \overline{H}_0 = \frac{H_0}{h}, \overline{\lambda}_D = \frac{\lambda_D}{h}$, where $u_{p,0} = \left(-\frac{dp}{dx}\right)\frac{h^2}{\eta}$ is the pressure-driven velocity scale, $E_0 = \frac{e\eta u_{p,0}}{\epsilon_0\epsilon_r k_B T} = \left(-\frac{dp}{dx}\right)\frac{eh^2}{\epsilon_0\epsilon_r k_B T}$ is the scale for the electric field and $\lambda_D = \sqrt{\epsilon_0\epsilon_r k_B T/(2e^2 n_\infty)}$ ($n_\infty = n_{+,\infty}$) is the Debye screening length of the electric double layer (EDL) based solely on the electrolyte concentration. Of course, λ_D approaches

the effective Debye screening length (due to all mobile ions) $\lambda_{D,eff} = \sqrt{\epsilon_0 \epsilon_r k_B T/[2e^2(n_\infty + n_{H^+,\infty})]}$ for large values of pH∞.

The velocity field is solved under the following boundary conditions:

$$(\overline{u})_{\overline{y}=-1} = 0, \left(\frac{d\overline{u}}{d\overline{y}}\right)_{\overline{y}=0} = 0, (\overline{u})_{\overline{y}=(-1+\overline{H}_0)^-} = (\overline{u})_{\overline{y}=(-1+\overline{H}_0)^+}, \left(\frac{d\overline{u}}{d\overline{y}}\right)_{\overline{y}=(-1+\overline{H}_0)^-} = \left(\frac{d\overline{u}}{d\overline{y}}\right)_{\overline{y}=(-1+\overline{H}_0)^+}. \tag{5.17}$$

The net ionic current through the nanochannel is zero since there is no applied external voltage. This leads to

$$2e\int_{-h}^{0}(u_+ n_+ - u_- n_- + u_{H^+} n_{H^+} - u_{OH^-} n_{OH^-})dy = 0, \tag{5.18}$$

where u_i $(i = \pm, H^+, OH^-)$ are the ion migration velocities expressed as:

$$u_i = u + \frac{e z_i E_s}{f_i}. \tag{5.19}$$

In eq.(5.19), f_i is the friction coefficient (the inverse of ionic mobility) for species i $(i = \pm, H^+, OH^-)$. Eq. (5.18) can be simplified in the presence of eqs.(5.6, 5.7, 5.8) and (5.19) to yield an expression for the non-dimensionalized streaming electric field as:

$$\overline{E}_s = \frac{\int_{-1}^{0} \overline{u}\,[-\overline{n}_{+,\infty}\exp(-\overline{\psi}) + \overline{n}_{-,\infty}\exp(\overline{\psi}) - \overline{n}_{H^+,\infty}\exp(-\overline{\psi}) + \overline{n}_{OH^-,\infty}\exp(\overline{\psi})]d\overline{y}}{\int_{-1}^{0} \overline{u}\,[R_+\overline{n}_{+,\infty}\exp(-\overline{\psi}) + R_-\overline{n}_{-,\infty}\exp(\overline{\psi}) + R_{H^+}\overline{n}_{H^+,\infty}\exp(-\overline{\psi}) + R_{OH^-}\overline{n}_{OH^-,\infty}\exp(\overline{\psi})]d\overline{y}},$$

(5.20)

where $R_i = \frac{e^2 z_i^2 \eta}{\epsilon_0 \epsilon_r k_B T f_i} (i = +, -, H^+, OH^-)$ is a dimensionless parameter, identified as the inverse of the ionic Peclet number. Substituting eq.(5.20) in eq.(5.16) we arrive at an integro-differential equation in u which is solved numerically. Having obtained u, the streaming electric field can be calculated from eq.(5.20). The downstream migration of mobile ions due to the flow also creates a streaming current (per unit width of the nanochannel) which can be expressed as:

$$i_s = 2e \int_{-h}^{0} u(n_+ - n_- + n_{H^+} - n_{OH^-})\, dy. \tag{5.21}$$

i_s can be calculated from the knowledge of the velocity field u. The knowledge of i_s and E_s allows us to express the net electrical power output (per unit area) as:

$$P_{out} = |\frac{1}{4} i_s E_s|. \tag{5.22}$$

On the other hand, the input power supplied (per unit area) to the system as a result of the applied pressure gradient is:

$$P_{in} = \left(-\frac{dp}{dx}\right) Q_{in}. \tag{5.23}$$

In eq.(5.23), Q_{in} is the volume flow rate (per unit width of the nanochannel) expressed as:

$$Q_{in} = 2 \int_{-h}^{0} u_{pp}\, dy, \tag{5.24}$$

where u_{pp} is the pure pressure velocity profile accounting for flow through the PE brush grafted nanochannel without the effects of the EDL body force on the ions. u_{pp} can be obtained by solving the following ODE's:

$$\eta\frac{d^2u_{pp}}{dy^2}-\frac{dp}{dx}-\frac{\eta}{\kappa_d}u_{pp}= \quad 0(-h\le y\le -h+H_0),$$
$$\eta\frac{d^2u_{pp}}{dy^2}-\frac{dp}{dx}= \qquad 0(-h+H_0\le y\le 0), \tag{5.25}$$

in presence of the following boundary conditions:

$$(u_{pp})_{y=-h}=0,\left(\frac{du_{pp}}{dy}\right)_{y=0}=0,(u_{pp})_{y=(-h+H_0)^-}$$
$$=(u_{pp})_{y=(-h+H_0)^+},\left(\frac{du_{pp}}{dy}\right)_{y=(-h+H_0)^-}=\left(\frac{du_{pp}}{dy}\right)_{y=(-h+H_0)^+} \tag{5.26}$$

Once P_{out} and P_{in} have been quantified, the corresponding electrochemomechanical energy conversion efficiency can be expressed as:

$$\xi=\frac{P_{out}}{P_{in}}$$
$$\Rightarrow\xi=\frac{[\int_{-1}^{0}\overline{u}\,[-\overline{n}_{+}\exp(-\overline{\psi})+\overline{n}_{-}\exp(\overline{\psi})-\overline{n}_{H^+,\infty}\exp(-\overline{\psi})+\overline{n}_{OH^-,\infty}\exp(\overline{\psi})]d\overline{y}]^2}{8\overline{\lambda}^2\int_{-1}^{0}\overline{u}_{pp}\,d\overline{y}\int_{-1}^{0}[\overline{n}_{+}\exp(-\overline{\psi})+\overline{n}_{-}\exp(\overline{\psi})+\overline{n}_{H^+,\infty}\exp(-\overline{\psi})+\overline{n}_{OH^-,\infty}\exp(\overline{\psi})]d\overline{y}}, \tag{5.27}$$

where $\bar{u}_{pp}=\frac{u_{pp}}{u_{p,0}}$ is the non-dimensional pure pressure-driven velocity field.

5.3. Results

We consider four different cases in this study - Case 1: Nanochannels grafted with short loose brushes (N = 400, ℓ = 60 nm), Case 2: Brush-free nanochannels with an

equivalent surface charge density ($\sigma_{c,eq}$) of short loose brushes (this equivalent charge density is the charge density obtained by integrating the volume charge density of the brushes along its length, i.e., $\sigma_{c,eq} = -e\int_{-h}^{-h+H_0} \phi n_{A^-} dy$), Case 3: Nanochannels grafted with dense brushes (N = 400, ℓ = 10 nm) and Case 4: Brush-free nanochannels with an equivalent charge density of long dense brushes. The cases 1 and 2 are studied for different values of salt concentration (c_∞), pH_∞, and γ, while the cases 3 and 4 are studied for different values c_∞ and for a given pH_∞. We refrain from reporting the results for larger pH_∞ for cases 3 and 4, since for such a pH_∞, the brush height for case 3 became much large than the chosen half height value (100 nm) of the nanochannel.

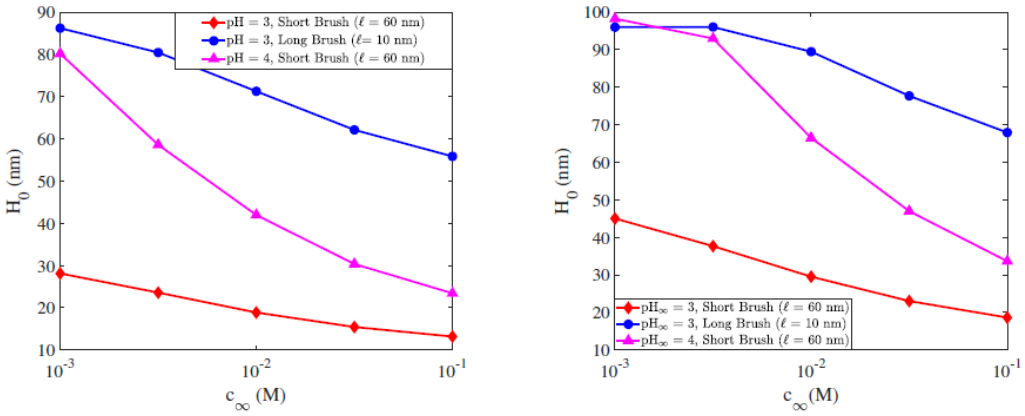

(a) γa^3=0.5 (b) γa^3=1

Figure 5.2: *Variation of equilibrium brush height H_0 with bulk salt concentration c_∞ and pH_∞ for pH-responsive, PE brush grafted nanochannels with (a) γa^3 = 0.5 and (b) γa^3 = 1. Here N = 400, h = 100 nm, a = 1 nm (Kuhn length), k_B = 1.38 x 10^{-23} JK^{-1}, T = 298 K, e = 1.6 x 10^{-19} C (electronic charge), ϵ_0 = 8.8 x 10^{-12} F m^{-1} (permittivity of free space), ϵ_r = 79.8 (relative permittivity of water), pK_a = 3.5, ν = 0.5, ω = 0.1. pK_w =14, pOH_∞ = pK_w - pH_∞, $c_{+,\infty} = c_\infty$, $c_{H^+,\infty} = 10^{-pH_\infty}$, $c_{OH^-,\infty} = 10^{-pOH_\infty}$, $c_{-,\infty} = c_\infty + c_{H^+,\infty} + c_{OH^-,\infty}$.*

Fig. 5.2 provides the variation of the brush height for the loosely grafted (ℓ = 60 nm) and densely grafted (ℓ = 10 nm) PE brushes as a function of the salt concentration, pH_∞, and values. For a given pH_∞ and, an increase in the salt concentration decreases the brush height [see Figs. 5.2(a,b)]. A larger salt concentration leads to a smaller EDL screening length; accordingly, the brush inter-segmental repulsion gets screened over a much smaller distance enforcing a much weaker repulsion-driven stretching of the PE brushes and a much smaller value of H_0. On the other hand, a larger pH_∞ signals a weaker bulk concentration of the H^+ ions, which will enforce a stronger ionization of the PE brushes as this ionization produces H^+ ions. Of course, a stronger ionization leads to a larger charge on the PE brush facilitating a larger inter-segmental repulsion induced enhanced value of the brush height H_0. Finally, a larger value of γ[results are shown in Fig. 5.2(b)] will signify a larger charge on the brush segments and accordingly, a larger electrostatic-repulsion mediated enhanced brush height for a given value of salt concentration and pH_∞.

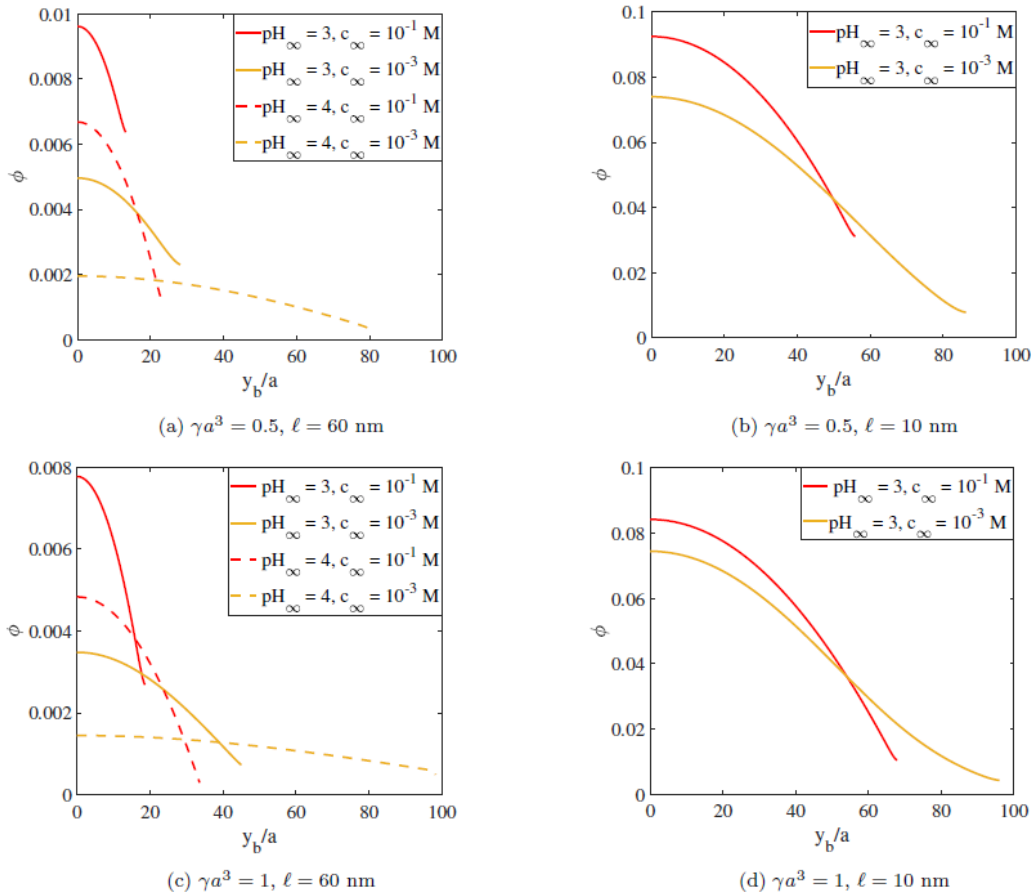

Figure 5.3: *Variation of monomer distribution profile ϕ with bulk salt concentration c_∞ and pH_∞ for pH-responsive, PE brush grafted nanochannels with (a) $\gamma a^3 = 0.5$, ℓ = 60 nm, (b) $\gamma a^3 = 0{:}5$, ℓ = 10 nm, (c) $\gamma a^3 = 1$, ℓ = 60 nm and (d) $\gamma a^3 = 1$, ℓ = 10 nm. All the other parameters are same as those used in Fig. 5.2.*

Fig. 5.3 provides the variation of the monomer distribution ϕ. Shorter brush height implies that the monomers are more densely packed near the grafting wall. Accordingly, for a given grafting density (i.e., a given value of ℓ), we find a larger value of near the wall for the cases of smaller pH_∞ (effect of the variation of pH_∞ is shown for weakly grafted brushes, i.e., ℓ = 60 nm) [see Figs. 5.3(a,c)] and larger salt concentration [see Figs. 5.3(a-d)]. Also, the smaller brush height for these cases (smaller pH_∞ and larger salt concentration) ensures that the profile no longer exists at larger distances away from the grafting wall. A larger grafting density (or smaller ℓ) ensures a larger value of at a given y since $\phi \sim \sigma$ (see eq.(5.3)) [compare Fig. 5.3(a) with Fig. 5.3(b) and Fig. 5.3(c) with Fig. 5.3(d)]. Finally, a larger value of γ leads to a larger brush height, which ensures, for a given pH_∞, c_∞, and grafting density, a weaker value of the monomer density at near-wall locations and the existence of the ϕ profile over larger distances away from the wall [compare Fig. 5.3(a) with Fig. 5.3(c) and Fig. 5.3(b) with Fig. 5.3(d)].

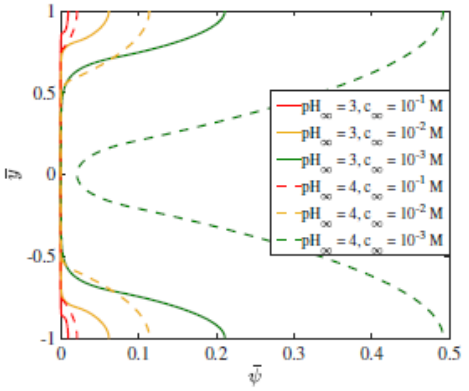

(a) $\gamma a^3 = 0.5$, $\ell = 60$ nm

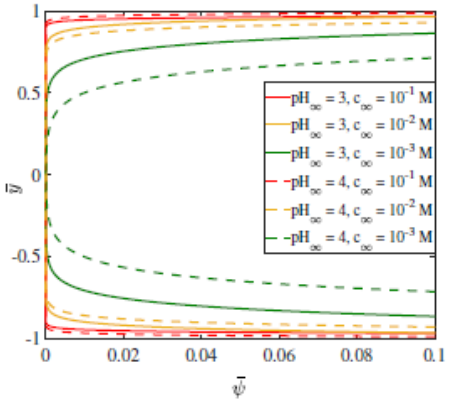

(b) $\gamma a^3 = 0.5$, No Brush ($\ell = 60$ nm)

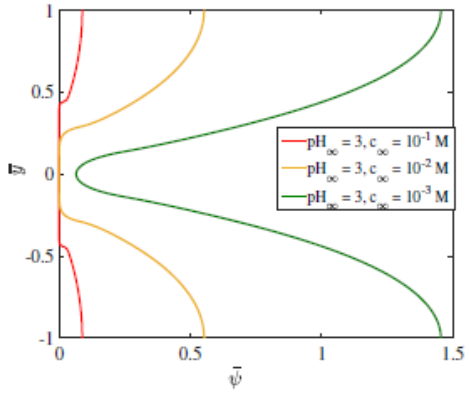

(c) $\gamma a^3 = 0.5$, $\ell = 10$ nm

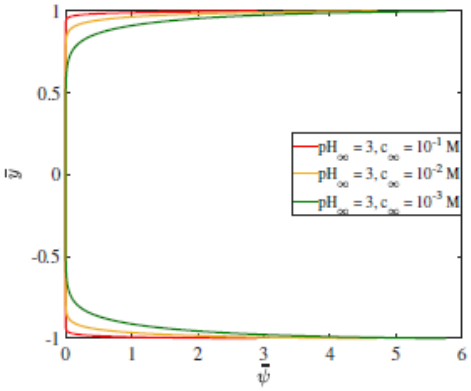

(d) $\gamma a^3 = 0.5$, No Brush ($\ell = 10$ nm)

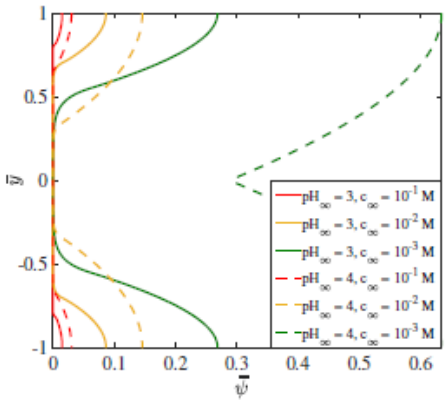

(e) $\gamma a^3 = 1$, $\ell = 60$ nm

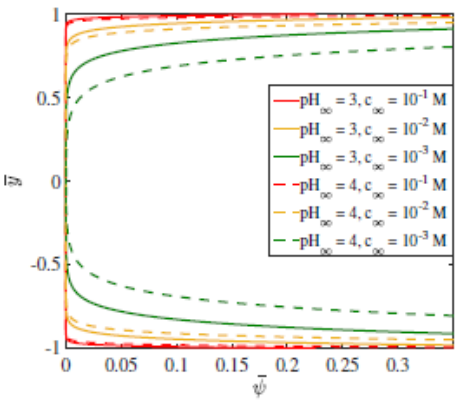

(f) $\gamma a^3 = 1$, No Brush ($\ell = 60$ nm)

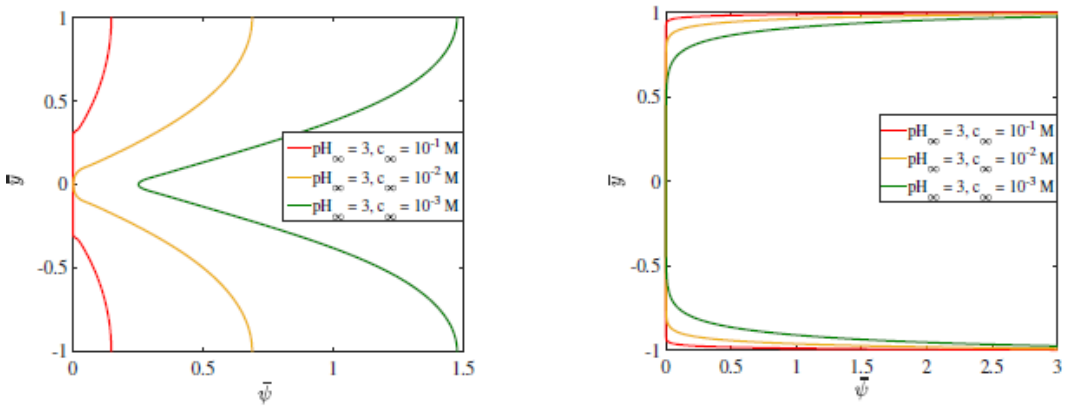

(g) $\gamma a^3 = 1$, $\ell = 10$ nm (h) $\gamma a^3 = 1$, No Brush ($\ell = 10$ nm)

Figure 5.4: *Transverse variation of the non-dimensional EDL electrostatic potential with bulk salt concentration c_∞ and pH_∞ for (a) PE brush-grafted nanochannel with $\gamma a^3 = 0.5$, $\ell = 60$ nm, (b) brush-free nanochannel with equivalent charge density $\sigma_{c,eq}$ identical to that of the brush-grafted nanochannels with $\gamma a^3 = 0.5$ and $\ell = 60$ nm, (c) PE brush-grafted nanochannel with $\gamma a^3 = 0.5$, $\ell = 10$ nm, (d) brush-free nanochannel with equivalent charge density $\sigma_{c,eq}$ identical to that of the brush-grafted nanochannels with $\gamma a^3 = 0.5$ and $\ell = 10$ nm, (e) PE brush-grafted nanochannel with $\gamma a^3 = 1$, $\ell = 60$ nm, (f) brush-free nanochannel with equivalent charge density $\sigma_{c,eq}$ identical to that of the brush-grafted nanochannels with $\gamma a^3 = 1$ and $\ell = 60$ nm, (g) PE brush-grafted nanochannel with $\gamma a^3 = 1$, $\ell = 10$ nm and (h) brush-free nanochannel with equivalent charge density $\sigma_{c,eq}$ identical to that of the brush-grafted nanochannels with $\gamma a^3 = 1$ and $\ell = 10$ nm. All the parameters are same as those mentioned in Fig. 5.2.*

Fig. 5.4 provides the transverse variation of the dimensionless EDL electrostatic potential distribution ($\bar{\psi}$) within the nanochannel as a function of (i) the presence and the absence of the brushes, (ii) brushes with different grafting densities, (iii) different values of pH_∞ and c_∞, and (iv) different values of γ. First, we compare the cases of short (weak grafting density) and tall (large grafting density) brushes for a given pH_∞, c_∞, and γ value [i.e., we compare Fig. 5.4(a) with Fig. 5.4(c) and Fig. 5.4(e) with Fig. 5.4(g)]. For a given γ, a taller brush represents a larger charge content, which leads to a larger ψ at a given transverse location. Furthermore, a larger brush height implies that ψ exists at larger distances away from the grafting wall. For the case of a given grafting density, γ and c_∞, a smaller pH_∞ causes a weaker charge density of the brushes leading to a weaker value of $\bar{\psi}$. Of course, this effect of the variation in pH_∞ has been portrayed for the case of weak grafting density [see Figs. 5.4(a,e)]. Also, an increase in c_∞ for a given grafting density, pH_∞, and γ ensures a weaker ψ stemming from the fact that $\psi \sim \sigma_c \lambda_{D,eff}$ (where σ_c is the charge density of the PE brushes and $\lambda_{D,eff}$, which decreases with c_∞, is the EDL thickness). Also, an increase in γ increases the charge of the PE brushes, thereby increasing $\bar{\psi}$ [compare Fig. 5.4(a) with Fig. 5.4(e) and Fig. 5.4(c) with Fig. 5.4(g)]. The most interesting comparison for ψ is between the cases of brush-free and brush-grafted nanochannels [compare Fig. 5.4(a) with Fig. 5.4(b), Fig. 5.4(c) with Fig. 5.4(d), Fig. 5.4(e) with Fig. 5.4(f), and Fig. 5.4(g) with Fig. 5.4(h)]. *For the brush-free nanochannels, the EDL electrostatic potential is entirely localized at near-wall locations – larger c_∞ leading to smaller EDL thickness leads to an even larger localization. On the other hand, the presence of the charged brushes grafted on*

chargeless nanochannel walls ensure that this EDL electrostatic potential gets distributed along the length of the brushes and accordingly, $\bar{\psi}$ is no longer localized at the nanochannel wall. Such a scenario obviously leads to an EDL charge density that is localized away from the wall, which in turn will massively influence the overall electrohydrodynamics (as discussed later).

Fig. 5.5 demonstrates the velocity field in the nanochannel as a function of (i) the presence and the absence of the brushes, (ii) brushes with different grafting densities, (iii) different values of pH_∞ and c_∞, and (iv) different values of γ. Before describing the influence of these different parameters, it is critical to identify the different components of the velocity field. Firstly, the flow is being driven by an externally imposed pressure gradient. This flow is retarded by the additional drag imparted by the brushes. Secondly, this pressure-driven flow induces a streaming electric field that triggers an electroosmotic (EOS) transport that opposes the pressure-driven transport. This retarding EOS transport itself also experiences the retarding influences of the additional drag imparted by the presence of the brushes. *However, more importantly, the streaming electric field and the streaming current are favored by the presence of the brushes stemming from the fact that the brushes localizes the average EDL charge density away from the wall (evident from the significantly large ψ values away from the wall, which is not the case for brush-free nanochannels, see Fig. 5.4), which ensures that the liquid velocity with which the EDL ions gets advected downstream (this downstream advection of the EDL charge density gradient induces the streaming current and the streaming electric field, see Fig. 5.1 for a schematic illustration) is*

much larger as compared to the case of the brush free nanochannel. We first consider the effect of salt and pH_∞ for a given type of (brush-grafted or brush-free) nanochannel and a given γ. Decrease in salt concentration or an increase in pH_∞ increases ψ and therefore will increase the EDL charge density. An increase in this EDL charge density will increase the body force (which is proportional to this charge density) that drives the EOS transport. Hence the overall velocity decreases with an increase in pH_∞ and a decrease in salt concentration. Next, we compare the velocity fields for the brush-free and brush-grafted (weakly grafted) nanochannels [i.e., we compare Fig. 5.5(a) with Fig. 5.5(b) and Fig. 5.5(e) with Fig. 5.5(f)]. The presence of the brushes decreases the overall velocity due to the additional drag and also due to the enhanced streaming electric field due to the EDL charge density localization away from the wall. For the case of the weakly grafted brushes, the effect of the enhanced drag is rather weak; on the other hand, the effect of the enhanced streaming electric field and the consequent enhanced back EOS transport is larger. Accordingly, for cases where the streaming electric field is weak (results discussed later), i.e., for large c_∞ and small pH_∞, we do not find a significant difference between the flow fields for the cases of brush-free and brush-grafted nanochannels. However, for the case of large pH_∞ (=4) and small c_∞ (= 10^{-3} M), the large streaming electric field and the resultant large retarding EOS transport significantly reduces the overall velocity. On the other hand, if we compare the cases of brush-free and brush-grafted (larger grafting density, ℓ = 10 nm) nanochannels [i.e., we compare Fig. 5.5(c) with Fig. 5.5(d) and Fig. 5.5(g) with Fig. 5.5(h)], the enhanced brush-induced drag plays the dominant role causing a significant reduction in the velocity for the brush-grafted nanochannels. For the case of the larger

γ, a larger charge of the brush leading to a larger ψ and hence a larger streaming electric field causes an even more noticeable reduction in the velocity field for the case of nanochannels with weakly grafted brushes at large pH_∞ and small c_∞ [compare Fig. 5.5(a) with Fig. 5.5(e) and Fig. 5.5(c) with Fig. 5.5(g)].

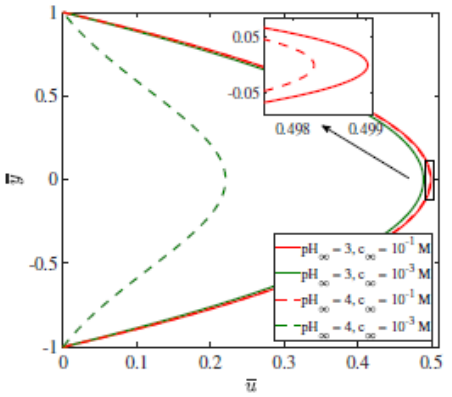

(a) $\gamma a^3 = 0.5$, $\ell = 60$ nm

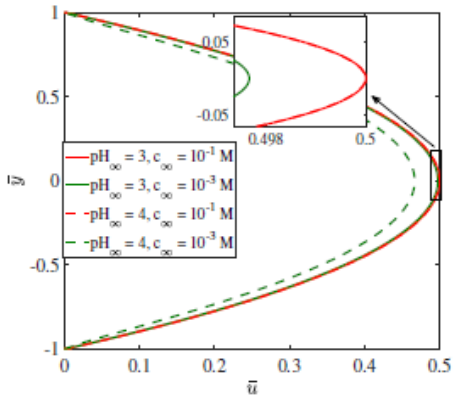

(b) $\gamma a^3 = 0.5$, No Brush ($\ell = 60$ nm)

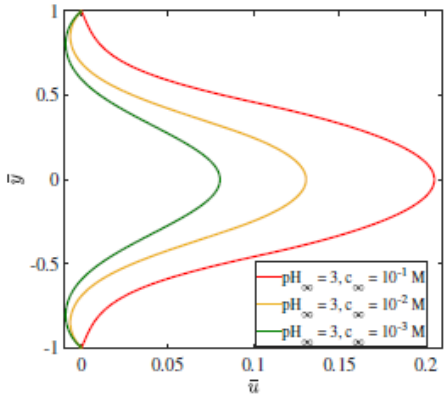

(c) $\gamma a^3 = 0.5$, $\ell = 10$ nm

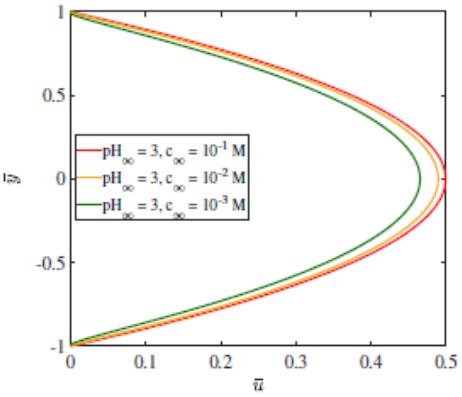

(d) $\gamma a^3 = 0.5$, No Brush ($\ell = 10$ nm)

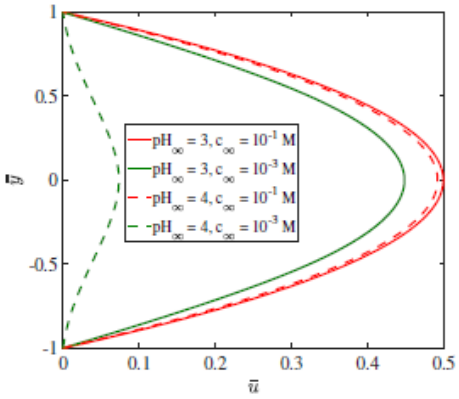

(e) $\gamma a^3 = 1$, $\ell = 60$ nm

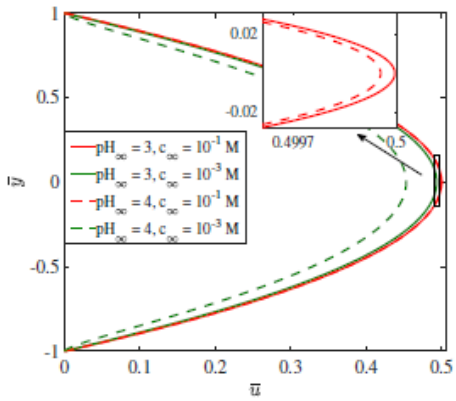

(f) $\gamma a^3 = 1$, No Brush ($\ell = 60$ nm)

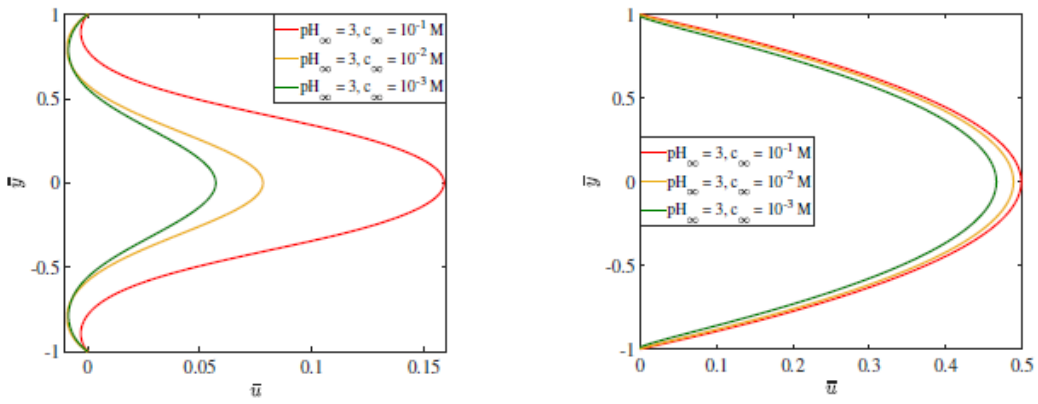

(g) $\gamma a^3 = 1$, $\ell = 10$ nm (h) $\gamma a^3 = 1$, No Brush ($\ell = 10$ nm)

Figure 5.5: *Transverse variation of the non-dimensional velocity profile u with bulk salt concentration c_∞ and pH_∞ for (a) PE brush-grafted nanochannel with $\gamma a^3 = 0.5$, $\ell = 60$ nm, (b) brush-free nanochannel with equivalent charge density $\sigma_{c,eq}$ identical to that of the brush-grafted nanochannels with $\gamma a^3 = 0.5$ and $\ell = 60$ nm, (c) PE brush-grafted nanochannel with $\gamma a^3 = 0.5$, $\ell = 10$ nm, (d) brush-free nanochannel with equivalent charge density $\sigma_{c,eq}$ identical to that of the brush-grafted nanochannels with $\gamma a^3 = 0.5$ and $\ell = 10$ nm, (e) PE brush-grafted nanochannel with $\gamma a^3 = 1$, $\ell = 60$ nm, (f) brush-free nanochannel with equivalent charge density $\sigma_{c,eq}$ identical to that of the brush-grafted nanochannels with $\gamma a^3 = 1$ and $\ell = 60$ nm, (g) PE brush-grafted nanochannel with $\gamma a^3 = 1$, $\ell = 10$ nm and (h) brush-free nanochannel with equivalent charge density $\sigma_{c,eq}$ identical to that of the brush-grafted nanochannels with $\gamma a^3 = 1$ and $\ell = 10$ nm. Here $R_i = 1$ ($i = +, -, H^+, OH^-$). All other parameters are same as those mentioned in Fig. 5.2.*

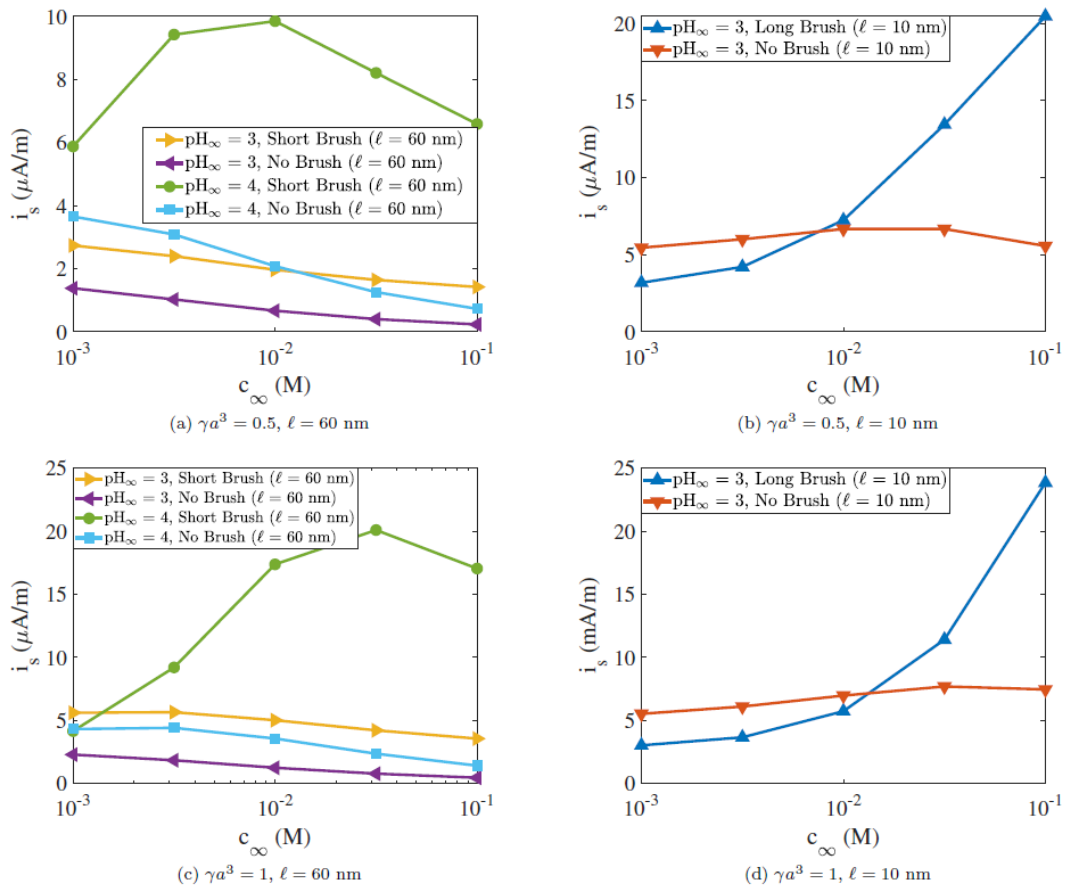

Figure 5.6: *Variation of streaming current is with bulk salt concentration c_∞ and pH_∞ for (a) brush-grafted nanochannels (with $\gamma a^3 = 0.5$, $\ell = 60$ nm) and brush-free nanochannels with equivalent charge density $\sigma_{c,eq}$ identical to that of the brush-grafted nanochannels with $\gamma a^3 = 0{:}5$ and $\ell = 60$ nm, (b) brush-grafted nanochannels (with $\gamma a^3 = 0.5$, $\ell = 10$ nm) and brush-free nanochannels with equivalent charge density $\sigma_{c,eq}$ identical to that of the brush-grafted nanochannels with $\gamma a^3 = 0.5$ and $\ell = 10$ nm, (c) brush-grafted nanochannels (with $\gamma a^3 = 1$, $\ell = 60$ nm) and brush-free nanochannels with equivalent charge density $\sigma_{c,eq}$ identical to that of the brush-grafted nanochannels with $\gamma a^3 = 1$ and $\ell = 60$ nm and (d) brush-grafted nanochannels (with $\gamma a^3 = 1$, $\ell = 10$ nm) and brush-free nanochannels with equivalent charge density $\sigma_{c,eq}$ identical to that of the brush-grafted nanochannels with $\gamma a^3 = 1$*

and ℓ = 10 nm. Here = 8.9 x 10^{-4} Pa.s, dp/dx = -5 x 10^{8} Pa/m. All other parameters are identical to those used in Fig. 5.5.

We next consider the different height-averaged quantities, namely the streaming current (i_s), streaming electric field (E_s), power output (P_{out}) and the overall energy conversion efficiency (ξ). Fig. 5.6 provides the variation of the streaming current for the same set of parameters for which the other variables have been considered. The streaming current is induced by the downstream advection of the EDL charge density (or the EDL ions). Thus, either an increase in the EDL charge density or an increase in the strength of the driving liquid flow will increase i_s. For a given nanochannel (brush-grafted or brush-free), an increase in pH_∞ or a decrease in salt concentration typically increases i_s, which can be directly attributed to a corresponding increase in ψ and hence the EDL charge density at such pH_∞ and c_∞ values. Let us now consider the case of brush-free and brush-grafted (short brushes or weakly grafted brushes) nanochannels [see Figs. 5.6(a,c)]. For such weak grafting densities, the brush-induced drag is not significant (as evidenced from the velocity profiles in Fig. 5.5). On the other hand, the effect of the brush induced localization of the EDL charge density away from the wall, which enforces the EDL charge density (or the EDL mobile ions) to be advected by a larger non-near-wall velocity, is significant. As a result, for a given pH_∞ and c_∞, i_s for the weakly brush-grafted nanochannel is always larger than the brush-free nanochannels. The most intriguing result is the comparison of i_s for brush-free and brush-grafted (strongly grafted) nanochannels [see Figs. 5.6(b,d)]. We find that for a weaker salt concentration, i_s is larger for the brush-free nanochannels, while for the

larger salt concentration i_s is much larger for the brush-grafted nanochannels. At a small c_∞, i_s is primarily dictated by the magnitude of the background flow velocity. Consequently, the extremely small (due to the combined influence of the drag from the brushes and the streaming electric field induced retarding EOS transport) value of the background velocity for the brush-grafted nanochannels ensures a weakened i_s despite the EDL charge localization away from the nanochannel wall. On the other hand, the significant increase in the background velocity with an increase in the salt concentration for the case of nanochannels with densely grafted brushes (see Fig. 5.5) ensures that the effect of localization of the charge density away from the nanochannel wall becomes severely strong. Accordingly, at a large salt concentration i_s is much larger for the nanochannels with densely grafted brushes in comparison to the brush-free nanochannels. In fact, this also explains why i_s for the nanochannels with densely grafted brushes shows a massive increase with an increase in c_∞. Interestingly, the large increase in the velocity with an increase in salt concentration (from 10^{-3} M to 10^{-2} M) at a large pH_∞ (=4) for nanochannels with weakly grafted brushes [see Figs. 5.5(a,e)] gets reflected as a corresponding increase in i_s for nanochannels with weakly grafted brushes at this pH_∞ and salt concentrations [see Figs. 5.6(a,c)]. However, as the salt concentration is increased further, velocity increases much less so that the effect of reduced ψ and charge density becomes important leading to a decrease in i_s. This explains the highly non-intuitive and non-monotonic variation of i_s with c_∞ for nanochannels with weakly grafted brushes at this pH_∞ =4. Very similar trends are noted for the case of larger γ [compare Fig. 5.6(a) with Fig. 5.6(c) and Fig. 5.6(b) with Fig.

5.6(d)], although for larger γ for most of the cases, i_s is larger due to a larger charge density of the brushes that lead to a larger ψ and a larger EDL charge density.

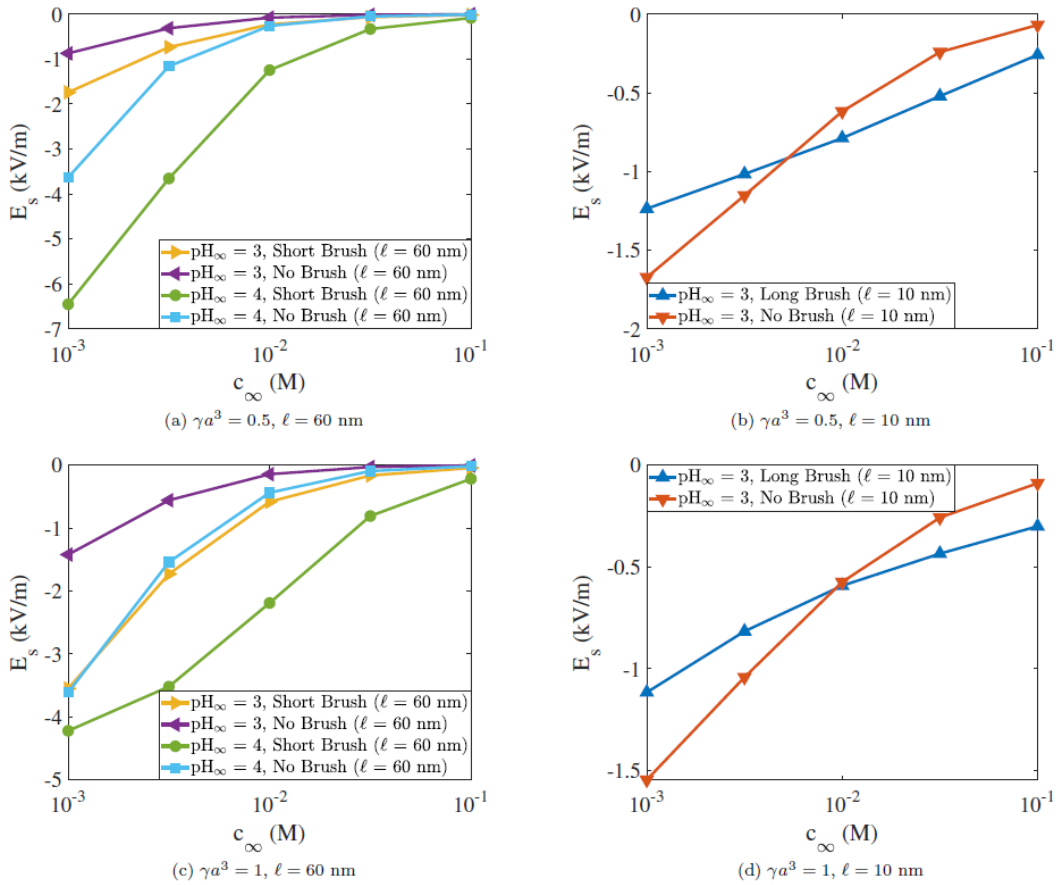

(a) $\gamma a^3 = 0.5$, $\ell = 60$ nm (b) $\gamma a^3 = 0.5$, $\ell = 10$ nm

(c) $\gamma a^3 = 1$, $\ell = 60$ nm (d) $\gamma a^3 = 1$, $\ell = 10$ nm

Figure 5.7: *Variation of streaming electric field E_s with bulk salt concentration c_∞ and pH_∞ for (a) brush-grafted nanochannels (with $\gamma a^3 = 0{:}5$, $\ell = 60$ nm) and brush-free nanochannels with equivalent charge density $\sigma_{c,eq}$ identical to that of the brush-grafted nanochannels with $\gamma a^3 = 0.5$ and $\ell = 60$ nm, (b) brush-grafted nanochannels (with $\gamma a^3 = 0.5$, $\ell = 10$ nm) and brush-free nanochannels with equivalent charge density $\sigma_{c,eq}$ identical to that of the brush-grafted nanochannels with $\gamma a^3 = 0{:}5$ and $\ell = 10$ nm, (c) brush-grafted nanochannels (with $\gamma a^3 = 1$, $\ell = 60$ nm) and brush-free nanochannels with equivalent charge density $\sigma_{c,eq}$ identical to that of the brush-*

grafted nanochannels with $\gamma a^3 = 1$ and $\ell = 60$ nm and (d) brush-grafted nanochannels (with $\gamma a^3 = 1$, $\ell = 10$ nm) and brush-free nanochannels with equivalent charge density $\sigma_{c,eq}$ identical to that of the brush-grafted nanochannels with $\gamma a^3 = 1$ and $\ell = 10$ nm. All other parameters are identical to those used in Fig. 5.6.

Fig. 5.7 shows the variation of the streaming electric field E_s, which can be related to i_s as $E_s \propto i_s/\Gamma$ [1] where Γ is the ionic conductivity that is proportional to the sum of the local concentration of the ions. Accordingly, the variation of E_s with the different parameters show mostly a similar trend as the corresponding variation of i_s, except for the variation with c_∞. As $\Gamma \sim c_\infty$, i.e., $E_s \sim 1/c_\infty$ (for a given i_s), E_s invariably decreases monotonically with an increase in c_∞. This is in contrast to the variation of i_s, which does not show a definite trend with respect to c_∞ (see Fig. 5.6). On the other hand, when we compare E_s for the cases of brush-free and brush-grafted (weakly grafted) nanochannels [see Figs. 5.7(a,c)], we invariably find that for a given value of c_∞ and pH_∞, E_s for the brush-grafted nanochannels is significantly more than that of the brush-free nanochannels. This behavior stems directly from the corresponding variation of i_s. As c_∞, i.e., $\Gamma \sim c_\infty$, i.e., $E_s \sim 1/c_\infty$ (for a given i_s), this difference in E_s between the cases of brush-free and brush-grafted nanochannels gets much more magnified at smaller c_∞. We next compare the cases of brush-free and brush-grafted (strongly grafted) nanochannels [see Figs. 5.7(b,d)]. Very much like the variation of i_s, here too we find that E_s is smaller (larger) for the brush-grafted nanochannels in comparison to the brush-free nanochannels for smaller (larger) c_∞ values. An interesting observation here is that, unlike the comparison between the brush-free and brush-grafted (weakly grafted) nanochannels, the streaming potential is not significantly large at small c_∞

despite the fact that $E_s \sim 1/c_\infty$ (for a given i_s). For the present case of brush-free and brush-grafted (strongly grafted) nanochannels, the magnitude of $\bar{\psi}$ is much higher leading to a much larger values of counterion concentration (c_+ or equivalently n_+) for a given value of c_∞. This ensures that $\Gamma \sim c_\infty \exp(-\bar{\psi})$ is not lowered significantly even at small c_∞ and hence E_s is not massively enhanced. Finally, in Fig. 5.7c and 5.7d we study the effect of increasing γ on E_s. Increase in γ increases i_s, but at the same time also increases ψ that leads to an increase in Γ. Therefore, the change in E_s with this increase in Γ is dictated by this competitive interplay of an increase in i_s and Γ. Accordingly, for some parameter combination E_s increases with γ, while for other it decreases with an increase in γ. Of course, the overall trend with respect to other variables (i.e., c_∞, pH_∞, presence or absence of the brushes, grafting density of the brushes, etc.) remain unchanged with an increase in γ. Fig. 5.7 is a key finding of this chapter. Streaming electric field (E_s) has been considered as a key measure of induced electrokinetic effects in charged nanochannels. *Fig. 5.7 establishes that the presence of the brushes can significantly enhance E_s by localizing the EDL charge density away from the nanochannel walls and this enhancement can be witnessed across a wide range of salt concentration, pH, and grafting density values.*

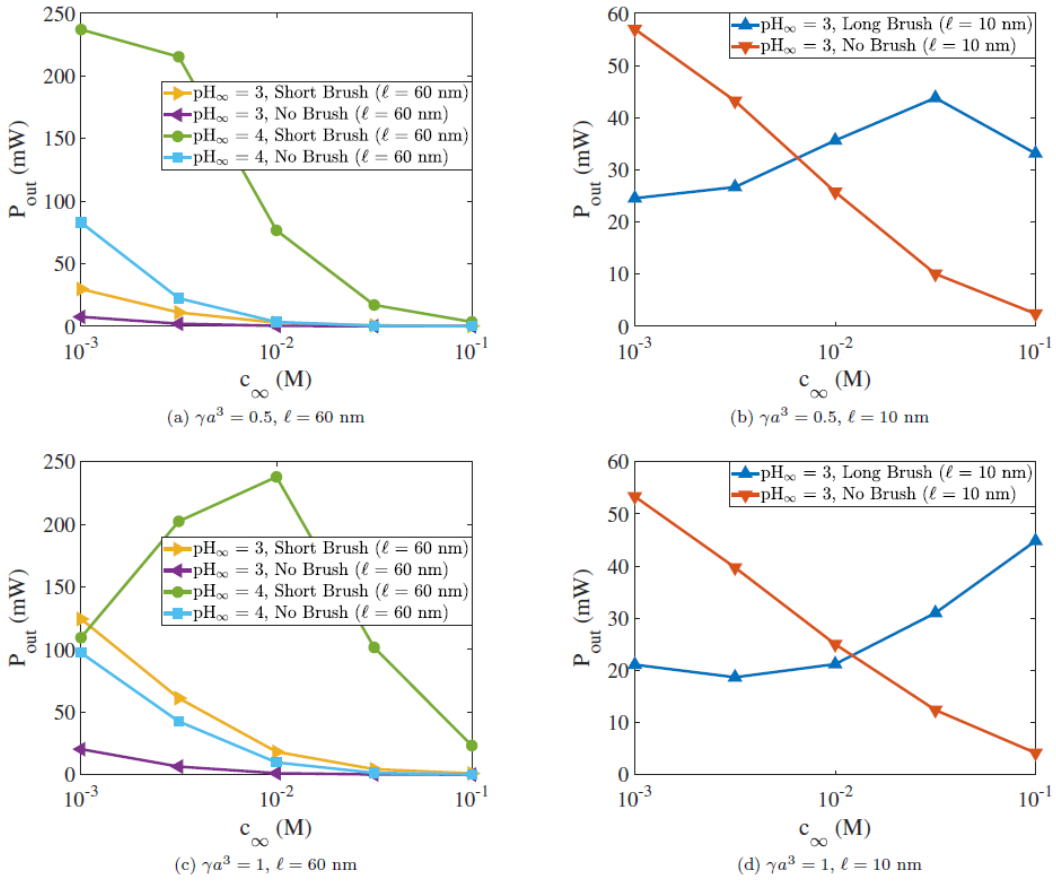

Figure. 5.8: *Variation of net power output P_{out} with bulk salt concentration c_∞ and pH_∞ for (a) brush-grafted nanochannels (with $\gamma a^3 = 0.5$, $\ell = 60$ nm) and brush-free nanochannels with equivalent charge density $\sigma_{c,eq}$ identical to that of the brush-grafted nanochannels with $\gamma a^3 = 0{:}5$ and $\ell = 60$ nm, (b) brush-grafted nanochannels (with $\gamma a^3 = 0.5$, $\ell = 10$ nm) and brush-free nanochannels with equivalent charge density $\sigma_{c,eq}$ identical to that of the brush-grafted nanochannels with $\gamma a^3 = 0.5$ and $\ell = 10$ nm, (c) brush-grafted nanochannels (with $\gamma a^3 = 1$, $\ell = 60$ nm) and brush-free nanochannels with equivalent charge density $\sigma_{c,eq}$ identical to that of the brush-grafted nanochannels with $\gamma a^3 = 1$ and $\ell = 60$ nm and (d) brush-grafted nanochannels (with $\gamma a^3 = 1$, $\ell = 10$ nm) and brush-free nanochannels with equivalent charge density $\sigma_{c,eq}$ identical to that of the brush-grafted nanochannels with $\gamma a^3 = 1$ and $\ell = 10$ nm. A microchip (with dimensions of 1mm x 10cm x 10cm and a porosity of 0.5) containing multiple nanochannels of half-height h = 100 nm is considered for*

the calculation of output power[1]. All other parameters are identical to those used in Fig. 5.6.

Fig. 5.8 shows the variation of the electrokinetically induced output electrical power P_{out} which is proportional to the product of i_s and E_s. Accordingly, P_{out} is invariably larger for the brush-grafted (weakly grafted) nanochannels as compared to the brush-free nanochannels for any given value of c_∞ and pH_∞ [see Figs. 5.8(a,c)], since both i_s and E_s are larger for these parameters for the brush-grafted (weakly grafted) nanochannel. On the other hand, P_{out} is smaller (larger) for brush-grafted (strongly grafted) nanochannel as compared to brush-free nanochannels for smaller (larger) salt concentration, stemming from the exact similar variation for i_s and E_s. The variation of P_{out} with c_∞ for a given type of nanochannel (brush-free or brush-grafted) for a given pH_∞ and γ becomes interesting since it depends on the relative variation of i_s and E_s with c_∞. Except for the case of nanochannels with densely grafted brushes and nanochannels with weakly grafted brushes for large pH_∞ and large γ, the decrease in E_s and i_s (typically) with c_∞ ensures a decrease in P_{out} with c_∞. For the nanochannels with densely grafted brushes, different trends are observed for different values of γ. For larger (smaller) γ, the significant increase (decrease) in i_s (E_s) becomes the dominant factor at large c_∞ leading to an increase (decrease) in P_{out} for c_∞ ranging from 10^{-2} M to 10^{-1} M [see Figs. 5.8(b,d)]. Finally, for nanochannels with weakly grafted brushes and large pH_∞ and large γ, the dominant role of i_s for small c_∞ values ensures that P_{out} increases with c_∞ for c_∞ ranging from 10^{-3} M to 10^{-2} M, while the overwhelming

influence of E_s for large c_∞ values ensure a decrease in P_{out} with c_∞ for c_∞ ranging from 10^{-2} M to 10^{-1} M [see Figs. 5.8(a,c)].

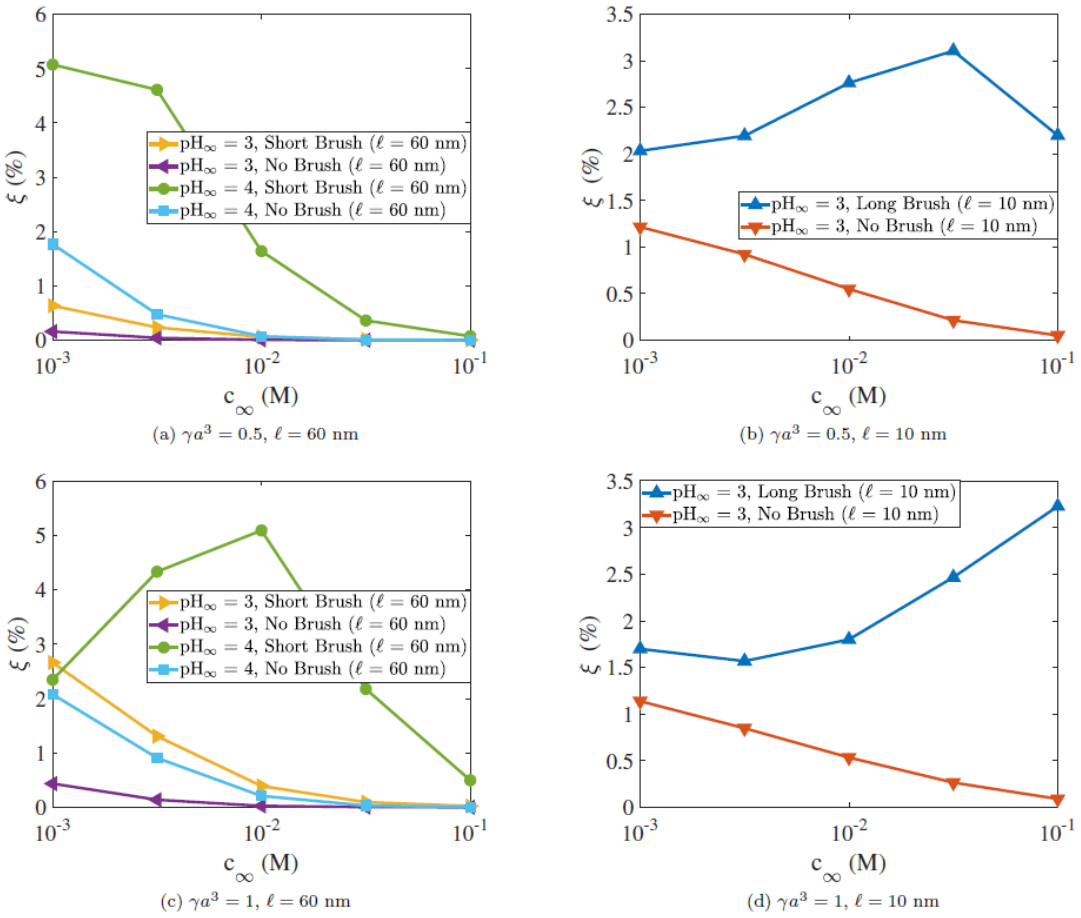

Figure 5.9: *Variation of electrokinetic energy efficiency ξ with bulk salt concentration c_∞ and pH_∞ for (a) brush-grafted nanochannels (with $\gamma a^3 = 0.5$, $\ell = 60$ nm) and brush-free nanochannels with equivalent charge density $\sigma_{c,eq}$ identical to that of the brush-grafted nanochannels with $\gamma a^3 = 0.5$ and $\ell = 60$ nm, (b) brush-grafted nanochannels (with $\gamma a^3 = 0.5$, $\ell = 10$ nm) and brush-free nanochannels with equivalent charge density $\sigma_{c,eq}$ identical to that of the brush-grafted nanochannels with $\gamma a^3 = 0.5$ and $\ell = 10$ nm, (c) brush-grafted nanochannels (with $\gamma a^3 = 1$, $\ell = 60$ nm) and brush-free nanochannels with equivalent charge density $\sigma_{c,eq}$ identical to that of the brush-grafted nanochannels with $\gamma a^3 = 1$ and $\ell = 60$ nm and (d) brush-*

grafted nanochannels (with $\gamma a^3 = 1$, $\ell = 10$ nm) and brush-free nanochannels with equivalent charge density $\sigma_{c,eq}$ identical to that of the brush-grafted nanochannels with $\gamma a^3 = 1$ and $\ell = 10$ nm. All other parameters are identical to those used in Fig. 5.6.

Finally, Fig. 5.9 shows the variation of the efficiency (ξ) of the electrokinetic energy conversion, which refers to this generation of the electrical energy from a combined mechanical energy (associated with the pressure driven flow) and chemical energy (associated with the EDL). ξ is proportional to P_{out}. Therefore, ξ is much larger for the brush-grafted nanochannels (weakly grafted) as compared to the brush-free nanochannels for any given value of pH_∞, c_∞, and γ [see Figs. 5.9(a,c)]. Also, for small γ, the nanochannel with weakly grafted brushes demonstrate a monotonic decrease in ξ with c_∞ for all pH_∞. However, for larger γ at a large pH_∞, ξ, very much like P_{out} is non-monotonic with c_∞ for nanochannels with weakly-grafted PE brushes [see Fig. 5.9(c)]. A much more interesting situation arises when we compare the cases of brush-free nanochannels and brush-grafted (densely grafted) nanochannels [see Figs. 5.9(b,d)]. Here too ξ for the brush-grafted nanochannels is always larger than the brush-free nanochannels (i.e., for any given value of c_∞ and γ), despite the fact that P_{out} for the brush-grafted nanochannels is smaller than the brush-free nanochannels for small c_∞. This deviation in the trend between P_{out} and ξ for small c_∞ stems from the fact that $\xi = P_{out}/P_{in}$ and P_{in} is significantly reduced in presence of the densely-grafted brushes enforcing an enhancement of ξ even for the situation where P_{out} is reduced. It is also worthwhile to note that for nanochannels with weakly grafted brushes for relatively small c_∞ (~10^{-3} M), large pH_∞ and small γ, we get an extremely large conversion efficiency of 5%, which is several times larger than that obtained for the corresponding

brush-free nanochannels [see Fig. 5.9(a)]. On the other hand, for a larger γ, similar efficiency (5%) is obtained at an intermediate c_∞ (~10^{-2} M) for large pH_∞ for nanochannels with weakly grafted brushes [see Fig. 5.9(c)]. For the densely grafted brushes, the efficiency numbers are slightly smaller (~3%), although they are always larger than the corresponding brush-free nanochannels and also they are witnessed for intermediate c_∞ (~10^{-2} M) and large c_∞ (~10^{-1} M) values for small and large γ values [see Figs. 5.9(b,d)].

5.4. Conclusions

In this chapter, we describe the electrokinetic energy generation in a nanochannel grafted with pH-responsive PE brushes by modelling the PE brushes with our recently developed augmented SST model. Such advanced theoretical description of the PE brushes ensures that to the best of our knowledge this is the most advanced and rigorous description of electrokinetic transport in PE-brush-grafted nanochannels. Our results establish that the brushes localize the EDL charge density away from the nanochannel wall, enforcing the advection of this charge density or the EDL ions with a much large background liquid velocity. This advection is responsible for the generation of the streaming current and the streaming electric field. As a consequence, depending on salt concentration, pH, γ, and the grafting density of the brushes, there is a significant enhancement of the streaming current and streaming electric field. In fact, this enhancement is so pronounced that it leads to an energy conversion efficiency as large as 5% for a wide combination of system parameters and more importantly, this energy conversion for nanochannels functionalized with both weakly-grafted and strongly

grafted brushes can be several times larger than the corresponding brush-free nanochannels. In summary, the present chapter through an extremely rigorous and complete theoretical model shows the utility of functionalizing nanochannels with PE brushes for highly efficient electrokinetic energy conversion.

Chapter 6: Molecular Dynamics Simulations of Pressure-Driven Transport in Polyelectrolyte-Brush-Grafted Nanochannels

Abstract: *We conduct molecular dynamics (MD) simulations of water transport in polyelectrolyte (PE) brush-grafted nanochannels with a fully atomistic representation of the PE chains, mobile ions, and water molecules. Our atomistic framework helps capture highly non-trivial phenomenon such as the overscreening of the grafted PE layer, which signifies a higher number of counterions within the brushes than that needed for neutralizing the charges on the PE chains. Moreover, we show that there is a significant tilting of the PE chains due to the flow-induced drag forces, which considerably changes the configuration of the brushes as well as the distribution of mobile ions inside the nanochannel. From our MD simulations, we calculate the flow velocity profiles and nanoscale energy conversion characteristics such as the streaming current, streaming electric field, and electrical power output for two different values of applied pressure gradient. We show that the results of our all-atom MD simulations are in reasonable agreement to the predictions of our continuum calculations. The continuum calculations are only off by a factor of ~1.5-4 with respect to the quantities measured from the MD simulations. We attribute the discrepancy between the continuum predictions and MD results to the inability of the continuum models to capture the factors such as the flow-induced tilting of the brushes, overscreening of the grafted PE layer, and the hydrophilic interactions of the PE chains with the brush-trapped water molecules. Finally, we show that our results for the*

streaming conductance are within the range of values reported by a prior experimental study, thereby increasing our confidence in the feasibility of the numbers obtained from our system.

6.1. Introduction

Liquid flow in charged nanochannels, triggered by the application of an axial pressure gradient has been utilized as a method for nanoscale generation of electrical energy.[205-206] In such systems, the mechanical energy of the pressure-driven flow along with the chemical energy of the electric double layer (EDL) formed on the inner walls of the charged nanochannel is converted into an electrical power output. This mechanism is known as electrochemomechanical energy conversion. End-grafting of polyelectrolyte (PE) chains on flat and curved surfaces has been utilized in a wide variety of applications such as current rectification,[25-26] stabilization of emulsions,[5] nanoscale energy conversion,[1,113,166] drug delivery,[6-7] oil recovery,[8] etc. These end-grafted PE chains assume a "brush"-like conformation above a critical grafting density (number of chains per unit grafted area). It has been shown that decorating the walls of a nanochannel with a layer of PE brushes can enhance the electrical power output and the nanoscale energy conversion efficiency by shifting the location of the EDL away from the retarding effects of the nanochannel wall-induced drag force.[1,113,166] Moreover, the stimuli-responsiveness of the brushes to changes in environmental conditions such as the solvent quality, bulk salt concentration, pH, temperature, etc. provides a way to tune/optimize the energy conversion characteristics of the system.

Given the ability of PE brushes to enhance the energy conversion characteristics of nano systems, a number of studies have investigated pressure-driven liquid transport in PE brush-grafted nanochannels.[1,18,113,166] However, none of these studies has adopted a fully atomistic framework. Even though Ref. 18 has performed MD simulations of pressure-driven flow in PE brush-grafted nanochannels, they have considered a coarse-grained representation of the PE chains and water molecules. In this chapter, we report the first MD study to probe a pressure-driven flow in nanochannels grafted with backbone-charged PE brushes with an explicit atomistic treatment of the PE chains, water molecules (solvent), and mobile ions. We study the fully developed flow field and nanoscale energy conversion characteristics for two different values of the applied pressure gradient. Our simulations show that the brushes experience a significant tilt due to the flow-induced drag force, especially at high values of the imposed pressure gradient such as the ones used in this study. Our fully atomistic framework plays an instrumental role in capturing a highly complex phenomenon such as the overscreening of the grafted PE layer. Overscreening refers to a situation where a negatively (positively) charged PE brush layer is net positive (negative) due to the presence, inside the brush layer, of a larger number of counterions than needed for screening the charge of the PE brush layer. Also such overscreening results in a highly non-trivial distribution of the mobile ions inside the nanochannel with an excess of coions (relative to counterions) inside the brush-free bulk, and thereby significantly altering the nanoscale energy conversion characteristics. Most importantly, we evaluate several important quantities associated with the pressure-driven transport such as the flow velocity profile, streaming current, streaming electric field, and electrical power output

for different values of applied pressure gradients. We further go on to utilize our continuum framework[113,207] (Chapters 4 and 5) to generate predictions for the aforementioned properties calculated from the MD simulations. This helps us to provide a one-to-one comparison between the results of our MD simulations and the theoretical calculations. Fascinatingly, our continuum predictions for the volume flux, streaming current, and streaming electric field only differ from their MD counterparts by a factor of ~1.5-4. This highlights the ability of our continuum framework to capture the highly complex physics of liquid transport in PE brush-grafted nanochannels with considerable accuracy despite having numerous underlying simplifications. We also discuss several important factors that are responsible for the observed discrepancy in the predictions of the continuum models and the results of the all-atom MD simulations. Finally, we provide a brief comparison of our results for the streaming conductance with the values reported by a prior experimental study[19] on the pressure-driven transport of water in a charged nanochannel.

6.2. Simulation Details

Figure 6.1 depicts a snapshot of our MD simulation domain. Our simulation domain consists of a nanochannel (having a length, width, and height of 234.75 Å, 93.9 Å, and 120.4509 Å respectively) made of two parallel walls of explicitly resolved atoms. The walls consist of a single layer of discrete particles arranged in an FCC lattice with a lattice constant of 3.612 Å. 90 fully ionized polyacrylic acid (PAA) chains are end-grafted in an 18 x 5 array on each of the nanochannel walls. Each PAA chain consists

of exactly 49 backbone carbon atoms. The grafting density of the brushes was maintained at $0.05/\sigma^2$ [σ=3.5 Å is the Lennard Jones (LJ) distance parameter associated with the backbone carbon atoms of the PAA chains] by providing a lateral spacing of 15.65 Å between the grafted ends of adjacent PAA chains. The charges on the PAA chains are neutralized by adding 4320 Na^+ counterions to the system. SPC/E water molecules are added to the system and act as a "good' solvent for the brushes.[64] A salt concentration of 0.1 M was maintained inside the nanochannel by adding an adequate number of Na^+ - Cl^- ion pairs.

The PAA chains were modelled using the OPLS-AA force field.[96] The bonded (bonds, angles, dihedrals, and impropers) and non-bonded (partial charges and LJ parameters) interaction parameters for the various atom types associated with the PAA chains were taken from the OPLS-AA database and are provided in section 2.6 of chapter 2. The LJ parameters for the Na^+ and Cl^- ions were taken from the work of Joung and Cheatham (see Table 2.4).[98] Geometric mixing rules were followed to calculate the LJ interactions between dissimilar atom types. The only exceptions to this rule were the LJ interactions between oxygen atoms of water molecules and the mobile ions (Na^+ and Cl^-), as well as the LJ interactions between the Na^+ and Cl^- ions. These interactions followed the Lorentz-Berthelot mixing rules in accordance with Ref. 98. A shifted and truncated 12-6 Lennard Jones potential with a cutoff of 13 Å was used to model the short-ranged interactions between the atoms. The long-range coulombic interactions were modelled using a particle-particle particle-mesh (PPPM) solver.[97] Periodic boundary conditions were used in all directions. SHAKE algorithm[99] was used to fix the bonds and angles of the SPC/E water molecules.

Our initial configuration consisted of fully stretched PAA chains (configuration of minimum entropy). The Na^+ counterions and water molecules were distributed throughout the simulation domain, while the salt ion pairs were distributed randomly in the space outside the PAA chains. The system was first run in a NP_zT (the subscript z indicates that only the height of the simulation domain was allowed to change in order to maintain the pressure) ensemble to obtain the correct height of the nanochannel. The pressure and temperature of the system were maintained at 1 atm and 300 K respectively by using a Nosé -Hoover barostat and thermostat[92-93] (with time constants of 1 ps and 0.1 ps for pressure and temperature respectively). Subsequently, the system was equilibrated in the canonical (NVT) ensemble. This was done by using two separate Langevin thermostats[81] (with time constants of 0.1 ps) for the PAA chains and the mobile species (Na^+, Cl^-, and the water molecules). The average end-point brush height was carefully monitored to check for equilibration.

Following the equilibration of the PE brush system, a uniform pressure gradient was imposed by applying a constant force on the mobile species (oxygen atoms of the water molecules and the mobile ions). The magnitude of this applied force (F) was determined by $F = \frac{\nabla P}{\rho}$, where ρ is the average number density of the mobile species, and $\nabla P = \left|\frac{dp}{dx}\right|$ is the magnitude of the imposed pressure gradient in the axial direction.[208] Simulations were conducted for two different values of the pressure gradient, i.e., 1 MPa/nm and 2 MPa/nm. Proper care was taken to ensure that the thermostats do not affect the pressure-gradient-induced flow field. The Langevin thermostat (with a time constant of 0.1 ps) on the mobile species was only applied to

one-quarter of the nanochannel, and that too exclusively in the y and z directions. On the other hand, the Langevin thermostat on the PAA chains (with a time constant of 0.1 ps) was applied throughout the nanochannel and in all directions. In this way, the system was maintained at 300 K. The velocity profiles of the SPC/E water molecules (sampled from the three-quarters of the nanochannel where the mobile species were not thermostatted) as well as the average end-point height of the brushes were monitored for ensuring a fully developed flow field. The particle trajectories were integrated by using the Velocity Verlet algorithm with a time step of 2 fs. The atomic trajectories were dumped every 0.5 ps. All simulations were carried out on the MD package LAMMPS.[95] OVITO was used for visualization purposes.[100]

The equilibration and production run times for simulations with different applied pressure gradients are given in Table 6.1.

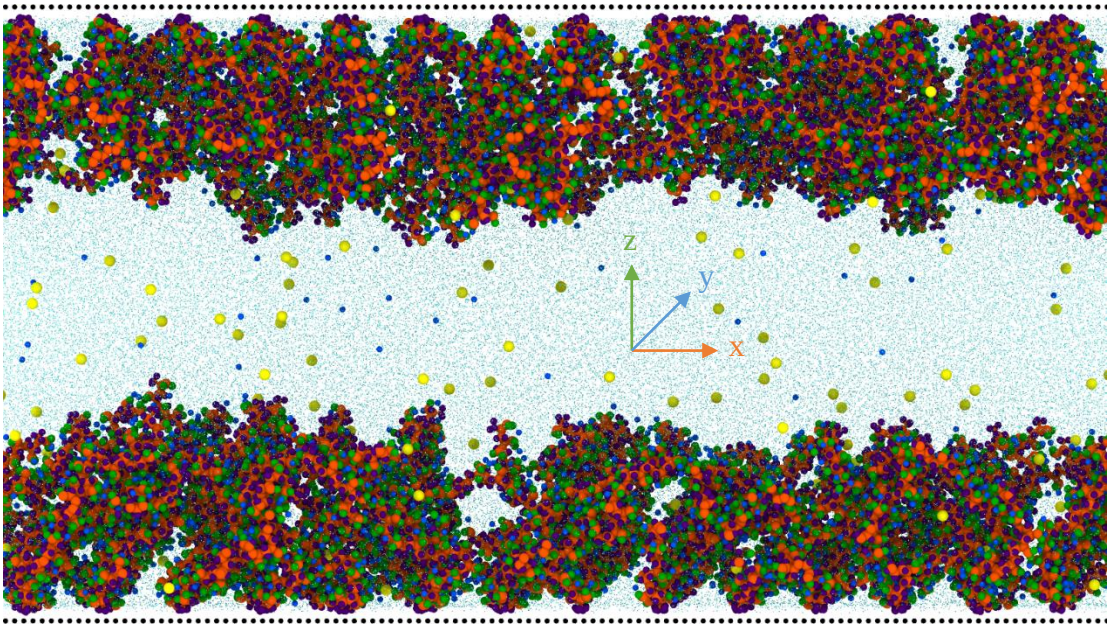

Figure 6.1: *Snapshot of the MD simulation domain for pressure-driven transport in PE-brush grafted nanochannel. Na^+ and Cl^- ions are depicted by blue and yellow spheres, respectively. The atoms forming the discrete walls at the top and bottom of the nanochannel are depicted as black spheres. All other colors represent the various atom types of the PAA chains. Water molecules are not shown explicitly for improved visualization.*

∇P (MPa/nm)	t_{equi} (ns)	t_{prod} (ns)
0	14.16	1.84
1	55	11.9
2	46	12

Table 6.1: *Equilibration time (t_{equi}) and production run time (t_{prod}) for different applied pressure gradients.*

6.3. Results

6.3.1. Flow-induced Tilting of the PE Brushes

Fig. 6.2(a) plots the average end-point brush height (H) inside the nanochannel for different magnitudes of applied pressure gradient. We can clearly observe a monotonic decrease in the brush height with an increase in the imposed pressure gradient. This is attributed to the flow-induced drag forces acting on the brushes, which leads to a tilting of the PE chains. Depending on the bending rigidity of the brushes, the angle of tilt can be significant at extremely high pressure gradients such as the ones used in our simulations. One way to visualize this tilt in the PE chains is by looking at the average chain conformation as a function of the applied pressure gradient. This is plotted in Fig. 6.2(b) in the form of a projection along the x-z plane (x, y, and z represent the directions along the length, width, and height of the nanochannel respectively; see Fig. 6.1). We can see that the chains are in an almost vertical configuration (no x-direction bias) when no axial pressure gradient is imposed. Upon the application of an external pressure gradient, the chains bend in the direction of flow, and the extent of deformation increases with the magnitude of applied pressure gradient. It is this bending of the PE chains that is ultimately responsible for the observed reduction in brush height in Fig. 6.2(a).

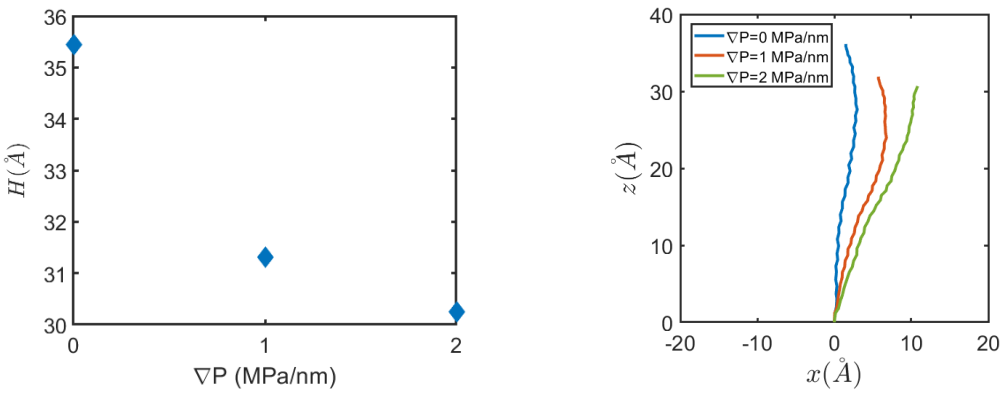

(a) (b)

Figure 6.2: *(a) Reduction in average end-point brush height (H) with applied axial pressure gradient, (b) average profile of the grafted PAA chains (projected on the x-z plane) as a function of the imposed pressure gradient. In (b), the grafted ends of the PAA chains are assumed to lie at the origin (with z=0 representing the grafting plane) and the flow occurs along the positive x-direction. The equilibrium end-point brush height and average chain profile for ∇P=0 MPa/nm were first obtained in Ref. 209.*

6.3.2. Overscreening of the Grafted PE Layer

Fig. 6.3 plots the transverse variation of the number densities (n) of Na^+ and Cl^- ions for various applied pressure gradients. We can observe that there is an abundance of Na^+ ions (relative to Cl^- ions) inside the grafted PE layers in order to neutralize the negative charges on the PE chains. However, as we move away from the PE brushes to the brush-free bulk (region near the center of the nanochannel that is outside the EDL created by the brushes), we observe that the number density of Cl^- coions becomes greater than that of the Na^+ counterions [see insets of Fig. 6.3(a-c)]. This indicates an interesting phenomenon of the net abundance of coions in the brush-free bulk, instead of the expected parity in the number of coions and counterions outside of the PE brush-induced EDL. Moreover, given the net electroneutrality of the system, this signifies that there are a higher number of Na^+ counterions within the grafted PE layer than that needed to neutralize the PE brush charges. This phenomenon is known as overscreening. We see that the extent of overscreening is maximum in the absence of pressure-driven transport and reduces considerably upon the application of an external pressure gradient [compare insets of Fig. 6.3(a-c)]. This can be explained via the reduction in brush height as a result of the flow-induced drag force [see Fig. 6.2(a)]. The decrease in brush height enforces a release of excess counterions from the grafted PE layer into the brush-free bulk, thereby decreasing the disparity in the number of coions and counterions in the brush-free bulk.

We must point out that the results for overscreening for the case of $\nabla P = 0$ were first obtained in another manuscript from our group.[209] The presence of overscreening in

our system can be attributed to three different factors. These factors have been discussed extensively Ref. 209. However, we repeat them here for the sake of continuity. The first factor is the physical confinement created by the nanochannel (note that this is different from the confinement created by the PE brushes). The nanochannel-induced confinement reduces the volume of the brush-free bulk. As a result, the osmotic pressure of the mobile ions present in the brush-free bulk increases. In order to counteract this increase in osmotic pressure, some of the Na^+ counterions migrate into the grafted PE layer. This is the reason that we did not witness any overscreening in our MD simulations of a single grafted PE layer[124] (Chapter 2) i.e., in the absence of nanochannel-induced confinement. The second factor has to do with the small size of the Na^+ counterions. Due to their relatively small size, it is easier for the excess Na^+ ions to accommodate themselves inside the brushes without incurring significant steric repulsion. In contrast, the larger size of the Cl^- ions deters them from entering the fully neutralized grafted PE layer. The third factor is the ability of the Na^+ counterions to form an energetically favorable Na^+-COO^- complex with the carboxylate functional groups of the PAA chains. Inside the PE brushes, the carboxylate oxygens ($O_{Carboxylate}$) can be either solvated by the Na^+ counterions or the hydrogen atoms of water molecules (H_{Water}). However, it is energetically more favorable for the Na^+ ions to solvate the $O_{Carbxylate}$ atoms given their higher charge density (relative to H_{Water}). The excess counterions present inside the overscreened brushes replace additional H_{Water} atoms from the solvation shell of the $O_{Carboxylate}$ atoms, thereby reducing the free energy of the system. Thus, overscreening leads to an enhanced stabilization of the system.

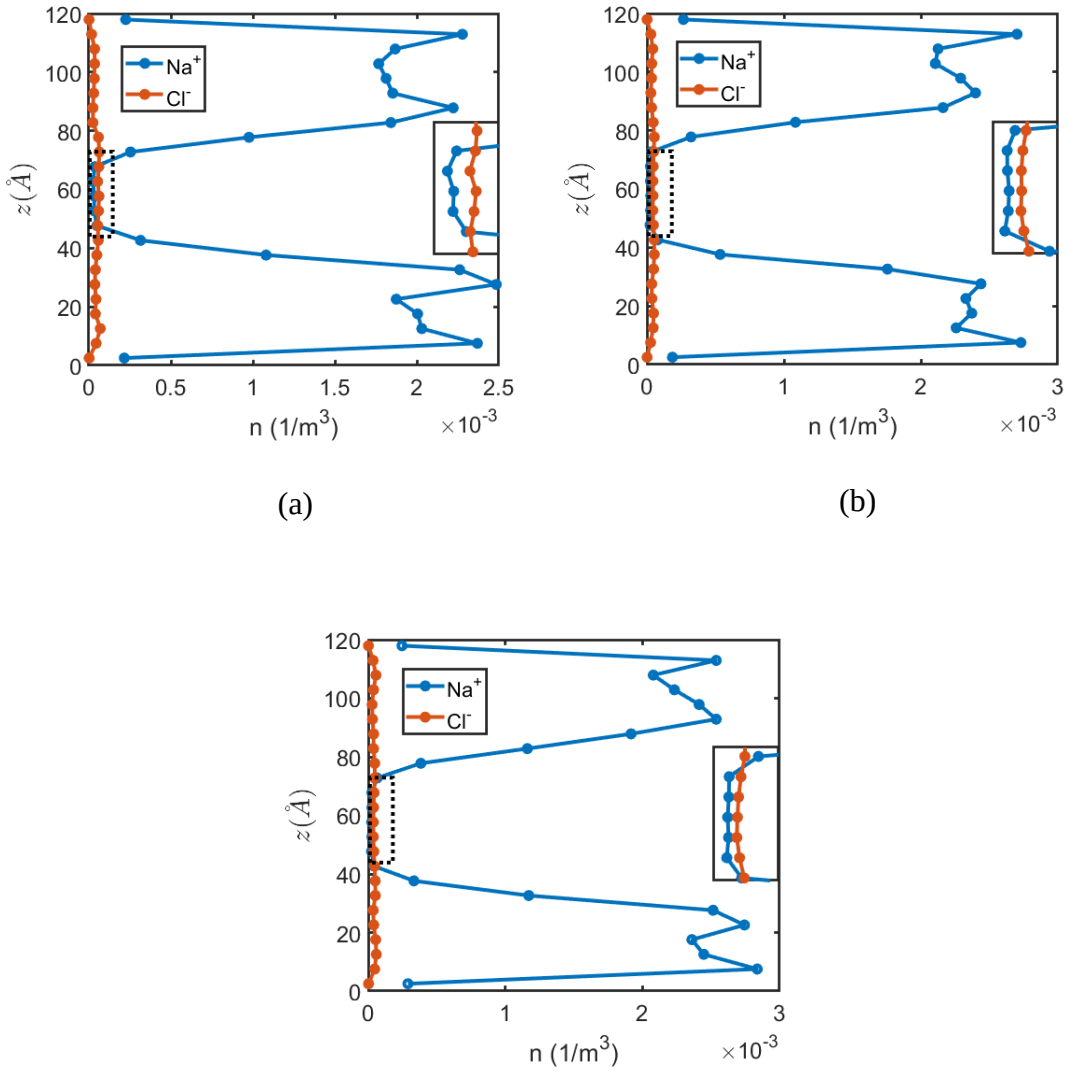

Figure 6.3: *Transverse distribution of the number density of Na^+ and Cl^- ions inside the nanochannel for (a) $\nabla P = 0$ MPa/nm (no applied pressure gradient), (b) $\nabla P = 1$ MPa/nm, and (c) $\nabla P = 2$ MPa/nm. A zoomed view of the ionic distributions in the brush-free bulk are depicted in the insets. The transverse ionic distributions for $\nabla P = 0$ MPa/nm were first obtained in Ref. 209.*

6.3.3. Flow Profile and Nanoscale Energy Conversion Characteristics

Fig. 6.4 plots the velocity profiles of the water molecules inside the nanochannel for the two imposed pressure gradients. Clearly, the flow velocity increases with an increase in the pressure gradient. The flow velocity leads to a downstream advection of the mobile ions, which gives rise to a streaming current. The streaming current (i_s) can be expressed as:

$$i_s = ew \int_{-h}^{h} u(n_{Na^+} - n_{Cl^-})dy, \qquad (6.1)$$

where e is the electronic charge, w is the width of the nanochannel, n_{Na^+} and n_{Cl^-} are the average number densities of the Na^+ and Cl^- ions respectively at a transverse location y, and u is the average axial flow velocity (in the x-direction) at a transverse location y. The integration is carried out over the entire height of the nanochannel ($-h < y < h$). Unlike the continuum framework (see Chapter 5), that always predicts a counterion dominated streaming current,[113] it is difficult to predict the direction of streaming current in our system due to the presence of overscreening. Essentially, there are two competing effects at play here. On the one hand, the number of counterions supersedes the number of coions inside the nanochannel to ensure the overall electroneutrality of the system. This tends to promote a counterion dominated streaming current. However, due to the presence of overscreening there is an excess of coions in the brush-free bulk where the flow velocity is at its highest. On the other hand, the excess counterions (that are involved in the overscreening phenomenon) are concentrated inside (or in the vicinity of) the grafted PE layer where the flow velocity is relatively weaker. This tends to promote a preferential advection of the coions over

the counterions, and thereby contributes to a coion dominated streaming current. Fascinatingly, the former effect dominates the later for both values of imposed pressure gradients and we see a counterion dominated streaming current as predicted by the continuum framework.

Next, we quantify the streaming electric field (E_s) generated inside the nanochannel due to the pressure-driven flow. This streaming electric field gives rise to a conduction current which opposes the streaming current and ensures a net zero current through a given cross section of the nanochannel. The constraint of net zero current across the nanochannel cross section emerges from the fact that there is no net applied potential difference across the ends of the nanochannel. Mathematically, this condition is expressed as:

$$i_{net} = 0, \qquad (6.2)$$

$$\Rightarrow ew \int_{-h}^{h} (n_{Na^+} u_{Na^+} - n_{Cl^-} u_{Cl^-}) dy = 0, \quad (6.3)$$

where i_{net} is the net current through a cross-section of the nanochannel, u_{Na^+} and u_{Cl^-} are the average axial velocities of Na^+ and Cl^- ions respectively at a transverse location y. The integration is carried out over the entire height of the nanochannel ($-h < y < h$; h is the half-height of the nanochannel). The ionic velocities can be decomposed into the advection and conduction components to yield:

$$ew \int_{-h}^{h} [n_{Na^+}(u + \mu_{Na^+} E_s) - n_{Cl^-}(u - \mu_{Cl^-} E_s)] dy = 0, \quad (6.4)$$

where u is the average axial flow velocity at the transverse location y, μ_{Na^+} and μ_{Cl^-} represent the electrophoretic mobilities of the Na^+ and Cl^- ions respectively. In the above equation, the direction of E_s is taken in the positive x-direction (i.e., in the

direction of flow). Therefore, $E_s > 0$ indicates that the streaming electric field acts in the direction of flow, while $E_s < 0$ indicates that the streaming electric field acts in the direction opposite to flow. In our calculations, we have considered the mobilities of Na^+ and Cl^- ions in SPC/E water at 25°C ($\mu_{Na^+} = 4.98 \times 10^{-8}$ m^2/Vs and $\mu_{Cl^-} = 6.88 \times 10^{-8}$ m^2/Vs).[210] We must point out that prior studies have reported a dependence of the electrophoretic mobilities of Na^+ and Cl^- ions on the magnitude of the driving electric field.[211] However, we assume a constant value for the electrophoretic mobilities (corresponding to the linear response regime) irrespective of the strength of the streaming electric field. The reason for making this assumption is that the variation of the electrophoretic mobilities of ions as a function of the driving electric field is largely unknown, especially at the significantly high values of electric fields observed in MD simulations. Rearranging eq. 6.4, and utilizing eq. 6.1, we obtain the streaming electric field as:

$$E_s = \frac{-i_s}{ew\int_{-h}^{h}(n_{Na^+}\mu_{Na^+} + n_{Cl^-}\mu_{Cl^-})dy}, \qquad (6.5)$$

$$\Rightarrow E_s = \frac{-i_s L}{e(N_{Na^+}\mu_{Na^+} + N_{Cl^-}\mu_{Cl^-})} \qquad (6.6)$$

where $N_{Na^+} = 4460$ and $N_{Cl^-} = 140$ are the total number of Na^+ and Cl^- ions in our system, and $L = 234.75$ Å is the length of the nanochannel. The negative sign in equations 6.5 and 6.6 indicates that the direction of electric field is opposite to that of the streaming current in order to ensure a zero net current.

Finally, the total electrical power output from the nanochannel can be calculated as:

$$P_{out} = \left|\frac{1}{4} i_s E_s\right| L \qquad (6.7)$$

Table 6.2 lists the values of the volume flux ($Q = w \int_{-h}^{h} u\, dy$; where the integration is carried out over the entire height of the nanochannel), streaming current, streaming electric field, and electrical power output for the two applied pressure gradients. We can observe that the volume flux, streaming current, streaming electric field, and power output increases with an increase in the imposed pressure gradient. This behavior is in line with the predictions of our continuum framework[113] (Chapter 5). However, Q, i_s and E_s values obtained from our MD simulations do not scale linearly with the applied pressure gradient (doubling the imposed pressure gradient from 1MPa/nm to 2 MPa/nm does not double the values of Q, i_s and E_s in table 6.2) as predicted by the continuum calculations (see Chapter 5). As a result of the non-linearity of i_s and E_s, the power output also does not scale quadratically with the applied pressure gradient (doubling the imposed pressure gradient from 1MPa/nm to 2 MPa/nm does not quadruple the value of P_{out} in table 6.2) as suggested by the theoretical calculations of Chapter 5. The reasons for this discrepancy between the results obtained from the MD simulations and the predictions of the continuum models will be discussed section 6.4.

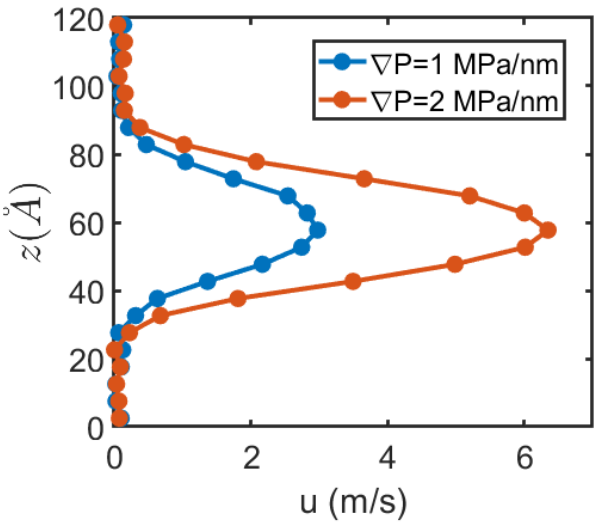

Figure 6.4: *Axial flow profiles (obtained from our all-atom MD simulations) for the pressure-driven transport of water inside the nanochannel as a function of the applied pressure gradient.*

Quantity	∇P=1 MPa/nm	∇P=2 MPa/nm
Volume Flux (Q) (μm^3/s)	93.8	201.9
Streaming Current (i_s) (nA)	2.70	4.63
Streaming Electric Field (E_s) (mV/nm)	1.71	2.93
Power Output (P_{out}) (nW)	0.027	0.080

Table 6.2: *Volume flux for water transport and nanoscale energy conversion characteristics obtained from the all-atom MD simulations (for different applied pressure gradients).*

6.4. Comparison with Continuum Predictions

In this section, we shall compare our MD results for the nanofluidic energy conversion characteristics with the theoretical predictions of our continuum framework[113,207] provided in Chapters 4 and 5. The configuration of the PE brushes along with the distribution of the mobile ions will be modelled by using our state-of-the-art modified Strong Stretching Theory or MSST (see section 4.5).[207] In order to obtain a one-to-one match between the MD and continuum systems, we carefully set the parameters in our MSST model in accordance with our all-atom MD framework. The length of each Kuhn monomer (a) is set to 1 C-C bond length, i.e., 1.53 Å. Accordingly, the number of Kuhn monomers per chain (N) was set equal to the number of backbone C-C bonds on each grafted PAA molecule. i.e., 48. The number of polyelectrolyte chargeable sites per Kuhn monomer (γ) was set to $0.5/a^3$, since every alternate backbone carbon atom is attached to a carboxylate functional group. The distance between adjacent monomers (ℓ) was set to 15.65 Å (corresponding to a grafting density of $0.05/\sigma^2$). By setting $pH_\infty >> pK_a$ [pH_∞ is the bulk pH and pK_a=-ln(K_a), where K_a is the dissociation constant for the ionization of PE functional groups], it was ensured that the chains are fully ionized in accordance with our MD simulations. One important aspect to note is that the MSST model does not differentiate between the counterions released from the ionization of the brushes and the cations released by the dissociation of the added salt. On the other hand, the atomistic MD simulations contain explicit counterions in order to maintain a state of net electroneutrality within the simulation domain. In fact, the concentration of counterions (released by the ionization of the brushes) within the

grafted PE layer in our MD simulations can be significantly larger than that of the cations released by the salt. Thus, in order to make a fair comparison between the MD and continuum systems, it was ensured that the net concentration of Na^+ ions inside the PE brushes in our continuum calculations matches the value obtained from our MD simulations in the absence of an applied pressure gradient. This was done by varying the bulk salt concentration (c_∞) in our MSST model until a match was obtained for $c_\infty = 1.02$ M. Table 6.3 provides a comparison between the equilibrium brush heights obtained from the MSST model and the all-atom MD simulations in the absence of an applied pressure gradient. The brush heights are in excellent agreement to each other with a difference of less than 10%.

After obtaining the equilibrium brush configuration and the distribution of the mobile ions from our MSST model, we utilized the framework[113] of Chapter 5 to calculate the flow velocity and the nanofluidic energy conversion characteristics for different applied pressure gradients. Table 6.4 provides a comparison between the continuum predictions of the volume flux, streaming current, streaming conductance (C_s) (this quantity will be discussed in section 6.5), streaming electric field, and power output and their corresponding values obtained from our all-atom MD simulations. We observe that the continuum model does a very reasonable job in predicting the values of several nanofluidic energy conversion quantities such as Q, i_s, C_s, and E_s. The values of these quantities are only off by a factor of ~1.5-4 from their corresponding MD values. In addition, the flow velocity profiles obtained from the two methods are also in satisfactory agreement to each other (see Fig. 6.5), with the continuum model overpredicting the centerline velocity by a factor of ~2. It must be emphasized that the

level of agreement between our continuum calculations and all-atom MD simulations is remarkable, since these methods are designed to operate at significantly different length scales. In addition, the MD simulations can capture extremely intricate and complex atomistic interactions which are impossible to model in the continuum framework. Despite that, the continuum calculations are able to provide an estimate of the flow field and energy conversion characteristics correct to the order of magnitude (off by only a factor of ~1.5-4).

Now, we focus our attention to the reasons for the discrepancy between the results of our continuum predictions and the MD simulations. The first major difference between the two frameworks is the ability to capture the tilt of the brushes. From Fig. 6.2, we can see that the application of an external pressure gradient can result in a significant tilting of the grafted PE chains, and consequently a reduction in the brush height. However, our continuum model is unable to capture these flow-induced changes in the brush configuration. In other words, our continuum framework only considers a one way coupling between the brush configuration/ionic distribution and the pressure-driven flow field. We utilize the equilibrium PE brush configuration and the associated PE-brush-induced EDL electrostatics (in the absence of applied pressure gradient) to calculate the pressure-driven flow field but neglect the influence of the flow field on the underlying PE brush configuration (and the corresponding distribution of the mobile ions). While the assumption of a one-way coupling between the PE brush configuration and the pressure-driven flow field is a good one for relatively weak flow fields, this assumption tends to break down at high flow velocities such as the ones observed in our MD simulations.

The second factor contributing to the discrepancy between the continuum and MD predictions is the presence of overscreening in our system. Overscreening is a highly complex phenomenon which arises from the atomistic correlations between the charged PE chains and the Na^+ counterions. As a result of overscreening, we observe a highly non-trivial ionic distribution with an excess of coions in the brush-free bulk. This ionic distribution cannot be captured by our continuum model. Despite its ability to capture ion-ion correlations, the MSST model still operates within a mean-field framework.[207] This makes it impossible for the MSST model to match the accuracy of fully atomistic MD simulations in capturing highly complex interactions occurring at the atomistic length scales. Having said that, the MSST model still does a much better job than other existing models for PE brushes that do not consider non-Poisson Boltzmann effects such as solvent polarization, ion-ion correlations, and finite size of the ions and solvent molecules.

The third reason for the difference between continuum and MD results can be attributed to the strongly hydrophilic nature of the PAA brushes. The hydrophilicity of the PAA chains significantly restricts the mobility of the brush-trapped water molecules as quantified by their mean squared displacement [see Fig. 2.5(f)].[124] This is a result of strong ion-dipole interactions between the condensed counterions and the water molecules, the spatial nanoconfinement induced the grafted PE chains, as well as the formation of hydrogen bonds between the water molecules and the $O_{Carboxylate}$ atoms.[124,212-213] Therefore, the flow velocity is significantly reduced inside the grafted PE layer. Our all-atom MD simulations can easily capture these effects while the continuum models cannot. This leads to a notable difference in the shape of the flow

profile within the PE brushes obtained by the MD simulations and the continuum calculations (see Fig. 6.5), and thereby leads to significant differences in the energy conversion characteristics.

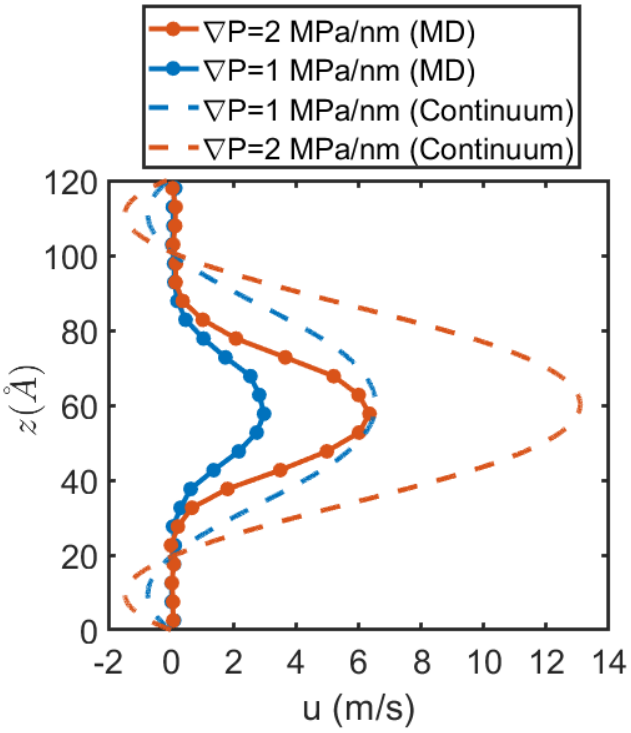

Figure 6.5: *Comparison of the axial flow profiles for the pressure-driven transport of water (for different applied pressure gradients) obtained from all-atom MD simulations and continuum calculations. Parameters used in the MSST model are* a*=1.53 Å,* ℓ *=15.65 Å,* c_∞*=1.02 M,* $\gamma=0.5/a^3$*,* h*=60.225 Å,* N*=48,* pK_a*=3.5,* pH_∞*=7. All other parameters for the MSST model are identical to that used in Fig. 4.20. Parameters used in the continuum flow calculations are* $\eta = 8.9 \times 10^{-4}$ *Pa.s,* $\mu_{Na^+} = 4.98 \times 10^{-8}$ *m²/Vs, and* $\mu_{Cl^-} = 6.88 \times 10^{-8}$ *m²/Vs.*

Method	Average cation concentration inside the PE brushes (M)	Average end-point brush height (Å)
All-atom MD simulations	4.355	35.44
Continuum Calculations	4.358	37.00

Table 6.3: *Comparison of the average cation concentration inside the grafted PE layer and equilibrium brush heights obtained from the continuum calculations and all-atom MD simulations (for the case of no applied pressure gradient). Parameters used in the MSST model are* $a=1.53$ *Å,* $\ell = 15.65$ *Å,* $c_\infty = 1.02$ *M,* $\gamma = 0.5/a^3$*,* $h=60.225$ *Å,* $N=48$*,* $pK_a=3.5$*,* $pH_\infty=7$*. All other parameters for the MSST model are identical to that used in Fig. 4.20.*

Physical Quantity	All-atom MD simulations		Continuum Calculations	
	∇P=1 MPa/nm	∇P=2 MPa/nm	∇P=1 MPa/nm	∇P=2 MPa/nm
Volume Flux (Q) (μm^3/s)	93.8	201.9	139.4	278.8
Streaming Current (i_s) (nA)	2.70	4.63	9.54	19.09
Streaming Conductance (C_s) (pA/bar)	11.51	9.87	40.66	40.66
Streaming Electric Field (E_s) (mV/nm)	1.71	2.93	4.73	9.46
Power Output (P_{out}) (nW)	0.027	0.080	0.265	1.060

Table 6.4: *Comparison of the volume flux for water transport and nanoscale energy conversion characteristics obtained from the continuum calculations and all-atom MD simulations (for different applied pressure gradients). Parameters used in the MSST model are a=1.53* Å, ℓ *=15.65* Å, c_∞*=1.02 M,* γ*=0.5/a*^{3}*, h=60.225* Å*, N=48,* pK_a*=3.5,* pH_∞*=7. All other parameters for the MSST model are identical to that used in Fig. 4.20. Parameters used in the calculations of the flow rate and nanoscale energy conversion characteristics are* $\eta = 8.9 \times 10^{-4}$ *Pa.s,* $\mu_{Na^+} = 4.98 \times 10^{-8}$ *m*^{2}*/Vs,* $\mu_{Cl^-} = 6.88 \times 10^{-8}$ *m*^{2}*/Vs, L=234.75* Å*, and w=93.9* Å*.*

6.5. Comparison with Prior Experimental Study

In this section, we provide a comparison of the nanoscale energy conversion characteristics (associated with the pressure-driven transport of water in PE brush-grafted nanochannels) obtained from our all-atom MD simulations as well as our continuum framework with a prior experimental study conducted by Heyden and coworkers.[19] The purpose of this comparison is not to provide a direct validation of our continuum/MD framework but rather to gain a sense of feasibility of the numbers obtained from the continuum/MD models. Heyden *et al* probed the pressure-driven transport of aqueous KCl solution in Silica nanochannels of length, L=4.5 mm and width, w=50 μm. The dissociation of the Silanol groups ($SiOH \rightleftharpoons SiO^- + H^+$) results in the accumulation of negative charges on the nanochannel walls, thereby giving rise to an EDL. Several experimental runs were conducted with different nanochannel heights and bulk salt concentrations. Before providing a comparison of our results with the experiments, we would like to point out that there are significant differences between our continuum/MD system and that of Heyden *et al*. Firstly, the channel dimensions for Heyden *et al* are orders of magnitude larger than ours. Our system has a nanochannel height of ~12 nm, while Heyden *et al* conducted experiments on nanochannels with heights between 70 nm and 1147 nm. Secondly, we consider PE brush grafted nanochannels while Heyden *et al* ran experiments on bare nanochannels with surface charges (no PE brush grafting). Thirdly, Heyden *et al* considered KCl as the added salt in contrast to the NaCl used in our studies. Fourthly, the nanochannel walls used in our MD simulations do not mimic the surface properties of the Silica

nanochannel used by Heyden *et al*. Fifthly, the applied pressure gradient used in our system is orders of magnitude of higher than that probed in Heyden *et al*. As a result, one-to-one comparison between our work and Heyden *et al* is not possible. However, as mentioned before, this comparison will provide us a sense of feasibility of the results obtained from our continuum/MD framework.

Heyden *et al* reported their nanoscale energy conversion characteristics in the form of a quantity known as the streaming conductance (C_s). The streaming conductance is defined as the ratio of the streaming current (i_s) and the pressure difference applied across the length of the nanochannel ($L\nabla P$). Heyden *et al* observed a streaming conductance in the range of ~1-100 pA/bar (see Fig. 3 in Ref. 19) depending on the height of the nanochannel (which was varied from 70 nm to 1147 nm) and the KCl salt concentration (which was varied from 5.6 μM to 1 M). In an attempt to compare our results to the experimental findings of Heyden *et al*, we calculated the streaming conductance from our MD simulations and continuum calculations for both values of applied pressure gradients (see Table 6.4). We obtain streaming conductance values of ~10 pA/bar from our MD simulations, and ~40 pA/bar from our continuum framework (see Table 6.4), which are both within the range of values reported by Heyden *et al*. This serves as a check for the feasibility of our all-atom MD and theoretical results. However, this comparison does not illustrate the role played by the brushes in dictating the observed value of streaming conductance in our system (remember that Heyden *et al* conducted experiments on brush-free nanochannels). To quantify the effect of brushes on the streaming conductance, we perform two separate continuum

calculations: 1) Brush-free nanochannels with parameters corresponding to Heyden *et al* and 2) Nanochannels grafted with PE brushes carrying the same charge density as the surface charge density of the nanochannel walls for the brush-free case. Since, Heyden *et al* probed various combinations of nanochannel height and bulk salt concentration, we pick a particular combination with nanochannel height of 140 nm and bulk salt (KCl) concentration of 0.1 M for our continuum calculations. We utilize our Augmented Strong Stretching Theory (see Chapter 4) for the continuum calculations since the non-Poisson Boltzmann effects are negligible at 0.1 M bulk salt concentration (see Figures 4.20, 4.21 and 4.22). First, we calculated the surface charge density on the walls of the Silica nanochannels used by Heyden *et al* (for channel height of 140 nm and bulk salt concentration of 0.1 M). According to the Behrens-Grier model, the zeta potential (ζ) of the Silica nanochannel surface can be related to its surface charge density (σ) as:[214,215]

$$\zeta(\sigma) = \frac{k_B T}{e} ln\left(\frac{-\sigma}{e\Gamma+\sigma}\right) + ln(10)\frac{k_B T}{e}(pK_a - pH_\infty) - \frac{\sigma}{C} \tag{6.8}$$

where $k_B = 1.38 \times 10^{-23}$ J/K is the Boltzmann constant, e=1.6×10^{-19} C is the electronic charge, T=298 K is the temperature, $\Gamma = 8nm^{-2}$ is the surface density of Silanol groups, $pK_a = -ln(K_a)$ =7.9 (where K_a is the dissociation constant for Silanol groups), $pH_\infty = 8$ is the bulk pH of the electrolyte, and $C = 0.3\ F/m^2$ is the capacitance of the Stern layer. The values of Γ, pK_a, pH_∞, and C have been taken from Heyden *et al*. Moreover, the Grahame equation relates the zeta potential and surface charge density for non-overlapping EDLs as:[214]

$$\sigma(\zeta) = \frac{2\epsilon_0\epsilon_r k_B T}{\lambda_D e} sinh\left(\frac{e\zeta}{2k_B T}\right) \tag{6.9}$$

where $\epsilon_0 = 8.854 \times 10^{-12}\ F/m$ is the permittivity of free space, $\epsilon_r = 78.54$ is the relative permittivity of water, and $\lambda_D = \sqrt{\frac{\epsilon_0 \epsilon_r k_B T}{2e^2 n_\infty}}$ is the Debye screening length ($n_\infty = 1000 \times N_A \times c_\infty$; $c_\infty = 0.1\ M$ is the bulk Molarity of KCl and $N_A = 6.022 \times 10^{23}$ is the Avogadro's number). Note that the EDL thickness (λ_D) corresponding to our chosen bulk salt concentration of 0.1 M is ~1 nm, which is significantly lower than the half height of the nanochannel (70 nm). Thus, there is no EDL overlap, and eq. (6.9) is valid for our system. Solving eqs. (6.8,6.9) simultaneously yields the values of the equilibrium surface charge density, $\sigma = 23.36\ mC/m^2$ and zeta potential, $\zeta = 30.53$ mV for our chosen parametric combination (bulk salt concentration, $c_\infty = 0.1\ M$ and nanochannel half-height, h=70 nm). Next, we utilized our continuum framework (Chapters 4 and 5) to obtain the streaming conductance, $C_{s,\ no\ brush} = 3.65\ pA/bar$ for a bare (brush-free) nanochannel with the calculated surface charge density of $\sigma = 23.36\ mC/m^2$ (with $c_\infty = 0.1\ M, h = 70\ nm, L = 4.5\ mm, w = 50\ \mu m, and\ pH_\infty = 8$). The electrophoretic mobility of K^+ ions, $\mu_{K^+} = 7.12 \times 10^{-8}\ m^2/Vs$ and Cl^- ions, $\mu_{Cl^-} = 6.88 \times 10^{-8}\ m^2/Vs$ were taken from Ref. 210, and the dynamic viscosity of water was taken as $\eta = 8.904 \times 10^{-4}\ N/m^2 s$. The value of $C_{s,\ no\ brush} = 3.65\ pA/bar$ obtained from our continuum calculations is in excellent agreement with the value of streaming conductance reported by Heyden *et al* (~3.5 pA/bar) for nanochannel of height 140 nm and bulk salt concentration 0.1 M (see Fig. 2 in Ref. 19).

Next, we proceed to calculate the streaming conductance for the case of brush-grafted nanochannel carrying the same charge density (σ_{brush}) as the surface charge density of

the brush-free nanochannel ($\sigma = 23.36\ mC/m^2$). For this purpose, we chose short lose brushes with $\ell = 60\ nm\ and\ N = 400$. Calculations were performed for $c_\infty = 0.1\ M, h = 70\ nm, L = 4.5\ mm, w = 50\ \mu m,\ pH_\infty = 8, \mu_{K^+} = 7.12 \times 10^{-8}\ m^2/Vs, \mu_{Cl^-} = 6.88 \times 10^{-8}\ m^2/Vs, \eta = 8.904 \times 10^{-4}\ N/m^2 s$. All other parameters (except number density of polyelectrolyte chargeable sites, γ) were identical to those used in Figure 5.2. γ was varied iteratively until the charge density of the brushes, $\sigma_{brush} = -e \int_{-h}^{-h+H_0} \phi n_{A^-} dy$ (where ϕ is the monomer volume fraction, n_{A^-} is the number density of ionized sites on the PE chains, and $H_0 = 47.36\ nm$ is the equilibrium brush height) matched the surface charge density of the bulk nanochannel ($\sigma = 23.36\ mC/m^2$). This procedure yielded a value of $\gamma = 2.415/a^3$. Finally, we obtained a value of streaming conductance, $C_s = 55.36\ pA/bar$ for the brush-grafted nanochannel, which is more than an order of magnitude greater than the value obtained for the brush-free nanochannel ($C_{s,\ no\ brush} = 3.65\ pA/bar$). This analysis shows that the presence of grafted PE brushes plays an instrumental role in increasing the streaming conductance associated with the pressure-driven flow. Thus, we anticipate that PE brush grafting (with the appropriate brush parameters) can be utilized as a mechanism to significantly increase the magnitude of streaming conductance obtained in the experimental study of Heyden *et al*.

6.6. Conclusions

We conducted the first fully atomistic MD study of pressure-driven transport of water in nanochannels grafted with backbone charged PE brushes. Our system exhibits a most interesting phenomenon of overscreening of the grafted PE layer which results in more counterions inside the brushes than that needed to neutralize the PE chains. As a result, the number of coions exceeds the counterions in the brush-free bulk, thereby dramatically impacting the nanoscale energy conversion characteristics. In addition, we observe a significant tilting of the PE chains due to the large flow-induced drag for the applied values of pressure gradients. We went on to calculate several pertinent quantities associated with the pressure-driven transport such as the flow velocity profile, volume flux, streaming current, streaming conductance, streaming electric field, and electrical power output. The qualitative trend of these quantities with respect to the magnitude of imposed pressure gradient was observed to be in line with the predictions of our continuum model. However, the predictions of the continuum calculations were off by a factor of ~1.5-4 relative to the all-atom MD results. This discrepancy between the continuum methods and MD simulations can be attributed to the inability of the continuum framework in capturing factors such as the flow-induced tilting of the brushes, overscreening of the grafted PE layer, and the hydrophilicity of the brushes. Finally, we show that our MD and continuum results for the streaming conductance are within the range of prior experimentally reported values for the pressure-driven transport of water in nanochannels, acting as a check for the feasibility of the numbers obtained from our models.[19] Future MD simulation-based studies can investigate the water transport in PE brush-grafted nanochannels for different grafting

densities of the brushes. This will help understand the role of grafting density in dictating the nanoscale energy conversion characteristics and help optimize nano-systems for maximum electrical power output and energy conversion efficiency.

Chapter 7: Validation, Verification, and Summary of Contributions

In this chapter, we provide a validation/verification of our fully atomistic molecular dynamics (MD) simulations and continuum models. This is done by showing that our all-atom MD results are in excellent agreement to the theoretical predictions of existing as well as our own continuum models. In addition, we also provide a comparison of our MD and continuum results against prior experimental studies. Several of the validatory studies in the present chapter have been taken directly from previous chapters of this thesis. This is done to reorganize all the validations/verifications of our work and present them together for improved readability. Finally, we end by summarizing the major contributions of this thesis to the existing body of knowledge.

7.1. Comparison of All-atom MD Simulations with Continuum Models

7.1.1. Match between All-atom MD Results of Brush Height and Scaling Laws of the Non-linear Osmotic Brush Regime[*]

The detailed procedure for carrying out our all-atom MD simulations of densely grafted planar polyacrylic acid (PAA) brushes is provided in section 2.5. Figure 7.1(a) depicts the variation of the end-point brush height $< z_e >$ with *N*, which denotes the number

[*] The contents of this subsection have been published as the following journal article: Sachar, H. S.; Pial, T. H..; Desai, P. R.; Etha, S. A.; Wang, Y.; Chung, P. W.; Das, S. "Densely Grafted Polyelectrolyte Brushes Trigger "Water-in-Salt"-like Scenarios and Ultraconfinement Effect." *Matter* **2020**, *2*, 1509-1521.

of backbone carbon atoms of the polyelectrolyte (PE) brush molecule. We observe $< z_e >$~*N*. On the other hand, in Fig. 7.1(b), we provide the variation of $< z_e >$ with the grafting density σ_g. In order to explain the trends of $< z_e >$ with *N* and σ_g, we invoke the scaling prediction on the brush height ($H_{osm,nl}$) for PE brushes in the *non-linear* osmotic regime.[65,66] This regime improves the predictions of the standard osmotic brush regime (in osmotic regime, the brush height is obtained by balancing the elastic energy of the brushes with the entropic energy of the counterions) by additionally accounting for the effects of self-volume of the polyelectrolyte chains on the counterion entropy. Following refs 65-66, we can write:

$$H_{osm,nl} = nb\frac{f+\sigma_{eff}^2\sigma_g}{1+f}, \quad (7.1)$$

where *n* is the number of repeating units [in our case n=(N-1)/2], *b* is the length of each repeating unit [in our case *b* is equal to 2 backbone C-C bond lengths. i.e., 3.058 Å], *f* is the fraction of charged monomers (f=1 for a fully ionized brush), and $\sigma_{eff} = \sqrt{2}\sigma$ [σ=3.5 Å is the Lennard Jones (LJ) distance parameter for backbone carbon atoms on the PE chains] is the effective monomer diameter (i.e., the diameter of the monomer accounting for the condensed counterions). Eq. (7.1) and n=(N-1)/2 explains the linear variation of $< z_e >$ with *N*. Also, we compute the variation of $H_{osm,nl}$ with σ_g from eq. (7.1) and compare the theoretical results with the MD predictions [see Fig. 7.1(b)]. The theoretical result accurately captures the rate of increase of $<z_e>$ with σ_g, although it under predicts the values of $<z_e>$ for all combinations of *N* and σ_g, which can be attributed to different factors such as the lateral inhomogeneity in counterion distribution, improper consideration of σ_{eff} (possibly due to the presence of pendant

groups attached to the PE backbone), short-range excluded volume interactions between the PE chains, etc.

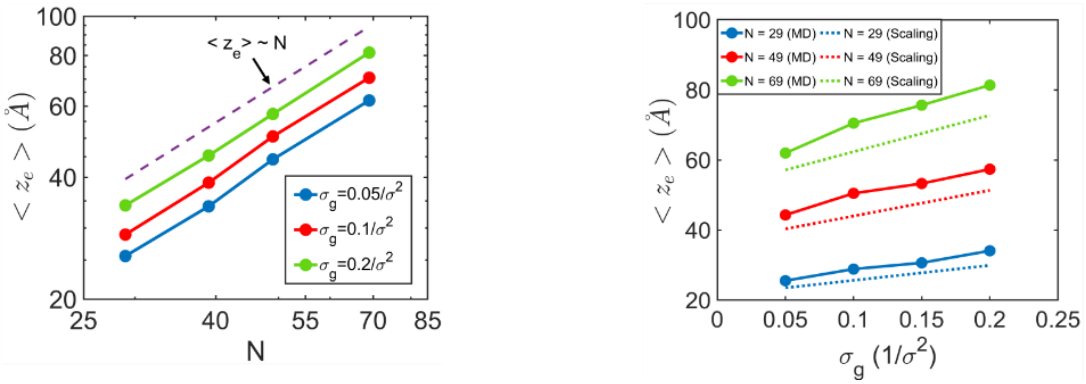

(a) (b)

Figure 7.1: *Equilibrium end-point height of the PE brushes. (a) Variation of the end-point brush height with N for different grafting densities. The dashed line denotes the* $< z_e >$*~N scaling as also confirmed by eq. (7.1). (b) Variation of the end point brush height with grafting density (*σ_g*) for different N. The dotted lines provide the result of the theoretical calculation of brush height obtained by employing eq. (7.1).*

7.1.2. Comparison of the Theoretical Predictions of the Modified Strong Stretching Theory (MSST) to the All-atom MD Results for Brush Height[#]

In this section, we compare the results (the brush height) from the modified Strong Stretching Theory (MSST) model (see section 4.5) with those obtained from our all-atom molecular dynamics (MD) simulation study on PE brushes (see chapter 2). The system probed by the all-atom simulations consist of fully ionized Polyacrylic acid (PAA) brushes neutralized by Na^+ counterions. The MD simulations probed different values of chain lengths (quantified by the number of backbone Carbon atoms) and grafting densities (quantified by the lateral separation between adjacent chains). We provide results for the brush height predicted from our MSST model and that obtained from the atomistic simulations (see Table 7.1) and we observe a most outstanding match (discussed in more details later).

In order to make a one-to-one comparison of our theoretical results with the simulations, we make a few assumptions. Firstly, we consider each C-C bond in the PAA backbone (along with the attached pendant groups) (as represented in the all-atom MD model) as one Kuhn segment in the MSST model. This gives us a Kuhn length of a=1.53 Å and the number of Kuhn segments equal to the number of C-C bonds (along the backbone of the individual PAA chains) for using in our MSST model. For example, a chain having 29 backbone Carbon atoms in the MD simulation will contain

[#] The contents of this subsection have been developed by a fellow Ph.D. student Sai Ankit Etha and have been published as the following journal article: Etha, S. A.; Sivasankar, V. S.; Sachar, H. S.; Das, S. "Strong Stretching Theory for pH-responsive Polyelectrolyte Brushes in Large Salt Concentrations." *Physical Chemistry Chemical Physics* **2020**, *22*, 13536-13553.

28 backbone C-C bonds and thus 28 Kuhn segments. Of course, with considerations we neglect the effect of the strong angular and torsional constraints along the PAA backbone; despite that, as we shall see later, we obtain an excellent match between the theory and simulation results. Moreover, since fully ionized PAA chains contain a carboxylate group on every alternate backbone carbon atom, we set the density of polyelectrolyte chargeable sites to $\gamma = 0.5/a^3$.

Our second assumption relates to the quantification of an equivalent bulk salt concentration for the MD simulations. The simulations have some fundamental differences from the theoretical model as they consider the effects of the counterions explicitly. In fact, most of the cation concentration within the brushes in our MD simulations was due to the presence of the explicit counterions. We had added 0.1 M NaCl salt in the simulation box as well (for our MD simulation study), but its concentration within the brushes was negligible in comparison to the counterions. On the other hand, our MSST model involves the effects of a bulk salt concentration but does not consider the counterions (in the vicinity of the PE brushes) separately. Thus, in order to make an appropriate comparison between the two systems, we have ensured that the cation (or counterion) concentration within the brushes is equal for the two cases (i.e., the case studied by the MD simulations and the MSST case). This was achieved by varying the bulk salt concentration in our MSST model (for each value of chain length and grafting density) until we obtained a nearly identical average cation concentration within the brushes to that obtained from the simulations. Of course, the anion concentration within the brushes is negligible due to the presence of negative

charges on the PE functional groups and the fact that the brushes are extremely densely grafted and hence can be ignored. The final bulk salt concentration values used in the theoretical (MSST) model as well as the average cation concentration within the brushes (for both theory and simulations) are provided in Table 7.1 and as one could see, we work with almost identical concentration values (for the two cases).

Finally, in order to enforce complete ionization of the PE functional groups in our MSST model, we set $pH_{\infty} \gg pK_a$. This was done to be consistent with the MD simulations that considered fully ionized PAA chains.

From Table 7.1, we observe an excellent match between the brush heights predicted by our MSST model and the all-atom MD simulations. In fact, the brush heights differ by less than 5% for all the different combinations of parameters that were considered. This level of agreement with the MD simulation results is remarkable, considering the sophistication involved in such atomistic simulations that considered an all-atom framework where each atom of the brushes, water and the mobile ions was modelled explicitly. This allows the simulations to attain levels of accuracy that are beyond the capabilities of any mean field continuum model. Despite that, our theoretical results are in outstanding agreement with the MD simulation results. This not only verifies our MSST model but also testifies its potential in capturing non-PB effects to an extent that is unprecedented in the continuum modelling of PE brushes.

Number of Carbon atoms (N)	Grafting Density (σ_g) ($1/\sigma^2$)	Bulk salt concentration used for the MSST model [c_∞ (M)]	Average counterion concentration within PE brushes for MD study (M)	Average cation concentration within PE brushes for the MSST model (M)	Brush Height (Å) obtained in MD study	Brush Height (Å) obtained using the MSST model
29	0.05	0.1	3.38	3.43	25.56	24.92
29	0.1	0.6	6.04	6.00	28.99	29.50
49	0.05	0.3	3.47	3.46	44.25	45.40
49	0.1	1.25	6.19	6.21	50.43	50.91
69	0.05	0.5	3.57	3.62	61.98	62.86
69	0.1	1.5	6.32	6.30	70.53	72.86

Table 7.1: *Comparison of brush heights obtained from the MSST model presented in section 4.5 and all-atom MD simulations of chapter 2 for various values of the number of carbon atoms (N) and grafting density (in units of $1/\sigma^2$), where $\sigma = 3.5$ Å is the Lennard Jones size parameter). The values of bulk salt concentration (c_∞ in M) used in MSST model, the equivalent average cation concentration within the brushes for the MSST model, and the average counterion concentration for the MD simulations are also provided. Please note for a given N and σ_g value, we consider such a value of the bulk salt concentration that yields nearly identical values of cation concentration and counterion concentration for the MSST model and the MD simulations, respectively. Only under such circumstances, we could compare that height values obtained from the present MSST model and the all-atom MD simulations. Other parameters used in the MSST model are as follow: Kuhn length, a, of 1 C-C bond length equivalent to 1.53 Å and the density of chargeable sites (γ) equal to $0.5/a^3$.*

7.1.3. Comparison of All-atom MD Results for Pressure Driven Flow in PE Brush-grafted Nanochannels to the Continuum Predictions

In this section, we shall compare our all-atom MD results for the nanofluidic energy conversion characteristics (Chapter 6) with the theoretical predictions of our continuum framework (Chapters 4 and 5). The configuration of the PE brushes along with the distribution of the mobile ions will be modelled by using our state-of-the-art modified Strong Stretching Theory or MSST (see section 4.5). In order to obtain a one-to-one match between the MD and continuum systems, we carefully set the parameters in our MSST model in accordance with our all-atom MD framework. The length of each Kuhn monomer (a) is set to 1 C-C bond length, i.e., 1.53 Å. Accordingly, the number of Kuhn monomers per chain (N) was set equal to the number of backbone C-C bonds on each grafted PAA molecule. i.e., 48. The number of polyelectrolyte chargeable sites per Kuhn monomer (γ) was set to $0.5/a^3$, since every alternate backbone carbon atom is attached to a carboxylate functional group. The distance between adjacent monomers (ℓ) was set to 15.65 Å (corresponding to a grafting density of $0.05/\sigma^2$). By setting $pH_\infty >> pK_a$ [pH_∞ is the bulk pH and pK_a=-ln(K_a), where K_a is the dissociation constant for the ionization of PE functional groups], it was ensured that the chains are fully ionized in accordance with our MD simulations. One important aspect to note is that the MSST model does not differentiate between the counterions released from the ionization of the brushes and the cations released by the dissociation of the added salt. On the other hand, the atomistic MD simulations contain explicit counterions in order to maintain a state of net electroneutrality within the simulation domain. In fact, the

concentration of counterions (released by the ionization of the brushes) within the grafted PE layer in our MD simulations can be significantly larger than that of the cations released by the salt. Thus, in order to make a fair comparison between the MD and continuum systems, it was ensured that the net concentration of Na^+ ions inside the PE brushes in our continuum calculations matches the value obtained from our MD simulations in the absence of an applied pressure gradient. This was done by varying the bulk salt concentration (c_∞) in our MSST model until a match was obtained for $c_\infty = 1.02$ M. Table 7.2 provides a comparison between the equilibrium brush heights obtained from the MSST model and the all-atom MD simulations in the absence of an applied pressure gradient. The brush heights are in excellent agreement to each other with a difference of less than 10%.

After obtaining the equilibrium brush configuration and the distribution of the mobile ions from our MSST model, we utilized the framework of Chapter 5 to calculate the flow velocity and the nanofluidic energy conversion characteristics for different applied pressure gradients. Table 7.3 provides a comparison between the continuum predictions of the volume flux (Q), streaming current (i_s), streaming conductance (C_s), streaming electric field (E_s), and power output (P_{out}) and their corresponding values obtained from our all-atom MD simulations. We observe that the continuum model does a very reasonable job in predicting the values of several nanofluidic energy conversion quantities such as Q, i_s, C_s, and E_s. These values of these quantities are only off by a factor of ~1.5-4 from their corresponding MD values. In addition, the flow velocity profiles obtained from the two methods are also in satisfactory agreement to each other (see Fig. 7.2), with the continuum model overpredicting the centerline

velocity by a factor of ~2. It must be emphasized that the level of agreement between our continuum calculations and all-atom MD simulations is remarkable, since these methods are designed to operate at significantly different length scales. In addition, the MD simulations can capture extremely intricate and complex atomistic interactions which are impossible to model in the continuum framework. Despite that, the continuum calculations are able to provide an estimate of the flow field and energy conversion characteristics correct to the order of magnitude (off by only a factor of ~1.5-4).

Now, we focus our attention to the reasons for the discrepancy between the results of our continuum predictions and the MD simulations. The first major difference between the two frameworks is the ability to capture the tilt of the brushes. From Fig. 6.2 of Chapter 6, we can see that the application of an external pressure gradient can result in a significant tilting of the grafted PE chains, and consequently a reduction in the brush height. However, our continuum model is unable to capture these flow-induced changes in the brush configuration. In other words, our continuum framework only considers a one way coupling between the brush configuration/ionic distribution and the pressure-driven flow field. We utilize the equilibrium PE brush configuration (in the absence of applied pressure gradient) to calculate the pressure-driven flow field but neglect the influence of the flow field on the underlying PE brush configuration (and the corresponding distribution of the mobile ions). While the assumption of a one-way coupling between the PE brush configuration and the pressure-driven flow field is a good one for relatively weak flow fields, this assumption tends to break down at high flow velocities such as the ones observed in our MD simulations.

The second factor contributing to the discrepancy between the continuum and MD predictions is the presence of overscreening in our system. Overscreening is a highly complex phenomenon which arises from the atomistic correlations between the charged PE chains and the Na^+ counterions. As a result of overscreening, we observe a highly non-trivial ionic distribution with an excess of coions in the brush-free bulk (see Fig. 6.3 of Chapter 6). This ionic distribution cannot be captured by our continuum model. Despite its ability to capture ion-ion correlations, the MSST model still operates within a mean-field framework. This makes it impossible for the MSST model to match the accuracy of fully atomistic MD simulations in capturing highly complex interactions occurring at the atomistic length scales. Having said that, the MSST model still does a much better job than other existing models for PE brushes that do not consider non-Poisson Boltzmann effects such as solvent polarization, ion-ion correlations, and finite size of the ions and solvent molecules.

The third reason for the difference between continuum and MD results can be attributed to the strongly hydrophilic nature of the PAA brushes. The hydrophilicity of the PAA chains significantly restricts the mobility of the brush-trapped water molecules as quantified by their mean squared displacement [see Fig. 2.5(f)].[124] This is a result of strong ion-dipole interactions between the condensed counterions and the water molecules, the spatial nanoconfinement induced the grafted PE chains, as well as the formation of hydrogen bonds between the water molecules and the $O_{Carboxylate}$ atoms.[124,212-213] Therefore, the flow velocity is significantly reduced inside the grafted PE layer. Our all-atom MD simulations can easily capture these effects while the continuum models cannot. This leads to a notable difference in the shape of the flow

profile within the PE brushes obtained by the MD simulations and the continuum calculations (see Fig. 7.2), and thereby leads to significant differences in the energy conversion characteristics.

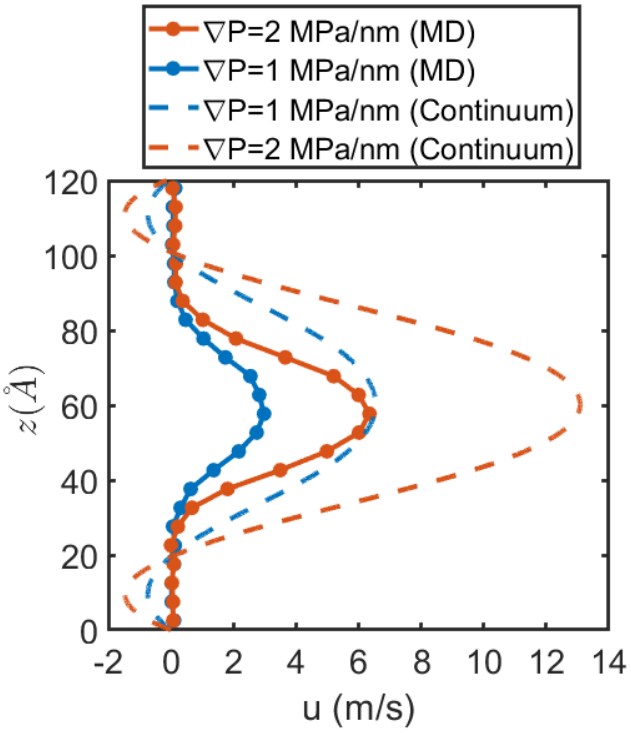

Figure 7.2: *Comparison of the axial flow profiles for the pressure-driven transport of water (for different applied pressure gradients) obtained from all-atom MD simulations and continuum calculations. Parameters used in the MSST model are* a*=1.53 Å,* ℓ *=15.65 Å,* c_∞*=1.02 M,* $\gamma=0.5/a^3$*,* h*=60.225 Å,* N*=48,* pK_a*=3.5,* pH_∞*=7. All other parameters for the MSST model are identical to that used in Fig. 4.20. Parameters used in the continuum flow calculations are* $\eta = 8.9 \times 10^{-4}$ *Pa.s,* $\mu_{Na^+} = 4.98 \times 10^{-8}$ *m²/Vs, and* $\mu_{Cl^-} = 6.88 \times 10^{-8}$ *m²/Vs.*

Method	Average cation concentration inside the PE brushes (M)	Average end-point brush height (Å)
All-atom MD simulations	4.355	35.44
Continuum Calculations	4.358	37.00

Table 7.2: *Comparison of the average cation concentration inside the grafted PE layer and equilibrium brush heights obtained from the continuum calculations and all-atom MD simulations (for the case of no applied pressure gradient). Parameters used in the MSST model are* $a=1.53$ *Å,* $\ell = 15.65$ *Å,* $c_\infty = 1.02$ *M,* $\gamma = 0.5/a^3$*,* $h=60.225$ *Å,* $N=48$*,* $pK_a=3.5$*,* $pH_\infty=7$*. All other parameters for the MSST model are identical to that used in Fig. 4.20.*

Physical Quantity	All-atom MD simulations		Continuum Calculations	
	∇P=1 MPa/nm	∇P=2 MPa/nm	∇P=1 MPa/nm	∇P=2 MPa/nm
Volume Flux (Q) (μm^3/s)	93.8	201.9	139.4	278.8
Streaming Current (i_s) (nA)	2.70	4.63	9.54	19.09
Streaming Conductance (C_s) (pA/bar)	11.51	9.87	40.66	40.66
Streaming Electric Field (E_s) (mV/nm)	1.71	2.93	4.73	9.46
Power Output (P_{out}) (nW)	0.027	0.080	0.265	1.060

Table 7.3: *Comparison of the volume flux for water transport and nanoscale energy conversion characteristics obtained from the continuum calculations and all-atom MD simulations (for different applied pressure gradients). Parameters used in the MSST model are a=1.53* Å, ℓ *=15.65* Å, c_∞*=1.02 M,* γ*=0.5/a*^{3}*, h=60.225* Å*, N=48,* pK_a*=3.5,* pH_∞*=7. All other parameters for the MSST model are identical to that used in Fig. 4.20. Parameters used in the calculations of the flow rate and nanoscale energy conversion characteristics are* $\eta = 8.9 \times 10^{-4}$ *Pa.s,* $\mu_{Na^+} = 4.98 \times 10^{-8}$ *m*^{2}*/Vs,* $\mu_{Cl^-} = 6.88 \times 10^{-8}$ *m*^{2}*/Vs, L=234.75* Å*, and w=93.9* Å*.*

7.2. Comparison of All-atom MD Simulations and Continuum Calculations with Prior Experiments

7.2.1. Comparison of All-atom MD Results for Electroosmotic Flow in PE Brush-grafted Nanochannels to Existing Experiments[!]

We conduct all-atom MD simulations to investigate the electroosmotic (EOS) transport of water in PE brush-grafted nanochannels. Our simulation domain [shown in Fig. 7.3] consists of fully ionized Polyacrylic acid (PAA) chains ($H[-CH_2-CH(COO^-)-]_nCH_3$) as the polyelectrolytes and SPC/E water[64] molecules. Sodium (Na^+) counterions screen the PE brush charges. In addition, we add 0.1 M NaCl salt. PE chains are grafted with a grafting density of $0.05/\sigma^2$ (σ=3.5 Å, is the LJ distance parameter of backbone carbon atoms). Each chain has 49 backbone carbon atoms. Purely repulsive walls are placed at the top and the bottom of the system to prevent the mobile ions and water molecules from escaping the system. 90 PE chains are grafted on each wall in a 15*6 (x*y) array. The particle trajectories are calculated using the Velocity-Verlet algorithm, with a time step of 2 fs. Non-bonded interactions are modelled as the sum of a shifted-truncated 12-6 Lennard Jones potential (U_{LJ}) with a cut-off of 13Å. Long range Columbic interaction is calculated using a PPPM (particle-particle particle-mesh) algorithm.[97] The bonds and angles of water molecules are conserved by using the SHAKE algorithm.[99] Our simulation system consists of a total

[!] The contents of this subsection were primarily developed by a fellow Ph.D. student Turash Haque Pial and have been published as the following journal article: Pial, T. H.; Sachar, H. S.; Desai, P. R.; Das, S. "Overscreening, Coion-Dominated Electroosmosis, and Electric Field Strength Mediated Flow Reversal in Polyelectrolyte Brush Functionalized Nanochannels" *ACS Nano* **2021**. https://doi.org/10.1021/acsnano.0c09248

of 277340 atoms. Dimensions in x, y, and z directions are 23.5 nm, 9.4 nm, and 12 nm respectively. Periodic boundary conditions are applied in x and y directions while the fixed boundary condition is incorporated in z direction. Simulations are performed in LAMMPS[95] and OVITO[100] is used to visualize the simulation system.

The system is first run in the NP_zT ensemble (the subscript z signifies that only the channel height is allowed to change) to obtain the correct simulation box height at 300 K and 1 atm, by applying the Nosé-Hoover thermostat and barostat.[92,93] Subsequently, the system is equilibrated in the NVT ensemble for 16 ns to obtain the correct equilibrium configuration of the system by applying the Langevin thermostat.[81] After initial equilibration, we have applied the electric field under the NVT ensemble to remove the heat dissipated due to the flow. NVT is applied only in the direction perpendicular to the axial electric field and to avoid a flow profile bias, we have removed bias velocity with the help of a binning method employed in a direction perpendicular to the flow field. For more caution, only polymers are thermostatted in the entire system, this mimics the experimental scenario where temperature can be controlled form the outer surface. Only, the water molecules and mobile ions in the extreme left quarter of the simulation domain (in the x-direction) were thermostatted. These simulations are performed for 8 ns to get steady-state velocity profile followed by a 12 ns production run.

We have used the OPLS-AA force field[96] to model the brush molecules and employed Joung et al.[98] for calculating the potentials for the mobile ions. These vastly used parameters for monovalent ions[98] were adjusted to the solvation free energy of ions in water and the lattice energy of ionic crystals. OPLS force field, which is used

to model the PE brush molecule, has been used for modeling a variety of polymer systems such as hydrocarbons,[216] proteins,[217] rubbers,[218] etc. as the most accurate force field parameter. Geometric mixing rules are used for the LJ interactions between dissimilar atoms, except for the ion-ion and ion -water interactions. For these ion-ion and ion-water, we have used Lorentz-Berthelot mixing rules to be consistent with Joung *et al*.[98]

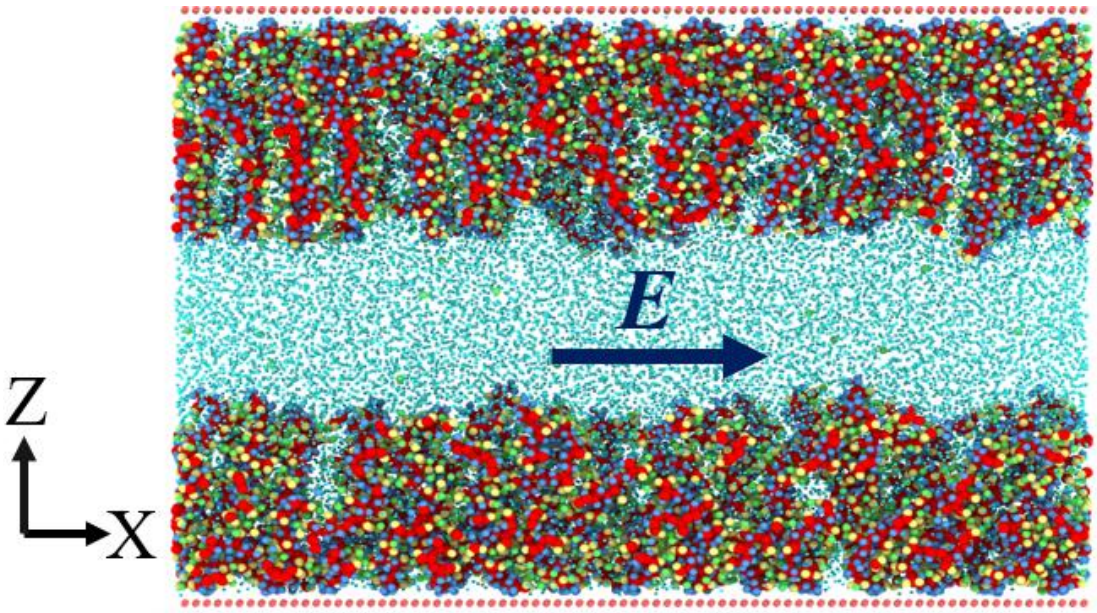

Figure 7.3: *A snapshot of the PE brush grafted nanochannel system.*

Our results indicate that, for no or small electric fields, there is an overscreening effect within the brushes, quantified by the presence of a larger number of counterions than needed to screen the PE charges. This excess counterions come from the added salt: accordingly, the number of coions will be greater than the number of counterions in the brush-free bulk [see Fig. 7.4]. For a larger electric field, i.e., $|\boldsymbol{E}|$ =1 V/nm on the other hand, we find a significant reduction in the overscreening effect within the PE brush layer, leading to an almost equal number of coions and counterions within the brush-free bulk. Charge inversion or overscreening is observed in experiments involving silicone nanochannels in presence of large concentrations of salts with multivalent ions.[219,220] Overpopulation of multivalent counterions in the Stern layer adjacent to nanochannel wall causes the overscreening. On the other hand, in our study we have observed this overscreening with monovalent counterions, where the interplay of the presence of a strong nanoconfinement and the presence of the densely grafted charged PE brushes create an environment that accumulates within the PE brush layer more than required counterions and triggers overscreening. Also, in these studies[219,220] this overscreening scenario cannot be altered by the application of electric field, while in our study we can make the overscreening disappear at significantly larger electric field.

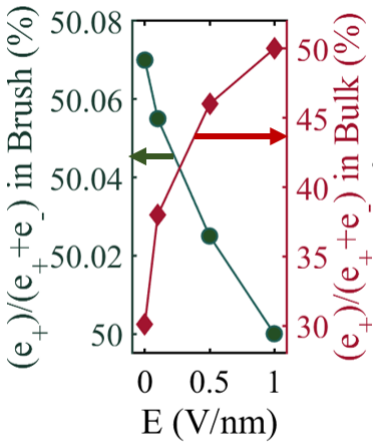

Figure 7.4: *Excess of the positive charges $\Delta e = (e_+ - e_-)$ inside brush and in brush-free bulk as a function of the electric field (E). e_+ and e_- indicate total number of positive charges (Na^+) and negative charges (Cl^- and PE charges) respectively.*

It is well known that in a nanochannel due to the surface charge of the wall, there will be an electric double layer or an EDL and hence an imbalance in the number density of the positive and negative ions within the EDL: in presence of an applied electric field, the mobile ions are transported, and this imbalance ensures that the water molecules are transported in the direction of the migration of the ions that are larger in number within the EDL. However, at low electric field strengths, we observe the presence of an overscreening effect within the PE brush layer, which implies that the coions are excess in number in the bulk. Hence, the EOS transport in presence of the applied electric field, occurs in the direction of migration of the coions. Therefore, for this case, we indeed find that the EOS (electroosmotic) motion occurs due to the imbalance in the number of coions and counterions, albeit for the classical scenario the EOS transport primarily occurs due to the excess of counterions within the EDL. On the other hand, for larger electric field, the overscreening within the PE brush layer becomes negligible and there is equal number of coions and counterions within the bulk: under such circumstances, the EOS transport occurs (in the direction of migration of the counterions) due to the larger residence time of water molecules within the counterions (Na^+ ions) than the coions (Cl^- ions). Therefore, the key mechanism of our reported EOS transport at large electric fields is different from that of the classical EOS transport. Despite that, the order of magnitude of our reported EOS transport at large electric fields is very similar to that reported in our previous experiments. For example, the EOS mobility, which is defined as EOS velocity per unit applied electric field has been reported to be in the order of $(1-10)\times 10^{-9}\, m^2/(Vs)$ for experiments,[221-223] while that computed for our simulations (for large electric field strength of 1 V/nm) is

~ $5.5 \times 10^{-9}\, m^2/(Vs)$. The purpose of this comparison is not to provide a direct validation of our MD framework but rather to gain a sense of feasibility of the numbers obtained from the MD simulations. We would like to point out that there are significant differences between our MD simulations and the experimental systems investigated in Refs. 221-223. Firstly, Refs. 221-223 have considered channels that are much larger than ours. The smallest channel used in these studies has a height of 20 nm (Ref. 221) which is considerably larger than our channel height of ~12 nm. Secondly, we consider PE brush grafted nanochannels while Refs. 221-223 ran experiments on bare channels without any PE brush grafting. Thirdly, the nanochannel walls used in our MD simulations do not mimic the surface properties of the channels used by Refs. 221-223. Fourthly, the applied axial electric field used in our system is orders of magnitude of higher than that probed in Refs. 221-223. As a result, one-to-one comparison between our work with Refs. 221-223 is not possible. However, as mentioned before, the fact that our EOS mobility lies within the range of values observed in prior experimental studies provides a sense of feasibility of the results obtained from our MD framework.

Also, in an experimental setup, there can be a reservoir of solution connected to a nanochannel and water and ions can move from the nanochannel to the reservoir and vice versa. To check the effect of reservoir in the overscreening scenario, we have performed one more simulation where the nanochannel is connected to two reservoirs at its two ends [Fig.7.5(A)]. In this system, the nanochannel grafted with PAA brushes (with a grafting density of $0.05/\sigma^2$ *and having* Na^+ *ions as the screening counterions and an added 0.1 M NaCl salt*) is connected to two reservoirs at its two ends and approximately 1/5th of the total water stays in the nanochannel (and the rest is within

the two reservoirs). Initially the salt ions are distributed randomly in the nanochannel and in the reservoirs. A total of 156 chains are grafted in the nanochannel. The changes in the brush height and ion distributions are monitored to check for equilibrium. To check for the possible overscreening inside the PE brush layer in the nanochannel, we have plotted the ion distribution profile in Figure 7.5(B). We can clearly see that the density of coions are larger within the bulk, confirming the occurrence of overscreening within the PE brush layer of the nanochannel even when the nanochannel is connected to two reservoirs on its two ends.

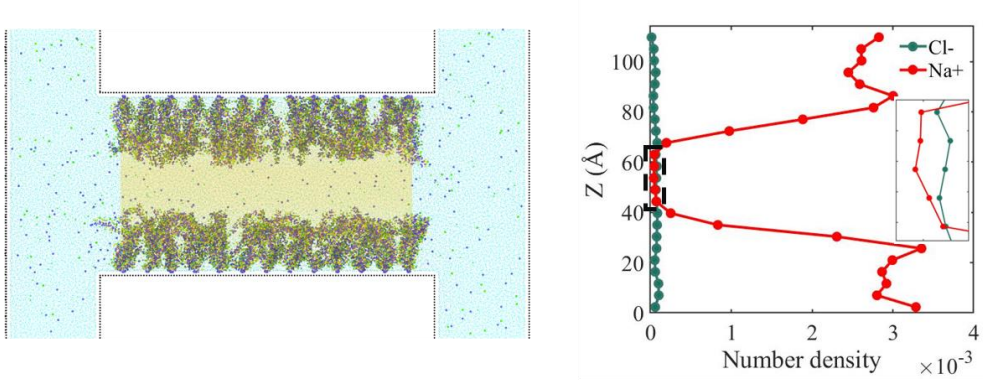

Figure 7.5: *(A) Simulation setup of the PE brush grafted nanochannel with the nanochannel being connected to two reservoirs at its two ends. (B) Ion distribution profile in the nanochannel. Yellow shaded region in (A) is considered for calculating the ion distribution profile [reported in (B)] within the nanochannel.*

7.2.2. Comparison of All-atom MD simulations and Continuum Calculations for Pressure-driven Transport in PE Brush-grafted Nanochannels to Prior Experimental Study

In this section, we provide a comparison of the nanoscale energy conversion characteristics (associated with the pressure-driven transport of water in PE brush-grafted nanochannels) obtained from our all-atom MD simulations (Chapter 6) as well as our continuum framework (Chapters 4 and 5) with a prior experimental study conducted by Heyden and coworkers.[19] The purpose of this comparison is not to provide a direct validation of our continuum/MD framework but rather to gain a sense of feasibility of the numbers obtained from the continuum/MD models. Heyden *et al* probed the pressure-driven transport of aqueous KCl solution in Silica nanochannels of length, L=4.5 mm and width, w=50 μm. The dissociation of the Silanol groups ($SiOH \rightleftharpoons SiO^- + H^+$) results in the accumulation of negative charges on the nanochannel walls, thereby giving rise to an EDL. Several experimental runs were conducted with different nanochannel heights and bulk salt concentrations. Before providing a comparison of our results with the experiments, we would like to point out that there are significant differences between our continuum/MD system and that of Heyden *et al*. Firstly, the channel dimensions for Heyden *et al* are orders of magnitude larger than ours. Our system has a nanochannel height of ~12 nm, while Heyden *et al* conducted experiments on nanochannels with heights between 70 nm and 1147 nm. Secondly, we consider PE brush grafted nanochannels while Heyden *et al* ran experiments on bare nanochannels with surface charges (no PE brush grafting). Thirdly, Heyden *et al* used KCl as the added salt in contrast to the NaCl used in our

studies. Fourthly, the nanochannel walls used in our MD simulations do not mimic the surface properties of the Silica nanochannel used by Heyden *et al*. Fifthly, the applied pressure gradient used in our system is orders of magnitude of higher than that probed in Heyden *et al*. As a result, one-to-one comparison between our work and Heyden *et al* is not possible. However, as mentioned before, this comparison will provide us a sense of feasibility of the results obtained from our continuum/MD framework.

Heyden *et al* reported their nanoscale energy conversion characteristics in the form of a quantity known as the streaming conductance (C_s). The streaming conductance is defined as the ratio of the streaming current (i_s) and the pressure difference applied across the length of the nanochannel ($L\nabla P$). Heyden *et al* observed a streaming conductance in the range of ~1-100 pA/bar (see Fig. 3 in Ref. 19) depending on the height of the nanochannel (which was varied from 70 nm to 1147 nm) and the KCl salt concentration (which was varied from 5.6 μM to 1 M). In an attempt to compare our results to the experimental findings of Heyden *et al*, we calculated the streaming conductance from our MD simulations and continuum calculations for both values of applied pressure gradients (see Table 7.3). We obtain streaming conductance values of ~10 pA/bar from our MD simulations, and ~40 pA/bar from our continuum framework (see Table 7.3), which are both within the range of values reported by Heyden *et al*. This serves as a check for the feasibility of our all-atom MD and theoretical results. However, this comparison does not illustrate the role played by the brushes in dictating the observed value of streaming conductance in our system (remember that Heyden *et al* conducted experiments on brush-free nanochannels). To quantify the effect of

brushes on the streaming conductance, we perform two separate continuum calculations: 1) Brush-free nanochannels with parameters corresponding to Heyden *et al* and 2) Nanochannels grafted with PE brushes carrying the same charge density as the surface charge density of the nanochannel walls for the brush-free case. Since, Heyden *et al* probed various combinations of nanochannel height and bulk salt concentration, we pick a particular combination with nanochannel height of 140 nm and bulk salt (KCl) concentration of 0.1 M for our continuum calculations. We utilize our Augmented Strong Stretching Theory (see Chapter 4) for the continuum calculations since the non-Poisson Boltzmann effects are negligible at 0.1 M bulk salt concentration (see Figures 4.20, 4.21 and 4.22). First, we calculated the surface charge density on the walls of the Silica nanochannels used by Heyden *et al* (for channel height of 140 nm and bulk salt concentration of 0.1 M). According to the Behrens-Grier model, the zeta potential (ζ) of the Silica nanochannel surface can be related to its surface charge density (σ) as:[214,215]

$$\zeta(\sigma) = \frac{k_B T}{e} ln\left(\frac{-\sigma}{e\Gamma+\sigma}\right) + ln(10)\frac{k_B T}{e}(pK_a - pH_\infty) - \frac{\sigma}{C} \tag{7.2}$$

where $k_B = 1.38 \times 10^{-23}$ J/K is the Boltzmann constant, e=1.6×10^{-19} C is the electronic charge, T=298 K is the temperature, $\Gamma = 8nm^{-2}$ is the surface density of Silanol groups, $pK_a = -ln(K_a)$ =7.9 (where K_a is the dissociation constant for Silanol groups) , $pH_\infty = 8$ is the bulk pH of the electrolyte, and $C = 0.3\ F/m^2$ is the capacitance of the Stern layer. The values of Γ, pK_a, pH_∞, and C have been taken from Heyden *et al*. Moreover, the Grahame equation relates the zeta potential and surface charge density for non-overlapping EDLs as:[214]

$$\sigma(\zeta) = \frac{2\epsilon_0\epsilon_r k_B T}{\lambda_D e} sinh\left(\frac{e\zeta}{2k_B T}\right) \quad (7.3)$$

where $\epsilon_0 = 8.854 \times 10^{-12}\ F/m$ is the permittivity of free space, $\epsilon_r = 78.54$ is the relative permittivity of water, and $\lambda_D = \sqrt{\frac{\epsilon_0\epsilon_r k_B T}{2e^2 n_\infty}}$ is the Debye screening length ($n_\infty = 1000 \times N_A \times c_\infty$; $c_\infty = 0.1\ M$ is the bulk Molarity of KCl and $N_A = 6.022 \times 10^{23}$ is the Avogadro's number). Note that the EDL thickness (λ_D) corresponding to our chosen bulk salt concentration of 0.1 M is ~1 nm, which is significantly lower than the half height of the nanochannel (70 nm). Thus, there is no EDL overlap, and eq. (7.3) is valid for our system. Solving eqs. (7.2,7.3) simultaneously yields the values of the equilibrium surface charge density, $\sigma = 23.36\ mC/m^2$ and zeta potential, $\zeta = 30.53$ mV for our chosen parametric combination (bulk salt concentration, $c_\infty = 0.1\ M$ and nanochannel half-height, h=70 nm). Next, we utilized our continuum framework (Chapters 4 and 5) to obtain the streaming conductance, $C_{s,\ no\ brush} = 3.65\ pA/bar$ for a bare (brush-free) nanochannel with the calculated surface charge density of $\sigma = 23.36\ mC/m^2$ (with $c_\infty = 0.1\ M, h = 70\ nm, L = 4.5\ mm, w = 50\ \mu m, and\ pH_\infty = 8$). The electrophoretic mobility of K^+ ions, $\mu_{K^+} = 7.12 \times 10^{-8}\ m^2/Vs$ and Cl^- ions, $\mu_{Cl^-} = 6.88 \times 10^{-8}\ m^2/Vs$ were taken from Ref. 210, and the dynamic viscosity of water was taken as $\eta = 8.904 \times 10^{-4}\ N/m^2 s$. The value of $C_{s,\ no\ brush} = 3.65\ pA/bar$ obtained from our continuum calculations is in excellent agreement with the value of streaming conductance reported by Heyden *et al* (~3.5 pA/bar) for nanochannel of height 140 nm and bulk salt concentration 0.1 M (see Fig. 2 in Ref. 19).

Next, we proceed to calculate the streaming conductance for the case of brush-grafted nanochannel carrying the same charge density (σ_{brush}) as the surface charge density of the brush-free nanochannel ($\sigma = 23.36\, mC/m^2$). For this purpose, we choose short lose brushes with $\ell = 60\, nm\ and\ N = 400$. Calculations were performed for $c_\infty = 0.1\, M, h = 70\, nm, L = 4.5\, mm, w = 50\, \mu m,\ pH_\infty = 8, \mu_{K^+} = 7.12 \times 10^{-8}\, m^2/Vs, \mu_{Cl^-} = 6.88 \times 10^{-8}\, m^2/Vs, \eta = 8.904 \times 10^{-4}\, N/m^2 s$. All other parameters (except number density of polyelectrolyte chargeable sites, γ) were identical to those used in Figure 5.2. γ was varied iteratively until the charge density of the brushes, $\sigma_{brush} = -e \int_{-h}^{-h+H_0} \phi n_{A^-} dy$ (where ϕ is the monomer volume fraction, n_{A^-} is the number density of ionized sites on the PE chains, and $H_0 = 47.36\, nm$ is the equilibrium brush height) matched the surface charge density of the bulk nanochannel ($\sigma = 23.36\, mC/m^2$). This procedure yielded a value of $\gamma = 2.415/a^3$. Finally, we obtained a value of streaming conductance, $C_s = 55.36\, pA/bar$ for the brush-grafted nanochannel, which is more than an order of magnitude greater than the value obtained for the brush-free nanochannel ($C_{s,\ no\ brush} = 3.65\, pA/bar$). This analysis shows that the presence of grafted PE brushes plays an instrumental role in increasing the streaming conductance associated with the pressure-driven flow. Thus, we anticipate that PE brush grafting (with the appropriate brush parameters) can be utilized as a mechanism to significantly increase the magnitude of streaming conductance obtained in the experimental study of Heyden *et al*.

7.3. Summary of Contributions

In this section, we summarize the major contributions of our work to the existing body of knowledge in the form of bullet points.

- Probe the microstructure of densely grafted water-swollen PE brushes via all-atom MD simulations.
    - Elucidate the local structure and arrangement of brush-trapped counterions. We investigated the effect of brush-induced confinement on the counterion distribution profile, counterion-water radial distribution function, counterion solvation structure, and mean squared displacement. We also establish the occurrence of PE brush-induced "water-in-salt"-like scenarios at high grafting densities of the brushes.
    - Elucidate the local structure and arrangement of the brush-trapped water molecules. We reveal how the presence of brushes changes the properties of water such as the orientational tetrahedral order parameter, dielectric constant, mass density, water-water radial distribution function, hydrogen bonding, and mean squared displacement.

- Probe the effect of charge density on the microstructure of water-swollen PE brushes via all-atom MD simulations.
    - Elucidate the effect of degree of ionization of weak polyionic brushes on the local structure and arrangement of brush-trapped counterions. We

quantify the role of charge density of the brushes in dictating properties such as counterion condensation, counterion solvation structure, counterion-water radial distribution function, and mean squared displacement. We show that "water-in-salt"-like scenarios can be triggered above a critical degree of ionization of the brushes.

- Elucidate the effect of degree of ionization of weak polyionic brushes on the local structure and arrangement of brush-trapped water molecules. We investigate the effect of charge density of the brushes on several water properties such as mass density, water-water radial distribution function, dielectric constant, hydrogen bonding, orientational tetrahedral order parameter, and mean squared displacement.

- Develop the augmented strong stretching theory (or augmented SST) model for pH-responsive PE brushes by improving the existing state-of-the-art continuum model (strong stretching theory or SST) to include the effects of excluded volume interactions and a generic mass action law. Using the augmented SST model, we elucidate the effects of excluded volume interactions and variation of the density of PE chargeable sites on brush height, monomer distribution profile, distribution of chain ends, and the brush-induced electrostatic potential profile.

- Develop the first continuum model (modified augmented strong stretching theory or MSST) that can capture the thermodynamics of pH-responsive PE brushes at ultra-large salt concentrations by incorporating several non-Poisson Boltzmann effects, namely ion-ion correlations, solvent polarization, and finite size of the ions and solvent dipoles. We elucidate the role of non-Poisson Boltzmann effects on the equilibrium brush height, monomer distribution profile, as well as the brush-induced electrostatic potential profile. We proceed to show that the results of the MSST model are in excellent agreement with our all-atom MD simulations.

- Develop a continuum framework to study the pressure driven transport of liquids in backbone charged PE brush-grafted nanochannels, where the thermodynamics of the brushes is calculated in a self-consistent fashion using our augmented SST model. This is a significant improvement over previous studies that do not consider a thermodynamically self-consistent description of the brushes. We show that under certain conditions, PE brush-grafting can help improve the nanoscale energy conversion efficiency associated with the pressure driven transport of liquids in nanochannels.

- Conduct MD simulations with a fully atomistic framework to probe the pressure-driven transport of water in PE brush-grafted nanochannels. Our MD simulations capture the presence of intriguing phenomena such as the flow-induced tilting of the PE chains and the overscreening of the brushes. We reveal

that the streaming current in our system is counterion-dominated despite the presence of overscreening. Finally, we proceed to show that our MD simulations and continuum models are in reasonable agreement with each other and discuss the reasons for the observed disparities in the values of streaming current, streaming electric field, velocity flux, etc. obtained from the two approaches.

Appendix A

We employ variational calculus to carry out the minimization of the free energy functional [eq. (4.12)]. Assuming that the chain is flexible (p=1) and taking the variation of each free energy component w.r.t. $E(x,x')$, $g(x')$, ψ, n_{A^-}, $n_{\pm}$, n_{H^+} and n_{OH^-}, we shall get:

$$\frac{\delta F'_{els}}{k_BT} = \frac{3}{2a^2}\left[\int_0^H g(x')dx' \int_0^{x'} \delta E(x,x')dx + \int_0^H \delta g(x')dx' \int_0^{x'} E(x,x')dx\right] + \lambda_1 \frac{\sigma}{a^3}\int_0^H \delta\phi(x)dx - \int_0^H \lambda_2(x')dx' \int_0^{x'} \frac{\delta E(x,x')}{E^2(x,x')}dx \tag{A1}$$

$$\frac{\delta F_{EV}}{k_BT} = \frac{\sigma}{a^3}\int_0^H \left(\frac{\delta f_{conc}}{\delta\phi}\right)\delta\phi dx \tag{A2}$$

$$\begin{aligned}\frac{\delta F_{elec}}{k_BT} + \frac{\delta F_{EDL}}{k_BT} &= \frac{\sigma}{k_BT}\int_0^\infty \left[-\frac{\epsilon_0\epsilon_r}{2}\delta\left|\frac{d\psi}{dx}\right|^2 + e\delta\psi(n_+ - n_- + n_{H^+} - n_{OH^-}) + e\psi(\delta n_+ \right.\\ &\left. - \delta n_- + \delta n_{H^+} - \delta n_{OH^-})\right]dx - \frac{\sigma}{k_BT}\int_0^H \delta\left[e\psi n_{A^-}(x)\phi\right]dx \\ &+ \sigma\int_0^\infty \delta\left[n_+\left(ln\left(\frac{n_+}{n_{+,\infty}}\right) - 1\right) + n_-\left(ln\left(\frac{n_-}{n_{-,\infty}}\right) - 1\right) + n_{H^+}\left(ln\left(\frac{n_{H^+}}{n_{H^+,\infty}}\right) - 1\right)\right. \\ &\left. + n_{OH^-}\left(ln\left(\frac{n_{OH^-}}{n_{OH^-,\infty}}\right) - 1\right) + \left(n_{+,\infty} + n_{-,\infty} + n_{H^+,\infty} + n_{OH^-,\infty}\right)\right]dx \\ &= \frac{\sigma}{k_BT}\int_0^\infty \left[\epsilon_0\epsilon_r\left(\frac{d^2\psi}{dx^2}\right)\delta\psi + e\delta\psi(n_+ - n_- + n_{H^+} - n_{OH^-}) + e\psi(\delta n_+ \right.\\ &\left. - \delta n_- + \delta n_{H^+} - \delta n_{OH^-})\right]dx - \frac{\sigma}{k_BT}\int_0^H \left[e\phi\left(\frac{K'_a\gamma}{K'_a + n_{H^+}}\right)\delta\psi \right.\\ &\left. - e\phi\psi\frac{K'_a\gamma}{(K'_a + n_{H^+})^2}\delta n_{H^+} + e\psi\left(\frac{K'_a\gamma}{K'_a + n_{H^+}}\right)\delta\phi\right]dx + \sigma\int_0^\infty \left[\delta n_+ ln\left(\frac{n_+}{n_{+,\infty}}\right)\right. \\ &\left. + \delta n_- ln\left(\frac{n_-}{n_{-,\infty}}\right) + \delta n_{H^+} ln\left(\frac{n_{H^+}}{n_{H^+,\infty}}\right) + \delta n_{OH^-} ln\left(\frac{n_{OH^-}}{n_{OH^-,\infty}}\right)\right]dx\end{aligned} \tag{A3}$$

$$\frac{\delta F_{ion}}{k_B T} = \frac{\sigma}{a^3}\int_0^H \delta\phi[(1-\frac{n_{A^-}}{\gamma})ln(1-\frac{n_{A^-}}{\gamma}) + \frac{n_{A^-}}{\gamma}ln(\frac{n_{A^-}}{\gamma}) + \frac{n_{A^-}}{\gamma}ln(\frac{n_{H^+,\infty}}{K_a'})]dx$$
$$+\frac{\sigma}{a^3}\int_0^H \phi\,\delta[(1-\frac{n_{A^-}}{\gamma})ln(1-\frac{n_{A^-}}{\gamma}) + \frac{n_{A^-}}{\gamma}ln(\frac{n_{A^-}}{\gamma}) + \frac{n_{A^-}}{\gamma}ln(\frac{n_{H^+,\infty}}{K_a'})]dx$$

$$= \frac{\sigma}{a^3}\int_0^H \delta\phi[(1-\frac{n_{A^-}}{\gamma})ln(1-\frac{n_{A^-}}{\gamma}) + \frac{n_{A^-}}{\gamma}ln(\frac{n_{A^-}}{\gamma}) + \frac{n_{A^-}}{\gamma}ln(\frac{n_{H^+,\infty}}{K_a'})]$$
$$+\frac{\sigma}{a^3}\int_0^H \phi\,\delta n_{A^-}[-\frac{1}{\gamma}ln(1-\frac{n_{A^-}}{\gamma}) + \frac{1}{\gamma}ln(\frac{n_{A^-}}{\gamma}) + \frac{1}{\gamma}ln(\frac{n_{H^+,\infty}}{K_a'})]dx$$

(A4)

Substituting eq.(A1), (A2), (A3) and (A4) in (4.13), we get:

$$\frac{\delta F'}{k_B T} = \frac{3}{2pa^2}\left[\int_0^H g(x')dx'\int_0^{x'}\delta E(x,x')dx + \int_0^H \delta g(x')dx'\int_0^{x'}E(x,x')\,dx\right]$$
$$+\lambda_1\frac{\sigma}{a^3}\int_0^H \delta\phi(x)\,dx - \int_0^H \lambda_2(x')dx'\int_0^{x'}\frac{\delta E(x,x')}{E^2(x,x')}dx$$
$$+\frac{\sigma}{a^3}\int_0^H (\frac{\delta f_{conc}}{\delta\phi})\delta\phi dx + \frac{\sigma}{k_B T}\int_0^\infty [\,\epsilon_0\epsilon_r(\frac{d^2\psi}{dx^2})\delta\psi + e\delta\psi(n_+ - n_-$$
$$+ n_{H^+} - n_{OH^-}) + e\psi(\delta n_+ - \delta n_- + \delta n_{H^+} - \delta n_{OH^-})]dx$$
$$-\frac{\sigma}{k_B T}\int_0^H [\,e\phi n_{A^-}\delta\psi + e\phi\psi\delta n_{A^-} + e\psi n_{A^-}\delta\phi]dx$$
$$+\sigma\int_0^\infty [\,\delta n_+ ln(\frac{n_+}{n_{+,\infty}}) + \delta n_- ln(\frac{n_-}{n_{-,\infty}}) + \delta n_{H^+} ln(\frac{n_{H^+}}{n_{H^+,\infty}})$$
$$+\delta n_{OH^-} ln(\frac{n_{OH^-}}{n_{OH^-,\infty}})]dx$$
$$+\frac{\sigma}{a^3}\int_0^H \delta\phi\left[\left(1-\frac{n_{A^-}}{\gamma}\right)ln\left(1-\frac{n_{A^-}}{\gamma}\right) + \frac{n_{A^-}}{\gamma}ln\left(\frac{n_{A^-}}{\gamma}\right)\right.$$
$$\left.+\frac{n_{A^-}}{\gamma}ln\left(\frac{n_{H^+,\infty}}{K_a'}\right)\right]dx$$
$$+\frac{\sigma}{a^3}\int_0^H \delta n_{A^-}\,\phi\left[-\frac{1}{\gamma}ln\left(1-\frac{n_{A^-}}{\gamma}\right) + \frac{1}{\gamma}ln\left(\frac{n_{A^-}}{\gamma}\right) + \frac{1}{\gamma}ln\left(\frac{n_{H^+,\infty}}{K_a'}\right)\right]dx$$

(A5)

Variation of eq.(4.10) gives:

$$\delta\phi(x) = \frac{a^3}{\sigma}\int_x^H [\frac{\delta g(x')}{E(x,x')} - \frac{g(x')\delta E(x,x')}{E^2(x,x')}]dx' \tag{A6}$$

Substituting eq.(A6) in (A5) and rearranging gives:

$$\begin{aligned}
\frac{\delta F'}{k_BT} = \int_0^H dx' \int_0^{x'} \delta\, E(x,x')[&\frac{3g(x')}{2pa^2} - \frac{\lambda_2(x')}{E^2(x,x')} - (\frac{\delta f_{conc}}{\delta\phi} + \lambda_1 - \frac{ea^3\psi}{k_BT} n_{A^-} + (1 \\
&- \frac{n_{A^-}}{\gamma})ln(1 - \frac{n_{A^-}}{\gamma}) + \frac{n_{A^-}}{\gamma} ln(\frac{n_{A^-}}{\gamma}) + \frac{n_{A^-}}{\gamma} ln(\frac{n_{H^+,\infty}}{K_a'}))\frac{g(x')}{E^2(x,x')}]dx \\
&+ \int_0^H dx'\, \delta g(x') \int_0^{x'} [\frac{3E(x,x')}{2pa^2} + (\frac{\delta f_{conc}}{\delta\phi} + \lambda_1 - \frac{ea^3\psi}{k_BT} n_{A^-} + (1 \\
&- \frac{n_{A^-}}{\gamma})ln(1 - \frac{n_{A^-}}{\gamma}) + \frac{n_{A^-}}{\gamma} ln(\frac{n_{A^-}}{\gamma}) + \frac{n_{A^-}}{\gamma} ln(\frac{n_{H^+,\infty}}{K_a'}))\frac{1}{E(x,x')}]dx \\
&+ \frac{\sigma}{\gamma a^3}\int_0^H \delta n_{A^-}\, \phi\left[-\gamma a^3 \frac{e\psi}{k_BT} - ln\left(1 - \frac{n_{A^-}}{\gamma}\right) + ln\left(\frac{n_{A^-}}{\gamma}\right)\right. \\
&\left. + ln\left(\frac{n_{H^+,\infty}}{K_a'}\right)\right] dx \\
&+ \frac{\sigma}{k_BT}\int_0^H \delta\psi\left[\epsilon_0\epsilon_r\left(\frac{d^2\psi}{dx^2}\right) + e(n_+ - n_- + n_{H^+} - n_{OH^-} - n_{A^-}\phi)\right] dx \\
&+ \frac{\sigma}{k_BT}\int_H^\infty \delta\psi\left[\epsilon_0\epsilon_r\left(\frac{d^2\psi}{dx^2}\right) + e(n_+ - n_- + n_{H^+} - n_{OH^-})\right] dx \\
&+ \sigma\int_0^\infty \delta n_+\left[\frac{e\psi}{k_BT} + ln\left(\frac{n_+}{n_{+,\infty}}\right)\right] dx \\
&+ \sigma\int_0^\infty \delta n_-\left[-\frac{e\psi}{k_BT} + ln\left(\frac{n_-}{n_{-,\infty}}\right)\right] dx \\
&+ \sigma\int_0^\infty \delta n_{H^+}\left[\frac{e\psi}{k_BT} + ln\left(\frac{n_{H^+}}{n_{H^+,\infty}}\right)\right] dx \\
&+ \sigma\int_0^\infty \delta n_{OH^-}\left[-\frac{e\psi}{k_BT} + ln\left(\frac{n_{OH^-}}{n_{OH^-,\infty}}\right)\right] dx
\end{aligned} \tag{A7}$$

Equating $\delta F' = 0$ yields the desired eqs.(4.14 - 4.20) since $\delta E(x,x') \neq 0, \delta g(x') \neq 0, \delta\psi \neq 0, \delta n_{A^-} \neq 0, \delta n_{\pm} \neq 0, \delta n_{H^+} \neq 0, \delta n_{OH^-} \neq 0.$

Appendix B

Eq.(4.44) expresses δF_e in terms of δD. Using eqs.(4.45,4.46,4.47), we can write:

$$\delta \boldsymbol{D} = \frac{\delta P_{pol}}{\delta \boldsymbol{E}} \delta \boldsymbol{E} + \varepsilon_0 \varepsilon_r \delta \boldsymbol{E} - \varepsilon_0 \varepsilon_r l_c^2 \delta(\nabla \cdot \nabla) \boldsymbol{E}.$$

(B1)

Using eq.(B1) along with the vector identity $\nabla \cdot \nabla E = \nabla(\nabla \cdot E) - \nabla \times (\nabla \times E) = \nabla(\nabla \cdot E)$ (since $\nabla \times E = -\nabla \times \nabla \psi = 0$), we can re-write eq.(4.44) as:

$$\delta F_e = \int_V \left[\frac{\delta P_{pol}}{\delta \boldsymbol{E}} \boldsymbol{E} \cdot \delta \boldsymbol{E} + \varepsilon_0 \varepsilon_r \boldsymbol{E} \cdot \delta \boldsymbol{E} - \varepsilon_0 \varepsilon_r l_c^2 \boldsymbol{E} \cdot \nabla \delta(\nabla \cdot \boldsymbol{E}) \right] dV.$$

(B2)

The vector identity, $E \cdot \nabla \delta(\nabla \cdot E) = \nabla \cdot \big(E \delta(\nabla \cdot E)\big) - \nabla \cdot E \delta(\nabla \cdot E)$, can then be used, where divergence theorem can be employed so that the first term on the right-hand side of the equation vanishes because of zero electric field at the substrate and at infinity. Therefore, eq.(B2) reduces to:

$$\delta F_e = \int_V \left[\frac{\delta P_{pol}}{\delta \boldsymbol{E}} \boldsymbol{E} \cdot \delta \boldsymbol{E} + \varepsilon_0 \varepsilon_r \boldsymbol{E} \cdot \delta \boldsymbol{E} + \varepsilon_0 \varepsilon_r l_c^2 \nabla \cdot \boldsymbol{E} \delta(\nabla \cdot \boldsymbol{E}) \right] dV.$$

(B3)

We next take the variational integral of δF_e from 0 to F_e and enforce the condition, $\nabla \cdot D = \rho_e$ [where $\rho = e(n_+ - n_- + n_{H^+} - n_{OH^-})$ is the volume charge density of mobile ions] using a Lagrange multiplier λ, to yield:

$$F_e = \int_V \left[\frac{n_w}{\beta} \left(\beta p_w \nabla\psi \mathcal{L}(\beta p_w \nabla\psi) - \ln\left(\frac{sinh(\beta p_w \nabla\psi)}{\beta p_w \nabla\psi} \right) \right) + \frac{\varepsilon_0 \varepsilon_r}{2} \left(|\nabla\psi|^2 + l_c^2 |\nabla^2\psi|^2 \right) + \lambda(\rho_e - \nabla \cdot \boldsymbol{D}) \right] dV. \tag{B4}$$

Substituting eq.(4.45) in eq.(B4) and using the Frechet functional derivative, $\frac{\delta F_e}{\delta \psi} = \lim_{\epsilon \to 0} \frac{F_e(\psi + \epsilon\psi_0 \delta_\epsilon) - F_e(\psi)}{\epsilon\psi_0} = 0$, we obtain $\lambda = \psi$; hence eq.(B4) reduces to eq.(4.48).

Appendix C

We start with eq.(4.49) and apply the conditions $Q(\chi_j) = \omega_j e^{-\beta\epsilon_j\chi_j}$, $E_j = \epsilon_j\chi_j, \omega_j = \frac{N_t!}{\chi_j!(N_t-\chi_j)!}$, $\xi_j = v_j\,/v_{H^+}$, and $\tilde{\mu_j} = \mu_j - \epsilon_j$ to reduce eq.(4.49) to:

$$\Xi = \sum_{\chi_w=0}^{N_t/\xi_w} \omega_w e^{\beta\tilde{\mu}_w\chi_w} \cdot \sum_{\chi_-=0}^{(N_t-\xi_w\chi_w)/\xi_-} \omega_- e^{\beta\tilde{\mu}_-\chi_-} \cdot \sum_{\chi_+=0}^{(N_t-\chi_w-\xi_-\chi_-)/\xi_+} \omega_+ e^{\beta\tilde{\mu}_+\chi_+} \cdot \sum_{\chi_{H^+}=0}^{(N_t-\chi_w-\xi_-\chi_--\xi_+\chi_+)/\xi_{H^+}} \omega_{H^+} e^{\beta\tilde{\mu}_{H^+}\chi_{H^+}} \cdot \sum_{\chi_{OH^-}=0}^{(N_t-\chi_w-\xi_-\chi_--\xi_+\chi_+-\xi_{H^+})/\xi_{OH^-}} \omega_{OH^-} e^{\beta\tilde{\mu}_{OH^-}\chi_{OH^-}} .$$

(C1)

The summations in the partition function can then be evaluated using the binomial theorem, assuming a progressive filling of the lattice sites with each species. Accordingly, eq.(C1) reduces to

$$\Xi = \left[\left(\left(\left(\left\{ 1 + e^{\beta\tilde{\mu}_{OH^-}} \right\}^{\xi_{H^+}/\xi_{OH^-}} + e^{\beta\tilde{\mu}_{H^+}} \right)^{\xi_+/\xi_{H^+}} + e^{\beta\tilde{\mu}_+} \right)^{\xi_-/\xi_+} + e^{\beta\tilde{\mu}_-} \right)^{\xi_w/\xi_-} + e^{\beta\tilde{\mu}_w} \right]^{N_t/\xi_w} .$$

(C2)

Given that $PV_L = k_B T ln\Xi$, where $V_L = N_t v_{H^+}$, we can finally write from eq.(C2)

$$P = \frac{k_B T}{v_{H^+}} ln \left[\left(\left(\left(\left\{ 1 + e^{\beta\tilde{\mu}_{OH^-}} \right\}^{\xi_{H^+}/\xi_{OH^-}} + e^{\beta\tilde{\mu}_{H^+}} \right)^{\xi_+/\xi_{H^+}} + e^{\beta\tilde{\mu}_+} \right)^{\xi_-/\xi_+} + e^{\beta\tilde{\mu}_-} \right)^{\xi_w/\xi_-} + e^{\beta\tilde{\mu}_w} \right]^{1/\xi_w} ,$$

(C3)

or, by taking constants out of $\tilde{\mu_j}$, we can write,

$$P = \frac{k_B T}{v_{H^+}} ln \left[\left(\left(\left(\left\{ 1 + \xi_{OH^-} e^{\beta \tilde{\mu}_{OH^-}} \right\}^{\xi_{H^+}/\xi_{OH^-}} + \xi_{H^+} e^{\beta \tilde{\mu}_{H^+}} \right)^{\xi_+/\xi_{H^+}} + \xi_+ e^{\beta \tilde{\mu}_+} \right)^{\xi_-/\xi_+} + \xi_- e^{\beta \tilde{\mu}_-} \right)^{\xi_w/\xi_-} + \xi_w e^{\beta \tilde{\mu}_w} \right]^{1/\xi_w}, \tag{C4}$$

which is eq.(4.50).

Bibliography

1. Chen, G.; Sachar, H. S.; Das, S. Efficient Electrochemomechanical Energy Conversion in Nanochannels Grafted with End-charged Polyelectrolyte Brushes at Medium and High Salt Concentration. *Soft Matter* **2018**, 14, 5246–5255.
2. Ali, M.; Yameen, B.; Neumann, R.; Ensinger, W.; Knoll, W.; Azzaroni, O. Biosensing and Supramolecular Bioconjugation in Single Conical Polymer Nanochannels. Facile Incorporation of Biorecognition Elements into Nanoconfined Geometries. *J. Am. Chem. Soc.* **2008**, 130, 16351−16357.
3. Ali, M.; Schiedt, B.; Neumann, R.; Ensinger, W. Biosensing with Functionalized Single Asymmetric Polymer Nanochannels. *Macromol. Biosci.* **2010**, 10, 28−32.
4. Umehara, S.; Karhanek, M.; Davis, R. W.; Pourmand, N. Label-Free Biosensing with Functionalized Nanopipette Probes. *Proc. Natl. Acad. Sci.* **2009**, 106, 4611−4616.
5. Motornov, M.; Sheparovych, R.; Lupitskyy, R.; MacWilliams, E.; Hoy, O.; Luzinov, I.; Minko, S. Stimuli-Responsive Colloidal Systems from Mixed Brush-Coated Nanoparticles. *Adv. Funct. Mater.* **2007**, 17, 2307–2314.
6. Yang, Q.; Li, L.; Zhao, F.; Han, H.; Wang, W.; Tian, Y.; Wang, Y.; Ye, Z.; Guo, X. Hollow Silica–Polyelectrolyte Composite Nanoparticles for Controlled Drug Delivery. *J. Mater. Sci.* **2019**, 54, 2552–2565.

7. Saraswathy, M.; Gong, S. Recent Developments in the Co-Delivery of SiRNA and Small Molecule Anticancer Drugs for Cancer Treatment. *Mater. Today* **2014**, 17, 298–306.
8. ShamsiJazeyi, H.; Miller, C. A.; Wong, M. S.; Tour, J. M.; Verduzco, R. Polymer-Coated Nanoparticles for Enhanced Oil Recovery. *J. Appl. Polym. Sci.* **2014**, 131, 40576.
9. Csajka, F. S.; Seidel, C. Strongly Charged Polyelectrolyte Brushes: A Molecular Dynamics Study. *Macromolecules* **2000**, 33, 2728–2739.
10. He, G. L.; Merlitz, H.; Sommer, J. U. Molecular Dynamics Simulations of Polyelectrolyte Brushes under Poor Solvent Conditions: Origins of Bundle Formation. *J. Chem. Phys.* **2014**, 140, 104911.
11. Sandberg, D. J.; Carrillo; J. M. Y.; Dobrynin, A. V. Molecular Dynamics Simulations of Polyelectrolyte Brushes: From Single Chains to Bundles of Chains. *Langmuir* **2007**, 23, 12716–12728.
12. Desai, P. R.; Sinha, S.; Das, S. Polyelectrolyte Brush Bilayers in Weak Interpenetration Regime: Scaling Theory and Molecular Dynamics Simulations. *Phys. Rev. E* **2018**, 97, 032503.
13. Mei, Y.; Hoffmann, M.; Ballauff, M.; Jusufi, A. Spherical Polyelectrolyte Brushes in the Presence of Multivalent Counterions: The Effect of Fluctuations and Correlations as Determined by Molecular Dynamics Simulations. *Phys. Rev. E* **2008**, 77, 031805.
14. Zhulina, E. B.; Borisov, O. V. Poisson−Boltzmann Theory of pH-Sensitive (Annealing) Polyelectrolyte Brush. *Langmuir* **2011**, 27, 10615−10633.

15. McEldrew, M.; Goodwin, Z. A. H.; Kornyshev, A. A.; Bazant, M. Z. Theory of the Double Layer in Water-in-salt Electrolytes. *J. Phys. Chem. Lett.* **2018**, 9, 5840−5846.
16. Cao, Q.; You, H. Electroosmotic Flow in Mixed Polymer Brush-grafted Nanochannels. *Polymers* **2016**, 8, 438.
17. Cao, Q.; Tian, X.; You, H. Electrohydrodynamics in Nanochannels Coated by Mixed Polymer Brushes: Effects of Electric Field Strength and Solvent Quality. *Model. Simul. Mat. Sci. Eng.* **2018**, 26, 035003.
18. Ouyang, H., Xia, Z., & Zhe, J. Voltage-controlled Flow Regulating in Nanofluidic Channels with Charged Polymer Brushes. *Microfluid. Nanofluid.* **2010**, 9, 915-922.
19. van der Heyden, F. H.; Stein, D.; Dekker, C. Streaming Currents in a Single Nanofluidic Channel. *Phys. Rev. Lett.* **2005**, 95, 116104.
20. Toomey, R., and Tirrell, M. (2012). Functional polymer brushes in aqueous media from self-assembled and surface-initiated polymers. Annu. Rev. Phys. Chem. *59*, 493–517.
21. Azzaroni, O. (2012). Polymer brushes here, there, and everywhere: recent advances in their practical applications and emerging opportunities in multiple research fields. J. Polym. Phys. A *50*, 3225–3258.
22. Galvin, C. J., and Genzer, J. (2012). Applications of surface-grafted macromolecules derived from post-polymerization modification reactions. Prog. Polym. Sci. *37*, 871–906.

23. Krishnamoorthy, M., Hakobyan, S., Ramstedt, M., and Gautrot, J. E. (2014). Surface-initiated polymer brushes in the biomedical field: applications in membrane science, biosensing, cell culture, regenerative medicine and antibacterial coatings. Chem. Rev. *114*, 10976–11026.

24. Das, S., Banik, M., Chen, G., Sinha, S., and Mukherjee, R. (2015). Polyelectrolyte brushes: theory, modelling, synthesis and applications. Soft Matt. *11*, 8550–8583.

25. Ali, M., Yameen, B., Cervera, J., Ramirez, P., Neumann, R., Ensinger, W., Knoll, W., and Azzaroni, O. (2010). Layer-by-layer assembly of polyelectrolytes into ionic current rectifying solid-state nanopores: insights from theory and experiment. J. Am. Chem. Soc. *132*, 8338–8348.

26. Yameen, B., Ali, M., Neumann, R., Ensinger, W., Knoll, W., and Azzaroni, O. (2009). Single conical nanopores displaying pH-tunable rectifying characteristics. manipulating ionic transport with zwitterionic polymer brushes. J. Am. Chem. Soc. *131*, 2070–2071.

27. Ali, M., Ramirez, P., Mafe, S., Neumann, R., and Ensinger, W. (2009). A pH-tunable nanofluidic diode with a broad range of rectifying properties. ACS Nano *3*, 603–608.

28. Vilozny, B., Wollenberg, A. L., Actis, P., Hwang, D., Singaram, B., and Pourmand, N. (2013). Carbohydrate-actuated nanofluidic diode: switchable current rectification in a nanopipette. Nanoscale *5*, 9214–9221.

29. Key, J., and Leary, J. F. (2014). Nanoparticles for multimodal in vivo imaging in nanomedicine. Int. J. Nanomedicine *9*, 711.

30. Liu, G., Cai, M., Wang, X., Zhou, F., and Liu, W. (2014). Core–shell–corona-structured polyelectrolyte brushes-grafting magnetic nanoparticles for water harvesting. ACS Appl. Mater. Interfaces *6*, 11625–11632.
31. Pincus, P. (1991). Colloid stabilization with grafted polyelectrolytes. Macromolecules *24*, 2912–2919.
32. Ross, R. S., and Pincus, P. (1992). The polyelectrolyte brush: poor solvent. Macromolecules *25*, 2177–2183.
33. Miklavic, S. J., and Marcelja, S. (1988). Interaction of surfaces carrying grafted polyelectrolytes. J. Phys. Chem. *92*, 6718–6722.
34. Misra, S., Varanasi, S., and Varanasi, P. P. (1989). A polyelectrolyte brush theory. Macromolecules *22*, 4173–4179.
35. Borisov, O. V., Birshtein, T. M., and Zhulina, E. B. (1991). Collapse of grafted polyelectrolyte layer. J. Phys. II *1*, 521–526.
36. Zhulina, E. B., and Rubinstein, M. (2012). Ionic strength dependence of polyelectrolyte brush thickness. Soft Matter *8*, 9376–9383.
37. Zhulina, E. B., and Borisov, O. V. (1997). Structure and interaction of weakly charged polyelectrolyte brushes: self-consistent field theory. J. Chem. Phys. *107*, 5952–5967.
38. Mei, Y., Lauterbach, K., Hoffmann, M., Borisov, O. V., Ballauff, M., and Jusufi, A. (2006). Collapse of spherical polyelectrolyte brushes in the presence of multivalent counterions. Phys. Rev. Lett. *97*, 158301.
39. Sachar, H. S., Sivasankar, V. S., and Das, S. (2019). Revisiting the strong stretching theory for pH-responsive polyelectrolyte brushes: effects of

consideration of excluded volume interactions and an expanded form of the mass action law. Soft Matter *15*, 559–574.

40. Carrillo, J. M. Y., and Dobrynin, A. V. (2009). Morphologies of planar polyelectrolyte brushes in a poor solvent: molecular dynamics simulations and scaling analysis. Langmuir *25*, 13158–13168.
41. Hehmeyer, O. J., and Stevens, M. J. (2005). Molecular dynamics simulations of grafted polyelectrolytes on two apposing walls. J. Chem. Phys. *122*, 134909.
42. Jackson, N. E., Brettmann, B. K., Vishwanath, V., Tirrell, M., and de Pablo, J. J. (2017). Comparing solvophobic and multivalent induced collapse in polyelectrolyte brushes. ACS Macro Lett. *6*, 155–160.
43. Merlitz, H., Li, C., Wu, C., and Sommer, J. U. (2015). Polyelectrolyte brushes in external fields: molecular dynamics simulations and mean-field theory. Soft Matter *11*, 5688–5696.
44. Kumar, N. A., and Seidel, C. (2005). Polyelectrolyte brushes with added salt. Macromolecules *38*, 9341–9350.
45. Wittemann, A., Drechsler, M., Talmon, Y., and Ballauff, M. (2005). High elongation of polyelectrolyte chains in the osmotic limit of spherical polyelectrolyte brushes: a study by cryogenic transmission electron microscopy. J. Am. Chem. Soc. *127*, 9688–9689.
46. Biesalski, M., Johannsmann, D., and Rühe, J. (2004). Electrolyte-induced collapse of a polyelectrolyte brush. J. Chem. Phys. *120*, 8807–8814.
47. Balastre, M., Li, F., Schorr, P., Yang, J., Mays, J. W., and Tirrell, M. V. (2002). A study of polyelectrolyte brushes formed from adsorption of amphiphilic

diblock copolymers using the surface forces apparatus. Macromolecules *35*, 9480–9486.

48. Yu, J., Jackson, N. E., Xu, X., Morgenstern, Y., Kaufman, Y., Ruths, M., de Pablo, J. J., and Tirrell, M. (2018). Multivalent counterions diminish the lubricity of polyelectrolyte brushes. Science *360*, 1434–1438.
49. Yu, J., Jackson, N. E., Xu, X., Brettmann, B. K., Ruths, M., de Pablo, J. J., and Tirrell, M. (2017). Multivalent ions induce lateral structural inhomogeneities in polyelectrolyte brushes. Sci. Adv. *3*, eaao1497.
50. Yu, J., Mao, J., Yuan, G., Satija, S., Chen, W., and Tirrell, M. (2016). The effect of multivalent counterions to the structure of highly dense polystyrene sulfonate brushes. Polymer *98*, 448–453.
51. Yu, J., Mao, J., Yuan, G., Satija, S., Jiang, Z., Chen, W., and Tirrell, M. (2016). Structure of polyelectrolyte brushes in the presence of multivalent counterions. Macromolecules *49*, 5609–5617.
52. Mahalik, J. P., Yang, Y., Deodhar, C., Ankner, J. F., Lokitz, B. S., Kilbey, S. M., Sumpter, B. G., and Kumar, R. (2016). Monomer volume fraction profiles in pH responsive planar polyelectrolyte brushes. J. Polym. Sci., Part B: Polym. Phys. *54*, 956–964.
53. Farina, R., Laugel, N., Pincus, P., and Tirrell, M. (2013). Brushes of strong polyelectrolytes in mixed mono-and tri-valent ionic media at fixed total ionic strengths. Soft Matter *9*, 10458–10472.

54. Schneider, C., Jusufi, A., Farina, R., Pincus, P., Tirrell, M., and Ballauff, M. (2010). Stability behavior of anionic spherical polyelectrolyte brushes in the presence of La (III) counterions. Phys. Rev. E *82*, 011401.

55. Yin, D. W., Horkay, F., Douglas, J. F., and de Pablo, J. J. (2008). Molecular simulation of the swelling of polyelectrolyte gels by monovalent and divalent counterions. J. Chem. Phys. *129*, 154902.

56. Sing, C. E., Zwanikken, J. W., and Olvera de la Cruz, M. (2013). Effect of ion–ion correlations on polyelectrolyte gel collapse and reentrant swelling. Macromolecules *46*, 5053–5065.

57. Erbaş, A., and Olvera de la Cruz, M. (2016). Interactions between polyelectrolyte gel surfaces. Macromolecules *49*, 9026–9034.

58. Yin, D. W., Olvera de la Cruz, M., and de Pablo, J. J. (2009). Swelling and collapse of polyelectrolyte gels in equilibrium with monovalent and divalent electrolyte solutions. J. Chem. Phys. *131*, 194907.

59. Chremos, A., and Douglas, J. F. (2016). Influence of higher valent ions on flexible polyelectrolyte stiffness and counter-ion distribution. J. Chem. Phys. *144*, 164904.

60. Chremos, A., and Douglas, J. F. (2017). Communication: counter-ion solvation and anomalous low-angle scattering in salt-free polyelectrolyte solutions. J. Chem. Phys. *147*, 241103.

61. Stoltz, C., de Pablo, J. J., and Graham, M. D. (2007). Simulation of nonlinear shear rheology of dilute salt-free polyelectrolyte solutions. J. Chem. Phys. *126*, 124906.

62. Longo, G. S., Olvera de la Cruz, M., and Szleifer, I. (2016). Controlling swelling/deswelling of stimuli-responsive hydrogel nanofilms in electric fields. Soft Matter *12*, 8359–8366.

63. Longo, G. S., Olvera de la Cruz, M., and Szleifer, I. (2014). Equilibrium adsorption of hexahistidine on pH-responsive hydrogel nanofilms. Langmuir *30*, 15335-15344.

64. Berendsen, H. J. C., Grigera, J. R., and Straatsma, T. P. (1987). The missing term in effective pair potentials. *J. Phys. Chem*. *91*, 6269–6271.

65. Ahrens, H., Förster, S., Helm, C. A., Kumar, N. A., Naji, A., Netz, R. R., amd Seidel, C. (2004). Nonlinear osmotic brush regime: experiments, simulations and scaling theory. J. Phys. Chem. B *108*, 16870–16876.

66. Nair, A. (2006). Molecular Dynamics Simulations of Polyelectrolyte Brushes. Ph.D. Dissertation, King Abdullah University of Science and Technology, Saudi Arabia.

67. Naji, A., Netz, R. R., and Seidel, C. (2003). Non-linear osmotic brush regime: simulations and mean-field theory. Eur. Phys. J. E *12*, 223–237.

68. Suo, L., Borodin, O., Gao, T., Olguin, M., Ho, J., Fan, X., Luo, C., Wang, C., and Xu, K. (2015). "Water-in-salt" electrolyte enables high-voltage aqueous lithium-ion chemistries. Science *350*, 938–943.

69. Yang, C., Chen, J., Qing, T., Fan, X., Sun, W., von Cresce, A., Ding, M. S., Borodin, O., Vatamanu, J., Schroeder, M. A., amd Eidson, N. (2017). 4.0 V aqueous Li-ion batteries. Joule *1*, 122–132.

70. Suo, L., Oh, D., Lin, Y., Zhuo, Z., Borodin, O., Gao, T., Wang, F., Kushima, A., Wang, Z., Kim, H. C., and Qi, Y. (2017). How solid-electrolyte interphase forms in aqueous electrolytes. J. Am. Chem. Soc. *139*, 18670–18680.

71. Vatamanu, V, and Borodin, O. (2018). Ramifications of water-in-salt interfacial structure at charged electrodes for electrolyte electrochemical stability. J. Phys. Chem. Lett. *8*, 4362–4367.

72. Han, J., Zhang, H., Varzi, A., and Passerini, S. (2018). Fluorine-free water-in-salt electrolyte for green and low-cost aqueous sodium-ion batteries. ChemSusChem *11*, 3704–3707.

73. Yang, C., Chen, J., Ji, X., Pollard, T. P., Lü, X., Sun, C. J., Hou, S., Liu, Q., Liu, C., Qing, T., and Wang, Y. (2019). Aqueous Li-ion battery enabled by halogen conversion–intercalation chemistry in graphite. Nature *569*, 245–250.

74. He, S. Z., Merlitz, H., Chen, L., Sommer, J. U., and Wu, C. X. (2010). Polyelectrolyte brushes: MD simulation and SCF theory. Macromolecules *43*, 7845–7851.

75. Lee, S. H., and Rasaiah, J. C. (1996). Molecular dynamics simulation of ion mobility. 2. alkali metal and halide ions using the SPC/E model for water at 25 C. J. Phys. Chem. *100*, 1420–1425.

76. Grossfield, A., Ren, P., and Ponder, J. W. (2003). Ion solvation thermodynamics from simulation with a polarizable force field. J. Am. Chem. Soc. *125*, 15671–15682.

77. Mancinelli, R., Botti, A., Bruni, F., Ricci, M. A., and Soper, A. K. (2007). Hydration of sodium, potassium, and chloride ions in solution and the concept of structure maker/breaker. J. Phys. Chem. B *111*, 13570–13577.
78. Poisson, A., and Papaud, A. (1983). Diffusion coefficients of major ions in seawater. Mar. Chem. *13*, 265–280.
79. Nielsen, J. M., Adamson, A. W., and Cobble, J. W. (1952). The self-diffusion coefficients of the ions in aqueous sodium chloride and sodium sulfate at 25°. J. Am. Chem. Soc. *74*, 446–451.
80. Hawlicka, E. (1987). Self-diffusion of sodium, chloride and iodide ions in acetonitrile-water mixtures. Z. Naturforsch. A *42*, 1014–1016.
81. Schneider, T., and Stoll, E. (1978). Molecular-dynamics study of a three-dimensional one-component model for distortive phase transitions. Phys. Rev. B *17*, 1302–1322.
82. Clark, G. N., Cappa, C. D., Smith, J. D., Saykally, R. J., and Head-Gordon, T. (2010). The structure of ambient water. Mol. Phys. *108*, 1415–1433.
83. Han, S. (2018). Dynamic features of water molecules in superconcentrated aqueous electrolytes. Sci. Rep. *8*, 9347.
84. Duboué-Dijon, E., and Laage, D. (2015). Characterization of the local structure in liquid water by various order parameters. J. Phys. Chem. B *119*, 8406–8418.
85. Elton, D. C. (2016). Understanding the Dielectric Properties of Water. Ph.D. Dissertation, The Graduate School, Stony Brook University: Stony Brook, NY.

86. Guardia, E., Martí, J., García-Tarrés, L., and Laria, D. A molecular dynamics simulation study of hydrogen bonding in aqueous ionic solutions. J. Mol. Liq. *117*, 63−67.

87. Luzar, A., and Chandler, D. (1993). Structure and hydrogen bond dynamics of water–dimethyl sulfoxide mixtures by computer simulations. J. Chem. Phys. *98*, 8160−8173.

88. Smith, J. D., Cappa, C. D., Wilson, K. R., Messer, B. M., Cohen, R. C., and Saykally, R. J. (2004). Energetics of hydrogen bond network rearrangements in liquid water. Science *306*, 851−853.

89. Muscatello, J., Jaeger, F., Matar, O. K., and Muller, E. A. (2016). Optimizing water transport through graphene-based membranes: insights from nonequilibrium molecular dynamics. ACS Appl. Mater. Interfaces *8*, 12330–12336.

90. Haggis, G. H., Hasted, J. B., and Buchanan, T. J. (1952). The dielectric properties of water in solutions. J. Chem. Phys. *20*, 1452–1465.

91. Mark, P., and Nilsson, L. (2001). Structure and dynamics of the TIP3P, SPC, and SPC/E water models at 298 K. J. Phys. Chem. A *105*, 9954–9960.

92. Hoover, W. G. (1985). Canonical dynamics: equilibrium phase-space distributions. Phys. Rev. A *31*, 1695–1697.

93. Nosé, S. (1984). A unified formulation of the constant temperature molecular dynamics methods. J. Chem. Phys. *81*, 511–519.

94. Lebedeva, I. O., Zhulina, E. B., and Borisov, O. V. (2017). Self-consistent field theory of polyelectrolyte brushes with finite chain extensibility. J. Chem. Phys. *146*, 214901.

95. Plimpton, S. (1995). Fast parallel algorithms for short-range molecular dynamics. J. Comput. Phys. *117*, 1–19.

96. Jorgensen, W. L., Maxwell, D. S., and Tirado-Rives, J. (1996). Development and testing of the OPLS all-atom force field on conformational energetics and properties of organic liquids. *J. Am. Chem. Soc. 118*, 11225–11236.

97. Hockney, R. W., amd Eastwood, J. W. (1981). Computer Simulations Using Particles (McGraw-Hill International Book Co).

98. Joung, I. S., and Cheatham III, T. E. (2008). Determination of alkali and halide monovalent ion parameters for use in explicitly solvated biomolecular simulations. J. Phys. Chem. B *112*, 9020–9041.

99. Ryckaert, J.-P., Ciccotti, G., and Berendsen, H. J. (1977). Numerical integration of the cartesian equation of motion of a system with constraints: molecular dynamics of n-alkanes. J. Comput. Phys. *23*, 327–341.

100. Stukowski, A. (2010). Visualization and analysis of atomistic simulation data with ovito–the open visualization tool. Model. Simul. Mater. Sci. Eng. *18*, 015012.

101. Murat, M., and Grest, G. S. (1989). Structure of a grafted polymer brush: a molecular dynamics simulation. Macromolecules *22*, 4054–4059.

102. Li, P., Roberts, B. P., Chakravorty, D. K., and Merz Jr, K. M. (2013). Rational design of particle mesh ewald compatible lennard-jones parameters for +2 metal cations in explicit solvent. J. Chem. Theory Comput. *9*, 2733-2748.

103. Di Tommaso, D., Ruiz-Agudo, E., de Leeuw, N. H., Putnis, A., and Putnis, C. V. (2014). Modelling the effects of salt solutions on the hydration of calcium ions. Phys. Chem. Chem. Phys. *16*, 7772-7785.

104. Kwon, H. J.; Osada, Y.; Gong, J. P. Polyelectrolyte Gels-Fundamentals and Applications. *Polym. J.* **2006**, 38, 1211–1219.

105. Hong, W.; Zhao, X.; Suo, Z. Large Deformation and Electrochemistry of Polyelectrolyte Gels. *J. Mech. Phys. Solids* **2010**, 58, 558–577.

106. Harland, R. S.; Prud'homme, R. K. *Polyelectrolyte Gels: Properties, Preparation, and Applications*; Washington, DC (United States), American Chemical Society, 1992.

107. Dobrynin, A. V.; Rubinstein, M. Theory of Polyelectrolytes in Solutions and at Surfaces. *Prog. Poly. Sci.* **2005**, 30, 1049–1118.

108. Muthukumar, M. 50th Anniversary Perspective: A Perspective on Polyelectrolyte Solutions. *Macromolecules* **2017**, 50, 9528–9560.

109. Barrat, J. L.; Joanny, J. F. Theory of Polyelectrolyte Solutions. *Adv. Chem. Phys.* **1996**, 94, 1–66.

110. Sing, C. E.; Olvera de la Cruz, M.; Polyelectrolyte Blends and Nontrivial Behavior in Effective Flory–Huggins Parameters. *ACS Macro Lett.* **2014**, 3, 698–702.

111. Gao, L.; Seliskar, C. J. Formulation, Characterization, and Sensing Applications of Transparent poly (vinyl alcohol)− Polyelectrolyte Blends. *Chem. Mater.* **1998**, 10, 2481–2489.

112. Zeglio, E.; Vagin, M.; Musumeci, C.; Ajjan, F. N.; Gabrielsson, R.; Trinh, X. T., Son, N. T.; Maziz, A.; Solin, N.; Inganäs, O. Conjugated Polyelectrolyte Blends for Electrochromic and Electrochemical Transistor Devices. *Chem. Mater.* **2015**, 27, 6385–6393.

113. Sachar, H. S.; Sivasankar, V. S.; Das, S. Electrokinetic Energy Conversion in Nanochannels Grafted with pH-responsive Polyelectrolyte Brushes Modelled using Augmented Strong Stretching Theory. *Soft Matter* **2019**, 15, 5973–5986.

114. Perez Sirkin, Y. A.; Szleifer, I.; Tagliazucchi, M. Voltage-Triggered Structural Switching of Polyelectrolyte-Modified Nanochannels. *Macromolecules* **2020**, 53, 2616–2626.

115. Sappidi, P.; Natarajan, U. Polyelectrolyte Conformational Transition in Aqueous Solvent Mixture Influenced by Hydrophobic Interactions and Hydrogen Bonding Effects: PAA–Water–Ethanol. *J. Mol. Graph. Model.* **2016**, 64, 60–74.

116. Sulatha, M. S.; Natarajan, U. Origin of the Difference in Structural Behavior of poly (acrylic acid) and poly (methacrylic acid) in Aqueous Solution Discerned by Explicit-Solvent Explicit-ion MD Simulations. *Ind. Eng. Chem.* **2011**, 50, 11785–11796.

117. Sulatha, M. S.; Natarajan, U. Molecular Dynamics Simulations of Adsorption of poly (acrylic acid) and poly (methacrylic acid) on

dodecyltrimethylammonium chloride Micelle in Water: Effect of Charge Density. *J. Phys. Chem. B* **2015**, 119, 12526–12539.

118. Ramachandran, S.; Katha, A. R.; Kolake, S. M.; Jung, B.; Han, S. Dynamics of Dilute Solutions of poly (aspartic acid) and its sodium Salt Elucidated from Atomistic Molecular Dynamics Simulations with Explicit Water. *J. Phys. Chem. B* **2013**, 117, 13906–13913.
119. Meneses-Juárez, E.; Márquez-Beltrán, C.; González-Melchor, M. Influence of pH on the Formation of a Polyelectrolyte Complex by Dissipative Particle Dynamics Simulation: From an Extended to a Compact Shape. *Phys. Rev. E* **2019**, 100, 012505.
120. Hao, Q. H.; Liu, L. X.; Xia, G.; Liu, L. Y.; Miao, B. The Effects of Grafting Density and Charge Fraction on the Properties of Ring Polyelectrolyte Brushes: A Molecular Dynamics Simulation Study. *Colloid Polym. Sci.* **2020**, 298, 21–33.
121. Santos, D. E.; Li, D.; Ramstedt, M.; Gautrot, J. E.; Soares, T. A. Conformational Dynamics and Responsiveness of Weak and Strong Polyelectrolyte Brushes: Atomistic Simulations of Poly (dimethyl aminoethyl methacrylate) and Poly (2-(methacryloyloxy) ethyl trimethylammonium chloride). *Langmuir* **2019**, 35, 5037–5049.
122. An, S. W.; Thirtle, P. N.; Thomas, R. K.; Baines, F. L.; Billingham, N. C.; Armes, S. P.; Penfold, J. Structure of a Diblock Copolymer Adsorbed at the Hydrophobic Solid/Aqueous Interface: Effects of Charge Density on a Weak Polyelectrolyte Brush. *Macromolecules* **1999**, 32, 2731–2738.

123. Topham, P. D.; Glidle, A.; Toolan, D. T.; Weir, M. P.; Skoda, M. W.; Barker, R.; Howse, J. R. The Relationship between Charge Density and Polyelectrolyte Brush Profile using Simultaneous Neutron Reflectivity and In Situ Attenuated Total Internal Reflection FTIR. *Langmuir* **2013**, 29, 6068–6076.

124. Sachar, H. S.; Pial, T. H.; Desai, P. R.; Etha, S. A.; Wang, Y.; Chung, P. W.; Das, S. Densely Grafted Polyelectrolyte Brushes Trigger "Water-in-Salt"-like Scenarios and Ultraconfinement Effect. *Matter* **2020**.

125. Swift, T.; Swanson, L.; Geoghegan, M.; Rimmer, S. The pH-responsive Behaviour of poly (acrylic acid) in Aqueous Solution is Dependent on Molar Mass. *Soft Matter* **2016**, 12, 2542–2549.

126. de Groot, G. W.; Santonicola, M. G.; Sugihara, K.; Zambelli, T.; Reimhult, E.; Voros, J.; Vancso, G. J. Switching Transport through Nanopores with pH-Responsive Polymer Brushes for Controlled Ion Permeability. *ACS Appl. Mater. Interface.* **2013**, 5, 1400−1407.

127. Moya, S.; Azzaroni, O.; Farhan, T.; Osborne, V. L.; Huck, W. T. S. Locking and Unlocking of Polyelectrolyte Brushes: Toward the Fabrication of Chemically Controlled Nanoactuators. *Angewand. Chem. Int. Ed.* **2005**, 44, 4578−4581.

128. Xin, B.; Hao, J. Reversibly Switchable Wettability. *Chem. Soc. Rev.* **2010**, 39, 769−782.

129. Mura, S.; Nicolas, J.; Couvreur, P. Stimuli-Responsive Nanocarriers for Drug Delivery. *Nature Mater.* **2013**, 12, 991.

130. Patwary, J.; Chen, G.; Das, S. Efficient Electrochemomechanical Energy Conversion in Nanochannels Grafted with Poly-electrolyte Layers with pH-Dependent Charge Density. *Microfluid. Nanofluid.* **2016**, 20, 37.

131. Chen, G.; Das, S. Scaling Laws and Ionic Current Inversion in Polyelectrolyte-Grafted Nanochannels. *J. Phys. Chem. B* **2015**, 119, 12714−12726.

132. Chen, G.; Das, S. Electroosmotic Transport in Polyelectrolyte-Grafted Nanochannels with pH-Dependent Charge Density. *J. Appl. Phys.* **2015**, 117, 185304.

133. Chen, G.; Das, S. Electrostatics of Soft Charged Interfaces with pH-Dependent Charge Density: Effect of Consideration of Appropriate Hydrogen Ion Concentration Distribution. *RSC Adv.* **2015**, 5, 4493−4501.

134. Wittmer, J.; Joanny, J. F. Charged Diblock Copolymers at Interfaces. *Macromolecules* **1993**, 26, 2691−2697.

135. Borisov, O. V.; Zhulina, E. B.; Birshtein, T. M. Diagram of the States of a Grafted Polyelectrolyte Layer. *Macromolecules* **1994**, 27, 4795−4803.

136. Zhulina, E. B.; Birshtein, T. M.; Borisov, O. V. Theory of Ionizable Polymer Brushes. *Macromolecules* **1995**, 28, 1491−1499.

137. Israels, R.; Leermakers, F. A. M.; Fleer, G. J.; Zhulina, E. B. Charged Polymeric Brushes: Structure and Scaling Relations. *Macromolecules* **1994**, 27, 3249−3261.

138. Chen, G.; Das, S. Anomalous Shrinking−Swelling of Nanoconfined End-Charged Polyelectrolyte Brushes: Interplay of Confinement and Electrostatic Effects. *J. Phys. Chem. B* **2016**, 120, 6848−6857.

139. Chen, G.; Das, S. Massively Enhanced Electroosmotic Transport in Nanochannels Grafted with End-Charged Polyelectrolyte Brushes. *J. Phys. Chem. B* **2017**, 121, 3130−3141.

140. Maheedhara, R. S.; Sachar, H. S.; Jing, H.; Das, S. Ionic Diffusoosmosis in Nanochannels Grafted with End-Charged Polyelectrolyte Brushes. *J. Phys. Chem. B* **2018**, 122, 7450−7461.

141. Biesheuvel, P. M.; de Vos, W. M.; Amoskov, V. M. Semianalytical Continuum Model for Nondilute Neutral and Charged Brushes Including Finite Stretching. *Macromolecules* **2008**, 41, 6254−6259.

142. Lyatskaya, Y. V.; Leermakers, F. A. M.; Fleer, G. J.; Zhulina, E. B.; Birshtein, T. M. Analytical Self-Consistent-Field Model of Weak Polyacid Brushes. *Macromolecules* **1995**, 28, 3562−3569.

143. Zhulina, E. B.; Wolterink, J. K.; Borisov, O. V. Screening Effects in a Polyelectrolyte Brush: Self-Consistent-Field Theory. *Macromolecules* **2000**, 33, 4945−4953.

144. Wu, T.; Gong, P.; Szleifer, I.; Vlcek, P.; Subr, V.; Genzer, J. Behavior of Surface-Anchored Poly(acrylic acid) Brushes with Grafting Density Gradients on Solid Substrates: 1. Experiment. *Macromolecules* **2007**, 40, 8756−8764.

145. Ito, Y.; Park, Y. S.; Imanishi, Y. Visualization of Critical pH-Controlled Gating of a Porous Membrane Grafted with Polyelectrolyte Brushes. *J. Am. Chem. Soc.* **1997**, 119, 2739−2740.

146. Li, D.; He, Q.; Yang, Y.; Mohwald, H.; Li, J. Two-Stage pH Response of Poly(4-vinylpyridine) Grafted Gold Nanoparticles. *Macromolecules* **2008**, 41, 7254−7256.

147. Wang, M.; Zou, S.; Guerin, G.; Shen, L.; Deng, K.; Jones, M.; Walker, G. C.; Scholes, G. D.; Winnik, M. A. A Water-Soluble pH-Responsive Molecular Brush of Poly(N,N-dimethylaminoethyl methacrylate) Grafted Polythiophene. *Macromolecules* **2008**, 41, 6993−7002.

148. Murdoch, J. T.; Willott, J. D.; de Vos; Nelson, A.; Prescott, S. W.; Wanless, E. J.; Webber, G. B. Influence of Anion Hydrophilicity on the Conformation of a Hydrophobic Weak Polyelectrolyte Brush. *Macromolecules* **2016**, 49, 9605−9617.

149. Cheesman, B. T.; Neilson, A. J. G.; Willott, J. D.; Webber, G. B.; Edmondson, S.; Wanless, E. J. Effect of Colloidal Substrate Curvature on pH-responsive Polyelectrolyte Brush Growth. *Langmuir* **2013**, 29, 6131−6140.

150. Willott, J. D.; Murdoch, T. J.; Humphreys, B. A.; Edmondson, S.; Wanless, E. J.; Webber, G. B. Anion-Specific Effects on the Behavior of pH-Sensitive Polybasic Brushes. *Langmuir* **2015**, 31, 3707−3717.

151. Zhulina, E. B.; Pryamitsyn, V. A.; Borisov, O. V. Structure and Conformational Transitions in Grafted Polymer Chain Layers. A New Theory. *Pol. Sci. USSR* **1989**, 31, 205−216.

152. Willott, J. D.; Murdoch, T. J.; Leermakers, F. A. M.; de Vos, W. M. Behavior of Weak Polyelectrolyte Brushes in Mixed Salt Solutions. *Macromolecules* **2018**, 51, 1198−1206.

153. Hariharan, R.; Biver, C.; Russel, W. B. Ionic Strength Effects in Polyelectrolyte Brushes: The Counterion Correction. *Macromolecules* **1998**, 31, 7514−7518.

154. Uline, M. J.; Rabin, Y.; Szleifer, I. Effects of the Salt Concentration on Charge Regulation in Tethered Polyacid Monolayers. *Langmuir* **2011**, 27, 4679−4689.

155. Longo, G. S.; de la Cruz, M. O.; Szleifer, I. Molecular Theory of Weak Polyelectrolyte Gels: The Role of pH and Salt Concentration. *Macromolecules* **2011**, 44, 147−158.

156. Morochnik, S.; Nap, R. J.; Ameer, G. A.; Szleifer, I. Structural Behavior of Competitive Temperature and pH-Responsive Tethered Polymer Layers. *Soft Matt.* **2017**, 13, 6332−6331.

157. Longo, G. S.; Szleifer, I. Adsorption and Protonation of Peptides and Proteins in pH Responsive Gels. *J. Phys. D. Appl. Phys.* **2016**, 49, 323001.

158. Gilles, F. M.; Tagliazucchi, M.; Azzaroni, O.; Szleifer, I. Ionic Conductance of Polyelectrolyte-Modified Nanochannels: Nanoconfinement Effects on the Coupled Protonation Equilibria of Polyprotic Brushes. *J. Phys. Chem. C* **2016**, 120, 4789−4798.

159. Zhulina, E. B.; Rubinstein, M. Lubrication by Polyelectrolyte Brushes. *Macromolecules* **2014**, 47, 5825−5838.

160. Zeng, Z.; Yeh, L-H.; Zhang, M.; Qian, S. Ion Transport and Selectivity in Biomimetic Nanopores with pH-Tunable Zwitterionic Polyelectrolyte Brushes. *Nanoscale* **2015**, 7, 17020−17029.

161. Niu, B.; Xiao, K.; Huang, X.; Zhang, Z.; Kong, X-Y.; Wang, Z.; Wen, L.; Jiang, L. High-Sensitivity Detection of Iron(III) by Dopamine-Modified Funnel-Shaped Nanochannels. *ACS Appl. Mater. Interfaces* **2018**, 10, 22632−22639.

162. Liu, M.; Zhang, H.; Li, K.; Heng, L.; Wang, S.; Tian, Y.; Jian, L. A Bioinspired Potassium and pH Responsive Doublegated Nanochannel. *Adv. Func. Mater.* **2015**, 25, 421−426.

163. Lopez, L. G.; Nap, R. J. Highly Sensitive Gating in pH-Responsive Nanochannels as a Result of Ionic Bridging and Nanoconfinement. *Phys. Chem. Chem. Phys.* **2018**, 20, 16657−16665.

164. Zhang, M.; Hou, X.; Wang, J.; Tian, Y.; Fan, X.; Zhai, J.; Jiang, L. Light and pH Cooperative Nanofluidic Diode using a Spiropyran Functionalized Single Nanochannel. *Adv. Mater.* **2012**, 24, 2424−2428.

165. Azzaroni, O.; Brown, A. A.; Huck, W. T. S. Tunable Wettability by Clicking Counterions into Polyelectrolyte Brushes. *Adv. Mater.* **2007**, 19, 151−154.

166. Chen. G.; Patwary, J.; Sachar, H. S.; Das, S. Electrokinetics in Nanochannels Grafted with Polyzwitterionic Brushes. *Microfluid. Nanofluid.* **2018**, 22, 112.

167. Li, H.; Chen, G.; Das, S. Electric Double Layer Electrostatics of pH-Responsive Spherical Polyelectrolyte Brushes in the Decoupled Regime. *Colloid. Surf. B* **2016**, 147, 180−190.

168. Motornov, M.; Tam, T. K.; Pita, M.; Tokarev, I.; Katz, E.; Minko, S. Switchable Selectivity for Gating Ion Transport with Mixed Polyelectrolyte Brushes: Approaching Smart Drug Delivery Systems. *Nanotechnology* **2009**, 20, 434006.

169. Wang, S.; Chen, K.; Li, L.; Guo, X. Binding between Proteins and Cationic Spherical Polyelectrolyte Brushes: Effect of pH, Ionic strength, and Stoichiometry. *Biomacromolecules* **2013**, 14, 818−827.

170. Zhu, Y.; Chen, K.; Wang, X.; Guo, X. Spherical Polyelectrolyte Brushes as a Nanoreactor for Synthesis of Ultrafine Magnetic Nanoparticles. *Nanotechnology* **2012**, 23, 265601.

171. Kumar, R.; Sumpter, B. G.; Kilbey, S. M. Charge Regulation and Local Dielectric Function in Planar Polyelectrolyte Brushes. *J. Chem. Phys.* **2012**, 136, 234901.

172. Deshkovski, A.; Obukhov, S.; Rubinstein, M. Counterion Phase Transitions in Dilute Polyelectrolyte Solutions. *Phys. Rev. Lett.* **2001**, 86, 2341−2344.

173. Kilic, M. S.; Bazant, M. Z.; Ajdari, A. Steric Effects in the Dynamics of Electrolytes at Large Applied Voltages. I. Double-Layer Charging. *Phys. Rev. E* **2007**, 75, 021502.

174. Chanda, S.; Das, S. Effect of Finite Ion Sizes in an Electrostatic Potential Distribution for a Charged Soft Surface in Contact with an Electrolyte Solution. *Phys. Rev. E* **2014**, 89, 012307.

175. Misra, R. P.; Das, S.; Mitra, S. K. Electric Double Layer Force between Charged Surfaces: Effect of Solvent Polarization. *J. Chem. Phys.* **2013**, 138, 114703.

176. Storey, B. D.; Bazant, M. Z. Effects of Electrostatic Correlations on Electrokinetic Phenomena. *Phys. Rev. E* **2012**, 86, 056303.

177. Rathee, V. S.; Sikora, B. J.; Sidky, H.; Whitmer, J. K. Simulating the Thermodynamics of Charging in Weak Polyelectrolytes: the Debye-Huckel Limit. Mater. *Res. Exp.* **2018**, 5, 014010.

178. Alexander-Katz, A.; Moreira, A. G.; Fredrickson, G. H. Field-theoretic Simulations of Confined Polymer Solutions. *J. Chem. Phys.* **2003**, 118, 9030−9036.

179. Bazant, M. Z.; Storey, B. D.; Kornyshev, A. A. Double Layer in Ionic Liquids: Overscreening versus Crowding. *Phys. Rev. Lett.* **2011**, 106, 046102.

180. Fedorov, M. V.; Kornyshev, A. A. Ionic Liquids at Electrified Interfaces. *Chem. Rev.* **2014**, 114, 2978−3036.

181. Kornyshev, A. A. Double-layer in Ionic Liquids: Paradigm Change? *J. Phys. Chem. B* **2007**, 111, 5545−5557.

182. Han, Y.; Huang, S.; Yan, T. A Mean-field Theory on the Differential Capacitance of Asymmetric Ionic Liquid Electrolytes. *J. Phys. Condens. Matter* **2014**, 26, 284103.

183. Andrews, J. E.; Das, S. Anomalous Shrinking–Swelling of Nanoconfined End-Charged Polyelectrolyte Brushes: Interplay of Confinement and Electrostatic Effects. *RSC Adv.* **2015**, 5, 46873−46880.

184. Sin, J-S.; Kim, N-H.; Sin, C-S. Effect of Solvent Polarization on Electric Double Layer of a Charged Soft Surface in an Electrolyte Solution. *Colloid Surf. A* **2017**, 529, 972−978.

185. Perry, R. H.; Green, D. W.; Maloney, J. O. Perry's Chemical Engineers' Handbook, McGraw-Hill, New York, **1997**.

186. Celebi, A. T.; Cetin, B.; Beskok, A. Molecular and Continuum Perspectives on Intermediate and Flow Reversal Regimes in Electroosmotic Transport. *J. Phys. Chem. C* **2019**, 123, 14024−14035

187. Marcus, Y. Volumes of Aqueous Hydrogen and Hydroxide Ions at 0 to 200 C. *J. Chem. Phys.* **2012**, 137, 154501.

188. Poddar, A.; Maity, D.; Bandopadhyay, A.; Chakraborty, S. Electrokinetics in Polyelectrolyte Grafted Nanofluidic Channels Modulated by the Ion Partitioning Effect. *Soft Matter* **2016**, 12, 5968−5978.

189. Colombo, P.; Sonvico, F.; Colombo, G.; Bettini, R. Novel Platforms for Oral Drug Delivery. *Pharmaceutical Research* **2009**, *26*, 601−611.

190. Gullotti, E.; Yeo, Y. Extracellularly Activated Nanocarriers: A New Paradigm of Tumor Targeted Drug Delivery. *Molecular Pharmaceutics* **2009**, *6*, 1041−1051.

191. Choi, C. H. J.; Zuckerman, J. E.; Webster, P.; Davis, M. E. Targeting Kidney Mesangium by Nanoparticles of Defined Size. *Proceedings of the National Academy of Sciences* **2011**, *108*, 6656−6661.

192. Saleh, N.; Sarbu, T.; Sirk, K.; Lowry, G. V.; Matyjaszewski, K.; Tilton, R. D. Oil-in-Water Emulsions Stabilized by Highly Charged Polyelectrolyte-grafted Silica Nanoparticles. *Langmuir* **2005**, *21*, 9873−9878.

193. Maheedhara, R. S.; Jing, H.; Sachar, H. S.; Das, S. Highly Enhanced Liquid Flows via Thermoosmotic Effects in Soft and Charged Nanochannels. *Physical Chemistry Chemical Physics* **2018**, *20*, 24300−24316.

194. Chanda, S.; Sinha, S.; Das, S. Streaming Potential and Electroviscous Effects in Soft Nanochannels: Towards Designing more Efficient Nanofluidic Electrochemomechanical Energy Converters. *Soft Matter* **2014**, *10*, 7558−7568.

195. Chen, G.; Das, S. Streaming Potential and Electroviscous Effects in Soft Nanochannels beyond Debye–Hückel Linearization. *Journal of Colloid and Interface Science* **2015**, *445*, 357−363.

196. Jian, Y.; Li, F.; Liu, Y.; Chang, L.; Liu, Q.; Yang, L. Electrokinetic Energy Conversion Efficiency of Viscoelastic Fluids in a Polyelectrolyte-grafted Nanochannel. *Colloids and Surfaces B: Biointerfaces* **2017**, *156*, 405−413.

197. Milne, Z.; Yeh, L. H.; Chou, T. H.; Qian, S. Tunable Donnan Potential and Electrokinetic Flow in a Biomimetic Gated Nanochannel with pH-regulated Polyelectrolyte Brushes. *The Journal of Physical Chemistry C* **2014**, *118*, 19806−19813.

198. Yeh, L. H.; Zhang, M.; Hu, N.; Joo, S. W.; Qian, S.; Hsu, J. P. Electrokinetic Ion and Fluid Transport in Nanopores Functionalized by Polyelectrolyte Brushes. *Nanoscale* **2012**, *4*, 5169−5177.

199. Yeh, L. H.; Zhang, M.; Joo, S. W.; Qian, S.; Hsu, J. P. Controlling pH-regulated Bionanoparticles Translocation through Nanopores with Polyelectrolyte Brushes. *Analytical Chemistry* **2012**, *84*, 9615−9622.

200. Benson, L.; Yeh, L. H.; Chou, T. H.; Qian, S. Field Effect Regulation of Donnan Potential and Electrokinetic Flow in a Functionalized Soft Nanochannel. *Soft Matter* **2013**, *9*, 9767−9773.

201. Zhou, C.; Mei, L.; Su, Y. S.; Yeh, L. H.; Zhang, X.; Qian, S. Gated Ion Transport in a Soft Nanochannel with Biomimetic Polyelectrolyte Brush Layers. *Sensors and Actuators B: Chemical* **2016**, *229*, 305−314.

202. Li, F.; Jian, Y.; Chang, L.; Zhao, G.; Yang, L. Alternating Current Electroosmotic Flow in Polyelectrolyte-grafted Nanochannel. *Colloids and Surfaces B: Biointerfaces* **2016**, *147*, 234−241.

203. Li, F.; Jian, Y.; Xie, Z.; Liu, Y.; Liu, Q. Transient Alternating Current Electroosmotic Flow of a Jeffrey Fluid through a Polyelectrolyte-grafted Nanochannel. *RSC Advances* **2017**, *7*, 782−790.

204. Sin, J. S.; Kim, U. H. Ion Size Effect on Electrostatic and Electroosmotic Properties in Soft Nanochannels with pH-dependent Charge Density. *Physical Chemistry Chemical Physics* **2018**, *20*, 22961−22971.

205. Park, H. G., & Jung, Y. (2014). Carbon nanofluidics of rapid water transport for energy applications. *Chemical Society Reviews*, *43*(2), 565-576.

206. Gillespie, D. (2012). High energy conversion efficiency in nanofluidic channels. *Nano letters*, *12*(3), 1410-1416.

207. Etha, S. A., Sivasankar, V. S., Sachar, H. S., & Das, S. (2020). Strong stretching theory for pH-responsive polyelectrolyte brushes in large salt concentrations. *Physical Chemistry Chemical Physics*, *22*(24), 13536-13553.

208. Jin, Y., Ng, T., Tao, R., Luo, S., Su, Y., & Li, Z. (2020). Coupling effects in electromechanical ion transport in graphene nanochannels. *Physical Review E*, *102*(3), 033112.

209. Pial, T. H., Sachar, H. S., Desai, P. R., & Das, S. (2021). Overscreening, coion-dominated electroosmosis, and electric field strength mediated flow reversal in polyelectrolyte brush functionalized nanochannels. *ACS Nano*. https://doi.org/10.1021/acsnano.0c09248

210. Koneshan, S., Rasaiah, J. C., Lynden-Bell, R. M., & Lee, S. H. (1998). Solvent structure, dynamics, and ion mobility in aqueous solutions at 25 C. *The Journal of Physical Chemistry B, 102*(21), 4193-4204.

211. Cassone, G., Creazzo, F., Giaquinta, P. V., Saija, F., & Saitta, A. M. (2016). Ab initio molecular dynamics study of an aqueous NaCl solution under an electric field. *Physical Chemistry Chemical Physics*, *18*(33), 23164-23173.

212. Sachar, H. S., Pial, T. H., Chava, B. S., & Das, S. (2020). All-atom molecular dynamics simulations of weak polyionic brushes: influence of charge density on the properties of polyelectrolyte chains, brush-supported counterions, and water molecules. *Soft Matter*, *16*(33), 7808-7822.

213. Sachar, H. S., Chava, B. S., Pial, T. H., & Das, S. (2021). Hydrogen bonding and its effect on the orientational dynamics of water molecules inside polyelectrolyte brush-induced soft and active nanoconfinement. *Macromolecules*, 54(4), 2011-2021.

214. Behrens, S. H., & Grier, D. G. (2001). The charge of glass and silica surfaces. *The Journal of Chemical Physics*, *115*(14), 6716-6721.

215. Sachar, H. S., Sivasankar, V. S., & Das, S. (2019). Electrostatics and interactions of an ionizable silica nanoparticle approaching a plasma membrane. *Langmuir 35*(11), 4171-4181.

216. Odegard, G. M.; Clancy, T. C.; Gates, T. S.; 46th AIAA/ASME/ASCE/AHS/ASC Structures, Structural Dynamics and Materials Conference, Austin, **2005**.

217. Smith, M. D.; Rao, J. S.; Segelken, E.; Cruz, L.; Force-Field Induced Bias in the Structure of Aβ21–30: A Comparison of OPLS, AMBER, CHARMM, and GROMOS Force Fields. *J. Chem. Inf. Model.* **2015**, 55, 2587.

218. Sharma, P.; Roy, S.; Karimi-Varzaneh, H. A.; Validation of force fields of rubber through glass-transition temperature calculation by microsecond atomic-scale molecular dynamics simulation. *J. Phys. Chem. B.* **2016**, 120, 1367-1379.

219. Heyden, F. H. J. v. d.; Stein, D.; Besteman, K.; Lemay, S. G.; Dekker., C.; Charge inversion at high ionic strength studied by streaming currents. *Phys. Rev. Lett,* **2006**, 96, 224502.

220. Besteman, K.; Zevenbergen, M. A. G.; Lemay, S. G.; Charge inversion by multivalent ions: Dependence on dielectric constant and surface-charge density. *Phys. Rev. E*, **2005**, 72, 061501.

221. Peng R.; Li, D.; Electroosmotic flow in single PDMS nanochannels, *Nanoscale* 8, **2016**, 12237-12246.

222. Paratore, F.; Boyko, E.; Kaigala, G. V.; Bercovici, M.; Electroosmotic flow dipole: Experimental observation and flow field patterning. *Phys. Rev. Lett.* **2019**, 122, 224502.

223. Wu, D.; Qin, J.; Lin, B.; Self-assembled epoxy-modified polymer coating on a poly(dimethylsiloxane) microchip for EOF inhibition and biopolymers separation. *Lab Chip,* **2007**, 7, 1490-1496.